Catalytic control in out-of-equilibrium assembly systems

Important note
To cite this publication, please use the final published version (if applicable).
Please check the document version above.

Catalytic control in out-of-equilibrium assembly systems

Proefschrift

ter verkrijging van de graad van doctor
aan de Technische Universiteit Delft,
op gezag van Rector Magnificus, Prof. dr. ir. T.H.J.J. van der Hagen
voorzitter van het College voor Promoties,
in het openbaar te verdedigen op

Dinsdag 29 oktober 2019 om 15:00 uur

door

Susanne Alida Petronella VAN ROSSUM

Master of Science in Chemistry
Universiteit Utrecht
geboren te Vlist, Nederland

Dit proefschrift is goedgekeurd door de promotoren.

Samenstelling promotiecommissie bestaat uit:

Rector magnificus,	voorzitter
Dr. R. Eelkema	Technische Universiteit Delft, promotor
Prof. dr. J.H. van Esch	Technische Universiteit Delft, promotor

Onafhankelijke leden:

Prof. dr. S.J. George	Jawaharlal Nehru Centre for Advanced Scientific Research
Prof. dr. P. Besenius	Johannes Gutenberg Universiteit Mainz
Prof. dr. A.R.A. Palmans	Technische Universiteit Eindhoven
Prof. dr. U. Hanefeld	Technische Universiteit Delft
Prof. dr. S.J. Picken	Technische Universiteit Delft, reservelid

Andere leden:

Prof. dr. W.K. Kegel	Universiteit Utrecht

An electronic version of this thesis is freely available at http://repository.tudelft.nl

Table of contents

Chapter 1

Introduction

Over the last decades, the focus of material science has shifted from a static to a dynamic viewpoint. Originally, enhancing the stability and durability of materials was limited to maximizing their mechanical and structural properties.[1-4] Nowadays, we realize that structural response to the environment instead of inertness can also be beneficial for many fields, such as drug delivery, sensors, optics and electronics.[5-7] In addition, we became aware that response to the environment can also reinforce the durability of materials by e.g., self-healing.[8] Achieving this dynamic structural behavior can be achieved in structures that reside in equilibrium, but is remarkably more accessible using the dynamics of out-of-equilibrium assembly. Therefore, in this thesis we investigate and expand the knowledge and potential of out-of-equilibrium assembly with the focus on catalysis.

1.1. Self-assembly vs. out-of-equilibrium assembly

Self-assembly is the spontaneous formation of organized structures from small components based on reversible non- or weak-covalent interactions.[9] This method has become popular last decennia as a large variety of structures can be achieved depending on the molecular or particle properties (Figure 1.1).[10-13] The assembled structure can be tuned by the strength and directionality of the non-covalent interactions between the components itself and the environment (e.g., Van der Waals, electrostatic and hydrophobic interactions).[9, 14] The self-assembled structures are dynamic, but have a static overall composition. Accordingly, they are in a chemical equilibrium, which either is the thermodynamic equilibrium or a kinetically trapped state.[15] Only when a trigger is added they can switch to a new stable state.[7, 16]
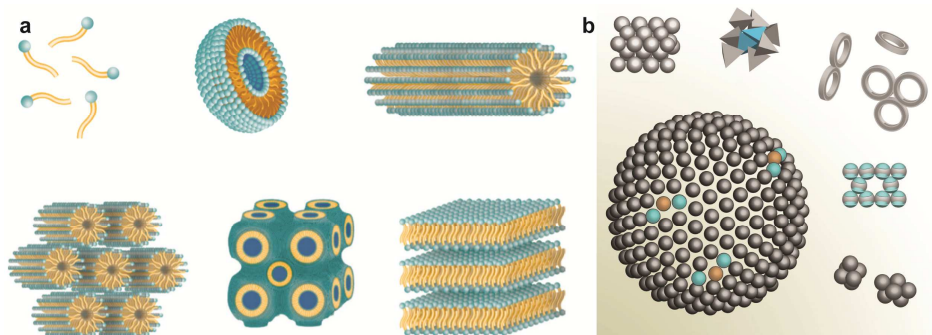
Figure 1.1. Various reversible and chemically stable self-assembled structures formed from **(a)** surfactants and **(b)** colloids as examples of the potential of self-assembly. Adapted from reference 12 and 13.

Assembled structures that reside at equilibrium are stable and do not change over time. Sometimes assembled structures need to form, change and break down again to carry out a transient function. Microtubuli in cells are for example repeatedly formed and broken down, driven by the conversion of GTP (guanosine-5'-triphosphate).[17, 18] When an assembly process needs an energy input to be maintained, the assembly is called out-of-equilibrium assembly or fuel-driven assembly.[15] Here, soluble, stable building blocks are activated with an energy source (fuel) resulting in the formation of activated building blocks that can assemble (Figure 1.2).[19] These structures are in an unstable state and spontaneously fall apart into the original stable building blocks. Out-of-equilibrium assembly is a general method to control the kinetics of formation, lifetime and dissolution of the assembled structure. More general, it can regulate functions and properties, such as color, motion, density or stiffness of materials over time.[20-23]
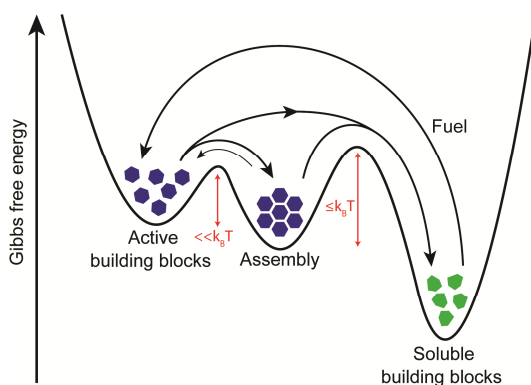
Figure 1.2. Energy landscape during the fuel-driven assembly. Soluble building blocks in a chemical equilibrium are activated with a chemical fuel. These activated building blocks assemble into an unstable structure and spontaneously react back to the soluble building blocks.

1.2. Chemical reaction networks

In more detail the kinetics of the formation and dissolution of the assembled structure is controlled by the chemical reaction network (CRN). The CRN consists of multiple reaction pathways which are responsible for the formation and depletion of activated building blocks (Figure 1.3). A molecular fuel reacts with the soluble building block to the activated building block resulting in its assembly at high concentrations. The activated building block is unstable and reacts therefore with an omnipresent environmental substrate, such as water, oxygen, protons, to the original soluble

building blocks. To control the kinetics of the individual reactions the concentration of the individual components can be regulated. Increasing the fuel concentration increases the formation rate of the activated building block resulting in a faster assembly rate.[24-27] The depletion rate of the activated building blocks can often be controlled using environmental factors such as pH or ionic strength.[23, 28] Overall, the kinetics of the CRN can be controlled using several reaction parameters, in turn leading to kinetic control over assembly behavior.

Several thermodynamic and kinetic design rules need attention upon making these fuel-driven assembled structures.[23, 29] First, at least one interaction within the building block should depend on reaction with the supplied fuel. Second, a molecule that switches between a soluble and an assembled state is required. Third, balanced repulsive and attractive interactions are required to make a reversible switch. Fourth, the deactivating step needs to restore the original repulsive force in the molecule. Fifth, different pathways are required for the activation and deactivation step, otherwise a chemical equilibrium is established. Including these rules during design will help establishing suitable building blocks and proper kinetic timescales for fuel-driven assembly.
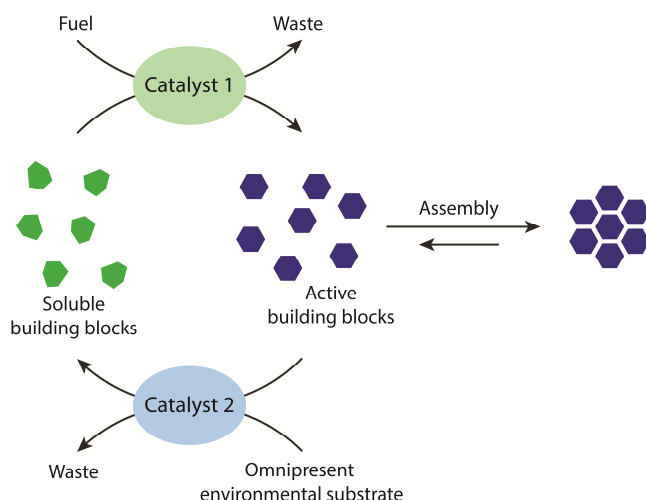
Figure 1.3. Schematics of a chemical reaction network. Soluble building blocks are activated by the consumption of a fuel. The activated building blocks have the appropriate interactions to assemble into larger structures. The assembled structure is spontaneously dissolved with an omnipresent substrate. The kinetics of both pathways can be controlled by catalysis.

1.3. Catalysis

The CRN described above has only three variables to control the kinetic and structural aspect within the transient assembly: the fuel and building block concentration and the environmental conditions. Incorporating catalysis in the CRN would increase the flexibility of the system (Figure 1.3). A catalyst accelerates a reaction by lowering the activation energy without being consumed during the reaction. So one molecule of catalyst can convert many reactants into products. Moreover, fuel and environmental substrates are often present at a high concentration in the CRN. This is often a major drawback as varying these parameters results in a significant change of the system. Catalysis can solve this problem as the catalyst is present at a low concentration and a small change influences the kinetics substantially without affecting the composition of the system.

1.4. Main research goals

Currently, most fuel-driven CRNs do not have a catalyst incorporated in the system. The few systems that rely on catalysis only have one synthetic catalyst in the network[30] or include two enzymatic catalysts[24, 31-33]. Enzymes generally severely limit operating conditions thereby restricting the system. Incorporating synthetic catalysts that can operate under a wide range of conditions is beneficial for investigating more complex fuel-driven assembly.

Therefore the main research question of this PhD thesis is:
How can we regulate the kinetics of out-of-equilibrium assembly using catalysis in the chemical reaction network and which functions can be achieved using a catalytic controlled system?

1.5. Thesis outline

This thesis reports a CRN in which two catalysts control the kinetics of the CRN. Coupling this CRN to several assembled processes demonstrates kinetic control in fuel-driven transient crystallization and polymer agglomeration. Furthermore, promising results are obtained by applying the CRN to a colloidal and supramolecular fiber system as well.

In Chapter 2 we present a literature overview about out-of-equilibrium assembly in which we elaborate on the strategies, advantages, applications and future directions of this field. Chapter 3 demonstrates the kinetic impact of two catalysts in the CRN and its effect on transient crystallization behavior. In Chapter 4 we apply the CRN to a coil-

globule transition of a polymer that is used for transient compartmentalization of slightly hydrophobic nano-objects. Chapter 5 describes the synthesis of colloidal building blocks and the first results towards fuel-driven colloidal agglomeration. In Chapter 6 the synthesis and analysis towards CRN-based supramolecular fibers are described.

1.6. References

1. S. Yabuki, *Anal. Sci.*, 2014, **30**, 213-217.
2. G. Wilde, *Surf. Interface Anal.*, 2006, **38**, 1047-1062.
3. J. D. Venables, *J. Mater. Sci.* , 1984, **19**, 2431-2453.
4. M. G. Mateu, *Arch. Biochem. Biophys.*, 2013, **531**, 65-79.
5. X. Du, J. Zhou, J. Shi and B. Xu, *Chem. Rev.*, 2015, **115**, 13165-13307.
6. T. Manouras and M. Vamvakaki, *Polym. Chem.*, 2017, **8**, 74-96.
7. M. A. C. Stuart, W. T. S. Huck, J. Genzer, M. Müller, C. Ober, M. Stamm, G. B. Sukhorukov, I. Szleifer, V. V. Tsukruk, M. Urban, F. Winnik, S. Zauscher, I. Luzinov and S. Minko, *Nat. Mater.*, 2010, **9**, 101-113.
8. F. Herbst, D. Dohler, P. Michael and W. H. Binder, *Macromol. Rapid Commun.*, 2013, **34**, 203-220.
9. G. M. Whitesides and B. A. Grzybowski, *Science*, 2002, **295**, 2418-2422.
10. A. R. Hirst, B. Escuder, J. F. Miravet and D. K. Smith, *Angew. Chem. Int. Ed.*, 2008, **47**, 8002-8018.
11. Z. Nie, A. Petukhova and E. Kumacheva, *Nat. Nanotechnol.*, 2010, **5**, 15-25.
12. *Phase behavior of surface-active solutes*, Particle Sciences, 2012.
13. V. N. Manoharan, *Science*, 2015, **349**, 1253751.
14. P. Atkins and J. de Paula, *Atkins' Physical Chemistry*, 8th edn., 2006.
15. A. Sorrenti, J. Leira-Iglesias, A. J. Markvoort, T. F. A. de Greef and T. M. Hermans, *Chem. Soc. Rev.*, 2017, **46**, 5476-5490.
16. M. Grzelczak, J. Vermant, E. M. Furst and L. M. Liz-Marzán, *ACS Nano*, 2010, **4**, 3591-3605.
17. G. M. Cooper and R. E. Hausman, *The Cell: A Molecular Approach*, 2nd edn., 2007.
18. B. Alberts, A. Johnson, J. Lewis, M. Raff, K. Roberts and P. Walter, *Molecular Biology of the Cell*, 5th edn., **2002**.
19. E. Mattia and S. Otto, *Nat. Nanotechnol.*, 2015, **10**, 111-119.
20. R. Klajn, P. J. Wesson, K. J. M. Bishop and B. A. Grzybowski, *Angew. Chem. Int. Ed.*, 2009, **48**, 7035-7039.
21. O. Chovnik, R. Balgley, J. R. Goldman and R. Klajn, *J. Am. Chem. Soc.*, 2012, **134**, 19564-19567.
22. R. Eelkema, M. M. Pollard, J. Vicario, N. Katsonis, B. S. Ramon, C. W. M. Bastiaansen, D. J. Broer and B. L. Feringa, *Nature*, 2006, **440**, 163.
23. J. Boekhoven, W. E. Hendriksen, G. J. M. Koper, R. Eelkema and J. H. van Esch, *Science*, 2015, **349**, 1075-1079.
24. S. Dhiman, A. Jain and S. J. George, *Angew. Chem. Int. Ed.*, 2016, **55**, 1-6.
25. M. Tena-Solsona, B. Rieß, R. K. Grötsch, F. C. Löhrer, C. Wanzke, B. Käsdorf, A. R. Bausch, P. Müller-Buschbaum, O. Lieleg and J. Boekhoven, *Nat. Commun.*, 2017, **8**, 15895.
26. S. Maiti, I. Fortunati, C. Ferrante, P. Scrimin and L. J. Prins, *Nat. Chem.*, 2016, **8**, 725-731.
27. T. Heuser, A.-K. Steppert, C. M. Lopez, B. Zhu and A. Walther, *Nano Lett.*, 2015, **15**, 2213-2219.
28. L. S. Kariyawasam and C. S. Hartley, *J. Am. Chem. Soc.*, 2017, **139**, 11949-11955.
29. M. Fialkowski, K. J. M. Bishop, R. Klajn, S. K. Smoukov, C. J. Campbell and B. A. Grzybowski, *J. Phys. Chem. B*, 2006, **110**, 2482-2496.

30.   C. S. Wood, C. Browne, D. M. Wood and J. R. Nitschke, *ACS Cent. Sci.*, 2015, **1**, 504-509.
31.   S. Dhiman, A. Jain, M. Kumar and S. J. George, *J. Am. Chem. Soc.*, 2017, **139**, 16568-16575.
32.   A. Sorrenti, J. Leira-Iglesias, A. Sato and T. M. Hermans, *Nat. Commun.*, 2017, **8**, 15899.
33.   L. Heinen, T. Heuser, A. Steinschulte and A. Walther, *Nano Lett.*, 2017, **17**, 4989-4995.
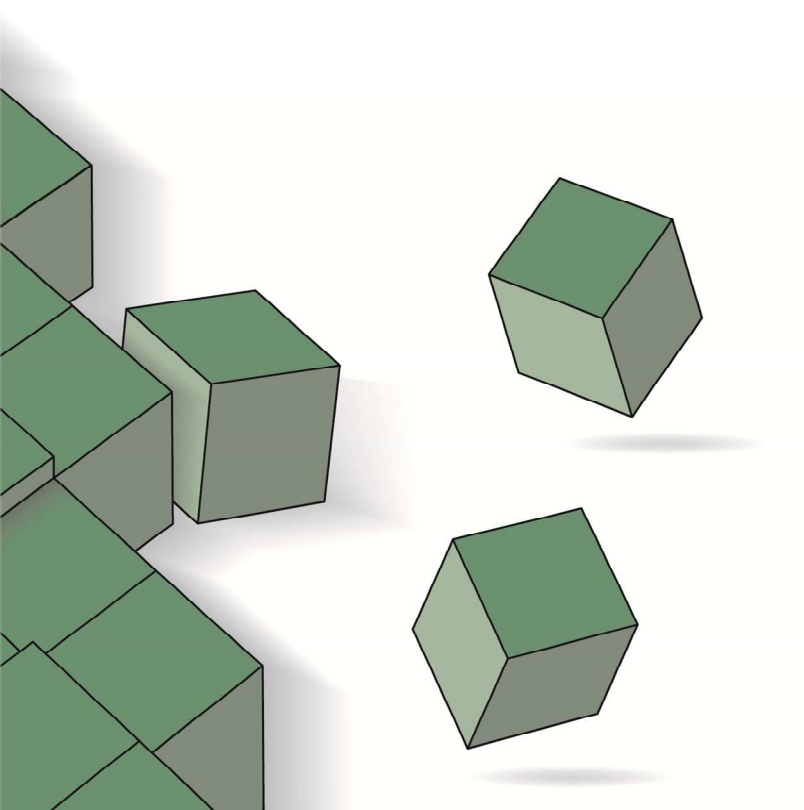
Chapter 2

Dissipative out-of-equilibrium assembly of man-made supramolecular materials

The use of dissipative self-assembly driven by chemical reaction networks for the creation of unique structures is gaining in popularity. In dissipative self-assembly, precursors are converted into self-assembling building blocks by the conversion of a source of energy, typically a photon or a fuel molecule. The self-assembling building block is intrinsically unstable and spontaneously reverts to its original precursor, thus giving the building block a limited lifetime. As a result, its presence is kinetically controlled, which gives the associated supramolecular material unique properties. For instance, formation and properties of these materials can be controlled over space and time by the kinetics of the coupled reaction network, they are autonomously self-healing and they are highly adaptive to small changes in their environment. By means of an example of a biological dissipative self-assembled material, the unique concepts at the basis of these supramolecular materials will be discussed. We then review recent efforts towards man-made dissipative assembly of structures and how their unique material properties have been characterized. In order to help further the field, we close with loosely defined design rules that are at the basis of the discussed examples.

2.1. Introduction

Most man-made materials reside in equilibrium, where the forward and backward rates of assembly and bond formation are balanced. At equilibrium, we understand many of the processes at play. Furthermore, because we understand, we are able to control the properties of existing materials or even create new materials with new functions.[1] Structures and materials may also exist out-of-equilibrium in which there is a net exchange of matter and energy with their environment. In fact, life and the structures it comprises are thermodynamically unstable and can therefore not exist in-equilibrium. For instance, the cytoskeletal networks, parts of the extracellular matrix, and the mitotic spindle[2] are all biomolecular structures that consume energy and materials via irreversible processes to sustain their structure and function. While the out-of-equilibrium nature of these structures gives the resulting biological materials unique properties, the development of analogous man-made out-of-equilibrium supramolecular materials is still in its infancy. In this review, we illustrate the opportunities that dissipative out-of-equilibrium structures bring, we demonstrate recent efforts towards man-made counterparts and we lay out the challenges on the road towards man-made out-of-equilibrium supramolecular materials.

The boundaries of this tutorial review are set to energy dissipating structures on the molecular scale, and we limit the driving force to irreversible chemical reactions. Within that framework, we will mostly focus on man-made out-of-equilibrium structures. In this review, we will use the term dissipative self-assembly (DSA) for the process of out-of-equilibrium self-assembly driven by irreversible chemical reactions. Other terms, including dynamic self-assembly,[3, 4] have been used to describe the same or very similar processes. Since dynamic self-assembly does not exclude all forms of in-equilibrium assemblies, e.g. the rapid exchange of surfactants between micelles and bulk solution, we prefer the term dissipative self-assembly in the context of our boundary conditions. We will include examples of colloidal assembly driven by chemical reaction networks, even though, strictly speaking, this is not molecular assembly. The choice to include them was made as they follow similar design principles as dissipative molecular self-assembly and their collective work has provided important insights into the field of molecular DSA.

In this review, we will give an overview of recent examples and extract the general features in their molecular design. We will define the differences between in-equilibrium and out-of-equilibrium structures, and we will give a flavor of why out-of-equilibrium assembly can lead to unique material properties, demonstrated by pioneering examples of applications. In order to aid the further development of the

field, we close with loosely defined design rules that are at the basis of the discussed examples.

2.2. Out-of-equilibrium assembly: energy landscapes and an example from biology

Self-assembly of artificial (synthetic) molecules is an active research area with many highlights over its half a century of history. Based on the thermodynamic and kinetic stability of precursors, building blocks, and self-assembled structures, one can identify three different types of self-assembly processes which we compare in terms of their energy landscapes (Figure 2.1).

In equilibrium self-assembly, the self-assembled structure resides in the global minimum of the energy landscape (Figure 2.1b, left). The state associated with non-assembled building-blocks is slightly higher in that landscape, and it is thus thermodynamically favorable to assemble the building blocks. The population distribution between assembled and non-assembled state depends on their difference in energy level and available free energy, and is thus determined thermodynamically. In equilibrium self-assembly, exchange between the two states is possible, meaning that building blocks can escape the assemblies and dissolved building blocks can enter assemblies, but this happens with equal rates. As a result, there is no net flow of energy and matter and the assembly is thus in equilibrium.

The assemblies can also reside somewhat higher in the energy landscape, in a local, but not the global minimum of the thermodynamic energy landscape (Figure 2.1b, middle).[5] Depending on the height of the activation barriers around this minimum, two states are possible. Either the energy barrier towards surrounding minima is high and the structure does not exchange matter or energy with its surrounding. In this state, referred to as "kinetically trapped", the self-assembled state has an infinite lifetime. Technically, an infinite lifetime is immeasurable, so the more common definition is a lifetime that is greater than the time of the experiment. If, on the other hand, the energy barrier towards a surrounding lower minimum is relatively low, building blocks in the self-assembled state can "escape" towards that state. This conversion of building blocks towards a lower energy state implies that the self-assembled state has a finite lifetime, and is thus metastable. It also means that this state is not in equilibrium. These so called metastable states are extensively reviewed by Hermans, De Greef and coworkers.[6]

The focus of this review is on a self-assembled state that is higher in the energy landscape than the states mentioned so far. In this scenario, which we call "dissipative
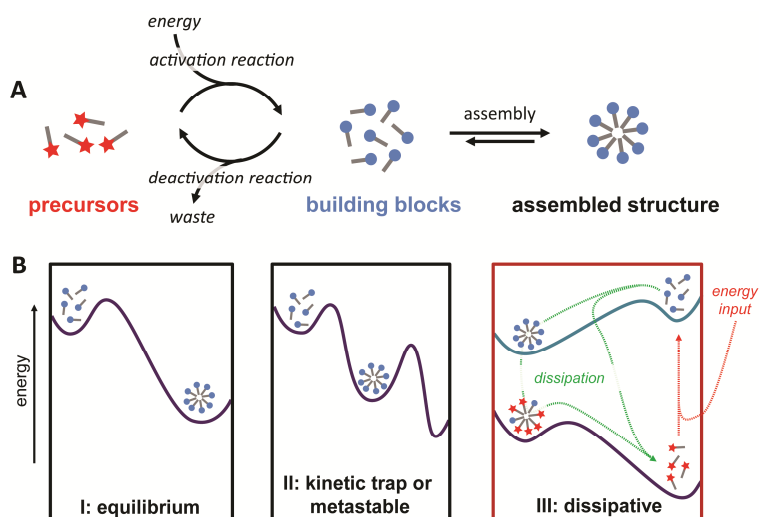
Figure 2.1. Comparison of the free energy landscapes of static self-assembly and dissipative self-assembly. **(a)** Definition of the participants in a self-assembly process. In equilibrium self-assembly and in kinetically trapped and metastable self-assembly, only the building blocks and assembled structures take place in the assembly process. In dissipative non-equilibrium self-assembly, the assembly of building blocks is coupled to an energy-driven chemical reaction network. It is important to note that deactivation of the building blocks can either occur in solution or in the assembled structure. **(b)** One can identify three types of self-assembly based on the relative stability of the self-assembled structure, the building blocks and precursors. In equilibrium self-assembly, the assembly resides in the global minimum (left). Kinetically trapped assemblies reside in a local minimum and cannot escape to the global minimum. In contrast, metastable assemblies can escape that minimum and thus have a finite lifetime (middle). In dissipative self-assembly (right), the assemblies reside high in the energy landscape and can only be sustained by continuous input of external energy (e.g. fuel molecule or a photon). Dissipative self-assembly is the major subject of this review.

self-assembly" or DSA, the self-assembly of a building block is coupled to a chemical reaction network (CRN), i.e. a network of at least two irreversible chemical reactions that control the activation and deactivation of building blocks (Figure 2.1a). In the CRN, a non-assembling precursor, that is at the global minimum in the energy landscape, is converted into a building block by an activation reaction (Figure 2.1b, right). This reaction is driven by the irreversible conversion of a high-energy entity that "pushes" the precursor into a high-energy building block state. After this activation, self-assembly of multiple building blocks can take place leading to larger structures or even materials. Crucially, a second chemical reaction in the network deactivates the high-energy building blocks and reverts them into their original precursors. In this step, the high-energy building block dissipates the energy it absorbed during the activation reaction into the environment as it deactivates to its original precursor. This deactivation process can either happen in solution or in the assembled structure.[7]

Hence, the building blocks in the self-assembled state reside out of thermodynamic equilibrium and the structures are thermodynamically labile. Following the Second Law of Thermodynamics, structures formed through DSA can only be maintained by a constant conversion of energy that keeps them out-of-equilibrium, as nature strives to reach equilibrium. When a finite amount of energy is added as a batch, assembly will take place for as long as the energy source is available to the system. After removal or depletion, the formed unstable structures will start to disintegrate, having the system return to the non-assembled state. In contrast, when there is a continuous supply of energy to sustain the assemblies, the system can in principle reach a non-equilibrium steady state where assembled and non-assembled structures coexist and are continuously converted into each other. It is in this scenario that emergent phenomena such as chaotic behavior, oscillations and bifurcations can occur, depending on the kinetics of the CRN. For a more in-depth discussion of the energetics of such processes, we refer to a book by Casas-Vazquez.[8]

Within the boundary conditions of this *Tutorial Review*, the energy source driving DSA is a chemical reaction that uses a high-energy entity (photon or fuel molecule) to convert a molecular precursor into a building block that is now activated for an assembly process. The term "chemical reaction" should be taken somewhat loosely here. For instance, we will discuss classical chemical reactions that drive self-assembly, such as *cis-trans* isomerization of an azobenzene group driven by UV-light, but also processes that involve non-covalent ATP-complexation to activate self-assembly. Whether these reactions are classical chemical reactions that make and break covalent bonds or supramolecular processes that form non-covalent bonds, similar principles hold: a high-energy source drives the conversion of a molecular precursor into a building block for assembly. We will also discuss examples of Cs that drive morphological transition from one self-assembled state to another and even examples of self-assembled structures that are disassembled by their CRN. Strictly, these examples fall out of the definition of DSA as depicted in Figure 2.1b. We chose to include them, because, from a supramolecular material's points of view, the exact nature of the precursor state is irrelevant as long as the externally applied energy induces a transient change in material properties.

A particularly illustrative example of biological structure formed via DSA is the guanosine triphosphate (GTP)-driven DSA of microtubules.[9] Microtubules are part of the cytoskeleton and are vitally important in maintaining the structure of the cell. Besides scaffolding, the microtubule network is involved in intracellular transport of vesicles, organelles and other macromolecules. The network also assists in the process of cell migration and is the major component of the mitotic spindle, which is the

complex cell machinery responsible for separation of the chromosomes in eukaryotic mitosis. To perform any of these functions, a dynamic material is required that can rapidly remodel on demand to adapt its morphology to the required tasks. Microtubules are endowed with the required dynamics because their dissipative self-assembly is coupled to a CRN that activates precursors and deactivates building blocks. The CRN, in turn, is driven by the hydrolysis of GTP.

Microtubules are self-assembled from tubulin dimers that consist of two tubulin segments, α- and β-tubulin. Each segment can bind one molecule of GTP in its GTP-binding site, and doing so activates tubulin for self-assembly. Assembly occurs in a head-to-tail fashion with the α-domain binding the β-segment of the adjacent dimer resulting in tubes with a diameter of roughly 25 nm. While α-subunit-bound GTP is chemically stable, the β-subunit catalyzes hydrolysis GTP to guanosine diphosphate (GDP) in its binding site. Moreover, the hydrolytic activity is drastically higher for tubulin in the assembled state compared to activated tubulin in solution, as self-assembly of tubulin activates its GTPase.[10] Hydrolysis of the GTP bound to β-tubulin destabilizes the microtubule, but only if all GTP at the end-cap of the microtubule has hydrolyzed to GDP, the microtubule rapidly disassembles, referred to as the catastrophe phase. Taken together, the dissipative self-assembly of microtubules is driven by the hydrolysis of GTP, and as long as addition of activated tubulin outcompetes deactivation of assembled tubulin, self-assembly will take place. As soon as the opposite is the case, the tubules will collapse. The competition between both processes result in a dynamic ensemble referred to as dynamic instability. It is these dynamics driven by the CRN that allow for rapid morphological transitions when required.

As is clear from the example above, coupling the self-assembly of materials to CRNs comes with unique properties. One of those is the ability to control assembly both in space and time by controlling the kinetics of the CRN at play. In the case of the microtubules, this is clearly demonstrated by the ability of tubulin to take place in many processes at different times throughout a cell's life cycle. Even during mitosis of eukaryotic cells, the tubulin precursors play very diverse roles ranging from the formation of the mitotic spindle to the formation of microtubule-asters that help with the spatial and temporal organization of the organelles. Both structures are required at very specific times and very specific locations in the process of mitosis, and that spatial and temporal control is in part regulated by gradients of GTP and in part regulated by microtubule-associated proteins. Thus, the kinetics of the CRN, in part, determine where and when microtubules carry out their function. It is this autonomous control of material function material function in space and time that is unique to DSA and can be

attractive to materials science.

Besides the possibility to control dynamic assembly in space and time, these assemblies can be extremely adaptive towards changes in their environment such as fuel levels or the presence of entities that change the kinetics of one of the pathways in the CRN (e.g. the microtubule-associated proteins). Spatial fluctuations in these parameters can favor assembly at one place and favor disassembly at other places. Because of the dynamic nature of DSA, the system can rapidly adapt by forming a new assembly while breaking down the old one. One extreme case of adaptivity is the ability of the assemblies to repair themselves after externally applied damage. Provided that the CRN remains intact, the system can recover its self-assembled state even if all building blocks were converted. For instance, researchers have placed microtubules under externally applied mechanical stress for several cycles. With increasing numbers of cycles, the persistence length of the fibers decreased, which is a typical sign of material fatigue. When the system was given the time to repair between stress cycles, typically in the range of 100 seconds, the material fatigue was not observed. By means of microscopy, the healing process was shown to take place by incorporation of active tubulin dimers in defect sites along the microtubule, a process that was not observed in undamaged microtubules.[11]

Because of the sensitivity of the assemblies to local fluctuations in fuel fluxes, structures that are formed via DSA have the ability to self-organize, i.e. to form dynamic patterns of the assemblies at much greater length-scales than the original building blocks. Although the exact requirements for such emerging phenomena are not fully understood, the patterns can only exist under non-linear energy dissipating conditions where the assembly exerts feedback on its own CRN. As an example, the abovementioned microtubules can organize into patterns including asters, vortices and cortical bundles, depending on kinetic parameters,[12] but also on physical confinement.[13] For materials science and especially microelectronics, controlling the formation of patterns of macroscopic sizes while retaining structure at the molecular level has been a longstanding challenge.

Taken together, even though creating structures via DSA costs energy and comes with demanding requirements, it has certain unique properties that can be beneficial to materials science. These benefits include spatial and temporal control over function, adaptive and self-healing behavior of the material and self-organization into patterns. Inspired by biological DSA, scientists have started to explore some of these unique features in the recent past. In the next sections, we will show examples of molecular DSA that explore the concept for control over material behavior, and come with design rules to aid further development.

2.3. Trends in non-biological approaches towards DSA

The dynamic self-assembly of microtubules shows that materials formed via DSA can be endowed with unique material properties. Fortunately, DSA is not limited to biological structures, but can also be man-made. In this section, we give an overview of synthetic structures formed via DSA. We categorize the various DSA systems by the energy source that drives their CRN, which can either be light or chemical fuels. Within this division, we further distinguish the way the conversion of energy is coupled to structure formation, be it direct, i.e. where the precursors and assemblers are directly coupled to the CRN, or indirect, i.e. where the precursors and assemblers respond to a change in their environment induced by the CRN.

2.3.1. Energy sources

Within our boundary conditions, DSA is driven by CRNs. In these CRNs, a precursor is converted into a building block at the expense of an energy source (Figure 2.1a). A second reaction deactivates the building block to form the original precursor. The energy source in these networks is a crucial element. We will discuss chemical energy sources in which a fuel molecule gets converted into waste products and thermal energy, and we will give examples of reaction networks that use light as energy source, in which light is converted to thermal energy.

Fuel-driven CRNs that are used to drive DSA will lead to the formation of waste products, e.g. GDP in the microtubule example. These waste products can have significant consequences for repeated operation of a dissipative self-assembled system and in some cases, result in failure.[14, 15] In contrast, CRNs that are driven by light can often perform many DSA cycles,[16, 17] as they typically dissipate their energy via thermal relaxation. A current complication of using chemical fuels to drive CRNs is their challenging design and their restriction in suitable chemical reactants and reactions. Finally, the choice of energy source affects the lifetime of the supramolecular structures. When a finite amount of fuel is added, the system will continue the formation of building blocks until all fuel has reacted, i.e. the fuel can serve as some sort of buffer of energy. In contrast, when the system is irradiated with a finite amount of light, the activation reaction stops immediately after removing the source of energy.

**Light-driven chemical reaction networks**

UV-light has been used as a source of energy in many other DSA systems including gelators[18] and the assembly of nanoparticles.[16] A particular example has been described by Sleiman and coworkers.[19] They used a system containing carboxylic acid-derived azobenzenes, which are prone to form extended linear tapes held together by

hydrogen bonds between the carboxylic acids (Figure 2.2). UV-light irradiation of the azobenzene precursors led to the formation of hydrogen-bonded cyclic structures that subsequently stacked to form larger aggregates. The *cis*-form reverted to the more stable *trans*-form over time by thermal relaxation, leading to the formation of linear tapes once the irradiation source was removed. Notably, the system could be reactivated by re-irradiation with UV-light.

Fuel-driven chemical reaction networks

Despite the vast amount of known chemical reactions, chemical reactions networks that drive dissipative self-assembled systems remain rare. The basic requirements for such networks are that all reactions have to take place within a single environment, that is under the same conditions (e.g. temperature, solvent, ionic strength). Moreover, the activation and deactivation reactions should proceed through two different pathways. Finally, it is important that the reagents involved in the activation and deactivation reaction do not react with one another, or at least at low rates compared to the activation reaction, to ensure limited unwanted background reaction.

An example of a dissipative self-assembled system activated by a chemical fuel is the membrane transport system designed by Fyles and coworkers, which is based on dynamic thioester-thiol exchange chemistry.[20] In this system, a thioester was used as chemical fuel, which underwent a thiol-thioester exchange with the precursor (Figure 2.3). This reaction led to the formation of the building blocks which assembled to form a transient membrane pore. Meanwhile the building block gradually reacted
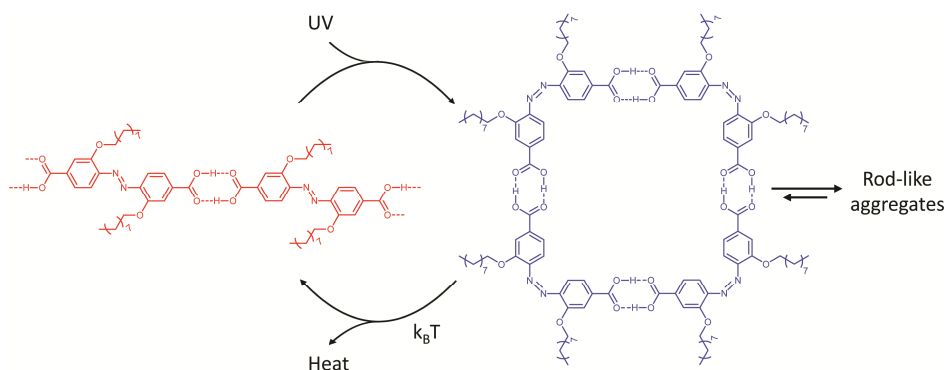
Figure 2.2. The trans-azobenzene molecules (in red) formed linear tapes. Under UV-light the isomerization from the trans- to the activated cis-conformation molecules (in blue) led to the formation of cyclic structures, which stack into rod-like aggregates. The cis-form reverted back to the more stable trans-form over time, resulting in the disassembly of the rod-like aggregates. Adapted from ref (19). Copyright 2003, John Wiley and Sons.

through an intramolecular thioester displacement, resulting in the formation of the precursor and a ring-closed waste product. Clearly, the activation and deactivation proceeded via two different pathways. Moreover, the deactivation by intramolecular rearrangement results in the formation of a stable cyclic amide product that can thus not interfere with the activation reaction.

We would like to mention that, although strictly not DSA by our definition, fuel-driven CRNs can also induce disassembly of a self-assembled precursor. From a dissipative supramolecular material's point of view, the result is the same, i.e. the CRN induces a transient change in material properties driven by the addition of fuel. Recently, Hermans and coworkers described such a system in which a redox reaction was coupled to the collapse and growth of supramolecular fibers.[21] In that system, neutral perylenediimide molecules assembled to form long fibers in thermodynamic equilibrium. When these fibers were allowed to grow for an extended period they irreversibly precipitated out of solution. However, when the fibers were still in solution, the fiber length could be controlled using redox chemistry. When the reductant sodium dithionite was added as fuel, the fibers started to break apart into smaller fibers. Here, reduction with dithionite led to the formation of negatively charged precursors, which resulted in an increase in electrostatic repulsion and thus the breaking of the fibers. Nevertheless, as the negatively charged molecules were unstable, they were slowly oxidized back to the neutral building blocks, again resulting in the formation of long fibers.
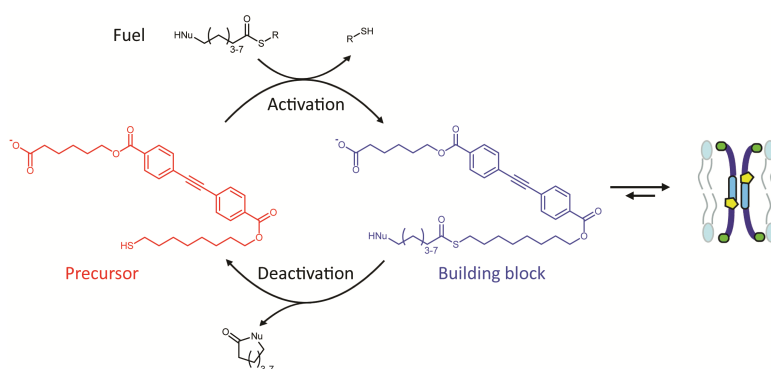
Figure 2.3. Thioester-driven dissipative assembly of membrane pores. The thioester (fuel, Nu = O, NH) undergoes a thiol-thioester exchange with the precursor (red) to form a building block that can form pores in a supramolecular membrane. The building block (blue) reacts intramolecularly to form the precursor and a waste product. Adapted from ref. (20). Copyright 2014, The Royal Society of Chemistry.

2.3.2. Direct vs. indirect DSA

In the fuel-driven example mentioned above, the precursor reacts directly with the energy source to form the building block. We introduce the term "direct DSA" for these examples. In contrast, the energy source can also indirectly result in the conversion of precursors to building blocks. For instance, the energy source can induce a change in pH, which will be reverted when all energy has been dissipated. In such cases, self-assembly can be coupled to that oscillation in pH, in which case we speak of "indirect DSA". In indirect self-assembly, the energy source is responsible for the assembly process, but it does not react directly with the precursor.

Additional complexity can be introduced by the use of chemical oscillators in which one reactant with oscillating concentration induces a morphological transition of a supramolecular material. Both the direct and indirect methods using light-driven or fuel-driven CRNs have been described to obtain transient supramolecular materials.

Direct DSA

In the assemblies formed via direct DSA, the precursor reacts directly with the energy source, which can be light or a chemical fuel, and the examples mentioned in section 2.3.1 are thus examples of direct self-assembly. In recent literature, we can find examples of supramolecular structures that are obtained using direct DSA, such as aggregated colloids, fibers, gels, and surfactant-based structures.[7, 15, 16, 21]

Indirect DSA

For indirect dissipative self-assembled systems, the precursor does not directly react with the fuel, but an intermediate reagent is first generated by reaction with the energy source. Subsequently, the intermediate species reacts with the precursor to form the building block, leading to self-assembly of the building blocks through non-covalent interactions. Examples of liquid crystals, nanoparticles, gels or dynamic monolayers can be found in literature.[17, 22-24] Among them, the most abundant examples of indirect dissipative self-assembled systems are found in the light-driven reorganization of liquid crystals. In these systems, a dopant, dissolved in the liquid crystal matrix, undergoes a reversible isomerization upon irradiation with UV-light.[22, 25, 26] This change induces a reorganization of the liquid crystal matrix. After removal of the light source, these systems revert to the initial organization resulting from the thermally activated reversal of the dopant to its most stable state. The conformation of the dopant is only changed upon a continuous energy input which leads to the rotation of the liquid crystal matrix. Thus, the supramolecular structure is not only in an out-of-equilibrium state, but the conformation of the dopant is as well.

Klajn and coworkers designed a system in which the assembly[17] of non-light responsive nanoparticles is indirectly coupled to irradiation with light. In this system, a spiropyran derivative in solution released a proton upon light-driven ring closure, leading to protonation of the negatively charged functional groups on the nanoparticles and subsequent aggregation. Importantly, the switches were not attached to the nanoparticle building blocks; they remained in solution throughout the entire process. This design makes the system more versatile, because different nanoparticles can be used for transient aggregation. When protons would be directly added to the system, it would not lead to transient aggregates, but it would just re-position thermodynamic equilibrium. Thus, the use of the spiropyran switches is crucial to obtain an out-of-equilibrium state.

Besides light as an energy source, chemical fuels can also be used to drive indirect DSA. A distinctive example is devised by Miravet and coworkers,[23] in which hydrogel formation was indirectly fueled by sucrose conversion (Figure 2.4). Sucrose was converted to ethanol and carbon dioxide using yeast. In water, the produced carbon dioxide is in equilibrium with bicarbonate, subsequently releasing a proton. Protonation of a soluble negatively charged amide surfactant resulted in surfactant assembly and the formation of a fibrous network. Remarkably, the aforementioned chemical equilibrium formed the basis for the indirect dissipative self-assembled system as the gaseous carbon dioxide gradually left the system. Hence, over time the
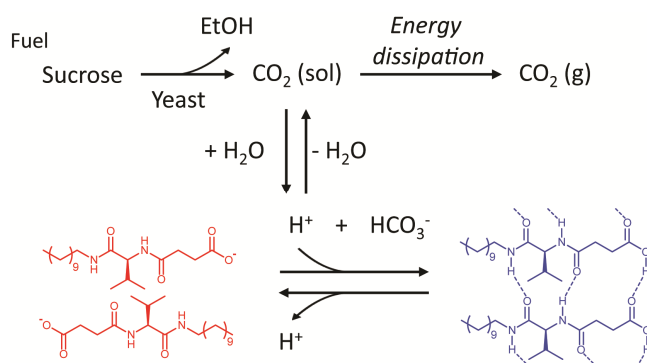
Figure 2.4. Dissipative assembly of hydrogels indirectly fueled by the oxidation of sucrose. The sucrose fuel was converted to CO_2 by yeast, amongst other molecules, which in turn formed a chemical equilibrium with a proton and bicarbonate. Protonation converted the negatively charged precursor molecule (red) into a self-assembling building block (blue), resulting in the formation of fibers and consequently hydrogelation. The hydrogel was only transiently stable because the CO_2 left the system, inducing a shift in the chemical equilibrium away from the protonated building block. Adapted from ref. (23). Copyright 2016, The Royal Society of Chemistry.

chemical equilibrium shifted to the carbon dioxide side and the protons were gradually removed from the fibers, resulting in the collapse of the hydrogel. When protons instead of sucrose would be added to the surfactants the hydrogel was indefinitely stable.

Oscillations

Chemically fueled oscillators, like the well-known Belousov-Zhabotinsky reaction, are CRNs in which the concentration of one or more reactants changes in a periodic fashion. Naturally, oscillators are out-of-equilibrium systems driven by the conversion of chemical fuel. Their periodically changing reactant concentrations can be used to drive self-assembly in a process that we classified as indirect DSA. The oscillation enables the system to go through multiple self-assembly cycles without any human intervention. Furthermore, when using an open system, the oscillation frequency can be controlled by the flow rate, which is a straightforward method to control material lifetimes.[27]

Two examples of oscillating dissipative self-assembled systems are reported by Grzybowski and coworkers. In these systems, supramolecular structure formation was controlled by the methylene glycol-sulfite-gluconolactone (MGSG) chemical oscillator.[28, 29] This oscillator periodically changed the pH of the solution. They used this oscillation for two systems: firstly, the oscillation of nanoparticle aggregation and secondly, the oscillation of a micelle-to-vesicle transition. In the first, gold nanoparticles were coated with 2-fluoro para-mercaptophenol ligands that are neutral at low pH and negatively charged at high pH.[28] Over time the oscillation reaction shifted the pH leading to the oscillatory aggregation of the nanoparticles at low pH and dispersion at high pH. With this oscillatory behavior, the authors were able to obtain more than ten aggregation cycles without any signs of fatigue. In the second system, the supramolecular structure was based on the assembly of oleic acid-based surfactants.[29] These surfactants formed micelles when they were negatively charged and vesicles when partially neutralized. Again, the MGSG oscillation regulated the pH of the solution and therefore the assembly behavior could be controlled. This system showed a pH oscillation that led to a two-minute micelle-vesicle-micelle cycle.

Zhang and coworkers used the $IO_3^--NH_3OH^+-OH^-$ chemical oscillator to control amphiphilic copolymer assembly.[30] The oscillator controls the iodine concentration, which was coupled to the assembly of a PEG-functionalized polymer (Figure 2.5). In the absence of iodine in solution, the polymer was hydrophilic and well-soluble. After initiation of the oscillation, the transiently formed iodine binds to the PEG-chains resulting in an increase in its hydrophobicity and the subsequent assembly of the
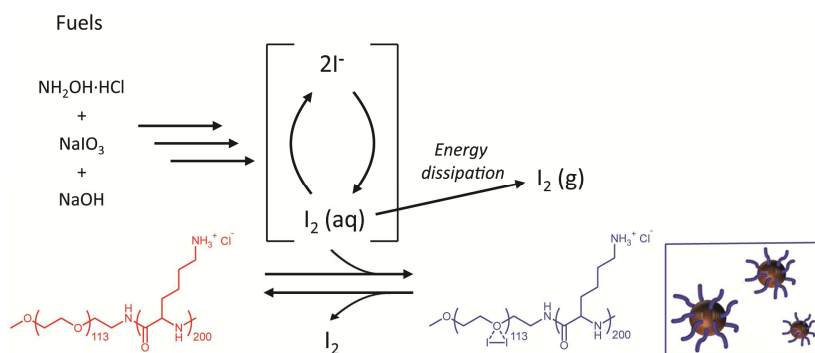
Figure 2.5. The use of a chemical oscillator for indirect DSA. An iodate-based chemical oscillator shows oscillation between iodide and iodine. The formed iodine can bind to a hydrophilic polyethylene glycol-based polymer (precursor in red) leading to an increase in hydrophobicity (blue) and its subsequent aggregation. Over time, the iodine escaped as gas resulting in the redispersion of the polymer. Adapted from ref. (30). Copyright 2016, The Royal Society of Chemistry.

amphiphiles. A decrease of the iodine concentration during an oscillation led to release of iodine from the polymer and subsequent dissolution of the assemblies. An open system was used to remove the waste products, thereby extending the time the oscillator could operate. However, it was found that the assembly was not completely reversible, as not all iodine was removed from the PEG-chains in the deactivation reaction.

2.4. Exploration of the unique properties of structures formed via DSA

In Section 2.2, we used the GTP-driven assembly of microtubules to illustrate that materials formed via DSA have unique properties as a result of their dynamic nature. Unfortunately, the use of microtubules as materials or other biologically derived dissipative structures is hampered by their availability, price, complexity, versatility and scalability. However, as we demonstrated in the previous section, more and more examples of man-made structures formed via DSA have become available in recent years. As a result of their dissipative nature, these structures possess some of the unique features that arise from the dynamic nature of their building blocks. In this section, we will discuss these unique characteristics and we will demonstrate each with prominent man-made examples. These properties include control over where and when an assembly is formed and disassembled, the ability to adapt to a change in its environment, the ability to be re-used and the ability to self-heal. While initially the focus will be on the unique properties of the self-assembled architectures, we will

emphasize, in a later section, the implication of these unique features on material properties.

2.4.1. Temporal control over supramolecular structure formation

Temporal and spatial control over assemblies represents a major challenge in the design of smart materials. As an example, supramolecular materials that release bioactive cues, like growth factors and anti-inflammatory agents, at prespecified sites with predefined rates is key in the successful regeneration of lost or damaged tissue.[31] Likewise, supramolecular structures that aid microfluidic guidance[32, 33] or assemble to form self-erasing inks[16, 34] require both spatial and temporal control over assembly and disassembly. Although disassembly of architectures can be encoded in the design of in-equilibrium assemblies, they inherently require a trigger that changes the environment, and thus the energy landscape, to induce disassembly, referred to as responsive self-assembly.[35] Changing the environment of an assembly is not always possible (i.e. changes in pH or temperature in vivo). In contrast, structures formed via DSA are kinetically controlled by where and when fuel is present and can thus be controlled over space and time, simply by only locally applying a finite amount of fuel. Using a DSA approach to control materials over time and space does not require an externally induced change of the environment, which in some cases can be advantageous. Here we list a few examples where supramolecular structures are controlled over time using a DSA approach.

When a finite amount of fuel is added to the precursors, it will induce their assembly resulting in the desired supramolecular material. Inherently, these materials will exist transiently and disappear as the system reaches equilibrium. Typically, equilibrium is reinstated sometime after all fuel has been converted. Understanding the kinetics at play allows the user to predetermine the lifetime of the material by the amount of fuel added. To that end, Van Esch, Eelkema and coworkers[7, 36] reported the first example of a chemically driven formation of an assembly and showed the possibility to tune the lifetimes of the assemblies by altering the rate of the chemical reactions involved. To do so, a water-soluble dicarboxylate precursor was converted into its corresponding methyl ester by reaction with a methylating agent (methyl iodide or dimethyl sulfate, Figure 2.6). As the methyl ester existed in an aqueous environment, it was thermodynamically unstable. Thus, simultaneous to the activation of building blocks, hydrolysis of the ester back to its soluble dicarboxylate precursor took place (Figure 2.6a). The ester building blocks were molecularly engineered to assemble into fibers that, in turn, formed a dense network which entrapped the
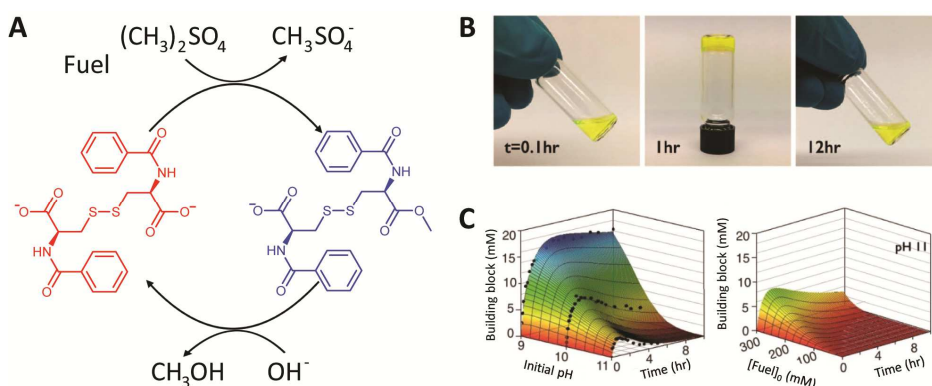
Figure 2.6. Fuel-driven direct DSA to control the lifetime of a material. **(a)** Reaction cycle describing the activation and deactivation reactions. The precursor (carboxylate in red) reacted with the fuel (dimethylsulfate) producing the active building block (methyl ester in blue) which self-assembled into fibrous structures. Hydrolysis of methyl esters resulted in the formation of the original inactive precursor. **(b)** Transient hydrogel formation in a typical reaction cycle. **(c)** Kinetics of transient hydrogelator formation at different pH values (left) and different initial fuel concentrations (right) as measured by HPLC (markers) and calculated by a kinetic model. Adapted from ref. (7). Copyright 2015, American Association for the Advancement of Science.

aqueous environment forming a hydrogel (Figure 2.6b). Crucially, the lifetime of the gels could be controlled by the kinetics of the reactions involved. For instance, the nature of the fuel could be used as a parameter to control the activation reaction. Methyl iodide, a relatively weak electrophile, showed slow activation and thus low yields of building blocks, prohibiting gel formation. In contrast, dimethyl sulfate, a more reactive methylating agent compared to methyl iodide, enabled the system to reach sufficient concentrations of methyl esters, leading to gel formation. The lifetimes of these gels could be further modified by changing the pH of the media, thereby altering the hydrolytic deactivation reaction. Using a buffered solution at pH 9 gave gels that persisted for more than a week, while at pH 11 gels were only present for hours. Alternatively, the concentration of fuel could be increased to give higher relative yields and thus greater lifetimes (Figure 2.6c). The possibility of repeating the out-of-equilibrium assembly process was assessed by adding a second batch of fuel. The concentration of methyl ester obtained was the same as during the first cycle, however the scattering intensity of the assemblies reached lower values than in the first cycle, because of the presence of waste products from the first cycle such as methanol, which disturbed the fiber formation.

Transient hydrogel formation driven by a batch of chemical fuel was also reported by Ulijn and coworkers.[14, 37] They showed the dissipative formation of

hydrogels in which both the activation and the deactivation reaction rate could be controlled by the same enzyme. This hydrogel formation was driven by an enzyme catalyzed peptide coupling between a methyl ester of an amino acid as fuel and an amine as precursor (Figure 2.7). Meanwhile, the hydrolysis of the resulting peptide building block coupling was catalyzed by the same enzyme, albeit at a lower rate. Over time the methyl ester fuel was consumed and the hydrolysis towards the amine precursor took over leading to the collapse of the hydrogel. As both reactions were catalyzed by the same enzyme, tuning the lifetime of the material was not straightforward. The activation reaction showed limited dependence on the concentration enzyme when greater than 0.5 mg/ml, which gave the authors the possibility to tune the deactivation reaction by varying the amount of enzyme, while the activation reaction remained mostly unaffected. For instance, at 0.5 mg/mL enzyme, the transformation of gel to liquid occurred after 16 h, while the gel state was sustained for only 3 h at 3 mg/mL. Likewise, control over the deactivation reaction was achieved by varying the pH. At more alkaline pH values, the hydrolysis rate increased and thus the lifetime of the gels decreased. Finally, varying amount of fuel allowed for
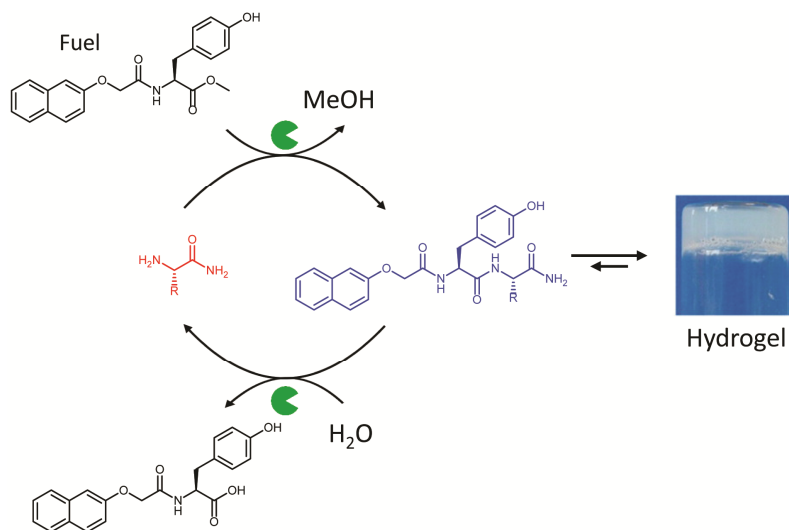
Figure 2.7. Enzyme catalyzed dissipative assembly of a hydrogel. The precursor (red) is activated by the enzyme-catalyzed reaction with the fuel (black). This reaction leads to the formation of a building block (dipeptide in blue) which self-assembles into fibers that eventually form a hydrogel. The hydrogel is unstable as the enzyme also catalyzes the hydrolysis of the building block leading to the collapse of the gel and the release of the precursor and a waste product. Adapted from ref. (14). Copyright 2013, American Chemical Society.

tuning the lifetime of the assemblies from minutes to hours. Addition of new fuel batches gave the possibility of repeated transient gel formation up to three cycles. After more than three fuel additions, the dipeptide conversion could not reach the minimum gelation concentration, most likely due to the accumulation of waste product. The latter two examples of temporal control over self-assembly by means of DSA illustrate that for repeated or continuous operation, waste management is essential.

A fine-tuned example of indirect DSA of which the lifetimes could be controlled was recently described by Walther and coworkers.[32, 38] They developed a clever concept of indirect DSA in which self-assembly of a plethora of building blocks is coupled to a transient jump in the pH value. In this work, a reactant rapidly changed the environment (promoters or activators), thereby inducing assembly, while a second class of reactants (dormant deactivators) slowly brings the environment back to the original state, thereby inducing disassembly. This unique approach required simultaneous injection of both reagents leading to the rapid formation of the transient species and a slow deactivation. Crucially, deactivators were generated in a kinetically controlled manner from the dormant deactivator. For instance, the urease-catalyzed conversion of urea into CO_2 and NH_3 progressively increased the pH value back to the initial stage while the spontaneous hydrolysis of ester-containing molecules released acid decreasing, therefore, the pH value. Changing the ratio between activator, typically an acid or basic buffer, and dormant deactivator, the duration of the transient non-equilibrium state was successfully tuned from minutes to days. When this chemical network was coupled to pH sensitive building blocks, different temporary supramolecular assemblies were achieved.

In the examples we described, a chemical fuel is added batch-wise to create a transient self-assembled structure. The lifetime of this transient assembled species can be controlled by tuning the rates of the reactions involved. When light is used to drive the formation of assemblies, similar principles hold. The lifetime can be increased by longer exposure times or by greater intensity of light, both subjecting the precursors to a greater number of photons. In the case of nanoparticles functionalized with photo-responsive azobenzene molecules, UV-light triggers the formation of assemblies by inducing an isomerization from the *trans-* to *cis*-azobenzene configuration.[16] Longer UV-light exposure times afforded a larger conversion from *trans* to *cis*, and thus a greater number of dipole moments on the nanoparticle. Analogous to the chemically fueled temporal control over structures, the lifetime of the UV-light induced self-assembled state can be decreased by an increased building block deactivation rate. In one example, the deactivation rate was increased by exposing the azobenzene

functionalized particles to visible light or by running the experiment at a higher temperature.[16] Particularly in the case of nanoparticles, the lifetime of the assemblies can also be significantly tuned by adjusting the surface concentration of the light-sensitive molecules.[16, 39] In general, the times required to achieve full disassembly increased with increasing coverage of the switches on the nanoparticles. Tuning of the lifetime is not limited to azobenzene functionalized nanoparticles, as a recent report by Klajn and coworkers showed spiropyran functionalized nanoparticles that self-assembled upon UV-light irradiation.[39] This system is based on the isomerization of spiropyran to the highly polar merocyanine isomer. The polarity of the solvent was chosen such that the polar merocyanine was insoluble and thus led to aggregation of the particles. Crucially, after switching off the UV-light, the disassembly process started immediately but completed within different times depending on the surface concentration of spiropyran. For instance, half-lives ranging from 9 to 72 seconds were observed increasing the molar content of spiropyran from 0.6 to 0.9 units, where 1 is full coverage and 0 is no coverage.

### 2.4.2. Spatiotemporal control over structure formation

Local availability of an energy source can lead to the formation of a reaction diffusion gradient that dictates the concentration of activated building blocks and thus the material properties in space. Similar to the examples above, if this gradient is created using a finite amount of fuel, the locally formed out-of-equilibrium material will show a finite lifetime and will cease to exist once equilibrium is reached. We would like to emphasize that the unique aspect of DSA is the ability to control structures both over space and time simultaneously.

In order to achieve such simultaneous temporal and spatial control over the DSA process, the energy supply needs to satisfy specific requirements. The energy source should be applied locally thus creating a gradient of activated building blocks in solution. Light, as source of energy, can be delivered locally and remotely and thus allows instant application and removal. These features make light a successful energy source to create spatial shapes and patterns.

As an example, Klajn and coworkers[34] demonstrated the self-assembly of nanoparticles in transient patterns in response to an energy source. Gold nanoparticles functionalized with acidic groups and spiropyran light sensitive molecules were embedded into a thin film of polyethylene glycol gel in methanol. Under ambient conditions these gels are yellow as a result of the self-assembled nanoparticles. However, when exposed to blue light the gels become red following the dispersion of the assembled clusters into single particles. The dispersion is caused by the spiropyran

molecules, which released a proton upon light-driven ring closure, leading to protonation of functional groups on the nanoparticles. As the particles could only be free in solution under constant irradiation, the gels turned yellow upon removing the light source. Similarly, when the gel was irradiated with blue light via a mask, only the exposed areas turned red. The images self-erased and could be rewritten at least a hundred times without deterioration of the material. It is worth to note that this is, strictly speaking, not an example of DSA, as the assembled state is thermodynamically favored while the out-of-equilibrium state is disassembled. We chose to describe the example because it does demonstrate an energy dissipating change in material property that can be used to achieve spatial and temporal control over material properties.

UV-light switchable organic molecules have also been used to induce order and disorder transitions when placed into liquid crystal mixtures. Typically, these organic molecules exhibit photo-induced conformational changes which lead to order-increasing or decreasing changes in the liquid crystal arrangement. In this manner, when the energy source is supplied locally, only the exposed areas undergo a transition.[25, 40] Liquid crystals have the ability to amplify the response of a dopant to external stimuli, which is at the basis of the following examples of indirect DSA. In these examples, a UV-light switchable organic molecule is dissolved in a liquid crystal. Upon switching the molecule, it destabilizes the liquid crystal arrangement and thus induces a morphological transition. As the activated state of the dopant is thermodynamically unfavored it relaxes back to its starting point configuration upon ceasing the energy flux, in this case UV-light, thereby allowing the liquid crystal to revert to its original state. Besides earlier work by Feringa,[26, 41] this strategy was applied by Bunning and coworkers[25] using a naphthopyran-based compound dissolved into a liquid crystal mixture. In its closed form, the switch destabilized the liquid crystal to give an isotropic phase at room temperature. Upon light-induced ring opening, the naphthopyran molecules became elongated and planar, stabilizing the liquid crystal phase and thus inducing a phase change from isotropic to liquid crystalline (Figure 2.8a). Again, a mask was used to drive the indirect DSA in local areas. As expected, upon exposure, only the illuminated areas underwent a transition from the isotropic to the nematic phase (Figure 2.8b). Once the energy influx was ceased, the naphthopyran compound reverted back to its closed form in minutes thereby undoing the morphological transition of the liquid crystals. Hedge and coworkers[40] applied a similar strategy to trigger a transition from nematic to smectic A liquid crystal phases, using a photoinduced *trans-* to *cis*-isomerization of azobenzene dopants. In the absence of UV-light the *trans*-azobenzene dopant was dissolved in the nematic host (Figure 2.8c).
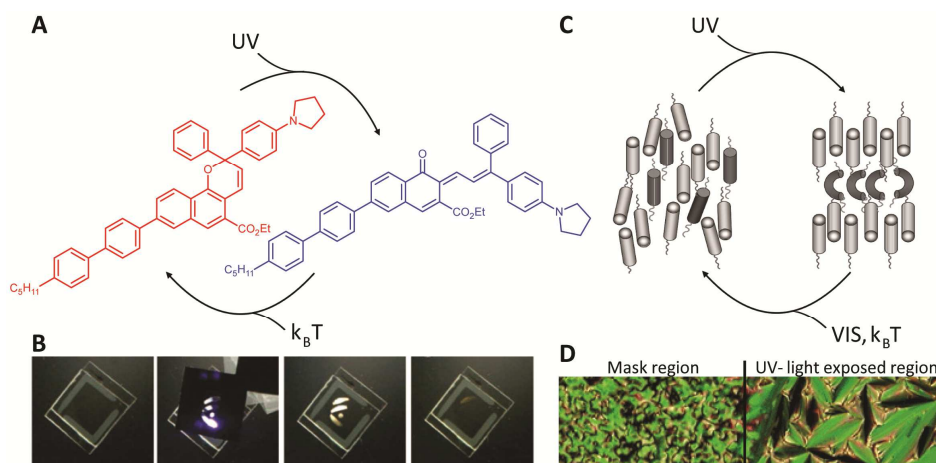
Figure 2.8. Light-driven liquid crystal reorganization. **(a)** Activation and deactivation chemical reactions of the naphthopyran derivative dopant. UV-light triggered the isomerization from the precursor (closed naphthopyran form in red) to the building block (open naphthopyran form in blue). Upon removal of UV-light irradiation, the open form reverted back to the original precursor. **(b)** Spatially controlled transition from isotropic to nematic liquid crystal phases upon UV-light irradiation using a mask. Adapted from ref. (25). Copyright 2012, Nature publishing group. **(c)** Schematic representation showing an order inducing phased transition triggered by UV-light irradiation. When UV-light is absent, the trans-form of the dopant (dark grey cylinder) coexisted with the host liquid crystal (light grey cylinder). Upon UV-light radiation the bent cis-isomer dopant segregated from the LC host giving rise to the ordered smectic A phase. **(d)** Spatially controlled transition from a nematic to a smectic A phase induced by UV-light irradiation through a mask. Adapted from ref. (40). Copyright 2005, John Wiley and Sons.

Under UV-light irradiation, the dopant molecules isomerized to the *cis*-form. The bent shape of *cis*-isomer was less compatible with the liquid crystal host, leading to segregation of the dopant and the host and the appearance of a layered smectic A phase. When the azobenzene-doped liquid crystals were locally exposed to UV-light, fan-shaped focal conical structures typical of a smectic A phase were found only at the irradiated regions (Figure 2.8d).

2.4.3. Adaptivity

A promising feature of structures formed via DSA is their adaptivity to external stimuli. In this context, adaptivity is defined as the ability of the assembly to respond to changes in their environment.[3] As structures formed via DSA require a continuous supply of energy to sustain, a small fluctuation in this energy flow can dramatically affect the assembly process. We would like to emphasize that adaptivity can be encoded into in-equilibrium assemblies as well, e.g. in pH-responsive assemblers. Still, the diversity of morphological transitions is far richer for out-of-equilibrium

assemblies, e.g. microtubules can self-assemble into asters, vortices, or a homogeneous network of fibers, all in response to different fuel flows.[12, 13] In terms of adaptivity in man-made materials formed via DSA, there may be an opportunity here. We are not aware of examples with similar sophisticated responses to small changes in the environment as those observed in microtubules.

In one example of adaptivity in DSA, light was used as an energy source to induce spatially controlled assembly of small molecules in organic solvents. Van Esch and coworkers[18] designed a diarylethene photochromic switch that could undergo ring-closure upon absorption of UV-light. In toluene, the open form of this diarylethene switch was well soluble. However, when energy was supplied in the form of UV-light, a reversible interconversion from the open to closed form induced self-assembly into fibers (Figure 2.9a). These fibers entrapped the toluene eventually resulting in formation of an organogel. Subsequent irradiation with visible light resulted in the diarylethene derivatives switching back to their open state which destabilized the assemblies and consequently resulted in the collapse of the gel state. When UV (activation) and visible light (deactivation) were applied simultaneously, a dynamic
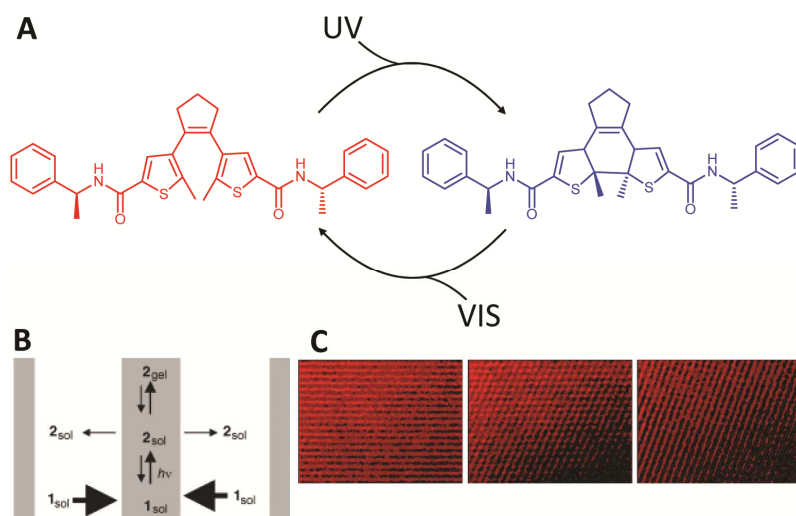
Figure 2.9. Light controlled dynamic pattern formation. **(a)** Reaction cycle describing the activation and deactivation chemical reactions. The open state of the diarylethene (precursor in red) converted into the building block (blue) by an electrocyclization driven by UV-light. The building block (blue) reverted back to the precursor (red) with visible light. **(b)** Diagram representing the kinetic scheme for the diffusion mechanism. Grey areas indicated UV-irradiation and the thickness of the arrow indicated the dominance of the process. **(c)** Dynamic and spatially controlled self-assembly in time. Assemblies adapted to changes in the UV irradiation grating angle. Adapted from ref. (18). Copyright 2005, John Wiley and Sons.

ensemble was obtained. A mask was used to locally expose the solution with UV-light while the entire solution was exposed to visible light. In this setup, gel formation only took place in the illuminated regions. The patterning was successfully achieved because the formation and immobilization of the assembly was faster than diffusion of molecules to the non-UV-light irradiated area (Figure 2.9b). The adaptivity of the light-driven dynamic structures was demonstrated by rotating the UV-light irradiation grating (Figure 2.9c). Changing the UV-light grating angle changed the local availability of energy to the system. The assemblies adapted to that change by reassembling the structure to match the new irradiation pattern. In the locations where the system was shielded from UV-light, the structures disappeared, while new fibers appeared in areas that were previously not irradiated. In other words, the self-assembled state could adapt to the change in energy availability.

2.4.4. Self-healing

One form of adaptivity of dynamic assemblies is their ability to respond to externally induced damage. Provided that the damage does not affect the CRN, the self-assembled states can restore the damage as the self-assembled structures are continuously formed and broken down in the presence of an energy source. Materials that are in or close to equilibrium are typically only self-healing in exceptional cases, for instance when the building block exchange dynamics are relatively fast. Prominent examples of such self-healing materials are viscoelastic networks formed by worm-like micelles that, even under equilibrium conditions, can self-heal their viscoelastic nature.[42] In the case of DSA, the monomer exchange dynamics are coupled to the dynamics of the CRN, and such materials are thus autonomously self-healing driven by energy conversion.

Examples of self-healing materials formed via DSA remain relatively scarce. Van Esch, Eelkema and coworkers[7] showed the self-regenerative behavior of the above described hydrogel materials driven by methylating agents (Figure 2.6). By means of rheometry, the authors demonstrated that a gel could be liquefied by applying a high strain. Next, the recovery of the gel was followed. Typically, similar low molecular weight gels that are in- or close to- equilibrium do not restore after such damage, mainly due to slow monomer-fiber exchange and even slower fiber-fiber reconnection. In contrast, the authors described that the gels were formed via DSA did recover after damage. Moreover, they tested how the self-healing behavior scaled with the availability of fuel. When the gels were disrupted early in the reaction cycle and thus contained relatively high amounts of fuel, they recovered their original state within minutes and then continued their cycle relatively unaffected by the damage. In

contrast, when the gels were disrupted at later stages of a dissipative cycle, as most fuel had reacted, the original gel stiffness did not recover and regenerative behavior was akin to in-equilibrium gels.

2.5. Transient control over the function of supramolecular materials

We have shown that DSA endows the structures it forms with unique properties as a result of their dynamic and out-of-equilibrium nature. Biology uses these features to its advantage to control function of materials over space and time, uses its adaptivity to rapidly adjust between self-assembled states or to heal damaged tissue. Here we will discuss recent man-made attempts to molecularly engineer similar control over material properties into materials formed via DSA, including control over chemical reactivity, optical properties and directional motion.

2.5.1. Temporal control over chemical reaction rates

Grzybowski and coworkers developed a dissipative self-assembled system that reversibly controlled catalytic activity using light-driven assembly of azobenzene-functionalized nanoparticles that aggregated upon irradiation with UV-light.[43] These nanoparticles were catalytically active in their dispersed state, but self-assembly led to a decreased catalytic activity due to a reduction in available surface area per particle. When the UV-light was switched off, i.e. when the fuel source was removed, the particles redispersed leading to an increase in catalytic activity. The authors were able to switch from a conversion of ~1% in the aggregated state to a conversion of 40% in 25 minutes in the dispersed state.

Another example of an out-of-equilibrium structure controlling chemical reaction rates used the transient assembly of nanoparticles of different nature (gold, silica, magnetite) functionalized with azobenzene groups.[44] Irradiation with UV-light drove the assembly of the dispersed apolar nanoparticles into aggregates. This aggregation was caused by the isomerization of the azobenzene groups to the polar *cis*-conformation. When hydrophilic reactants were added to the samples, the reactants were confined within the hydrophilic cavities of the aggregates leading to a higher reaction rate compared to non-aggregated system (Figure 2.10a). Crucially, removing the source of UV-light led to redispersion of the nanoparticles and stopped the chemical reaction between the hydrophilic precursors. Light-driven assembly not only increased the reaction rate, but also afforded control over the stereochemistry of the product. Without nanoparticles, the dimerization of anthracene would lead to the *anti*-product while the *syn*-product was obtained using nanoparticle aggregates (Figure
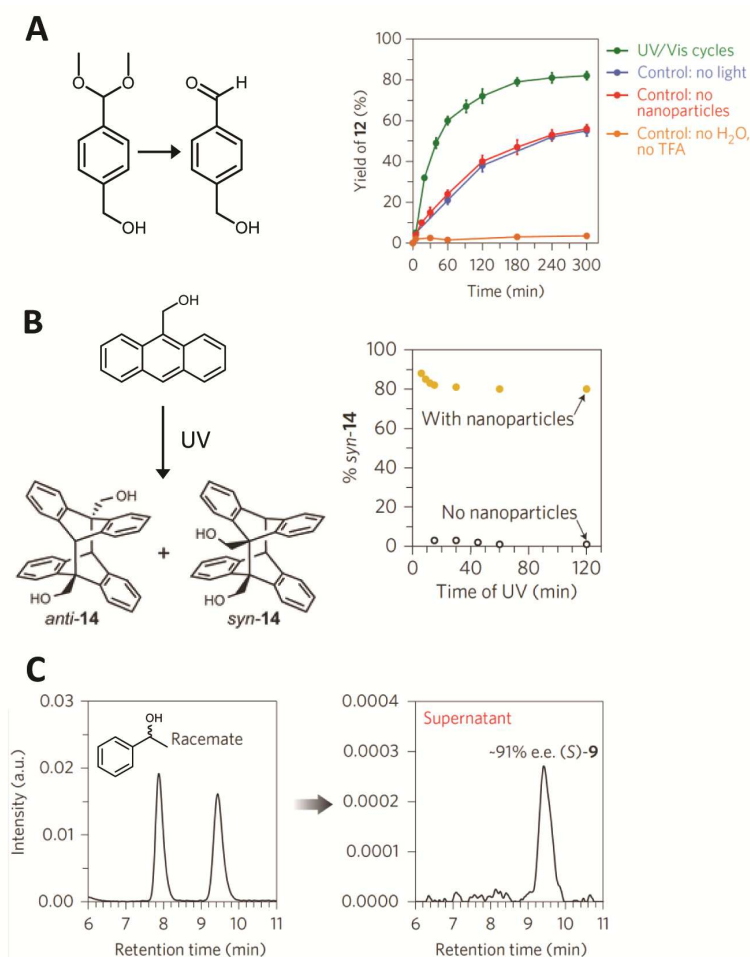
Figure 2.10. Control over reaction rates using transiently assembled nanoparticle structures. **(a)** Increased yield of the acetal hydrolysis in the presence of nanoparticle aggregates. **(b)** A chemical reaction in which the anti-product was obtained when the particles were dispersed and the syn-product was obtained in the presence of nanoparticle aggregates. **(c)** Separation of a racemate using aggregated chiral nanoparticles. Adapted from ref. (44). Copyright 2015, Nature Publishing Group.

2.10b). The addition of a chiral ligand to the nanoparticles also made it possible to separate enantiomers in the aggregated state (Figure 2.10c).

Prins and coworkers described the dissipative assembly of vesicles, that were able to increase the rate of a chemical reaction.[15] The assembly of these vesicles was driven by the electrostatic complexation of anionic ATP to cationic surfactants. Introduction of the enzyme potato apyrase, that hydrolyses ATP, induced breakdown of the formed
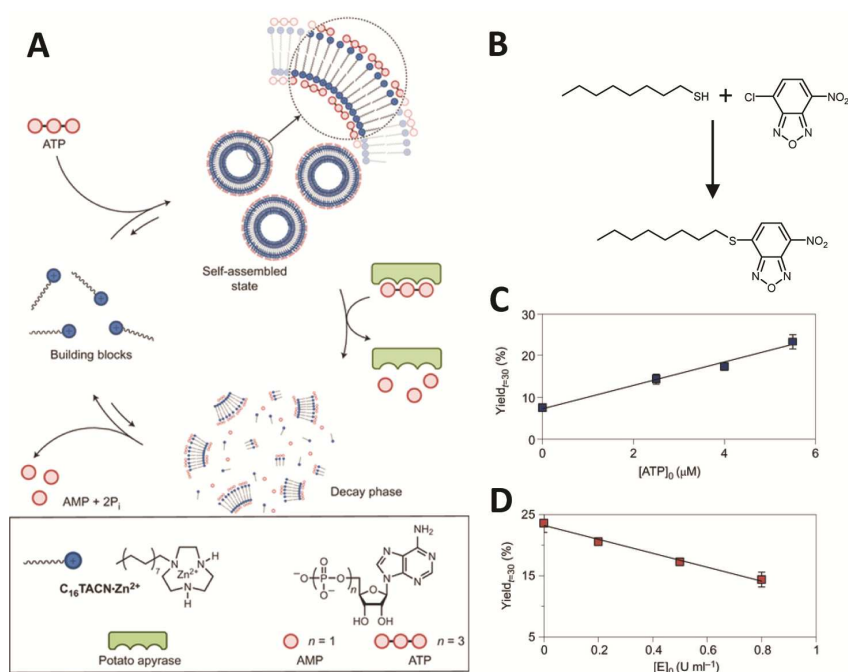
Figure 2.11. Overview of ATP-driven dissipative self-assembly of vesicles. **(a)** Schematic representation of the ATP-activated assembly of cationic surfactants and the potato apyrase catalyzed breakdown of their formed structures. **(b)** The alkylation reaction performed within the vesicle bilayer. **(c)** Relation between the ATP concentration and the yield of the alkylation. **(d)** Relation between the enzyme concentration and the yield of the alkylation. Adapted from ref. (15). Copyright 2016, Nature Publishing Group.

vesicles and allowed control over their lifetime (Figure 2.11a). The transient presence of the vesicles was used to accelerate a chemical reaction of two hydrophobic precursors within the hydrophobic domain of the vesicle bilayer (Figure 2.11b). The authors show that the conversion of the reaction increases with increasing vesicle concentration (Figures 2.11cd). An advantage of such catalysts is that the duration of the chemical reaction can be controlled by the kinetics of fuel conversion, which is subsequently affected by the ATP and potato apyrase concentrations. Moreover, this system could in principle be applied for many chemical reactions, because the only requirement is the hydrophobicity of the reactants.

2.5.2. Controlling motion

DSA is a promising approach to introduce energy-driven motion or actuation in soft materials. To that end, Klajn and coworkers designed a system in which directional motion only occurred in the dissipative self-assembled state.[33] Silica colloids were
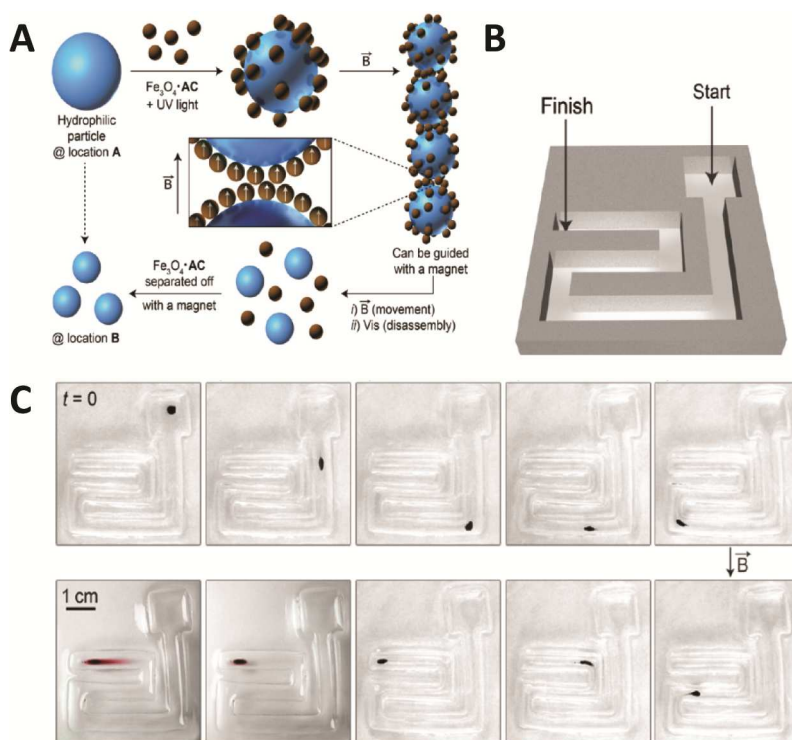
Figure 2.12. DSA and directed motion of particles. **(a)** Schematic overview of the system. Silica and iron oxide particles assemble upon UV-light irradiation. These assemblies can be further aligned with an externally applied magnetic field. Upon removal of the UV-light the assemblies fall apart. **(b)** The setup for the transport experiment. **(c)** Directed transport of the assembly upon a directional change in the magnetic field as imaged by microscopy. Adapted from ref. (33). Copyright 2012, American Chemical Society.

mixed with smaller azobenzene functionalized iron oxide particles. Upon irradiation with UV-light the dipole moment of the azobenzene groups was enlarged caused by the *trans*-to-*cis* configuration. This shift of the dipole moment subsequently resulted in the association of iron oxide particles with the larger silica colloid (Figure 2.12a). When a magnetic field was introduced to the system, the hybrid colloids assembled into elongated chains. Only the hybrid colloids were influenced by the magnetic field, as the externally applied magnetic field was insufficient to affect the unassembled iron oxide particles. The elongated chains could be directed to move to a specific location by controlling the direction of the magnetic field (Figures 2.12bc). When the supramolecular structure reached its destination, the UV-light was switched off and the assembly fell apart. Using this method, apolar diamagnetic particles, such as silica

and gold particles, can be captured and transported to a specific location to be released again.

Directional motion can also be generated using dissipative liquid crystal systems. Takeda and coworkers recently reported an example of a macroscopic system that performed oscillatory motion in response to DSA driven by light.[45] Thin crystalline assemblies made of a mixture of oleic acid and azobenzene derivatives were able to bend and unbend repetitively in an autonomous manner under continuous irradiation of blue light. The blue light increased the amount of *cis*-isomer of the azobenzene which induced instability of the original phase and thereby a morphological transition. As a consequence of this molecular rearrangement, a change in the photoisomerization quantum yield decreased the population of *cis*-isomer. When the amount of *trans*-isomer reached a threshold, the assembly reverted to its original morphology. This mechanical bending-unbending motion observed in this example was then achieved due to the combination of a change of photoisomerization efficiency and phase transitions of the assembly. The frequency of the movement could be tuned by changing the intensity of the light.

Two examples in which the conformation of liquid crystal director depended on irradiation with UV-light were developed by Feringa and coworkers[41, 46] and Tamaoki and coworkers.[22] In these systems, a liquid crystal was mixed with a chiral dopant: a molecular motor or switch. A few weight percentage of the chiral dopant induced a helical cholesteric order in the liquid crystal material. Irradiation with UV-light led to a conformational change in the dopant and an associated change in helical twisting power. This in turn led to a change in the pitch of the cholesteric liquid crystal, thus giving a change in supramolecular assembly. When confined in a thin film, this change in pitch caused a stress in the liquid crystal that was relaxed by the rotational reorganization of the entire film. If a solid object was added on top of the liquid crystal film, it rotated along the liquid crystal rotation (Figure 2.13). After continued UV-light irradiation, the motor or switch dopant reached its photostationary state and the rotational reorganization of the liquid crystal ceased. At this point, the liquid crystal
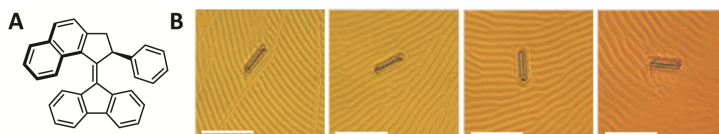

Figure 2.13. (a) UV-light active chiral dopant used by the group of Feringa. **(b)** Rotation of a microscale object and reorganization of a liquid crystal upon UV-light irradiation. Adapted from ref. (46). Copyright 2006, Nature Publishing Group.

was in a steady state that can only be maintained by continuous UV-light irradiation. When the UV-light was switched off, the liquid crystal relaxed back to its original configuration as the chiral dopant fell back to its most stable configuration in a heat activated process. Again, the solid object rotated (counter clockwise) along with the liquid crystal rotation. These examples show that a UV-light driven process can induce a rotational reorganization of a supramolecular structure that can exert a force large enough to rotate and move a microscale object.

Self-oscillating gels can also be used to obtain a directional motion, which in turn can be used for artificial motors and micropumps. Ichijo and coworkers developed a N-isopropylacrylamide (IPAAm) polymer gel functionalized with Ru(bpy)3 groups.[47] They were able to periodically change the oxidation state of the ruthenium from 2+ to 3+ with the Belousov-Zhabotinsky (BZ) reaction. As the Ru-catalyst was only present inside the gel, the oscillation only occurs inside the gel. The authors observed a self-oscillating pattern of 6 mm throughout the gel, caused by the diffusion of the reactants through the gel. The pattern changed in color, redox state and volume over time and space. When the shape of the gel was cut smaller than the pattern wavelength of the oscillation (<6 mm), the gel was homogeneously oscillating between the swollen and the shrunken state. Moreover, by changing the shape of the gel and by changing the period of the chemical oscillator the mechanical motion could be changed. Maeda and coworkers were then able to use this system to create a real micropump using microfluidics.[48] They observed that particles near the gel move about 200-400 µm caused by the swelling and shrinking of the gel.

2.5.3. Transient images

Grzybowski and coworkers designed self-erasing inks based on the DSA of *trans*-azobenzene-functionalized gold and silver nanoparticles that isomerize to *cis*-azobenzene in response to UV-light.[16] The *cis-trans* isomerization served as an activation reaction as it induced a significant increase of the dipole moment which mediated attractive interactions between nanoparticles resulting in their assembly (Figures 2.14ab). Crucially, in the absence of UV-light, the thermodynamically unfavored *cis*-azobenzene isomerized back to its *trans*-constituent, thereby losing the increased dipole moment. In turn, the nanoparticles disassembled to recover their initial dispersed state. In order to achieve spatial and temporal control over the self-assembled state, the nanoparticles were embedded into a thin and flexible organogel. When patterned UV-light was applied via a photomask or by using a laser pen (Figure 2.14c), only the area exposed to the UV-light showed signs of the assembly
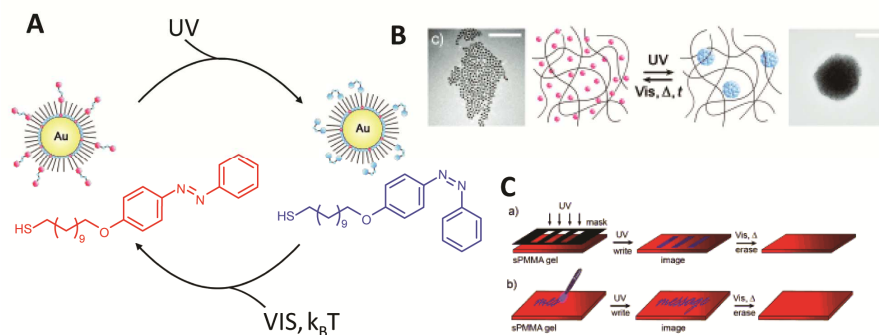
Figure 2.14. Light-driven dissipative self-assembly of nanoparticles. **(a)** Reaction cycle describing the activation-deactivation chemical reactions. The azobenzene trans-isomer on gold nanoparticles (red) isomerized to the cis-isomer (blue) when UV-light irradiation was applied. The cis-isomer reverted to the trans-form either spontaneously or upon irradiation with visible light or by heating. **(b)** TEM images and schematic representation of dispersed functionalized nanoparticles (in red) and spherical assemblies of cis-azobenzene nanoparticles (in blue). **(c)** Schematic representation of a photomask and a light pen used to create patterns of nanoparticles' assemblies upon UV-light irradiation. Adapted from ref. (16). Copyright 2009, Wiley and Sons.

process. Multiple color inks could be obtained by changing the size of the nanoparticle aggregates. Gold nanoparticle dispersions changed color upon UV-light irradiation from red to blue, while the silver nanoparticle dispersions transformed from yellow to red and purple upon UV-light exposure. Additionally, the color of the ink could be controlled by the intensity of UV-light irradiation.

2.6. Can DSA form the materials of the future?

DSA holds great potential for use in dynamic and responsive materials. Due to their dynamics, these structures are endowed with unique properties that open the door to self-healing and adaptive materials that have a level of autonomy that cannot be obtained in equilibrium. Examples from biology verify the importance of dissipative structures for the creation of materials with applications ranging from the diverse functions of the cytoskeleton to self-healing organs. However, the number of man-made materials formed via DSA remains limited to proof-of-concept studies until now. Probably the most explored feature of DSA is the spatial and temporal control over structure formation and associated properties, while the potential for self-healing or adaptive materials has only been explored superficially.

2.6.1. Design rules for DSA

Besides being a relatively new research area, a reason for the mismatch between what possibly can be achieved, and what has been achieved may be the lack of clear design rules for DSA. In contrast to DSA, materials formed via static self-assembly are widely used and the number of examples of applications and new material properties is continuously growing. This success can be partly attributed to the availability of clear design rules. In contrast, the field of DSA is still in an era of serendipity, even though the notion of DSA to create materials is established. One of the major drawbacks of structures formed via DSA is their relatively complicated design that comes with a large set of criteria. Not only should the thermodynamics of the entire system be taken into account, the kinetics of the system also have to match. Based on the experience from our own labs and observations from examples in the literature, we draw here some preliminary design rules that could aid the further development of materials formed by DSA. We anticipate that these rules will further crystallize in the years to come as the field is developing.

First, a reversible transition in supramolecular structure should be engineered between the thermodynamically favored precursor and the out-of-equilibrium building blocks. To obtain this reversible transition, the non-covalent attractive and repulsive interactions between the building blocks have to be balanced to favor assembly upon chemical activation, but favor disassembly upon deactivation. Moreover, the attraction-repulsion balance should be controlled by the CRN. A successful way to satisfy these criteria is the use of reaction networks that alter the ionization state of precursors, thereby changing electrostatic repulsion or attraction and thus inducing self-assembly. Other strategies include changing a dipole moment or activating the ability to form hydrogen bonds. As a result of the vast literature on responsive assemblies, this design criterion is relatively easy to satisfy.

A far more challenging design feature of DSA involves the matching of the kinetics of the chemical reactions involved, such that dissipative assembly is favored. In cases where the reaction network only comprises a building block activation and a deactivation reaction, satisfying this criterion is relatively straightforward, i.e. activation needs to be faster than deactivation to accumulate an amount of building block that is greater than its critical aggregation concentration and that survives for a long enough time to self-assemble. When a finite amount of fuel or a continuous input of fuel is applied, building blocks will be created and the deactivation reaction will commence. Since deactivation is slower than activation, building blocks will accumulate transiently in the case of batch addition, or building blocks will accumulate until the deactivation matches the activation rate and a steady state arises. In the case

of photochemical reactions, the network often only comprises an activation and deactivation step. In such cases, a photon is absorbed and induces an isomerization while a thermal reaction drives the isomerization back to the starting point. If thermal relaxation is sufficiently slow, the high-energy building blocks accumulate and a steady state is formed where building blocks can assemble. In the case of chemical fuels to drive DSA, the networks get more complicated. In such networks, side reactions of the fuel allow for dissipation of energy via non-assembling pathways. For instance, in the case of ATP-driven self-assembly, ATP will spontaneously hydrolyze to ADP, with a half-life in the order of days at room temperature and neutral pH,[49] while in the case of dimethylsulfate-driven self-assembly the half-life of the fuel is in the range of hours.[7] In the latter case, the activation reaction needs to outcompete both the deactivation and the background hydrolysis of the fuel which further complicates the design of the CRN. Taken together, when DSA is driven by photochemical reaction networks, thermal relaxation, i.e. deactivation, should be sufficiently slow to accumulate adequate amount of building blocks. When DSA is driven by CRNs, a fuel should be chosen that is sufficiently stable towards auto-deactivation (via non-assembling pathways) but adequately reactive towards precursors in order to outcompete the deactivation reaction.

Satisfying the criteria above does not have to be a matter of trial and error. In our experience, kinetic modeling of CRNs can be extremely helpful to predict the feasibility of the networks, without performing a single kinetic experiment. Many chemical reaction rates, including the abovementioned dimethylsulfate hydrolysis (background reaction), but also its reaction with carboxylates (activation) and the methyl ester hydrolysis (building block deactivation), can be found in the vast literature on chemical reaction kinetics. Simply implementing these rate constants in a kinetic model can determine whether a CRN follows the above criteria, and can form significant amounts of building block in response to fuel addition. The use of kinetic models that predict the kinetic parameters needed to achieve DSA using CRNs will therefore become a crucial tool to the further development of materials formed via DSA. For further information on the design of complex molecular systems we refer to a recent review by Taylor and coworkers.[50]

2.6.2. Technical challenges

The design rules above are written for the development of systems capable of dissipative assembly, which is not necessarily analogous to a useful material. Even though these structures possess unique features, their use as materials might not be directly obvious. For instance, self-healing materials formed via DSA can be desirable

from a material's point of view, e.g. a self-healing car tire or bumper, but these features require a constant supply of chemical energy to be sustained. This requirement implies that the material needs to be connected to a constant influx of fuel. Biology's solution to this problem is in situ regeneration of the fuel, but even that strategy requires, ultimately, the influx of some sort of energy carrier and building blocks, as well as an efflux of waste products. Until now, this challenge has mostly been ignored and all materials mentioned above deal with finite amounts of fuel that drive transient material formation, until fuel has been consumed and equilibrium is reinstated. To make use of all unique features of DSA, we should start thinking about approaches to overcome the technical challenges of continuous fuel input, e.g. by means of carriers that release large amounts of fuel or by use of fuels that are abundantly available in the environment such as certain metabolites or light.

2.7. Conclusions

Although common in biology, we are only now starting to see the development of the first man-made assemblies formed via DSA, driven directly by light or by chemical reagents, as well indirectly by energy dissipating processes. The variety of assemblies that has been formed via DSA is rich and includes fibers, nanoparticle clusters, vesicles and liquid crystals. These developments have opened the door to functional materials formed via DSA, and thus exploration of the unique properties that such materials possess. Indeed, some materials have been described that display properties unique to DSA, including self-erasing inks and patterns, self-healing supramolecular gels and catalysts with a tunable lifetime and activity. Even though the list of DSA materials remains rather short, the number of successful examples is ramping up and we foresee exciting new applications for DSA in the future.

2.8. References

1.   M. R. Chierotti and R. Gobetto, *Supramolecular Chemistry: From Molecules to Nanomaterials*, 2012.

2.   E. Karsenti, *Nat. Rev. Mol. Cell Biol.*, 2008, **9**, 255-262.

3.   M. Fialkowski, K. J. M. Bishop, R. Klajn, S. K. Smoukov, C. J. Campbell and B. A. Grzybowski, *J. Phys. Chem. B*, 2006, **110**, 2482-2496.

4.   B. A. Grzybowski, C. E. Wilmer, J. Kim, K. P. Browne and K. J. M. Bishop, *Soft Matter*, 2009, **5**, 1110-1128.

5.   F. Tantakitti, J. Boekhoven, X. Wang, R. V. Kazantsev, T. Yu, J. Li, E. Zhuang, R. Zandi, J. H. Ortony, C. J. Newcomb, L. C. Palmer, G. S. Shekhawat, M. O. de la Cruz, G. C. Schatz and S. I. Stupp, *Nat. Mater.*, 2016, **15**, 469-476.

6.   A. Sorrenti, J. Leira-Iglesias, A. J. Markvoort, T. F. A. de Greef and T. M. Hermans, *Chem. Soc. Rev.*, 2017, **46**, 5476-5490.

7. J. Boekhoven, W. E. Hendriksen, G. J. M. Koper, R. Eelkema and J. H. van Esch, *Science*, 2015, **349**, 1075-1079.

8. G. Lebon, D. Jou and J. Casas-Vázquez, *Understanding Non-equilibrium Thermodynamics*, 2008.

9. G. M. Cooper and R. E. Hausman, *The Cell: A Molecular Approach*, 2nd edn., 2007.

10. S. Roychuwdhury and M. M. Rasenick, *Biochemistry*, 1994, **33**, 9800-9805.

11. L. Schaedel, K. John, J. Gaillard, M. V. Nachury, L. Blanchoin and M. Thery, *Nat. Mater.*, 2015, **14**, 1156-1163.

12. F. J. Nédélec, T. Surrey, A. C. Maggs and S. Leibler, *Nature*, 1997, **389**, 305-308.

13. M. Pinot, F. Chesnel, J. Z. Kubiak, I. Arnal, F. J. Nédélec and Z. Gueroui, *Curr. Biol.*, 2009, **19**, 954-960.

14. S. Debnath, S. Roy and R. V. Ulijn, *J. Am. Chem. Soc.*, 2013, **135**, 16789-16792.

15. S. Maiti, I. Fortunati, C. Ferrante, P. Scrimin and L. J. Prins, *Nat. Chem.*, 2016, **8**, 725-731.

16. R. Klajn, P. J. Wesson, K. J. M. Bishop and B. A. Grzybowski, *Angew. Chem. Int. Ed.*, 2009, **48**, 7035-7039.

17. D. Samanta and R. Klajn, *Adv. Opt. Mater.*, 2016, **4**, 1373-1377.

18. J. J. D. de Jong, P. R. Hania, A. Pugžlys, L. N. Lucas, M. de Loos, R. M. Kellogg, B. L. Feringa, K. Duppen and J. H. van Esch, *Angew. Chem. Int. Ed.*, 2005, **44**, 2373-2376.

19. F. Rakotondradany, M. A. Whitehead, A.-M. Lebuis and H. F. Sleiman, *Chem.: Eur. J.*, 2003, **9**, 4771-4780.

20. A. K. Dambenieks, P. H. Q. Vu and T. M. Fyles, *Chem. Sci.*, 2014, **5**, 3396-3403.

21. J. Leira-Iglesias, A. Sorrenti, A. Sato, P. A. Dunne and T. M. Hermans, *Chem. Commun.*, 2016, **52**, 9009-9012.

22. Y. Kim and N. Tamaoki, *J. Mater. Chem. C*, 2014, **2**, 9258-9264.

23. C. A. Angulo-Pachón and J. F. Miravet, *Chem. Commun.*, 2016, **52**, 5398-5401.

24. S. O. Krabbenborg, J. Veerbeek and J. Huskens, *Chemistry*, 2015, **21**, 9638-9644.

25. T. Kosa, L. Sukhomlinova, L. Su, B. Taheri, T. J. White and T. J. Bunning, *Nature*, 2012, **485**, 347-349.

26. T. van Leeuwen, T. C. Pijper, J. Areephong, B. L. Feringa, W. R. Browne and N. Katsonis, *J. Mater. Chem.*, 2011, **21**, 3142-3146.

27. K. Kovacs, R. E. McIlwaine, S. K. Scott and A. F. Taylor, *Phys. Chem. Chem. Phys.*, 2007, **9**, 3711-3716.

28. I. Lagzi, B. Kowalczyk, D. Wang and B. A. Grzybowski, *Angew. Chem., Int. Ed.*, 2010, **49**, 8616-6819.

29. I. Lagzi, D. Wang, B. Kowalczyk and B. A. Grzybowski, *Langmuir*, 2010, **26**, 13770-13772.

30. G. Wang, B. Tang, Y. Liu, Q. Gao, Z. Wang and X. Zhang, *Chem. Sci.*, 2016, **7**, 1151-1155.

31. J. Boekhoven and S. I. Stupp, *Adv. Mater.*, 2014, **26**, 1642-1659.

32. T. Heuser, E. Weyandt and A. Walther, *Angew. Chem. Int. Ed.*, 2015, **54**, 13258-13262.

33. O. Chovnik, R. Balgley, J. R. Goldman and R. Klajn, *J. Am. Chem. Soc.*, 2012, **134**, 19564-19567.

34. P. K. Kundu, D. Samanta, R. Leizrowice, B. Margulis, H. Zhao, M. Börner, T. Udayabhaskararao, D. Manna and R. Klajn, *Nat. Chem.*, 2015, **7**, 646-652.

35. A. Wang, W. Shi, J. Huang and Y. Yan, *Soft Matter*, 2016, **12**, 337-357.

36. J. Boekhoven, A. M. Brizard, K. N. K. Kowlgi, G. J. M. Koper, R. Eelkema and J. H. van Esch, *Angew. Chem. Int. Ed.*, 2010, **122**, 4935-4938.

37. C. G. Pappas, I. R. Sasselli and R. V. Ulijn, *Angew. Chem., Int. Ed.*, 2015, **54**, 8119-8123.

38. T. Heuser, A.-K. Steppert, C. M. Lopez, B. Zhu and A. Walther, *Nano Lett.*, 2015, **15**, 2213-2219.

39. P. K. Kundu, S. Das, J. Ahrens and R. Klajn, *Nanoscale*, 2016, **8**, 19280-19286.

40. S. K. Prasad, G. G. Nair and G. Hegde, *Adv. Mater.*, 2005, **17**, 2086-2091.

41. R. Eelkema, M. M. Pollard, N. Katsonis, J. Vicario, D. J. Broer and B. L. Feringa, *J. Am. Chem. Soc.*, 2006, **128**, 14397-14407.
42. J.-F. Berret, in *Molecular Gels*, Springer, 2005, pp. 235-275.
43. Y. Wei, S. Han, J. Kim, S. Soh and B. A. Grzybowski, *J. Am. Chem. Soc.*, 2010, **132**, 11018-11020.
44. H. Zhao, S. Sen, T. Udayabhaskararao, M. Sawczyk, K. Kučanda, D. Manna, P. K. Kundu, J.-W. Lee, P. Král and R. Klajn, *Nat. Nanotechnol.*, 2016, **11**, 82-88.
45. T. Ikegami, Y. Kageyama, K. Obara and S. Takeda, *Angew. Chem. Int. Ed.*, 2016, **55**, 8239-8243.
46. R. Eelkema, M. M. Pollard, J. Vicario, N. Katsonis, B. S. Ramon, C. W. M. Bastiaansen, D. J. Broer and B. L. Feringa, *Nature*, 2006, **440**, 163.
47. B. R. Yoshida, T. Takahashi, T. Yamaguchi and H. Ichijo, *Adv. Mater.*, 1997, **9**, 175-178.
48. K. Takahashi, S. Nagasawa and S. Maeda, *IEEE Int. Conf. Intell. Robot. Syst.*, 2013, 4040-4045.
49. H. R. Hulett, *Nature*, 1970, **225**, 1248-1249.
50. G. Ashkenasy, T. M. Hermans, S. Otto and A. F. Taylor, *Chem. Soc. Rev.*, 2017, **46**, 2543-2554.

2
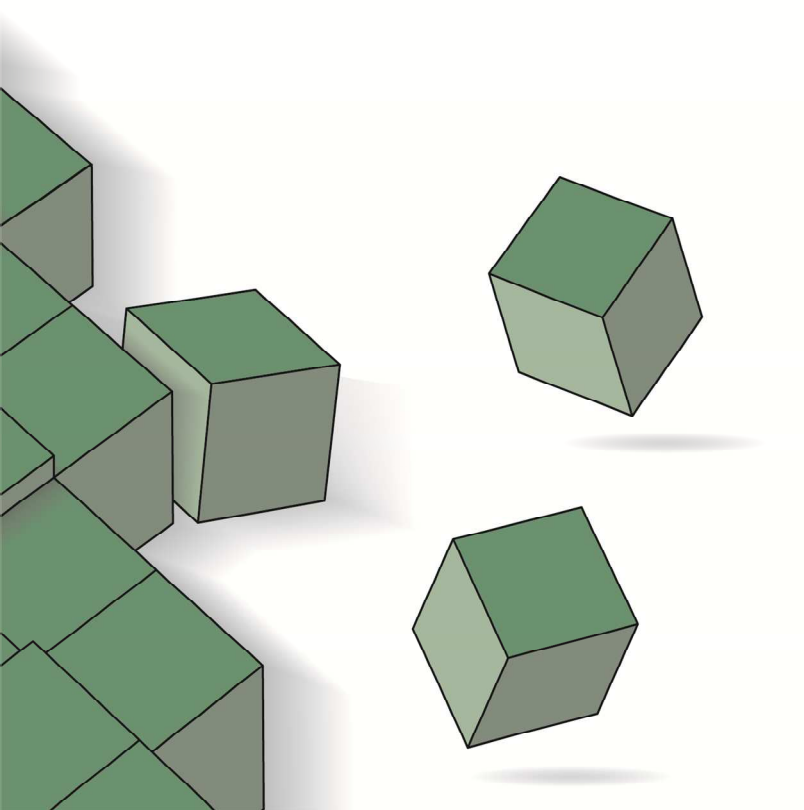
Chapter 3

Catalytic control over individual kinetic pathways in a chemical reaction network leading to transient crystallization

The dynamic behavior of responsive materials is attractive for many applications, but consecutive switching is only possible by manual addition of triggers. Out-of-equilibrium assembly with a fuel-driven chemical reaction network would overcome this problem as they disassemble spontaneously. Fuel concentration and system conditions within the chemical reaction network are mostly used to control the assembly and disassembly kinetics. However, varying these parameters usually has a major impact on the system. Catalysis can control the kinetics without changing the systems conditions significantly resulting in more flexible system. Herein we report a chemical reaction network regulated by two non-enzymatic catalysts, which individually control the assembly and disassembly pathway. The kinetics of the chemical reaction network based on synthetic nicotinamide analogues is regulated by two catalysts: rhodium catalyst and methylene blue catalyst, and the fuel sodium formate. Appling the chemical reaction network to a crystallizing NADH analogue leads to the formation of transient crystals. Our results demonstrate that incorporating two catalysts into the chemical reaction network allows individual control over the reaction pathways leading to temporal control over the material properties. Expanding these catalytically controlled out-of-equilibrium systems will facilitate the route towards to more complex systems such as incorporating spatio-temporal control and feedback loops.

3.1. Introduction

Responsive materials find many applications in drug delivery, catalysis, recycling and actuators.[1-4] Typically, an external trigger initiates a response, switching the material to a new stable state. Return to the original state can only be achieved by a second trigger, which is often a drastic change in environmental conditions (pH, temperature, salt, electric fields). For many applications, it would be beneficial if a material can autonomously revert back to its starting state. This challenge can be approached by coupling a switch in material behavior (e.g. a reversible assembly process) to a fuel-driven chemical reaction network[5-12] or to a dormant deactivator[13, 14]. A further challenge is control over the time scales describing this cyclic process. The behavior of the material is determined by changes in the composition of the coupled chemical reaction network (CRN), which is controlled by the kinetics of the chemical reactions making up the network. A typical CRN contains one reaction pathway that forms activated building blocks from soluble precursors driven by the conversion of a chemical fuel, while another reaction pathway simultaneously and spontaneously depletes the activated building blocks converting it back into the soluble precursor. Temporary accumulation of activated building blocks results in the transient formation of supramolecular structures as long as sufficient fuel is present. Adjusting the kinetics of the individual pathways in the CRN on the molecular scale allows control over the material properties, such as its lifetime and its morphology, on the macro scale.

More than changing environmental conditions or reagent concentrations, a particularly attractive method to control reaction kinetics is through catalysis of individual reaction pathways. As such, kinetics can be adjusted while the chemical environment stays the same. Also, it opens the door to the introduction of feedback loops[15], and spatio-temporal control over structure formation[16]. Maximizing the level of kinetic control requires the separate action of individual catalysts on the various pathways in the CRN. Some studies have a catalyst acting on one of the pathways, or use enzymes which severely limit the operation window of the CRN[11, 17, 18]. We set as a challenge to design a CRN-coupled fuel-driven transient assembly process where both activation and deactivation steps are controlled by catalysis, and determine the impact on the resulting material behavior.

At the start, we designed a CRN with two non-enzymatic catalysts, one accelerating the formation of the activated building blocks, the other accelerating the depletion of the activated building blocks. By coupling the CRN to an assembly structure, i.e. crystallization, we are able to control the lifetime and quantity of the crystals, by controlling the kinetics of the CRN through catalytic activity or fuel concentration. A kinetic model of the underlying CRN enabled a deeper understanding

in the CRN mechanism and explored additional features of the system. Finally, in stark contrast to common, thermodynamically controlled crystallization, we show that after depletion of the fuel, consecutive transient crystallization processes can occur within a single system by addition of a new batch of fuel.

3.2. Results and discussion

The CRN is based on the redox chemistry of synthetic nicotinamide analogues in aqueous solution (Figure 3.1). Important features of this CRN are that the constituents are biocompatible, the nicotinamide cofactor mimics show a large change in polarity upon reduction and oxidation, and the kinetics of their redox chemistry can be regulated by catalysis.[19, 20] The redox cycle starts with the reduction of a cationic nicotinamide mimic (mNAD$^+$) using the reductant sodium formate as chemical fuel. In the process, formate is converted to carbon dioxide. This reaction is catalyzed by [Cp*Rh(bpy-OMe)Cl]Cl (Rh-catalyst), and leads to the accumulation of the synthetic 1,4-dihydronicotinamide analogue (mNADH).[21] Subsequently, mNADH is spontaneously re-oxidized by dissolved molecular oxygen, catalyzed by methylene blue (MB).[20] Based on redox potentials, the mNAD$^+$ redox state is the predominant species in the designed system.[22] With the oxidation and reduction reactions taking place simultaneously, mNAD$^+$ and mNADH are continuously converted into each other during the redox cycle. The CRN is in an out-of-equilibrium state as the concentration of components, such as mNAD$^+$, mNADH, fuel and/or waste are changing over time. Accumulation of mNADH beyond the chemical equilibrium composition requires energy input (fuel conversion) to be maintained. This CRN can then be coupled to an assembly process by careful design of the R-group functionality of mNAD$^+$. Depending on the functionality, various transient assembled states such as finite 3D agglomerates (micelles, vesicles) or infinite 1D objects (fibers, supramolecular polymers) may be achieved.

We started with a glycine functionalized nicotinamide (**1a**, Figure 3.1) in which both the oxidized **1a** and reduced (**1b**, Figure 3.1) state are soluble in aqueous solution. This system was used to investigate the kinetics of the redox reactions and the impact of catalysis on the behavior of the CRN. Next, the CRN was coupled to a transient crystallization process for which the nicotinamide group was functionalized with a hydrophobic *n*-decyl chain (**2a**, Figure 3.1). Thirdly, nicotinamide was functionalized with a *n*-heptyl chain (**3a**, Figure 3.1) that was used to investigate the oxidation rates in the kinetic model.
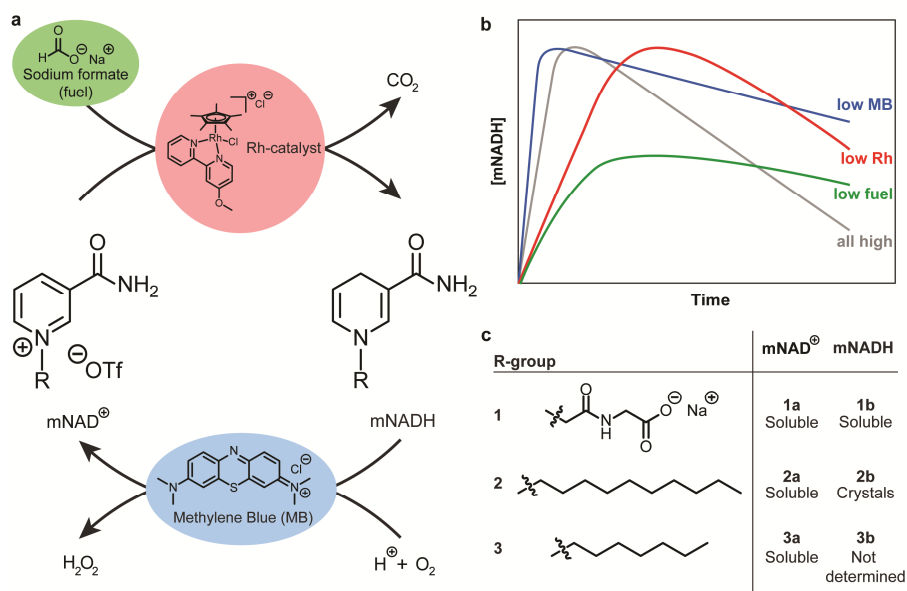
Figure 3.1. Schematic representation of the mNAD⁺/mNADH chemical reaction network. **(a)** Reduction of nicotinamide analogues (mNAD⁺, **1a, 2a, 3a**) using sodium formate as fuel and a rhodium catalyst leads to the transient formation of 1,4-dihydronicotinamide analogues (mNADH, **1b, 2b, 3b**), while the simultaneous oxidation of mNADH with molecular oxygen and methylene blue (MB) as catalyst gradually leads to the accumulation of the starting mNAD⁺. **(b)** Varying the catalysts and fuel concentrations control the accumulation and depletion rate of mNADH and the maximum mNADH concentration and lifetime. **(c)** mNAD⁺ analogues **1a, 1b** and mNADH analogue **2a** are soluble in the aqueous media, while **2b** crystallizes.

3.2.1. The chemical reaction network

To investigate the behavior of the CRN, we used UV-vis spectroscopy to monitor the concentration of **1b** over time. The redox cycles were performed in MOPS buffer (100 mM, pH 7.5) to minimize the degradation of mNAD⁺ and mNADH molecules[23] and the Rh-complex.[21] Typically, a stirred solution of 1.0 mM **1a** will convert to **1b** at a rate of 2.3 mM/h reaching a 100% conversion, in the presence of 0.3 mM Rh-catalyst and 100 mM sodium formate (Supplementary Figure S3.24). Vice versa, **1b** will oxidize back to **1a** using dissolved molecular oxygen and the MB catalyst (0.01 mM) at a rate of 0.73 mM/h (Supplementary Figure S3.25). It should be noted that changing the sample volume to air/water interface ratio and the stirring rate has a significant influence on the oxygen diffusion and thus the oxidation rate (Supplementary Figure S3.33). We used the reaction rates within the CRN such as these mentioned earlier, and its rate constants to construct a kinetic model describing the concentrations of all species in

the system over time (Supplementary Figures S3.23-S3.30). The kinetic model describes the general behavior of the CRN in response to component variation, albeit not a perfect match with the experimental data. The model shows that the kinetics of both the forward and return processes control mNADH levels over time. To experimentally test the response and sensitivity of the system, concentrations of three system constituents were varied: the Rh-catalyst, MB catalyst, and sodium formate. Figures 3.2a-c show that we can increase the accumulation rate of **1a** to **1b** by increasing the Rh-catalyst concentration from 0.1 to 0.3 mM or by increasing the sodium formate concentration from 10 to 100 mM. Furthermore, the accumulation rate can also be increased by decreasing the MB concentration from 0.2 to 0.001 mM as the oxidation rate from **1b** to **1a** decreases. This increase in accumulation rate implies that the system is dynamic, meaning that the reduction and oxidation reactions take place simultaneously during the accumulation of **1b**. Varying the Rh-catalyst and MB concentration shows a 100% conversion of **1a** to **1b**, while decreasing the sodium formate concentration results in lower conversion. This last phenomenon is also observed for the reduction reaction alone (Supplementary Figures S3.23 and S3.24) and it seems that the Michaelis-Menten approximation does not hold as a chemical equilibrium is established at low sodium formate concentrations during the reduction (Supplementary Figure S3.31). The kinetic model correctly describes the majority of the experimental results, only the impact of sodium formate variation and the Rh-catalyst degradation are not described accurately.

As predicted by the model, there are numerous ways to control the depletion rate of **1b** to **1a** and its profile. Most interestingly is the kinetic control of the catalysts over the chemical reaction network without changing the initial concentration of 1a or the fuel. Increasing the MB concentration from 0.001 to 0.1 mM results in a faster depletion rate of **1b** to **1a** leading to a shortening of the lifetime of **1b** from more than 8 h to 5 h (Figure 3.2a). Highly interesting, at [MB] = 0.2 mM a large drop in the maximum concentration of **1b** is observed and a steady state of at least 7 h is observed. Most likely, the low in situ concentration of hydrido Rh-catalyst and the excess of MB results in the equal reduction and oxidation rates (Supplementary information 3.5.11). Two unexpected behaviors are observed in the depletion rate which cannot be explained by only the reduction and oxidation pathway. First, the depletion rate is independent on the Rh-catalyst and second, increasing the sodium formate concentration leads to a decrease in depletion rate. These phenomena can be explained by the degradation of the Rh-catalyst. The active state of the Rh-catalyst, the hydrido Rh-complex, prefers to react with **1a**, however, it can also react with oxygen to irreversibly deactivate the Rh-catalyst. This deactivation leads to the gradual removal

3

of the **1a** reduction pathway from the reaction network, meaning that at the end of the redox cycle only the oxidation path is available. This is observed as an independence of the depletion rate profile on Rh-catalyst concentration. The decline in degradation rate of the Rh-catalyst also results in an increased lifetime of **1b** with decreasing fuel concentration. The binding between the sodium formate and the Rh-complex is a chemical equilibrium. In case of high sodium formate concentrations, the Rh-complex is mostly in the unstable hydrido state, leading to a relatively fast deactivation of the Rh-catalyst. In contrast, in the presence of low sodium formate concentrations, the hydrido Rh-complex concentration is only marginal and hence, the
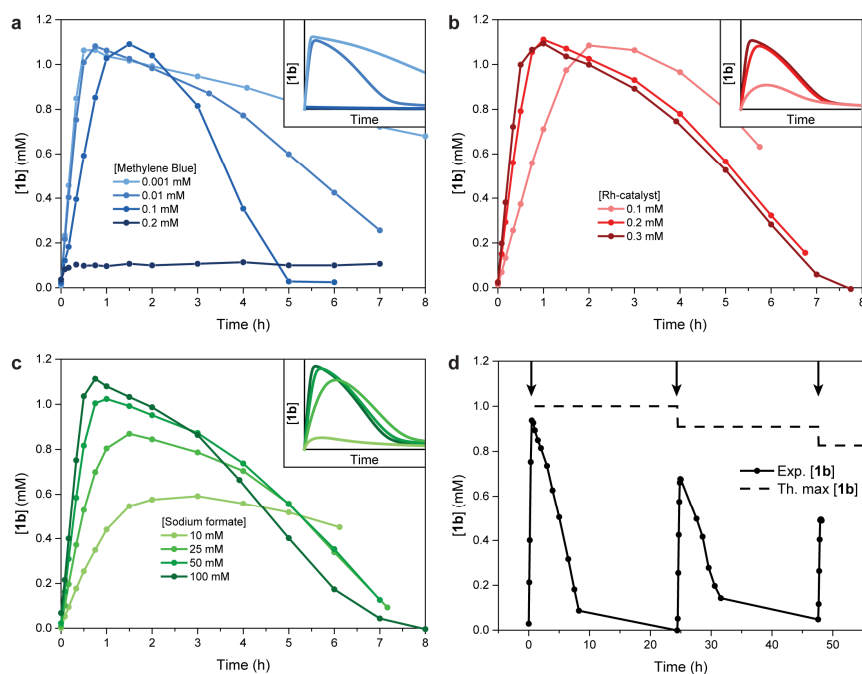
Figure 3.2. Experimental and kinetic model data of the **1a/1b** chemical reaction network. Main graphs show the concentration of **1b** measured experimentally, while the insets show the kinetically modeled concentration of **1b**. General conditions: T = 20°C, stirring rate = 750 rpm, sample volume = 1 mL in a 4 mL vial, [**1a**] = 1.0 mM. **(a)** Concentration of **1b** over time with varying MB concentrations. [Sodium formate] = 100 mM, [Rh-catalyst] = 0.3 mM. **(b)** Concentration of **1b** over time with varying Rh-catalyst concentrations. [Sodium formate] = 100 mM, [MB] = 0.01 mM. **(c)** Concentration of **1b** over time with varying sodium formate concentrations. [Rh-catalyst] = 0.3 mM, [MB] = 0.01 mM. **(d)** We initiated three consecutive redox cycles by adding fresh Rh-catalyst to the system (arrows). First cycle: sample volume = 3 mL in a 4 mL vial, [**1a**] = 1.0 mM, [sodium formate] = 100 mM, [Rh-catalyst] = 0.3 mM. Second cycle: sample volume = 2 mL (taken from previous cycle) in a 4 mL vial, added [Rh-catalyst] = 0.27 mM. Third cycle: sample volume = 2 mL (taken from previous cycle) in a 4 mL vial, added [Rh-catalyst] = 0.27 mM.

50

inactivation reaction is slow. Thus, by decreasing the sodium formate concentration, we can minimize the Rh-complex deactivation rate leading to a longer dynamic regime (Supplementary Figure S3.34). Overall, control over the kinetics of individual pathways using either catalyst or fuel concentrations enables tuning activation and deactivation behavior as well as constituent concentrations over time.

For the **1a**/**1b** CRN we demonstrated initiation of three consecutive cycles by adding fresh Rh-catalyst (Figure 3.2d). At the end of each cycle, the system had returned to [**1b**]~0 mM. Addition of fresh Rh-catalyst led to immediate formation of **1b**, without the need to add more fuel indicating that the system was not at thermodynamic equilibrium yet. In these three cycles, the maximum obtained concentration of **1b** slowly decreases from almost 100% conversion in the first cycle to 60% in the third cycle. This decrease can be explained by lowering of the sodium formate concentration with each cycle, as the maximum [**1b**] is lowered significantly with lower sodium formate concentration (Supplementary Figure S3.24b).

3.2.2. Induced starting delay

An interesting feature that should be further investigated is an induced delay before activation. For example, when coupling the CRN to an assembly process, it would be beneficial for biomedical applications to administer a solution that will form an assembly structure when guided to the desired location.[24, 25] We found that meldola blue is also an efficient oxidation catalyst that can oxidize **3b** to **3a** (Figure 3.3a). However, meldola blue shows a new intriguing characteristic. It can control the onset of the accumulation of **1b** from **1a**, even though the fuel is already added long before (Figures 3.3bc). In a typical experiment, 1.0 mM **1a**, 0.3 mM Rh-catalyst, 100 mM sodium formate and a variable amount of meldola blue is dissolved in MOPS buffer (100 mM, pH 7.5). The oxygen is supplied by slowly bubbling molecular oxygen through the solution. After the start of the redox cycle about 20% of **1b** is formed after which a steady state is obtained. We can control how long this steady state period is present by varying the concentration of meldola blue and molecular oxygen in the system. A concentration of 0.012 mM meldola blue does not show a steady state behavior, but when we increase this concentration to 0.024 mM and 0.060 mM we can extent this steady state period to 30 and 50 minutes, respectively (Figure 3.3b). Furthermore, comparison of the results in Chapter 3 and Chapter 4 where we stirred the solution and bubbled the solution with pure molecular oxygen, respectively, showed that bubbling with pure molecular oxygen increases the dissolved oxygen concentration in the solution (Figure 3.4c and Figure 4.3c). This result is also found here as the steady state period increases from 20 to 50 minutes when we bubble the solution with pure
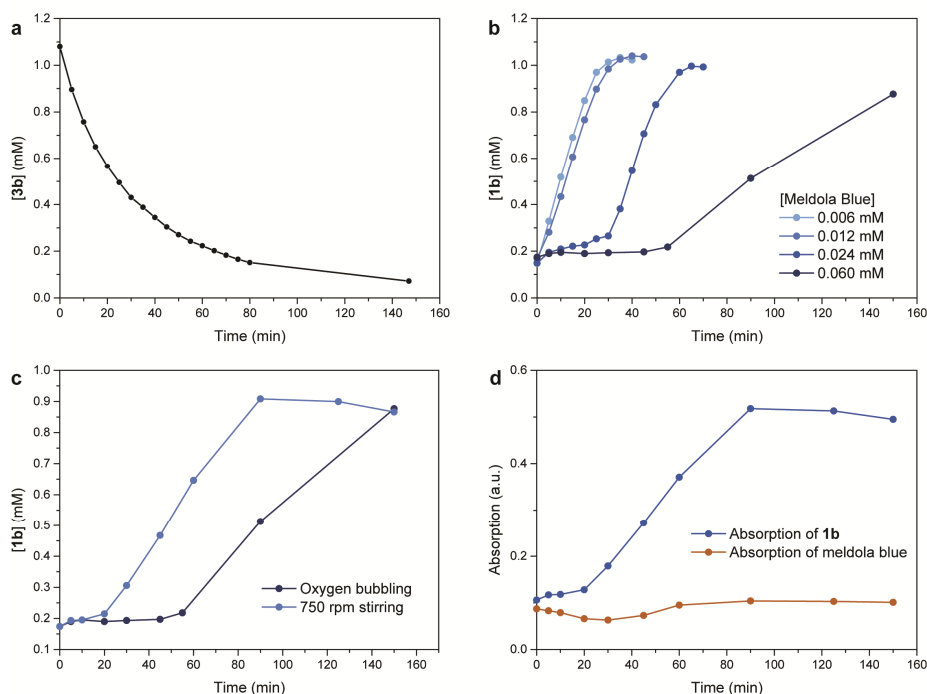
Figure 3.3. Kinetic behavior of the chemical reaction network of mNAD$^+$/mNADH using meldola blue as oxidation catalyst. **(a)** Oxidation of 1.1 mM **3b** with 0.1 mM meldola blue. **(b)** Formation of **1b** with different concentrations of meldola blue showing an induced starting delay in **1b** formation. General conditions: T = 20°C, slow molecular oxygen bubbling through the solution, 1.0 mM **1a**, 0.3 mM Rh-catalyst, 100 mM sodium formate. **(c)** A difference in formation rate of **1b** upon oxygen bubbling and upon stirring (750 rpm). General conditions: T = 20°C, 1.0 mM **1a**, 0.3 mM Rh-catalyst, 100 mM sodium formate, 0.06 mM meldola blue. **(d)** Meldola blue is being reduced during the steady state of **1b**. When all meldola blue is reduced the accumulation of **1b** starts.

molecular oxygen instead of stirring (Figure 3.3c). After this steady state period, the reduction of **1a** to **1b** starts and full conversion is reached.

Our hypothesis of the different kinetic behavior between MB and meldola blue within the CRN is the difference in oxidation rate with molecular oxygen. The reduced state of methylene blue oxidizes very slowly with molecular oxygen resulting in the accumulation of the reduced methylene blue state during the redox cycle. We believe that reduced meldola blue oxidizes faster resulting in a higher oxidized meldola blue concentration in the system during the steady state. The hydrido Rh-complex can therefore donate the hydride for a longer time period to the meldola blue. However, it seems that during the redox cycle the reaction of molecular oxygen with meldola blue is a faster than the dissolution of gaseous oxygen. Therefore, the dissolved molecular

oxygen concentration gradually lowers, resulting in a significant decrease in the oxidation rate of meldola blue. This decrease results in a decrease in oxidized meldola blue and subsequently the hydrido Rh-complex starts to donate the hydride to **1a** resulting in the accumulation of **1b**. The dependence on meldola blue concentration and dissolved molecular oxygen concentration support this theory as oxidized meldola blue is present when these concentrations are higher. Moreover, from the absorption spectrum we observe that the reduction of **1a** starts when most of the meldola blue is reduced (Figure 3.3d). Thus to conclude, meldola blue gives us the ability to control to some extent when activation starts and thus most likely also the onset of assembly. Exploring this feature in more detail could result in new developments in the biomedical and material field. For example, we could apply liquids to the human body that solidify after a desired time just like the extensively explored triggered assembly systems.[24, 25]

3.2.3. Transient crystallization

We coupled the mNAD$^+$/mNADH CRN to an assembly process by using the cationic NAD$^+$ group as the polar head group in surfactant **2a** (Figure 3.1). Using the CRN to temporarily reduce **2a** to **2b** will dramatically lower the surfactant solubility and should lead to transient structure formation. The critical aggregation concentration of **2a** in MOPS buffer (100 mM, pH 7.5) is higher than 5.0 mM (Supplementary Figure S3.35). As such, a 2.0 mM solution of **2a** remains an isotropic solution. **2b** has a low solubility in buffer and at a concentration of 2.0 mM we observed the formation of large sub-millimeter crystals (Figure 3.4ab). When using **2a/2b** CRN in a typical experiment (2.0 mM **2a**, 0.3 mM Rh-catalyst, 0.1 mM MB and 100 mM sodium formate) we observed the formation of sub-millimeter crystals 10 min after addition of the fuel. After 7 h these crystals have dissolved again, to yield a clear solution. The solution changes color during the redox cycle due to the change in the redox state of MB (the oxidized state is blue, the reduced state is pink at high MBH concentrations) (Figure 3.4a). 1.5 h into a cycle, isolated crystals we found to consist of 83% **2b** and 17% **2a** (^{1}H-NMR, Supplementary Figure S3.36).

We investigated the influence of the Rh-catalyst, MB and sodium formate concentration on the kinetics of crystal formation and dissolution (Figure 3.4). Most trends align with those found for the **1a/1b** CRN, for example the crystallization rate increases when increasing the Rh-catalyst or sodium formate concentration, or by decreasing the MB concentration. Furthermore, the crystal lifetime is not significantly influenced by the Rh-catalyst concentration, but increases with decreasing sodium formate concentration. Both trends are connected to Rh-catalyst deactivation during
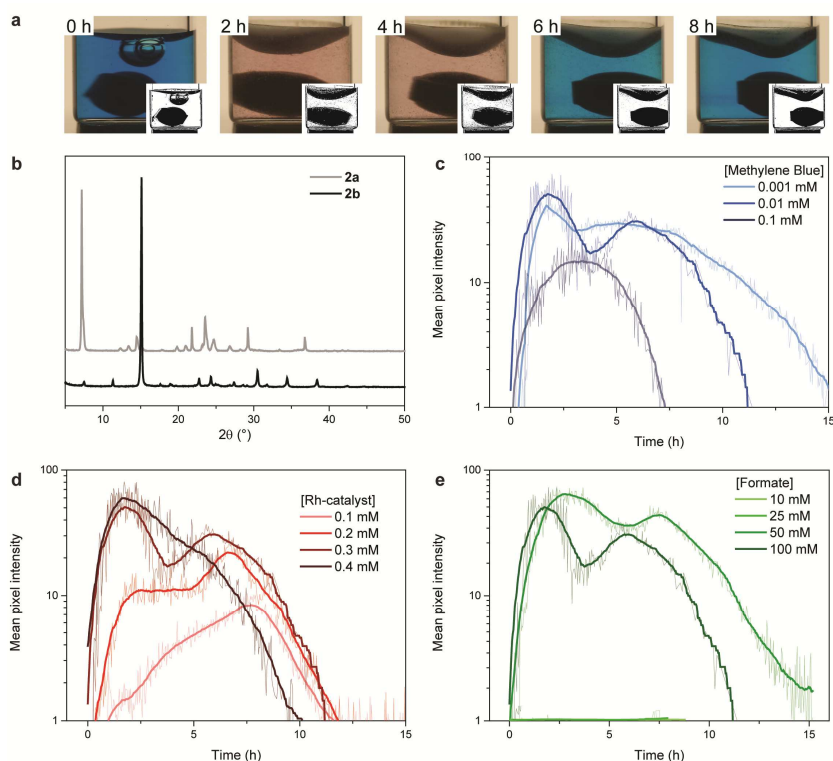
Figure 3.4. The kinetics of transient crystallization depends on reaction kinetics. General conditions: T = 20°C, stirring rate = 750 rpm, sample volume = 1 mL in a 4 mL vial, [**2a**] = 2.0 mM. **(a)** Photographs of the mixture over time. Inset: pictures after automated data treatment. The mean pixel intensity of the mixture is used as a measure for the number of crystals (Supplementary Information). [Sodium formate] = 100 mM, [Rh-catalyst] = 0.3 mM, [MB] = 0.1 mM. **(b)** X-ray diffraction spectra of **2a** (precipitated from diethyl ether), and **2b** particles isolated by filtration after 2 h in the redox cycle. [Sodium formate] = 100 mM, [Rh-catalyst] = 0.3 mM, [MB] = 0.1 mM, volume = 100 mL in a 250 mL round bottom flask. In **(c-e)** the mean pixel intensity in a fixed representative area of mixture is a measure for the number of crystals during a cycle. **(c)** shows the influence of the MB concentration ([sodium formate] = 100 mM, [Rh-catalyst] = 0.3 mM). **(d)** shows the influence of the Rh-catalyst concentration ([sodium formate] = 100 mM, [MB] = 0.01 mM). **(e)** shows the influence of the sodium formate concentration ([Rh-catalyst] = 0.3 mM, [MB] = 0.01 mM).

the cycle. Increasing the MB concentration from 0.001 to 0.1 mM decreases the crystal lifetime from 15 h to 7 h. Although a similar trend, the crystal lifetime is substantially longer than that of dissolved **1b** in the **1a/1b** CRN. This effect is likely caused by the low solubility of **2b** leading to a high concentration of solid **2b** and a low concentration of dissolved **2b**, resulting to a reduced contact interface between **2b** and MB. Near the end of the cycle, these samples turn blue while the crystals are still abundantly present. The blue color indicates that MB is already in the oxidized state, which

signifies that the oxidation rate is low although the total amount of **2b** is high. Furthermore, the **2a/2b** CRN shows a decrease in number of formed crystals upon decreasing the Rh-catalyst or sodium formate concentration, or increasing the MB concentration, caused by a lower conversion from **2a** to **2b** and thus a lower crystal concentration. Finally, it should be noted that the crystals tend to stick on the walls of the vial, which is possibly tied to the observable temporary drop in the number of freely suspended crystals (Figures 3.4c-e).

These results show that increasing the Rh-catalyst concentration increases the crystallization rate while increasing the MB concentration leads to the opposite behavior. Furthermore, a larger maximum amount of crystals can be obtained by increasing the Rh-catalyst or sodium formate concentration or by decreasing the MB concentration. Additionally, where conventional crystallizations lead to the formation of an infinitely stable product in a one-shot process, coupling a crystallization process to a fuel-driven CRN leads to the formation of crystals with a finite lifetime, as we show above. Moreover, within a single system this assembly process can take place several times by repeatedly making fuel available to the system. In the current reaction network, the kinetics of the activation (fuel conversion) pathway is mostly dictated by the availability of active Rh-catalyst. So, by adding fresh Rh-catalyst to the system after completing a crystallization cycle, we enable a second crystallization process to take place. This phenomenon is demonstrated by adding fresh Rh-catalyst (0.27 mM) to a
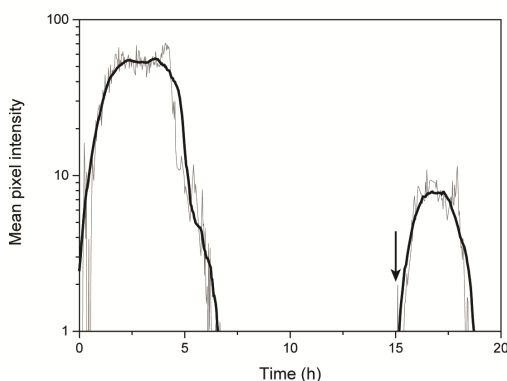
Figure 3.5. Repeated transient crystallization. Mean pixel intensity over time of a representative square in the mixture is taken as a measure for the number of crystals. Two consecutive crystallization cycles were performed. The arrow indicates when the 2nd redox cycle is initiated by addition of Rh-catalyst. Concentrations during the first cycle: [**2a**] = 2.0 mM, [sodium formate] = 100 mM, [Rh-catalyst] = 0.3 mM. For the second cycle Rh-catalyst solution (0.111 mL, 3.0 mM) was added. T = 20°C, stirring rate = 750 rpm, sample volume = 1 mL in a 4 mL vial.

mixture that had returned to the isotropic state after a 7 h crystallization cycle (Figure 3.5). We observed the formation and subsequent dissolution of new crystals. The number of crystals was significantly lower and their lifetime shorter than in the first cycle. A third redox cycle did not show any crystallization. This trend, where we observe a smaller output in consecutive redox cycles, is similar to that observed for the **1a/1b** CRN where the maximum amount of **1b** decreases significantly with each additional cycle.

3.3. Conclusions

Catalytic control over independent pathways in a chemical reaction network that is coupled to an assembly process can control its transient behavior. We demonstrate the impact of catalytic activity on a transient crystallization process by coupling it to a nicotinamide-based chemical reaction network. The network is driven by the conversion of sodium formate, with a rhodium complex catalyzing the reduction of mNAD$^+$, and methylene blue catalyzing the oxidation of mNADH. By balancing the availability of catalysts and fuel, the accumulation and depletion rate and the maximum concentration of mNADH can be controlled. Linking this chemical reaction network to a molecule undergoing a reversible polarity decrease leads to temporal control over crystal lifetime. Incorporating catalysis into transient assembly systems can lead to more control over out-of-equilibrium systems which can result in more complex out-of-equilibrium systems, such as spatio-temporal control and feedback loops.

3.4. References

1. X. Du, J. Zhou, J. Shi and B. Xu, *Chem. Rev.*, 2015, **115**, 13165-13307.
2. X. Hu, Y. Zhang, Z. Xie, X. Jing, A. Bellotti and Z. Gu, *Biomacromolecules*, 2017, **18**, 649-673.
3. M. A. C. Stuart, W. T. S. Huck, J. Genzer, M. Müller, C. Ober, M. Stamm, G. B. Sukhorukov, I. Szleifer, V. V. Tsukruk, M. Urban, F. Winnik, S. Zauscher, I. Luzinov and S. Minko, *Nat. Mater.*, 2010, **9**, 101-113.
4. T. Manouras and M. Vamvakaki, *Polym. Chem.*, 2017, **8**, 74-96.
5. S. A. P. van Rossum, M. Tena-Solsona, J. H. van Esch, R. Eelkema and J. Boekhoven, *Chem. Soc. Rev.*, 2017, **46**, 5519-5535.
6. J. Boekhoven, W. E. Hendriksen, G. J. M. Koper, R. Eelkema and J. H. van Esch, *Science*, 2015, **349**, 1075-1079.
7. M. Tena-Solsona, B. Rieß, R. K. Grötsch, F. C. Löhrer, C. Wanzke, B. Käsdorf, A. R. Bausch, P. Müller-Buschbaum, O. Lieleg and J. Boekhoven, *Nat. Commun.*, 2017, **8**, 15895.
8. S. Maiti, I. Fortunati, C. Ferrante, P. Scrimin and L. J. Prins, *Nat. Chem.*, 2016, **8**, 725-731.
9. S. Debnath, S. Roy and R. V. Ulijn, *J. Am. Chem. Soc.*, 2013, **135**, 16789-16792.
10. C. A. Angulo-Pachón and J. F. Miravet, *Chem. Commun.*, 2016, **52**, 5398-5401.
11. S. Dhiman, A. Jain and S. J. George, *Angew. Chem. Int. Ed.*, 2016, **55**, 1-6.

12. J. Leira-Iglesias, A. Sorrenti, A. Sato, P. A. Dunne and T. M. Hermans, *Chem. Commun.*, 2016, **52**, 9009-9012.
13. T. Heuser, A.-K. Steppert, C. M. Lopez, B. Zhu and A. Walther, *Nano Lett.*, 2015, **15**, 2213-2219.
14. T. Heuser, E. Weyandt and A. Walther, *Angew. Chem. Int. Ed.*, 2015, **54**, 13258-13262.
15. R. Tamate, T. Ueki, M. Shibayama and R. Yoshida, *Soft Matter*, 2017, **13**, 4559-4568.
16. C. Maity, W. E. Hendriksen, J. H. van Esch and R. Eelkema, *Angew. Chem. Int. Ed.*, 2015, **127**, 1012-1015.
17. A. Sorrenti, J. Leira-Iglesias, A. Sato and T. M. Hermans, *Nat. Commun.*, 2017, **8**, 15899.
18. L. Heinen, T. Heuser, A. Steinschulte and A. Walther, *Nano Lett.*, 2017, **17**, 4989-4995.
19. H. C. Lo, C. Leiva, O. Buriez, J. B. Kerr, M. M. Olmstead and R. H. Fish, *Inorg. Chem.*, 2001, **40**, 6705-6716.
20. P. Sevcik and H. B. Dunford, *J. Phys. Chem.*, 1991, **95**, 2411-2415.
21. F. Hollmann, B. Witholt and A. Schmid, *J. Mol. Catal. B Enzym.*, 2003, **19-20**, 167-176.
22. F. L. Rodkey and J. A. Donovan Jr, *J. Biol. Chem.*, 1959, **234**, 677-680.
23. H. K. Chenault and G. M. Whitesides, *Appl. Biochem. Biotechnol.*, 1987, **14**, 147-197.
24. J. Hu, G. Zhang and S. Liu, *Chem. Soc. Rev.*, 2012, **41**, 5933-5949.
25. J. Zhang, X. Li and X. Li, *Prog. Polym. Sci.*, 2012, **37**, 1130-1176.

3

3.5. Supplementary information

Contents

3.5.1.   Methods

NMR spectra were recorded on an Agilent-400 MR DD2 (399.7 MHz for ^{1}H, 100.5 MHz for ^{13}C and 376.7 MHz for ^{19}F) at 298 K using residual protonated solvent signals as internal standard. Mass spectra (MS) were obtained on a Shimadzu LCMS-2010 by electrospray ionization in positive and negative mode (ESI+ and ESI-). UV-vis spectroscopic measurements were performed on a Shimadzu UV-1800 spectrophotometer; quartz cuvettes with a path length of 0.1 cm were used. Kinetic modeling was done using Matlab 2015b. The photos were taken with a Canon single lens reflex camera and were analyzed with Fiji software. X-ray diffraction spectra were recorded in Bragg-Brentano reflection mode by a Bruker D8 Advance X-ray diffractometer with Co as source operating in an angular 2θ range of 5°-50°.

3.5.2. Synthesis

Materials

All compounds and solvents were used without further purification. The technical solvents were purchased from VWR and the reaction solvents were purchased from Sigma-Aldrich. All other chemicals were bought from Sigma-Aldrich with the exception of glycine (Fluka), silver triflate (Fluorochem), 3-fluoroaniline (Fluorochem), 1-bromoheptane (Alfa Aesar) and MOPS (Alfa Aesar).

Synthesis procedure of 1a
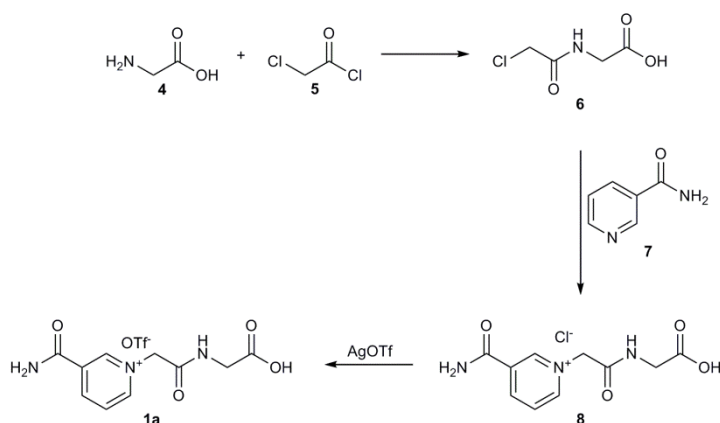
Figure S3.1. Synthetic route for the formation of **1a**.

(2-Chloroacetyl)glycine 6. Glycine **4** (13.8 g, 184 mmol) was suspended in acetonitrile (100 mL). Chloroacetyl chloride **5** (7.50 mL, 94.4 mmol) was added dropwise to the suspension. This suspension reacted at room temperature overnight. ^{1}H-NMR showed that the reaction was not complete. Therefore, chloroacetyl chloride (4.00 mL, 50.3 mmol) was added dropwise to the suspension, which reacted again overnight. The crude product was filtrated and the solid residue was recrystallized in acetonitrile. After drying in the vacuum oven **6** was obtained as a white solid (7.64 g, 55%). M.p. 93-94 °C. ^{1}H-NMR (399.7 MHz, CD3OD, ppm): δ 4.11 (s, 2H, CH2Cl), 3.95 (s, 2H, CH2). 13C-NMR (100.5 MHz, CD3OD, ppm): δ 171 (C=O), 168 (C=O), 42 (CH2), 41 (CH2). MS (ESI Neg.) m/z: 149.95 [(M-)] (expected m/z = 150.00).
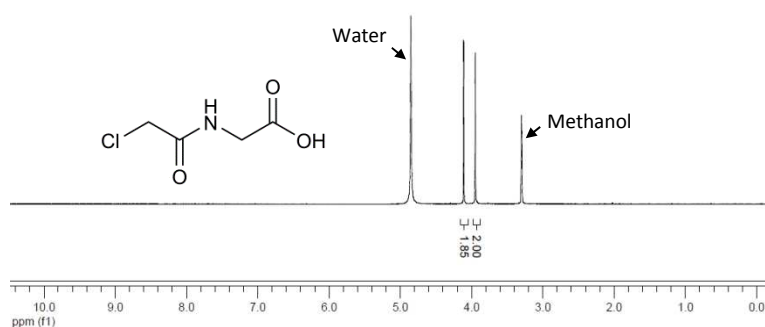
Figure S3.2. ^{1}H-NMR (CD$_3$OD) of **6**.
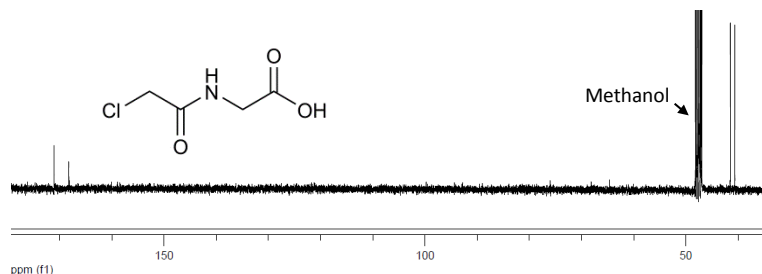
Figure S3.3. ^{13}C-NMR (CD$_3$OD) of **6**.

3-Carbamoyl-1-(2-((carboxymethyl)amino)-2-oxoethyl)pyridin-1-ium chloride 8. (2-Chloroacetyl)glycine **6** (7.50 g, 49.5 mmol) was suspended in acetonitrile (50 mL). Nicotinamide **7** (6.05 g, 49.5 mmol) was added and the suspension was refluxed for six days. The crude suspension was filtrated and the residue was the pure product **8** (12.1 g, 89%). M.p. 238-240 °C (decomposition); ^{1}H-NMR (399.7 MHz, D2O, ppm): δ 9.18 (s, 1H, Ar*H*), 8.86 (m, 2H, Ar*H*), 8.13 (t, J = 7.0 Hz, 1H, Ar*H*), 5.53 (s, 2H, C*H*2N), 3.96 (s, 2H, C*H*2). 13C-NMR (100.5 MHz, D2O, ppm): δ 173 (*C*=O), 166 (*C*=O), 148 (C_{Ar}), 146 (C_{Ar}), 145(C_{Ar}), 134 (C_{Ar}), 128 (C_{Ar}), 62 (*C*H$_2$), 42 (*C*H$_2$). MS (ESI Pos.) m/z: 238.95 [(M$^+$)] (expected m/z = 238.08).
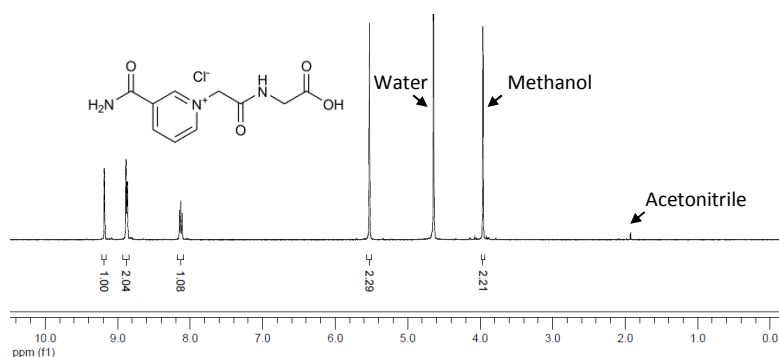
Figure S3.4. ^{1}H-NMR (D$_2$O) of **8**.
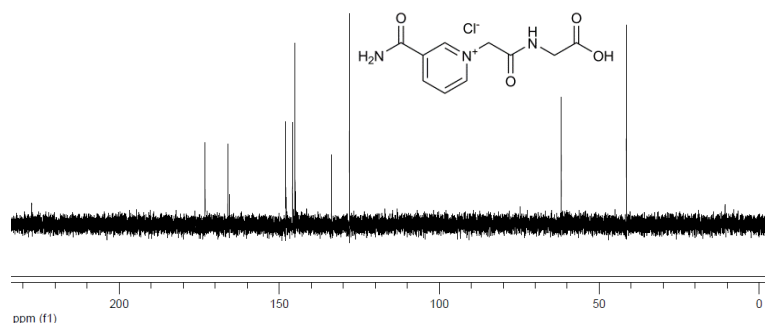
Figure S3.5. ^{13}C-NMR (D$_2$O) of **8**.

3-Carbamoyl-1-(2-((carboxymethyl)amino)-2-oxoethyl)pyridin-1-ium triflate 1a. 8 (12.1 g, 44.1 mmol) was dissolved in deionized water (200 mL) and silver triflate (AgOTf, 11.3 g, 44.1 mmol) was dissolved in deionized water (40 mL). The silver triflate solution was added dropwise to the **7** solution under vigorous stirring. After direct formation of a white suspension, the mixture was allowed to react further at room temperature for 30 minutes. Subsequently, the solid side product was filtrated using a paper filter and the water from the filtrate was evaporated. The solid was dried in the vacuum oven and afforded the solid grey product **1a** (14.5 g, 85%). 3-fluoroaniline was added to the NMR sample to determine the ion exchange conversion (103%). M.p. 133-137 °C; ^{1}H-NMR (399.7 MHz, CD$_3$OD, ppm): δ 9.37 (s, 1H, Ar*H*), 9.01 (m, 2H, Ar*H*), 8.21 (t, J = 7.2 Hz, 1H, Ar*H*), 5.57 (s, 2H, C*H*2N), 4.01 (s, 2H, C*H*2). ^{13}C-NMR (100.5 MHz, CD$_3$OD, ppm): δ 171 (*C*=O), 165 (*C*=O), 164 (*C*=O), 147 (*C*$_{Ar}$), 146 (*C*$_{Ar}$), 144 (*C*$_{Ar}$), 134 (*C*$_{Ar}$), 127(*C*$_{Ar}$), 62 (*C*H$_2$), 41 (*C*H$_2$). ^{19}F-NMR (376.7 MHz, CD$_3$OD, ppm): δ -80.10 (triflate),

-115.86 (3-fluoroaniline), MS (ESI Pos.) m/z: 237.90 [(M$^+$)] (expected m/z = 238.08), MS (ESI Neg.) m/z: 148.90 [(OTf$^-$)] (expected m/z = 148.95).
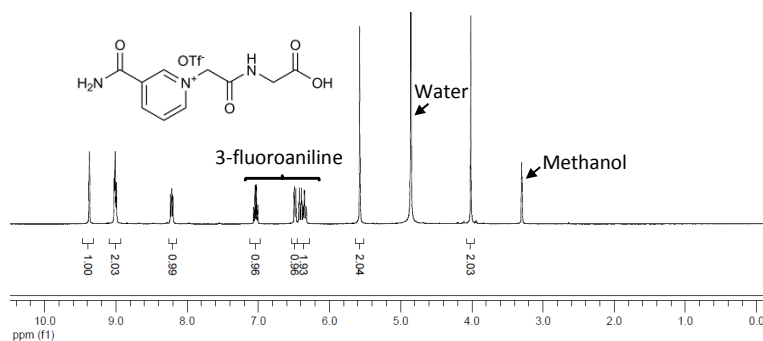
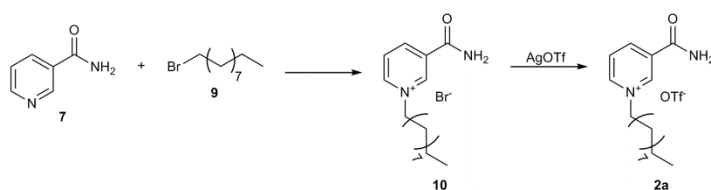**Figure S3.6.** ^{1}H-NMR (CD$_3$OD) of **1a** and 3-fluoroaniline.
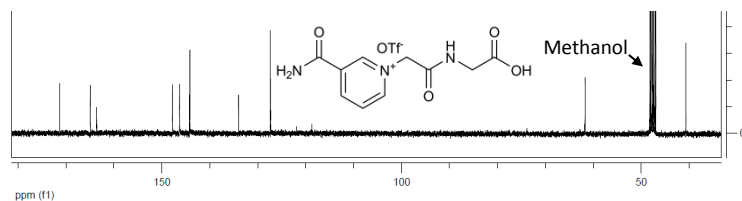
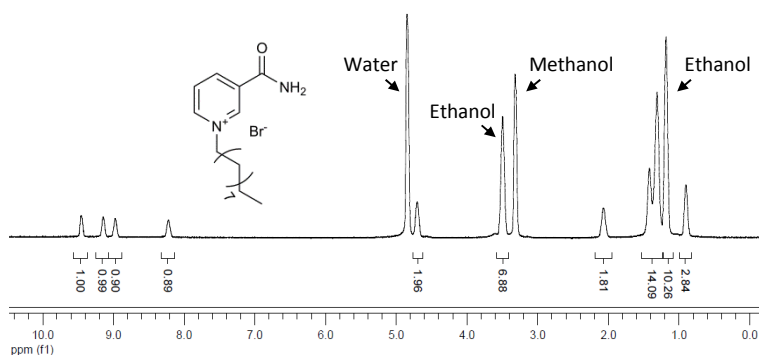**Figure S3.7.** ^{13}C-NMR (CD$_3$OD) of **1a**.
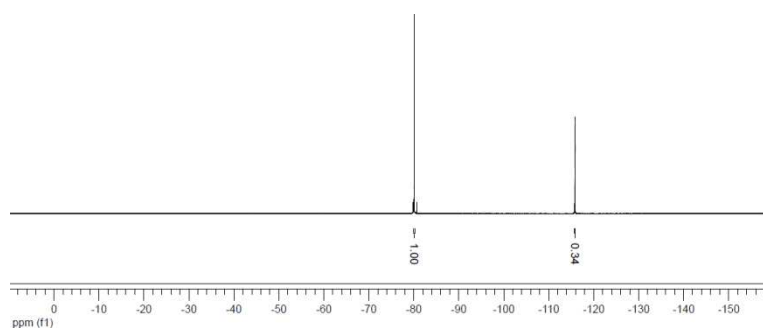
Figure S3.8. ^{19}F-NMR (CD$_3$OD) of **1a** and 3-fluoroaniline.

Synthesis procedure of 2a

Figure S3.9. Synthetic route for the formation of **2a**.

1-Decyl-3-carbamoylpyridinium bromide 10. Nicotinamide **7** (856 mg, 7.0 mmol) was suspended in acetonitrile (10 mL). Next, 1-bromodecane **9** (2.20 mL, 10.6 mmol) was added and the suspension was refluxed overnight. During refluxing, **7** dissolved. The next day a suspension was formed which was cooled down to room temperature. The acetonitrile was evaporated and the residue was dissolved in a minimum amount of ethanol. The solution was then added dropwise to diethyl ether. The mixture was filtrated. This filtration was done three times resulting in the white solid product **10** (1.42 g, 71%). M.p. 215-216 °C (decomposition); ^{1}H-NMR (399.7 MHz, CD$_3$OD, ppm): δ 9.46 (s, 1H, Ar*H*), 9.14 (1H, Ar*H*), 8.97 (1H, Ar*H*), 8.22 (1H, Ar*H*), 4.71 (2H, C*H*2N), 2.07 (2H, C*H*2), 1.4 (m, 14*H*, C*H*2). ^{13}C-NMR (100.5 MHz, DMSO, ppm): δ 163 (*C*=O), 147 (C_{Ar}), 145 (C_{Ar}), 144 (C_{Ar}), 134 (C_{Ar}), 128 (C_{Ar}), 62 (CH_2), 32 (CH_2), 31 (CH_2), 29 (CH_2), 29 (CH_2), 29 (CH_2), 29 (CH_2), 26 (CH_2), 23 (CH_2), 14 (CH_3). MS (ESI Pos.) m/z: 263.40 [(M$^+$)] (expected m/z = 263.21).
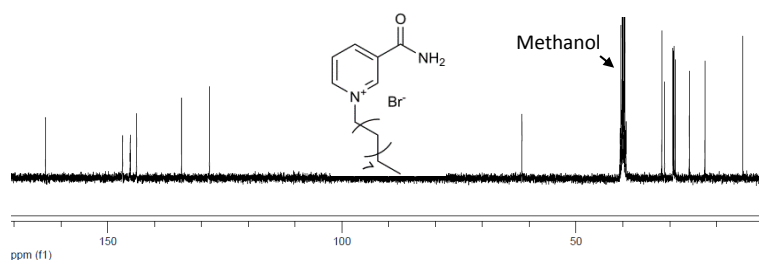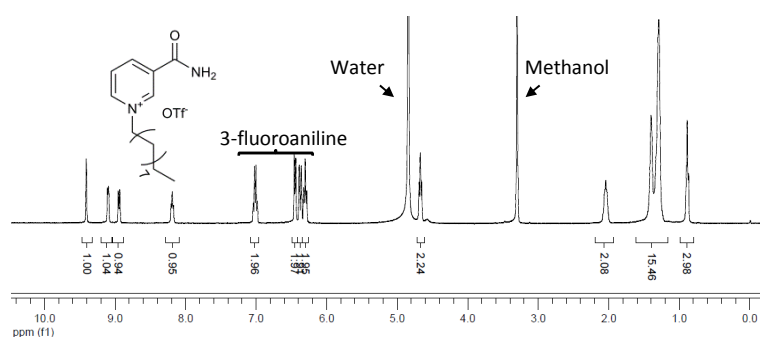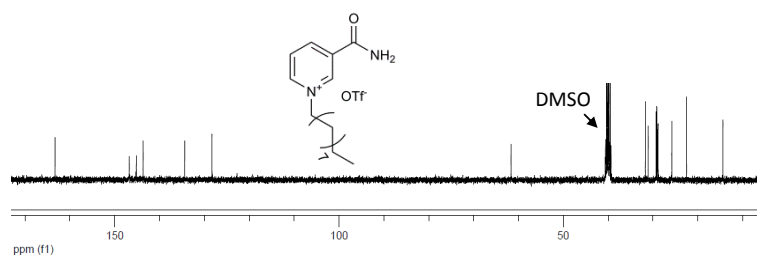

Figure S3.10. ^{1}H-NMR (CD$_3$OD) of **10**.

Figure S3.11. ^{13}C-NMR (DMSO) of **10**.

1-Decyl-3-carbamoylpyridinium triflate 2a. 1-Decyl-3-carbamoylpyridinium bromide **10** (711 mg, 2.07 mmol) was dissolved in methanol (5 mL) and silver triflate (AgOTf, 532 mg, 2.07 mmol) was dissolved in methanol (2 mL). The silver triflate solution was added dropwise to the **9** solution under vigorous stirring. After direct formation of a yellow suspension, the mixture was allowed to react further at room temperature for 1 h. Subsequently, the solid was filtrated using a paper filter and the methanol from the filtrate was evaporated. The solid was dried in the vacuum oven and afforded the solid white product **2a** (759 mg, 89%). 3-fluoroaniline was added to the NMR sample to determine the ion exchange conversion (90%). M.p. 131-133 °C; ^{1}H-NMR (399.7 MHz, CD$_3$OD, ppm): δ 9.41 (s, 1H, ArH), 9.11 (d, J = 5.6 Hz, 1H, ArH), 8.95 (d, J = 8.0 Hz, 1H, ArH), 8.19 (t, J = 6.6 Hz, 1H, ArH), 4.67 (t, J = 7.6 Hz, 2H, CH2N), 2.04 (m, 2H, CH2), 1.4-1.2 (m, 14H, CH2). ^{13}C-NMR (100.5 MHz, DMSO, ppm): δ 163 (C=O), 147 (C_{Ar}), 145 (C_{Ar}), 144 (C_{Ar}), 134 (C_{Ar}), 128 (C_{Ar}), 62 (CH_2), 32 (CH_2), 31 (CH_2), 29 (CH_2), 29 (CH_2), 29 (CH_2), 29 (CH_2), 26 (CH_2), 22 (CH_2), 14 (CH_3). ^{19}F-NMR (376.7 MHz, CD$_3$OD, ppm): δ -80.13 (triflate), -116.15 (3-fluoroaniline), MS (ESI Pos.) m/z: 263.35 [(M$^+$)] (expected m/z = 263.21), MS (ESI Neg.) m/z: 148.90 [(OTf$^-$)] (expected m/z = 148.95).

Figure S3.12. ^{1}H-NMR (CD$_3$OD) of **2a** and 3-fluoroaniline.
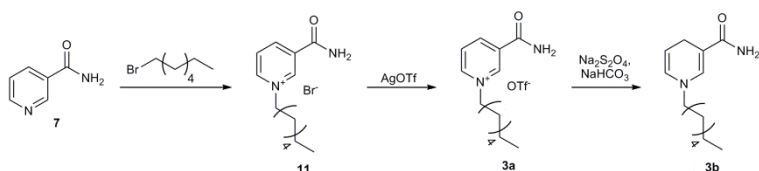

Figure S3.13. ^{13}C-NMR (DMSO) of **2a**.
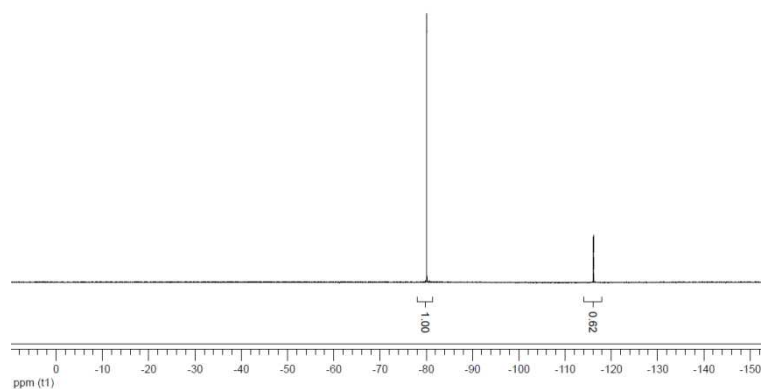
Figure S3.14. ^{19}F-NMR (CD$_3$OD) of **2a** and 3-fluoroaniline.

Synthesis procedure of 3b

Figure S3.15. Synthetic route for the formation of **3b**.

1-Heptyl-3-carbamoylpyridinium bromide 11. Nicotinamide **7** (4.88 g, 40.0 mmol) was suspended in acetonitrile (50 mL). Next, 1-bromoheptane (6.28 mL, 40.0 mmol) was added and the suspension was refluxed overnight. The next day the suspension was cooled down to room temperature and precipitated three times with diethyl ether. After filtration, **11** was obtained as a white powder (4.28 g, 71%). M.p. 204-206 °C (decomposition); ^{1}H-NMR (399.7 MHz, CD$_3$OD, ppm): δ 9.46 (s, 1H, ArH), 9.16 (d, J = 6.0 Hz, 1H, ArH), 8.98 (d, J = 8.0 Hz, 1H, ArH), 8.22 (t, J = 6.2, 1H, ArH), 4.71 (t, J = 7.8 Hz, 2H, CH2N), 2.07 (m, 2H, CH2), 1.42 (m, 4H, CH2), 1.34 (m, 4H, CH2) 0.91 (t, J = 7.0 Hz, 3H, CH3). ^{13}C-NMR (100.5 MHz, CD$_3$OD, ppm): δ 164 (C=O), 146 (C_{Ar}), 145 (C_{Ar}), 144 (C_{Ar}), 134 (C_{Ar}), 128 (C_{Ar}), 62 (CH_2), 31 (CH_2), 31 (CH_2), 28 (CH_2), 26 (CH_2), 22 (CH_2), 13 (CH_3). MS (ESI Pos.) m/z: 221.35 [(M$^+$)] (expected m/z = 221.16).
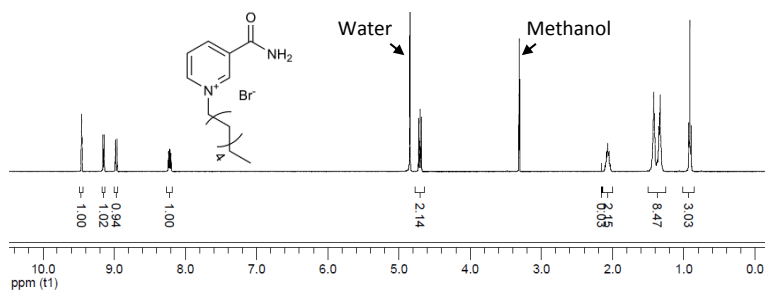
Figure S3.16. ^{1}H-NMR (CD$_3$OD) of **11**.
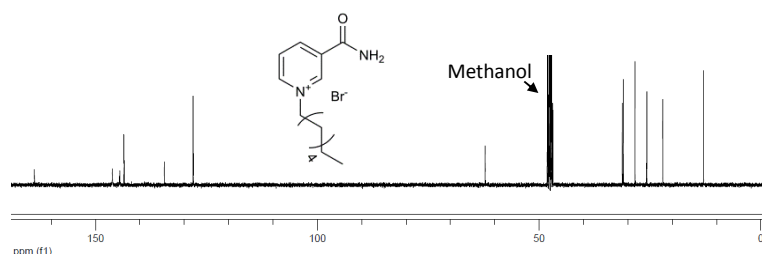
Figure S3.17. ^{13}C-NMR (CD$_3$OD) of **11**.

1-Heptyl-3-carbamoylpyridinium triflate 3a. 1-Heptyl-3-carbamoylpyridinium bromide **11** (10.8 g, 36.0 mmol) was dissolved in water (200 mL) and silver triflate (AgOTf, 9.25 g, 36.0 mmol) was dissolved in water (50 mL). The silver triflate solution was added dropwise to the 1-decyl-3-carbamoylpyridinium bromide solution under vigorous stirring. After direct formation of a yellow suspension, the mixture was allowed to react further at room temperature for 1 h. Then the solid was filtrated using a paper filter and the methanol from the filtrate was evaporated. The solid was dried in the vacuum oven and afforded the solid white product **3a** (4.07 g, 31%). M.p. 131-133 °C; ^{1}H-NMR (399.7 MHz, CD$_3$OD, ppm): δ 9.37 (s, 1H, Ar*H*), 9.05 (d, J = 6.0 Hz, 1H, Ar*H*), 8.90 (d, J = 8.0 Hz, 1H, Ar*H*), 8.15 (t, J = 7.0, 1H, Ar*H*), 4.64 (t, J = 7.8 Hz, 2H, C*H*2N), 2.01 (m, 2H, C*H*2), 1.38 (m, 4H, C*H*2), 1.30 (m, 4H, C*H*2) 0.89 (t, J = 7.0 Hz, 3H, C*H*3). ^{13}C-NMR (100.5 MHz, DMSO, ppm): δ 164 (*C*=O), 146 (*C*$_{Ar}$), 145 (*C*$_{Ar}$), 144 (*C*$_{Ar}$), 135 (*C*$_{Ar}$), 128 (*C*$_{Ar}$), 62 (*C*H$_2$), 31 (*C*H$_2$), 31 (*C*H$_2$), 28 (*C*H$_2$), 26 (*C*H$_2$), 22 (*C*H$_2$), 13 (*C*H$_3$). ^{19}F-NMR (376.7 MHz, CD$_3$OD, ppm): δ -80 (triflate), -116 (3-fluoroaniline), MS (ESI Pos.) m/z: 221.35 [(M$^+$)] (expected m/z = 221.16), MS (ESI Neg.) m/z: 148.95 [(OTf$^-$)] (expected m/z = 148.95).

67

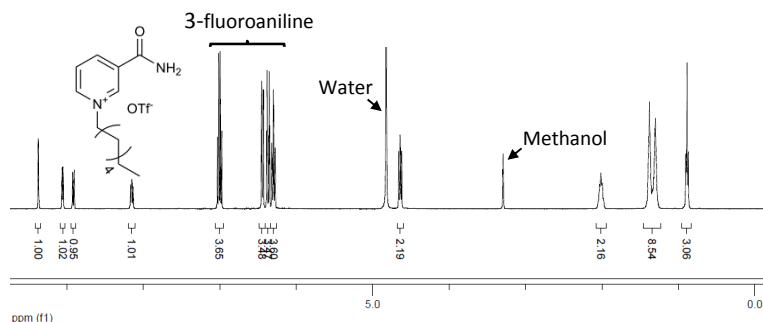**Figure S3.18.** ^{1}H-NMR (CD$_3$OD) of **3a** and 3-fluoroaniline.
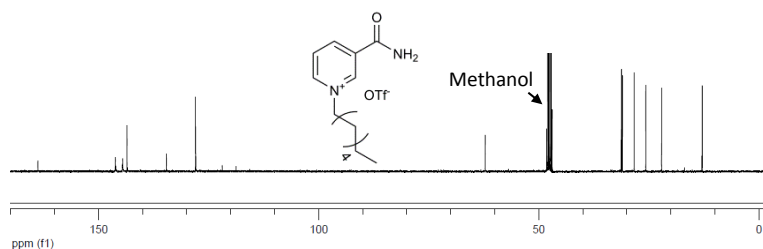
Figure S3.19. ^{13}C-NMR (CD$_3$OD) of **3a**.

Figure S3.20. ^{19}F-NMR (CD$_3$OD) of **3a** and 3-fluoroaniline.

1-Heptyl-1,4-dihydronicotinamide 3b. Under nitrogen atmosphere, 1-heptyl-3-carbamoylpyridinium triflate **3a** (2.90 g, 7.83 mmol) was dissolved in water (157 mL) and DCM (78 mL) at 0°C. Sodium bicarbonate (3.95, 47.0 mmol) was added to the mixture. Next, sodium dithionite (5.45 g, 31.3 mmol) was slowly added over a period of

10 minutes. The mixture was stirred at room temperature for 2 h in the dark. The organic phase was separated, washed with cold water (3x 10 mL), dried over $MgSO_4$ and the solvent was evaporated under reduced pressure. The yellow solid was recrystallized from MeOH-H_2O to obtain a bright yellow solid **3b** (0.74 g, 43%). M.p. 41-44 °C; ^{1}H-NMR (399.7 MHz, CD$_3$OD, ppm): δ 6.97 (s, 1H, C*H*), 5.80 (d, J = 8.4 Hz, 1H, C*H*), 4.75 (m, 1H, C*H*), 3.12 (t, J = 7.0, 2H, C*H*2N), 3.05 (m, 2H, C*H*2), 1.53 (m, 2H, C*H*2N), 1.31 (m, 10H, C*H*2), 0.89 (t, 3H, C*H*3). ^{13}C-NMR (100.5 MHz, CD$_3$OD, ppm): δ 172 (*C*=O), 140 (*C*H), 129 (*C*H), 103 (*C*), 97 (*C*H), 53 (*C*H$_2$), 31 (*C*H$_2$), 30 (*C*H$_2$), 29 (*C*H$_2$), 26 (*C*H$_2$), 22 (*C*H$_2$), 22 (*C*H$_2$), 13 (*C*H$_3$). MS (ESI Pos.) m/z: 221.25 [(M$^+$)] (expected m/z = 222.17).
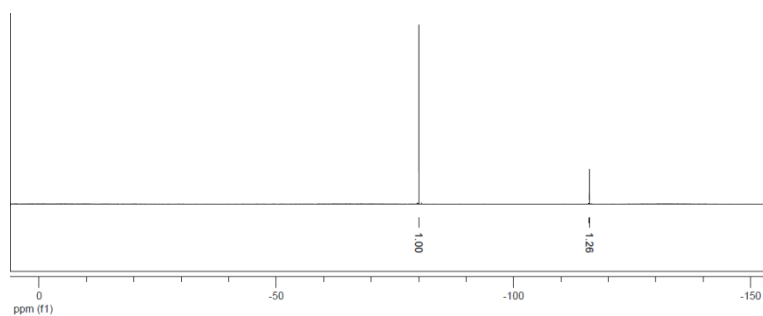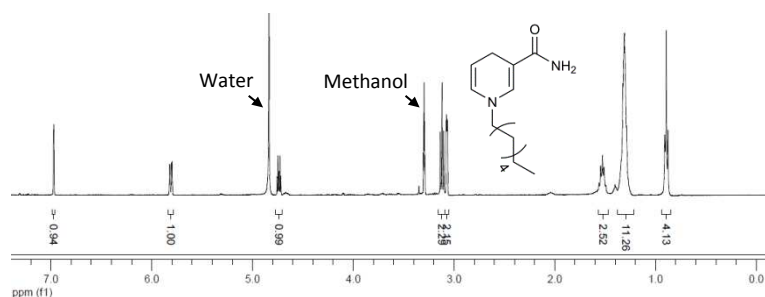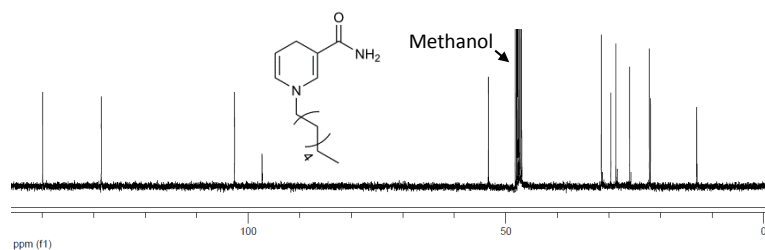

Figure S3.21. ^{1}H-NMR (CD$_3$OD) of **3b**.

Figure S3.22. ^{13}C-NMR (CD$_3$OD) of **3b**.

Synthesis procedure of [Cp*Rh(bpy-OMe)Cl]Cl

The Rh-catalyst was synthesized according to literature procedures. 4-nitro-2,2'-bipyridine-1-oxide was formed from 2,2'-bipyridine.[1] Next, 4-nitro-2,2'-bipyridine-1-oxide is converted to 4-methoxy-2,2'-bipyridine-1-oxide and finally to 4-methoxy-2,2'-bipyridine.[2] Lastly, the [Cp*Rh(bpy-OMe)Cl]Cl (Rh-catalyst) is formed.[3]

3.5.3.   Experimental reaction kinetics: 1a/1b CRN

The **1a/1b** CRN experiments were performed at room temperature (19-20°C) with the solution stirring (750 rpm) in an open vial (volume = 4 mL, Ø = 15 mm) to ensure a sufficiently high oxygen concentration. The reactions were carried out in MOPS buffer (100 mM, pH 7.5). All reagents were added to start the redox cycle and sodium formate was added lastly. Samples were taken after constant time intervals to measure the UV-vis absorbance spectrum in a 1.0 mm cuvette; the solution was put back in the vial after the measurement. The used extinction coefficients for the reagents are:

1a (265 nm):	$4.56 \cdot 10^3$ M^{-1} cm^{-1}
1b (350 nm):	$5.69 \cdot 10^3$ M^{-1} cm^{-1}
Rh-catalyst (300 nm):	$1.22 \cdot 10^4$ M^{-1} cm^{-1}
Rh-catalyst (350 nm):	$2.30 \cdot 10^3$ M^{-1} cm^{-1}
Methylene blue (350 nm):	$1.41 \cdot 10^3$ M^{-1} cm^{-1}
Methylene blue (665 nm):	$5.76 \cdot 10^4$ M^{-1} cm^{-1}

To measure the concentration of **1b** over time the absorbance at 350 nm was subtracted with the absorbance from the Rh-catalyst and methylene blue (MB) and is then converted to the concentration of **1b** using its extinction coefficient.

3.5.4.   Experimental reaction kinetics: 2a/2b particle crystallization

The redox cycles of **2a/2b** were performed at room temperature (19 - 20°C) with the solution stirring (750 rpm) in an open vial (volume = 4 mL, Ø = 15 mm) to ensure a sufficiently high oxygen concentration. The reactions were carried out in MOPS buffer (100 mM, pH 7.5). All reagents were added to start the redox cycle and sodium formate was added lastly. Photos of the vials were taken every 2 minutes.

The observed crystals were quantified by editing the images using Fiji. The color balance of the images was adjusted to Magenta -70 for Figure 3.4 and Magenta -110 for Figure 3.5. Next, the images were converted to 8-bit images following by the use of the 'Local threshold function'. The 'Bernsen method' with radius 5 was chosen to obtain black-white images with black agglomerates (pixel = 255) in a white solution (pixel = 0). To determine the relative amount of agglomeration over time the mean pixel intensity were measured in a representative area over time. The suspension at the start did not give clear visible particles, thus this period could not be analyzed with the 'Local threshold function'.

3.5.5. Kinetic model of the reduction of 1a

Reaction equations:
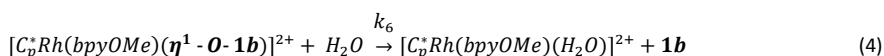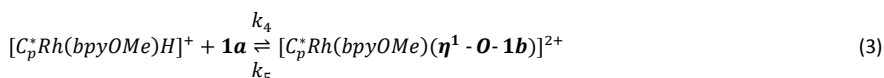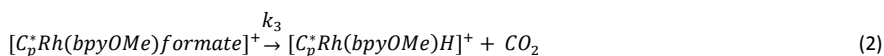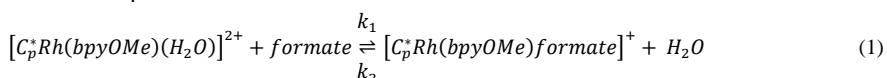
$$\left[C_p^*Rh(bpyOMe)(H_2O)\right]^{2+} + formate \underset{k_2}{\overset{k_1}{\rightleftharpoons}} \left[C_p^*Rh(bpyOMe)formate\right]^+ + H_2O \tag{1}$$

$$[C_p^*Rh(bpyOMe)formate]^+ \overset{k_3}{\rightarrow} [C_p^*Rh(bpyOMe)H]^+ + CO_2 \tag{2}$$

$$[C_p^*Rh(bpyOMe)H]^+ + \mathbf{1a} \underset{k_5}{\overset{k_4}{\rightleftharpoons}} [C_p^*Rh(bpyOMe)(\boldsymbol{\eta^1}\text{-}\boldsymbol{O}\text{-}\mathbf{1b})]^{2+} \tag{3}$$

$$[C_p^*Rh(bpyOMe)(\boldsymbol{\eta^1}\text{-}\boldsymbol{O}\text{-}\mathbf{1b})]^{2+} + H_2O \overset{k_6}{\rightarrow} [C_p^*Rh(bpyOMe)(H_2O)]^{2+} + \mathbf{1b} \tag{4}$$

Differential equations:

$$\frac{dformate}{dt} = -k_1\left[\left[C_p^*Rh(bpyOMe)(H_2O)\right]^{2+}\right][formate] +$$
$$k_2[[C_p^*Rh(bpyOMe)formate]^+][H_2O] \tag{5}$$

$$\frac{d[C_p^*Rh(bpyOMe)(H_2O)]^{2+}}{dt} =$$
$$-k_1\left[\left[C_p^*Rh(bpyOMe)(H_2O)\right]^{2+}\right][Formate] +$$
$$k_2[[C_p^*Rh(bpyOMe)formate]^+][H_2O] +$$
$$k_6[[C_p^*Rh(bpyOMe)(\boldsymbol{\eta^1}\text{-}\boldsymbol{O}\text{-}\mathbf{1b})]^{2+}][H_2O] \tag{6}$$

$$\frac{d[C_p^*Rh(bpyOMe)formate]^+}{dt} =$$
$$k_1\left[[C_p^*Rh(bpyOMe)(H_2O)]^{2+}\right][Formate] -$$
$$k_2\left[[C_p^*Rh(bpyOMe)formate]^+\right][H_2O] -$$
$$k_3\left[[C_p^*Rh(bpyOMe)formate]^+\right] \tag{7}$$

$$\frac{d[C_p^*Rh(bpyOMe)H]^+}{dt} =$$
$$k_3\left[[C_p^*Rh(bpyOMe)formate]^+\right] - k_4\left[[C_p^*Rh(bpyOMe)H]^+\right][\mathbf{1a}] +$$
$$k_5\left[[C_p^*Rh(bpyOMe)(\boldsymbol{\eta^1 \text{-} O\text{-} 1b})]^{2+}\right] \tag{8}$$

$$\frac{d[C_p^*Rh(bpyOMe)(\boldsymbol{\eta^1 \text{-} O\text{-} 1b})]^{2+}}{dt} =$$
$$k_4\left[[C_p^*Rh(bpyOMe)H]^+\right][\mathbf{1a}] -$$
$$k_5\left[[C_p^*Rh(bpyOMe)(\boldsymbol{\eta^1 \text{-} O\text{-} 1b})]^{2+}\right] - \tag{9}$$
$$k_6\left[[C_p^*Rh(bpyOMe)(\boldsymbol{\eta^1 \text{-} O\text{-} 1b})]^{2+}\right][H_2O]$$

$$\frac{d\mathbf{1a}}{dt} = -k_4\left[[C_p^*Rh(bpyOMe)H]^+\right][\mathbf{1a}] + k_5\left[[C_p^*Rh(bpyOMe)(\boldsymbol{\eta^1 \text{-} O\text{-} 1b})]^{2+}\right] \tag{10}$$

$$\frac{d\mathbf{1b}}{dt} = k_6\left[[C_p^*Rh(bpyOMe)(\boldsymbol{\eta^1 \text{-} O\text{-} 1b})]^{2+}\right][H_2O] \tag{11}$$

The reduction of **1a** with sodium formate and a Rh-catalyst is extensively described by Lo and coworkers.[4] During the reduction **1b** is coordinated to the Rh-catalyst via the carbonyl group, which is here specified as $(\boldsymbol{\eta^1 \text{-} O\text{-} 1b})$.[4] The reduction consists of six different steps. A Michaelis-Menten kinetics was used to determine the K_M and k_3 value using the method of Lo and coworkers.[4] k_3 and K_M is determined by plotting [Rh-catalyst]/initial rate against 1/[sodium formate] (Supplementary Figure S3.23). The intersect with the y-axis gives k_3 ($4.60 \cdot 10^{-3}$ s^{-1}), and K_M is determined by multiplying the slope with k_3 ($6.83 \cdot 10^{-2}$ M). Both the experimentally found k_3 and K_M value are in the range of the previous reported values.[3-5] As no lag-phase is observed in the experimental data (Supplementary Figure S3.24) k_1 is very high and the real value is not important for the model as k_3 is the limiting step, thus k_1 was set at 20 M^{-1} s^{-1}.[4] Furthermore, k_2 is determined by using the Michaelis-Menten equation: $k_2 = K_M k_1 - k_3$. k_4 is not known and is therefore fitted (30 M^{-1} s^{-1}). Lo and coworkers mentioned that k_5 is much smaller than k_6 and k_6 is much larger than k_3.[4] However these values

were not known as well, therefore k_5 was set very small (10^{-3} s^{-1}) and k_6 very big (20 M^{-1} s^{-1}). Supplementary Figure S3.24 shows the experimental data versus the kinetic modeling data with varying Rh-catalyst and sodium formate concentration. When varying the Rh-catalyst concentration the model fits very well to the experimental data. When varying the sodium formate concentration the initial rate fits very well, however the end value is incorrect. This is most likely caused by an equilibrium in the last step of the reaction mechanism (Equation 4, Supplementary Figure S3.31).
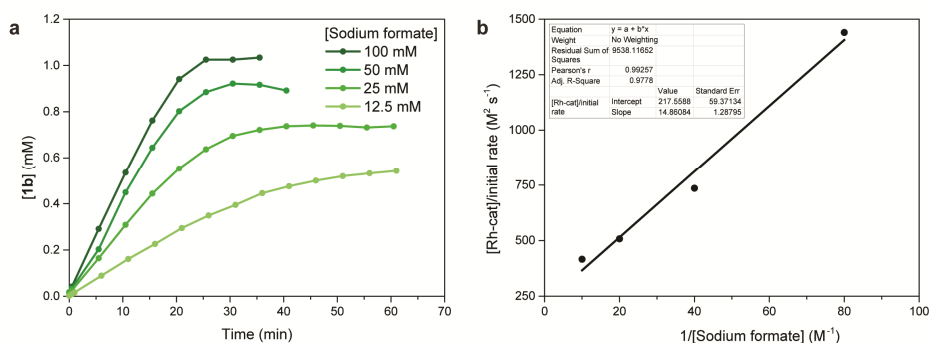
Figure S3.23. Influence of the sodium formate concentration on the reduction rate of **1b.** General conditions: T = 20°C, stirring rate = 750 rpm, sample volume = 1 mL in a 4 mL vial, [**1a**] = 1.0 mM, [Rh-catalyst] = 0.3 mM and varying [sodium formate]: 100 mM, 50 mM, 25 mM and 12.5 mM. **(a)** Reduction of **1a** to **1b** using different sodium formate concentrations. **(b)** Graph to determine k_3 and K_M by setting out [Rh-catalyst]/initial rate against 1/[sodium formate].
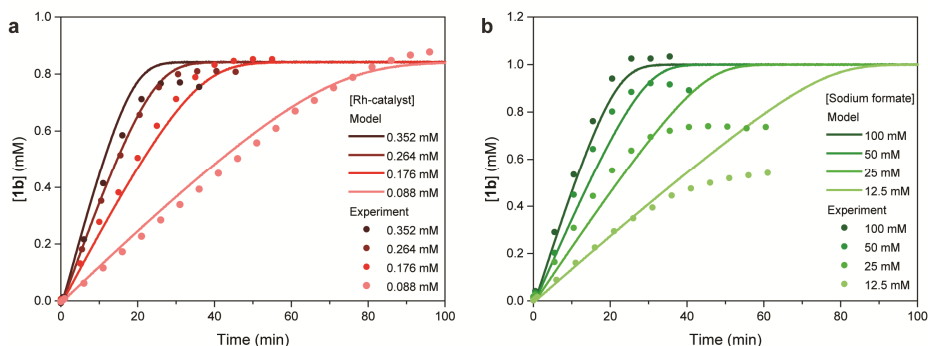
Figure S3.24. Comparison between the experimental data and the kinetic model of the reduction. The dots are the experimental data points and the lines calculated from the kinetic model. General experimental conditions: T = 20°C, stirring rate = 750 rpm, sample volume = 1 mL in a 4 mL vial. **(a)** The reduction of **1a** to **1b** using [**1a**] = 0.842 mM, [sodium formate] = 100 mM and varying [Rh-catalyst]: 0.352 mM, 0.264 mM, 0.176 mM and 0.088 mM. The *k*-values mentioned above are used to model the concentration of **1b** over time. **(b)** Reduction of **1a** to **1b** using [**1a**] = 1.0 mM, [Rh-catalyst] = 0.346 mM and varying [sodium formate]: 100 mM, 50 mM, 25 mM and 12.5 mM. The *k*-values mentioned above are used to model the concentration of **1b** over time.

3.5.6.   Kinetic model of the oxidation of 3b

Reaction equations:

$$\textbf{3b} + MB \overset{k_8}{\rightarrow} \textbf{3a} + MBH \tag{12}$$

$$MBH + O_2 + H^+ \overset{k_9}{\rightarrow} MB + H_2O_2 \tag{13}$$

Differential equations:

$$\frac{d\textbf{3b}}{dt} = -k_8[\textbf{3b}][MB] \tag{14}$$

$$\frac{d\textbf{3a}}{dt} = k_8[\textbf{3b}][MB] \tag{15}$$

$$\frac{dMB}{dt} = -k_8[\textbf{3b}][MB] + k_9'[MBH] \tag{16}$$

$$\frac{dMBH}{dt} = k_8[\mathbf{3b}][MB] - k_9'[MBH] \tag{17}$$

As we could not purify **1b** we used NADH-C_7H_{15} **3b** to analyze the kinetics of the oxidation of **1b**. The oxidation of **3b** consists of two steps: the reduction of MB and its subsequently oxidation. In the kinetic model the chemical equilibrium between **3b** and MB is simplified to an irreversible chemical reaction. The subsequent oxidation of MBH is dependent on the oxygen concentration, but this is assumed to be constant as the diffusion rate of oxygen into the sample is assumed to be constant. Moreover, the proton concentration is also assumed to be constant as an excess is present in the solution. k_8 and k_9' values are calculated by following the **3b** oxidation when varying the **3b** and MB concentration (Supplementary Figure S3.25). Both k-values are fitted to the experimental data and are 350 M^{-1} s^{-1} (k_8) and 0.023 s^{-1} (k_9'). When bigger sample volume was used the k_8 remained the same and k_9' decreased which is consistent with a lower oxygen diffusion rate into the sample.
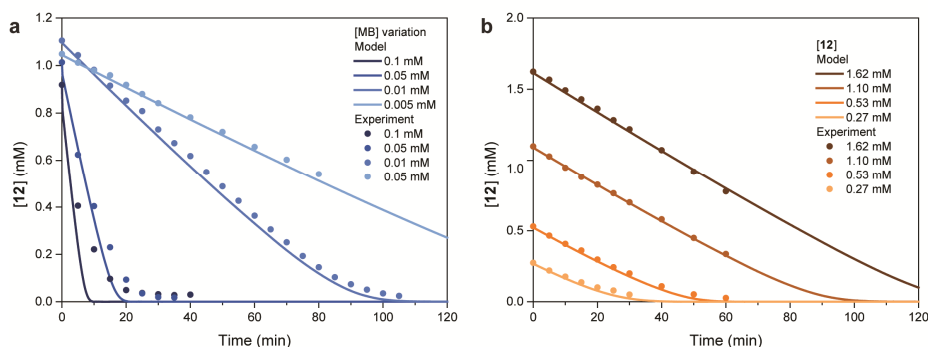
Figure S3.25. Oxidation of **3b** using different MB concentrations. General conditions: T = 20°C, stirring rate = 750 rpm, sample volume = 1 mL in a 4 mL vial. **(a)** [**3b**] = 1.0 mM and varying [MB]: 0.005 mM, 0.01 mM, 0.05 mM and 0.1 mM. **(b)** [MB] = 0.01 mM and varying [**3b**]: 1.62 mM, 1.10 mM and 0.53 mM, 0.27 mM.

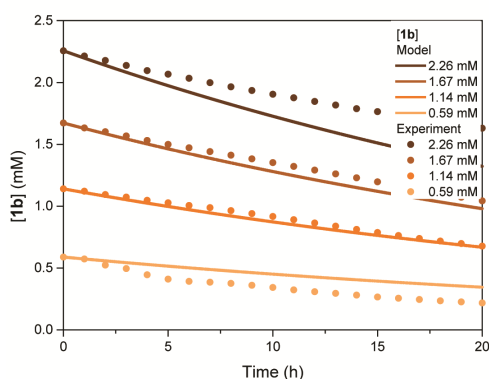### 3.5.7. Kinetic model of the degradation of 1b

Reaction equations:

$$\mathbf{1b} + H_2O \xrightarrow[H^+]{k_7} NADHX \tag{18}$$

Differential equations:

$$\frac{d\mathbf{1b}}{dt} = -k_7'[\mathbf{1b}] \tag{19}$$

$$\frac{dNADHX}{dt} = k_7'[\mathbf{1b}] \tag{20}$$

After the formation of **1b** we determined how fast its degradation is. **1b** is unstable over time and slowly degrades by reacting with protons and water in the solution. As an excess of protons and water is present the degradation rate is only dependent on the **1b** concentration itself. The value of k_7' was experimentally determined and fitted to $7.42 \cdot 10^{-6}$ s^{-1} (Supplementary Figure S3.26).

Figure S3.26. The degradation rate of **1b** with different concentrations. General conditions: T = 20°C, stirring rate = 0 rpm, [Rh-catalyst] = 0.3 mM, [sodium formate] = 100 mM, with varying [**1a**]: 2.26 mM, 1.67 mM, 1.14 mM and 0.59 mM.

3.5.8. Kinetic model of the deactivation of RhH

Reaction equations:

$$[C_p^*Rh(bpyOMe)H]^+ + O_2 \xrightarrow{k_{10}} [C_p^*Rh(bpyOMe)OOH]^+ \tag{21}$$
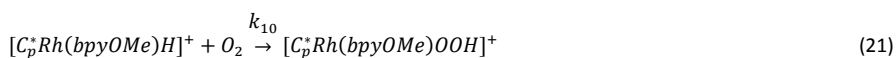
Differential equations:

$$\frac{d[C_p^*Rh(bpyOMe)H]^+}{dt} = -k_{10}'\big[[C_p^*Rh(bpyOMe)H]^+\big] \qquad (22)$$

$$\frac{d[C_p^*Rh(bpyOMe)OOH]^+}{dt} = k_{10}'\big[[C_p^*Rh(bpyOMe)H]^+\big] \qquad (23)$$
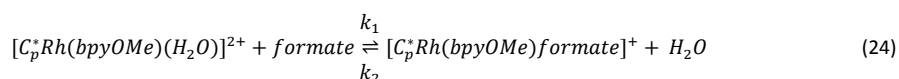
As we could not determine the RhH-catalyst deactivation with oxygen directly, we used an indirect method. In this method the Rh-catalyst was incubated with sodium formate to first form RhH and slowly forms the degraded product RhOOH. After a specific time **1a** was added to determine how much Rh-catalyst was still active for the reduction to **1b**. From this the rate of RhH-catalyst deactivation (k_{10}') was determined ($2.38\cdot10^{-4}$ s^{-1}).
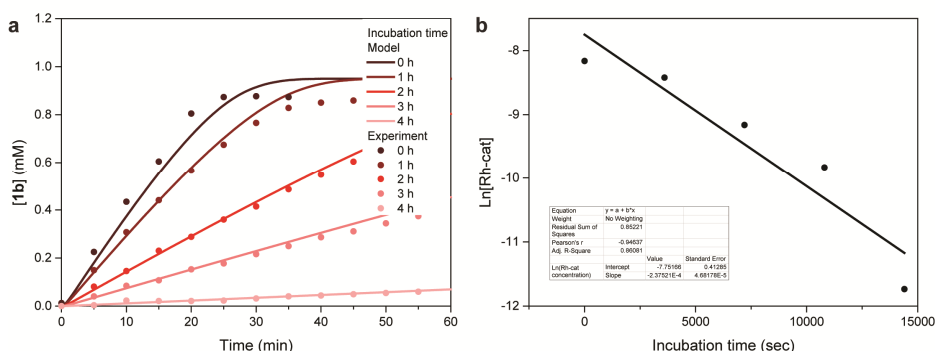
Figure S3.27. Determination of the RhH deactivation rate. General conditions: T = 20°C, stirring rate = 750 rpm, sample volume = 1 mL in a 4 mL vial. **(a)** Four vials with [Rh-catalyst] = 0.285 mM and [sodium formate] = 95 mM were stirred for 0 h, 1 h, 2 h, 3 h and 4 h. After this period [**1a**] = 0.95 mM was added and the reduction was followed over time. The amount of active Rh-catalyst still present was calculated with the kinetic model. **(b)** From this the reaction rate constant (k_{10}') was determined for the deactivation of the RhH catalyst.

3.5.9. Kinetic model of the 1a/1b CRN

Reaction equations:

$$[C_p^*Rh(bpyOMe)(H_2O)]^{2+} + formate \underset{k_2}{\overset{k_1}{\rightleftharpoons}} [C_p^*Rh(bpyOMe)formate]^+ + H_2O \qquad (24)$$

$$[C_p^*Rh(bpyOMe)formate]^+ \xrightarrow{k_3} [C_p^*Rh(bpyOMe)H]^+ + CO_2 \qquad (25)$$

$$[C_p^*Rh(bpyOMe)H]^+ + \mathbf{1a} \underset{k_5}{\overset{k_4}{\rightleftharpoons}} [C_p^*Rh(bpyOMe)(\boldsymbol{\eta^1} \text{-} \boldsymbol{O} \text{-} \mathbf{1b})]^{2+} \qquad (26)$$

$$[C_p^*Rh(bpyOMe)(\boldsymbol{\eta^1} \text{-} \boldsymbol{O} \text{-} \mathbf{1b})]^{2+} + H_2O \xrightarrow{k_6} [C_p^*Rh(bpyOMe)(H_2O)]^{2+} + \mathbf{1b} \qquad (27)$$

$$\mathbf{1b} + H_2O \overset{k_7}{\underset{H^+}{\rightarrow}} NADHX \qquad (28)$$

$$\mathbf{1b} + MB \xrightarrow{k_8} \mathbf{1a} + MBH \qquad (29)$$

$$MBH + O_2 + H^+ \xrightarrow{k_9} MB + H_2O_2 \qquad (30)$$

$$[C_p^*Rh(bpyOMe)H]^+ + O_2 \xrightarrow{k_{10}} [C_p^*Rh(bpyOMe)OOH]^+ \qquad (31)$$

Differential equations:

$$\frac{dformate}{dt} = -k_1\left[\left[C_p^*Rh(bpyOMe)(H_2O)\right]^{2+}\right][formate] +$$
$$k_2[[C_p^*Rh(bpyOMe)formate]^+][H_2O] \qquad (32)$$

$$\frac{d[C_p^*Rh(bpyOMe)(H_2O)]^{2+}}{dt} =$$
$$-k_1\left[\left[C_p^*Rh(bpyOMe)(H_2O)\right]^{2+}\right][Formate] +$$
$$k_2[[C_p^*Rh(bpyOMe)formate]^+][H_2O] +$$
$$k_6[[C_p^*Rh(bpyOMe)(\boldsymbol{\eta^1} \text{-} \boldsymbol{O} \text{-} \mathbf{1b})]^{2+}][H_2O] \qquad (33)$$

$$\frac{d[C_p^*Rh(bpyOMe)formate]^+}{dt} =$$
$$k_1\left[\left[C_p^*Rh(bpyOMe)(H_2O)\right]^{2+}\right][Formate] -$$
$$k_2\left[\left[C_p^*Rh(bpyOMe)formate\right]^+\right][H_2O] -$$
$$k_3\left[\left[C_p^*Rh(bpyOMe)formate\right]^+\right] \qquad (34)$$

$$\frac{d\left[C_p^*Rh(bpyOMe)H\right]^+}{dt} =$$
$$k_3\left[\left[C_p^*Rh(bpyOMe)formate\right]^+\right] - k_4\left[\left[C_p^*Rh(bpyOMe)H\right]^+\right][\mathbf{1a}] +$$
$$k_5\left[\left[C_p^*Rh(bpyOMe)(\boldsymbol{\eta^1\text{-}O\text{-}1b})\right]^{2+}\right] - k'_{10}\left[\left[C_p^*Rh(bpyOMe)H\right]^+\right] \qquad (35)$$

$$\frac{d\left[C_p^*Rh(bpyOMe)(\boldsymbol{\eta^1\text{-}O\text{-}1b})\right]^{2+}}{dt} =$$
$$k_4\left[\left[C_p^*Rh(bpyOMe)H\right]^+\right][\mathbf{1a}] -$$
$$k_5\left[\left[C_p^*Rh(bpyOMe)(\boldsymbol{\eta^1\text{-}O\text{-}1b})\right]^{2+}\right] - \qquad (36)$$
$$k_6\left[\left[C_p^*Rh(bpyOMe)(\boldsymbol{\eta^1\text{-}O\text{-}1b})\right]^{2+}\right][H_2O]$$

$$\frac{d\mathbf{1a}}{dt} = -k_4\left[\left[C_p^*Rh(bpyOMe)H\right]^+\right][\mathbf{1a}] + k_5\left[\left[C_p^*Rh(bpyOMe)(\boldsymbol{\eta^1\text{-}O\text{-}1b})\right]^{2+}\right] +$$
$$k_8[\mathbf{1b}][MB] \qquad (37)$$

$$\frac{d\mathbf{1b}}{dt} = k_6\left[\left[C_p^*Rh(bpyOMe)(\boldsymbol{\eta^1\text{-}O\text{-}1b})\right]^{2+}\right][H_2O] - k_8[\mathbf{1b}][MB] - k'_7[\mathbf{1b}] \qquad (38)$$

$$\frac{dMB^+}{dt} = -k_8[\mathbf{1b}][MB] + k'_9[MBH] \qquad (39)$$

$$\frac{dMBH}{dt} = k_8[\mathbf{1b}][MB] - k'_9[MBH] \qquad (40)$$

$$\frac{dNADHX}{dt} = k'_7[\mathbf{1b}] \qquad (41)$$

$$\frac{d\left[C_p^*Rh(bpyOMe)OOH\right]^+}{dt} = k'_{10}\left[\left[C_p^*Rh(bpyOMe)H\right]^+\right] \qquad (42)$$

Next, all separate kinetic models of the reduction, oxidation, **1b** degradation and RhH-catalyst deactivation were taken together and these kinetic models combined should give the kinetic model of the **1a/1b** CRN.

Methylene blue variation

When varying the MB concentration and comparing the experimental with the kinetic model data a few things stand out (Supplementary Figure S3.28). First, the general trend looks very good. With increasing MB concentration the accumulation of **1b** is slowed down, while the depletion rate of **1b** is increased. These results are in agreement with the UV-vis data (Figure 3.2). Even the steady state behavior at high MB concentrations is modeled accurately. However, quantitatively the kinetic model is incorrect unfortunately. Mostly, the end of the redox cycle is too slow, the tail is too long. This is because in the kinetic model the RhH is not accumulated and is therefore not deactivated in the model, while this is the case in the experiments.
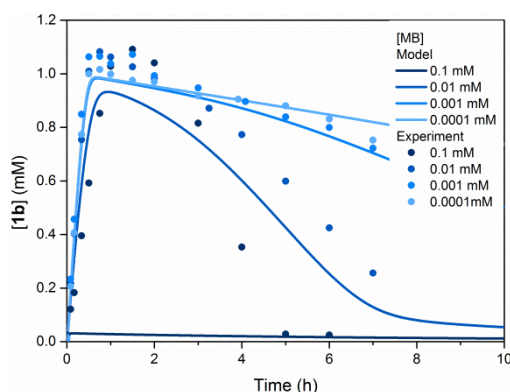
Figure S3.28. Influence of methylene blue (MB) concentration on the **1a/1b** chemical reaction network; kinetic model vs. experimental data. General conditions: T = 20°C, stirring rate = 750 rpm, sample volume = 1 mL in a 4 mL vial, [**1a**] = 1.0 mM, [Rh-catalyst] = 0.3 mM, [sodium formate] = 100 mM and varying [MB]: 0.0001 mM (black), 0.001 mM (red), 0.01 mM (green) and 0.1 mM (blue). The above mentioned k-values were used for kinetic model.

Rh-catalyst variation

When we compared the experimental data with the kinetic modeling data when we varied the Rh-catalyst concentration, some similarities and differences were observed. For example, the accumulation rate of **1a** to **1b** decreased indeed with decreasing Rh-catalyst concentration. Moreover, the accumulation rate of **1b** to **1a** did not change for 0.2 and 0.3 mM which was also the case for the experimental data. However, there are also some differences. For example, all similar trends are just qualitatively instead of quantitatively. Moreover, the maximum concentration of **1b** decreases in the kinetic model with decreasing Rh-catalyst concentration, which is not the case for the
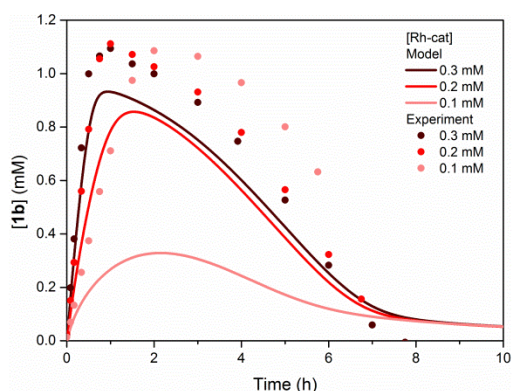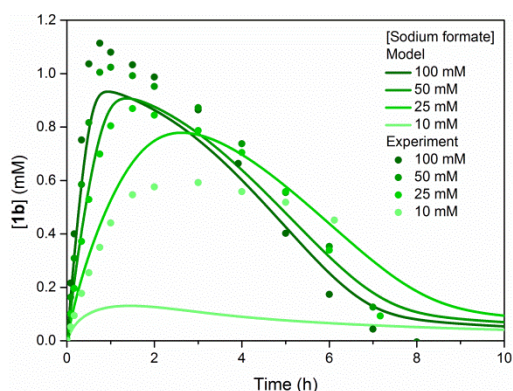
Figure S3.29. Influence of the Rh-catalyst concentration on the **1a/1b** chemical reaction network; kinetic model vs. experimental data. General conditions: T = 20°C, stirring rate = 750 rpm, sample volume = 1 mL in a 4 mL vial, [**1a**] = 1.0 mM, [sodium formate] = 100 mM, [MB] = 0.01 mM and varying [Rh-catalyst]: 0.3 mM (red), 0.2 mM (green) and 0.1 mM (blue). The above mentioned *k*-values were used for the kinetic model.

experimental data. Lastly, we again observe this tail at the end of the redox cycle indicating that in the kinetic model the Rh-catalyst is not completely degraded yet.

Sodium formate variation

We also compared the kinetic model with the experimental data when we varied the sodium formate concentration. Again, we cannot quantitatively compare these results as the differences are too big, we can only show the similarities within the trends. The accumulation rate of **1a** to **1b** decreases with sodium formate concentration, both in the experimental data and in the kinetic modeling data. Furthermore, the maximum concentration of **1b** decreases as well. And lastly, the very interesting observation we saw in the experimental data was observed in the kinetic modeling data as well: with decreasing sodium formate concentration the lifetime of the redox cycle is increased.

Figure S3.30. Influence of the sodium formate concentration on the **1a/1b** chemical reaction network; kinetic model vs. experimental data. General conditions: T = 20°C, stirring rate = 750 rpm, sample volume = 1 mL in a 4 mL vial, [**1a**] = 1.0 mM, [Rh-catalyst] = 0.3 mM, [MB] = 0.01 mM and varying [sodium formate]: 100 mM (black), 50 mM (red), 25 mM (green) and 10 mM (blue). The above mentioned *k*-values were used for the kinetic model.

3.5.10. Chemical equilibrium between 3b and Rh-catalyst
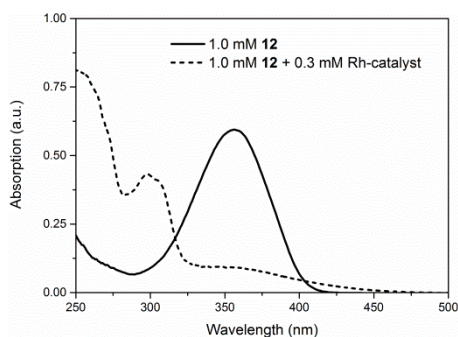
Figure S3.31. Decrease of [**3b**] upon addition of Rh-catalyst indicating a chemical equilibrium between **3b** and Rh-catalyst. In this experiment, Rh-catalyst is added to a solution of **3b**, mixed and the absorption spectrum is measured immediately. It seems that the hydrido Rh-complex gives the hydride to another species as more **3b** is depleted than Rh-catalyst present. Concentrations: [**3b**] = 1.0 mM (solid line). [**3b**] = 1.0 mM, [Rh-catalyst] = 0.3 mM (dashed line). All dissolved in 10 vol% methanol and 90 vol% MOPS buffer (100 mM, pH 7.5).

3.5.11. Detailed hypothesis of the steady state behavior

Upon high concentrations of MB in the CRN, a steady state is observed (Figure 3.2). Below a detailed explanation of this steady state behavior is given (Supplementary Figure S3.32).

Scenario 1)   [MB] is low
The reduction starts with the reduction of the Rh-catalyst to the hydrido Rh-complex, which can give the hydride to **1a** or MB. The hydrido Rh-complex will do both at specific rates. The hydride transfer to MB is thermodynamically more favorable than to **1a**.[6] As the oxidation of MBH in this cycle is the rate limiting step, the MB will convert to MBH and the hydrido Rh-complex gives the hydride to **1a** until all **1a** is reduced to **1b**. From that point on the hydrido Rh-complex accumulates as it can only slowly give the hydride to **1a** or MB depending on the slow oxidation rate of MBH. Meanwhile, the hydrido Rh-complex degrades to Rh-OOH by the reaction with molecular oxygen. Similarly, **1b** degrades slowly to the NADHX species. The redox cycle will continue until all hydrido Rh-complex is completely degraded to Rh-OOH. Therefore, the reduction rate decreases and ultimately stops. Meanwhile, the oxidation of **1b** to **1a** continues until all **1b** is converted.

Scenario 2)   [MB] is high
The reduction starts with the reduction of the Rh-catalyst to the hydrido Rh-complex, which can give the hydride to **1a** or MB. As the transfer to MB is thermodynamically favored and a high concentration of MB is present, most hydrides will attack MB, but some of the hydrides attack **1a** forming **1b**. MBH oxidizes slowly using the omnipresent oxygen. During the hydride transfer of **1b** to MB, the MB concentration decreases slowly while the MBH concentration increases. The reduction rate of MB to MBH is decreased as [MB] decreases, while the oxidation rate of MBH to MB is increased as MBH is being formed. At some MB/MBH ratio the two redox rates are equal resulting in a steady state of **1b**. Moreover, as the hydrido Rh-complex concentration is approximately constant, the steady state of MB/MBH holds until the sodium formate or oxygen concentration changes significantly.

This steady state is not present when the MB concentration is low because then the hydrido Rh-complex and **1b** concentrations are very high which increases the reduction rate of the MB. While in the case of very low concentrations of hydrido Rh-complex and **1b**, the hydrido Rh-complex can immediately give the hydride to MB. This immediate transfer to MB also implies that the hydrido Rh-complex is not degraded to
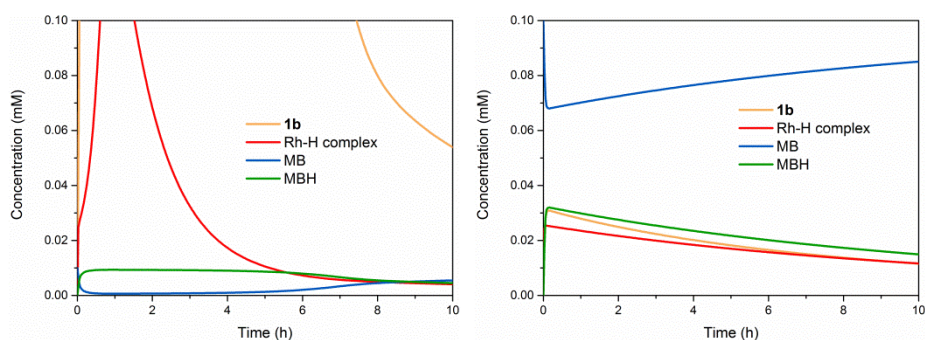
Figure S3.32. Kinetic model of the redox cycle using low and high MB concentrations. **Left)** When a low concentration of MB (0.01 mM) is used, all MB is reduced during the redox cycle and the hydrido Rh-complex is accumulated. **Right)** When a high concentration of MB (0.1 mM) is used, also a small part of the MB is reduced and the hydrido Rh-complex is only slightly present. Concentrations in the model are different than in the experiments (Figure 3.2) as the model shows some deviations. General concentrations: [**1a**] = 1.0 mM, [Rh-catalyst] = 0.3 mM, [sodium formate] = 100 mM.

Rh-OOH. Thus, the low concentration of hydrido Rh-complex leads to the continuous reduction of sodium formate until all fuel is consumed.

3.5.12. Influence of [O_2] on the 1a/1b CRN
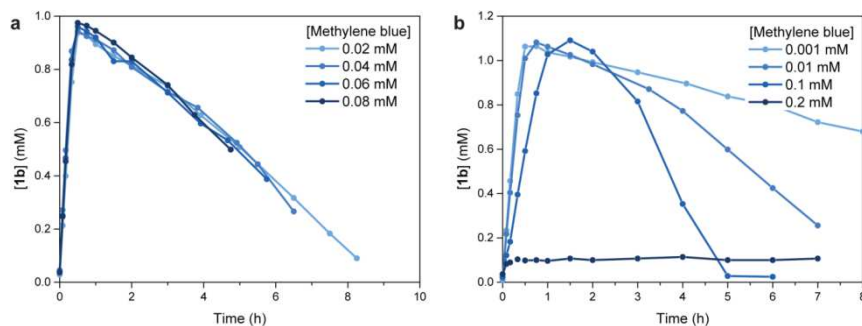
**Figure S3.33.** Difference in oxygen concentration on the **1a/1b** chemical reaction network. **(a)** Concentration of **1b** over time during the redox cycle using a 3 mL solution. **(b)** Concentration of **1b** over time during the redox cycle using a 1 mL solution. Concentrations: [**1a**] = 1.0 mM, [Rh-catalyst] = 0.3 mM, [sodium formate] = 100 mM, [MB] = see figure. T = 20°C, stirring speed = 750 rpm.

3.5.13. Influence of [sodium formate] on the rhodium catalyst deactivation rate
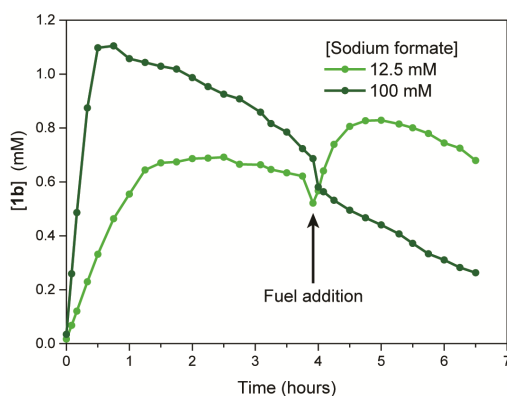
Figure S3.34. Difference in the dynamic regime when a high or low sodium formate concentration is used. At the start 12.5 mM and 100 mM sodium formate are added. After 4 h a new batch of sodium formate is added to the **1a/1b** chemical reaction network. Concentrations: [**1a**] = 1.0 mM, [Rh-catalyst] = 0.3 mM, [MB] = 0.01 mM, [sodium formate] = see figure. T = 20°C, stirring speed = 750 rpm.

3.5.14. Critical micelle concentration of 2a
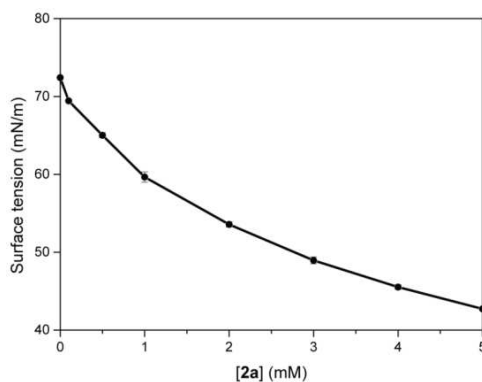
Figure S3.35. The surface tension of **2a** for different concentrations of **2a** in MOPS buffer (100 mM, pH 7.5) showing its critical micelle concentration is higher than 5 mM.

3.5.15. NMR spectrum of only the crystals
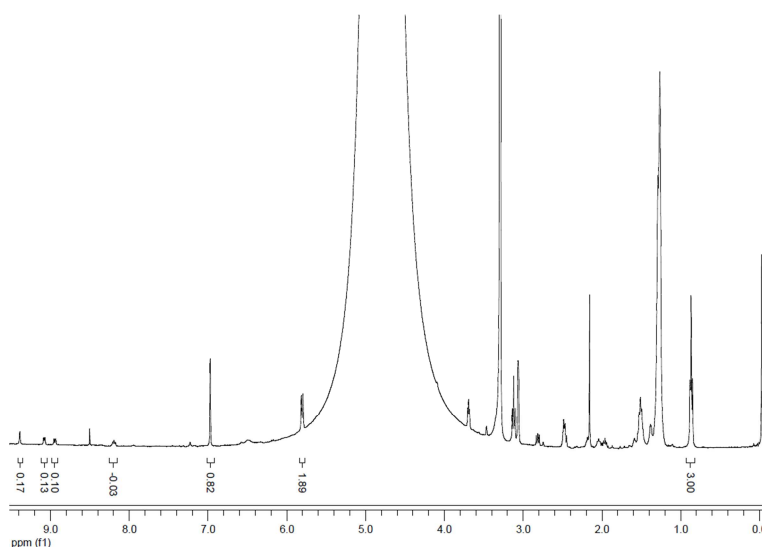
Figure S3.36. ^{1}H-NMR spectrum of the crystals consisting of mainly **2b**. The crystals consist of 83% **2b** and 17% **2a**. Redox cycle was performed and after 1.5 h the sample was filtrated and the residue was dissolved in deuterated methanol and measured by ^{1}H-NMR. General conditions: T = 20°C, stirring rate = 750 rpm, sample volume = 3 mL in a 4 mL vial, [2a] = 1.0 mM, [Rh-catalyst] = 0.3 mM, [MB] = 0.1 mM and [sodium formate] = 100 mM, all dissolved in MOPS buffer (100 mM, pH 7.5).

3.5.16. Supplementary references

1.   M. Zalas, B. Gierczyk, M. Cegłowski and G. Schroeder, *Chem. Pap.*, 2012, **66**, 733-740.
2.   D. Wenkert and R. B. Woodward, *J. Org. Chem.*, 1983, **48**, 283-289.
3.   F. Hollmann, B. Witholt and A. Schmid, *J. Mol. Catal. B Enzym.*, 2003, **19-20**, 167-176.
4.   H. C. Lo, C. Leiva, O. Buriez, J. B. Kerr, M. M. Olmstead and R. H. Fish, *Inorg. Chem.*, 2001, **40**, 6705-6716.
5.   J. H. van Esch, M. A. M. Hoffmann and R. J. M. Nolte, *J. Org. Chem.*, 1995, **60**, 1599-1610.
6.   J. Ye and R. P. Baldwin, *Anal. Chem.*, 1988, **60**, 2263-2268.
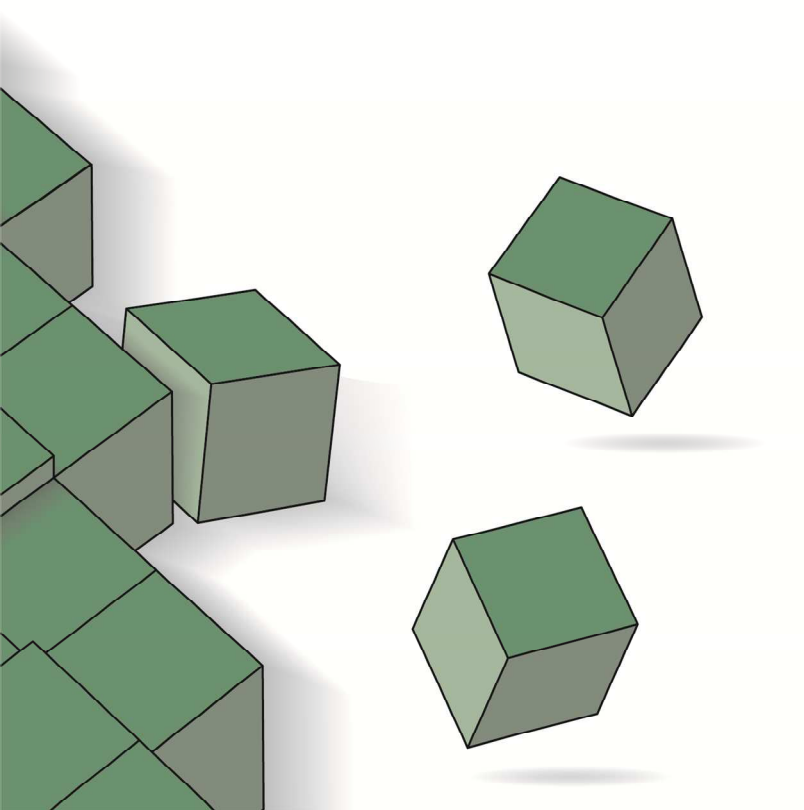
Chapter 4

Catalytic control over transient polymer agglomeration and its use for transient compartmentalization

Responsive polymers find applications in many fields, such as biomedical engineering and mechanical actuators. These polymers require a trigger each time we desire a change in mechanical properties. Using fuel-driven assembly overcomes this limitation as the polymer is activated by an energy source and is spontaneously reverted back to the original structure. We applied fuel-driven assembly to make a reversible agglomeration transition of a nicotinamide functionalized polymer. The hydrophilicity of the polymer is controlled over time by the kinetics of the chemical reaction network of nicotinamide. The kinetics of the chemical reaction network and thus the agglomeration is adjusted by the concentration of two catalysts and the fuel leading to a large variation in kinetic manipulation. Moreover, the hydrophobicity of these transient agglomerates is used to sequester and release somewhat hydrophobic nano-objects from the bulk solution. This fuel-driven agglomeration of polymer system provides us more kinetic control than responsive polymers. Moreover, including catalysis facilitates the design of more complex non-linear behavior within transient polymer assembly.

4.1. Introduction

Responsive polymer systems have a wide range of applications, ranging from drug delivery to actuators and micromachines.[1, 2] Most of these polymer systems require an external stimulus to trigger each step of a reversible response sequence, e.g. a change in temperature or pH.[3] It would be of great interest if a trigger can initiate a transient structural or functional change, meaning that the activated functional structure autonomously and spontaneously returns to the original state over time. Thereby, the function can be available only when needed. This concept can be realized by coupling molecular assembly to fuel-driven chemical reaction networks, enabling transient assembly of out-of-equilibrium structures. Using these chemical reaction networks has the added advantage that it is possible to control the lifetime and assembly/disassembly kinetics through the kinetics of the chemical reaction network. In these systems the assembling behavior is coupled to a so-called chemical reaction network (CRN). In such a CRN, soluble building blocks react with a chemical fuel to form activated building blocks which assemble into large supramolecular structures. Over time, spontaneous deactivation of the building blocks will then lead to dissolution of the formed structure.[4] We have previously shown that we can control the kinetics of assembly formation and dissolution by regulating the kinetics of the underlying CRN.[5]

A few examples of CRN-coupled dynamic polymers exist.[6, 7] In these studies the kinetics of the CRN is dependent on the fuel concentration and substrate concentrations for the deactivation step. However, large amounts of fuel or substrates are required within the CRN. Therefore, changing the kinetics by the fuel or substrate concentration results in a large change in environmental conditions (pH, salt) which can be a major disadvantage for the system. It could be beneficial to control the kinetics of the CRN by catalysis, as small changes in catalyst concentration or activity can have a large kinetic impact, without changing the system conditions substantially. Moreover, catalysis can enable more complex behavior, such as feedback loops and oscillations.[8]

In a previous article we demonstrated the development of a fuel-driven transient crystallization system in which the crystallization and dissolution kinetics were controlled using two catalysts (Chapter 3). This system is based on the redox chemistry of nicotinamide cofactor mimics (mNAD$^+$) in which the nicotinamide mimics are reduced by sodium formate as fuel, catalyzed by a soluble rhodium complex. The resulting 1,4-dihydronicotinamide groups (mNADH) are then oxidized by molecular oxygen using methylene blue (MB) as a catalyst. The mNADH group is more apolar than mNAD$^+$ resulting in a lowered solubility, and in this case, crystal formation. Importantly, the reduction and oxidation of nicotinamide mimics can take place

simultaneously, meaning that this dynamic system can proceed through a full cycle of crystal formation and dissolution autonomously, after initial introduction of the fuel.

In the current work, we applied this fuel-driven CRN to the polymer coil-to-globule transition. Using a nicotinamide functionalized polymer (mNAD[+]-polymer) we could obtain multiple transient coil-globule transitions of the polymer when coupled to a series of redox cycles. Furthermore, we were able to control the rate of collapse and dissolution by changing the concentrations of either catalyst. Ultimately, the polymer globule agglomerates could be used for transient compartmentalization of hydrophobic nano-objects such as proteins or nanoparticles, which could be interesting for biological applications.[9, 10]

4.2. Results and discussion

We designed a mNAD[+] functionalized linear polymer **1** that is soluble when in thermodynamic equilibrium while it collapses in its out-of-equilibrium state (Figure 4.1). The hydrophilicity of polymer **1** is controlled by the redox state of the nicotinamide groups. Using this CRN (redox cycle of nicotinamide mimics) we were able to control the coil-globule transition kinetics of polymer **1**. The positively charged mNAD[+]-polymer **1** is well soluble in MOPS buffer (100 mM, pH 7.5) at a concentration of 2.86 mg/mL. Upon reduction with sodium formate as fuel and [Cp*Rh(bpy-OMe)Cl]Cl as catalyst (Rh-catalyst), the mNAD[+] groups are reduced to neutral mNADH groups.[11] This results in an increase in hydrophobicity of the polymer, leading to collapse and subsequent polymer agglomeration, observed as insoluble particles in the mixture. Throughout the cycle, the presence of dissolved molecular oxygen and MB catalyst allows re-oxidation of the mNADH groups back to mNAD[+] groups.[12] The oxidation of mNADH groups increases the hydrophilicity of the polymer leading to the dissolution of the polymer agglomerates, affording a clear solution at the end of a cycle.

mNAD[+]-polymer **1** was synthesized by functionalizing commercially available poly(glycidyl methacrylate) (pGMA, M_n = 18–22 kDa) with nicotinamide groups in two steps. The pGMA epoxide groups were converted to azide functionalities by ring opening with sodium azide. Subsequently, reaction with butyne-functionalized nicotinamide using copper-catalyzed alkyne-azide cycloaddition chemistry afforded polymer **1**. ^{1}H-NMR and infrared spectroscopy showed that all epoxide groups were functionalized with mNAD[+] groups (Supplementary Figures S4.11-S4.13). Furthermore, the zeta-potential (+28.9 ± 5.58 mV) and hydrodynamic diameter in MOPS buffer (100 mM, pH 7.5) (number mean = 11.4 ± 5.60 nm) of polymer **1** show the formation of a positively charged, water-soluble polymer.
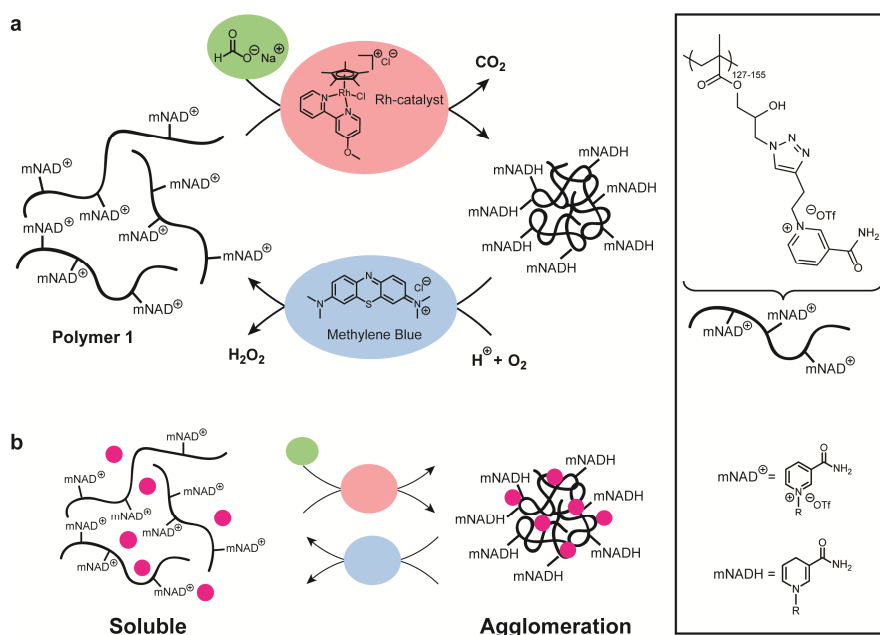
Figure 4.1. Structure of nicotinamide functionalized polymer **1**, its fuel-driven assembly cycle and its use for transient compartmentalization. **(a)** The chemical reaction network and the coupled transient coil-globule transition of the mNAD$^+$-polymer. The hydrophilic mNAD$^+$ groups on polymer **1** are reduced to more hydrophobic mNADH groups by sodium formate as fuel, using the Rh-complex as catalyst. Simultaneously, the formed mNADH groups are oxidized to mNAD$^+$ using molecular oxygen, catalyzed by methylene blue. **(b)** The transient agglomerating polymer is used as a tool for transient compartmentalization of hydrophobic nano-objects (pink) into the agglomerates.

To access the behavior of the mNAD$^+$-polymer when coupled to the CRN, we started by using a low concentration of polymer **1** (0.286 mg/mL; 0.1 mM mNAD$^+$ groups) in MOPS buffer (100 mM, pH 7.5) that remained soluble during the entire redox cycle (Supplementary Figure S4.14). The redox cycle was started by adding sodium formate (30 mM), the Rh-catalyst (0.09 mM) and the MB catalyst (0.002 mM). Oxygen was bubbled through the solution using a needle, to maximize the availability of molecular oxygen in the system, maximizing the oxidation rate. We could follow the kinetics of the redox reactions by UV-vis spectroscopy as the mNADH groups have a characteristic absorption at 350 nm. At the start of the cycle, the reduction rate is dominant over the oxidation rate due to the high sodium formate concentration, leading to the formation of mNADH groups on polymer **1** (Figure 4.2). After about 0.5 h the oxidation rate of mNADH to mNAD$^+$ becomes dominant and the mNADH groups start to deplete, reaching full conversion back to mNAD$^+$ after about 7 h. As the
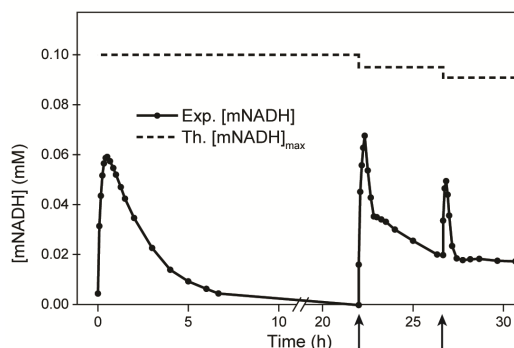
Figure 4.2. Consecutive redox cycles of mNAD$^+$-polymer **1**. The first redox cycle of mNAD$^+$-polymer **1** was started by addition of sodium formate, the Rh-catalyst and methylene blue (MB). The second and third cycles were induced by addition of a new batch of sodium formate and Rh-catalyst (arrows). General conditions: T = 20°C, 3 mL MOPS buffer (100 mM, pH 7.5) with 0.286 mg/mL mNAD$^+$-polymer **1** (0.1 mM mNAD$^+$ groups on the polymer), 0.09 mM Rh-catalyst, 0.002 mM MB and 30 mM sodium formate. The second and third cycles were initiated by the addition of Rh-catalyst solution (63 µL, 4.29 mM) and sodium formate solution (90 µL, 1 M).

original mNAD$^+$-polymer is recovered, a second and third redox cycle is initiated by adding a new batch of sodium formate and Rh-catalyst (Figure 4.2). New Rh-catalyst is necessary as it is irreversibly deactivated during the redox cycle through a side reaction with molecular oxygen (Chapter 3).

After establishing the redox cycle, we turned it into a transient agglomeration cycle by using a higher concentration of mNAD$^+$-polymer **1**. In a typical experiment, a 1.0 cm cuvette was filled with 3 mL aqueous buffer that was slowly bubbled with a constant flow of molecular oxygen gas. The aqueous solution consisted of 2.86 mg/mL polymer **1** (1.0 mM mNAD$^+$ groups on the polymer), 100 mM sodium formate, 0.3 mM Rh-catalyst and 0.01 mM MB, all dissolved in MOPS buffer (100 mM, pH 7.5). We quantified the agglomerate content using Dynamic Light Scattering (DLS) and used the scattering intensity of the sample (derived count rate) as a measure for the number of large agglomerates present in the system. Under these conditions, the mixture goes through a cycle of forming a suspension, flocculation and dissolution to end with a homogeneous solution (Figure 4.3e). In Figures 4.3b-d, the initial formation of a suspension is observed as a small increase in scattering intensity. This mixture flocculates after 1 h, leading to the formation of millimeter-sized agglomerates, showing large scattering intensity in Figure 4.3b-d. Simultaneous MB-catalyzed oxidation of the mNADH groups leads to dissolution of the agglomerates, affording a clear solution with low scattering after 3 h. After completion of an agglomeration
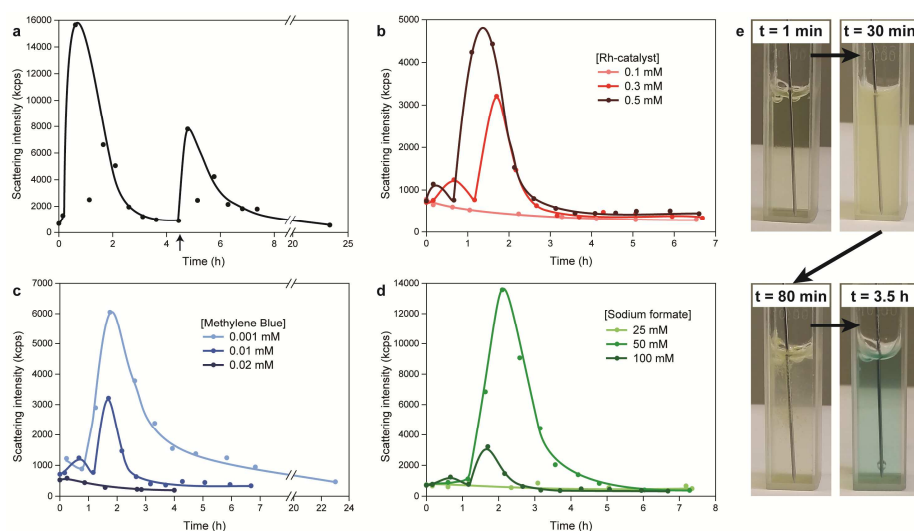
Figure 4.3. Influence of the catalyst and fuel concentration on the kinetics of the transient agglomeration. General conditions: T = 20°C, slow molecular oxygen bubbling, sample volume 3 mL MOPS buffer (100 mM, pH 7.5) in a cuvette, 2.86 mg/mL mNAD$^+$-polymer **1** (1.0 mM mNAD$^+$ groups on the polymer). **(a)** Two agglomeration cycles within a single system. The 2nd cycle is started after 4.5 h (arrow) by addition of sodium formate and Rh-catalyst. Concentrations first cycle: 0.3 mM Rh-catalyst, 0.1 mM MB and 100 mM sodium formate. Second cycle is initiated by the addition of sodium formate solution (60 µL, 5 M) and Rh-catalyst solution (24 µL, 37.5 mM). **(b)** Scattering intensity over time with varying Rh-catalyst concentrations. Concentrations: 0.02 mM methylene blue (MB) and 100 mM sodium formate. **(c)** Scattering intensity over time with varying MB concentrations. Concentrations: 0.3 mM Rh-catalyst and 100 mM sodium formate. **(d)** Scattering intensity over time with varying sodium formate concentrations. Concentrations: 0.3 mM Rh-catalyst and 0.02 mM MB. **(e)** Photos during the redox cycle showing a clear solution at the start that turns into a suspension, flocculation and dissolution over time. Concentrations: 0.3 mM Rh-catalyst, 0.01 mM MB and 100 mM sodium formate.

cycle, a 2nd agglomeration cycle was initiated by addition of sodium formate and fresh Rh-catalyst (Figure 4.3a). Additionally, we looked at the dependence of the agglomeration process kinetics on the sodium formate, Rh-catalyst and MB catalyst concentrations. The agglomeration rate increases at higher Rh-catalyst concentrations, as the reduction rate is increased (Figure 4.3b). The dissolution rate of the agglomerates is independent on the Rh-catalyst concentration as the Rh-catalyst is slowly deactivated over time by molecular oxygen. The dissolution rate could however be varied by changing other parameters: decreasing the MB concentration or decreasing the sodium formate concentration increases the lifetime of the agglomerates (Figures 4.3c and 4.3d, respectively). MB dictates the mNADH oxidation rate and can therefore extend the lifetime of the agglomerates. Decreasing the sodium formate concentration decreases the Rh-catalyst deactivation rate, resulting in a

longer dynamic regime in which the reduction and oxidation take place simultaneously. This increase in dynamic regime leads to a longer agglomerate lifetime (Chapter 3). Not only the agglomeration and dissolution rate can be controlled by the CRN but the maximum scattering intensity as well. If the oxidation rate is relatively fast compared to the reduction rate by using a high MB concentration or by using a low Rh-catalyst or sodium formate concentration, only a few mNAD$^+$ groups of the polymer are reduced to mNADH. Therefore, the polymer remains soluble in the aqueous medium and the scattering intensity stays low (Figure 4.3). On the other hand, when either a high Rh-catalyst or a low MB catalyst concentration is used, the scattering intensity is high indicating a large number of agglomerates resulting from many mNADH groups in the polymer. Decreasing the sodium formate concentration from 100 to 50 mM gives a surprising result as a higher scattering intensity is reached. We hypothesize that partial reduction of the mNAD$^+$ groups leads to a differently structured particle than complete reduction resulting in a difference in scattering behavior. Displaying the particle size instead of the scattering intensity shows a decreased particle size when using a lower initial sodium formate concentration (Supplementary Figure S4.15).

Transient compartmentalization or sequestration of specific molecules or particles is crucial for biological processes and finds application in the fields of catalysis and drug delivery.[8,9] The reduced polymer **1** transiently phase separates to form hydrophobic domains in aqueous solution. We wondered if we could use this transient compartmentalization process to catch and release slightly hydrophobic nano-objects from aqueous solution. We used 10 nm gold nanoparticles (Au NPs) and the protein bovine serum albumin (BSA) as cargos as these are somewhat hydrophobic and can be used for biological applications.[13] The Au NPs are colored and have a distinct absorption band at 518 nm, and can therefore be visualized with UV-vis spectroscopy, at any moment during the agglomeration cycle (Figure 4.4c). The Au NPs were mixed with polymer **1**, Rh-catalyst, MB and sodium formate. After 5 min, the polymer would agglomerate. UV-vis analysis of the supernatant showed a near complete disappearance of the 518 nm absorption, indicative of a close to 100% sequestration of the Au NPs in the polymer agglomerates. Subsequent dissolution of the polymer agglomerates overnight led to the release of Au NPs into solution, as shown by the reappearance of the 518 nm absorption. At this point, the solution contains around 75% of the Au NPs, some of the remainder is stuck to the glass of the reaction vial.

Next, we demonstrate that transient compartmentalization using polymer **1** can temporarily sequester BSA proteins from solution. We could quantify the BSA content using the Bradford Assay.[14] Unfortunately, polymer **1** interferes with the assay, so we
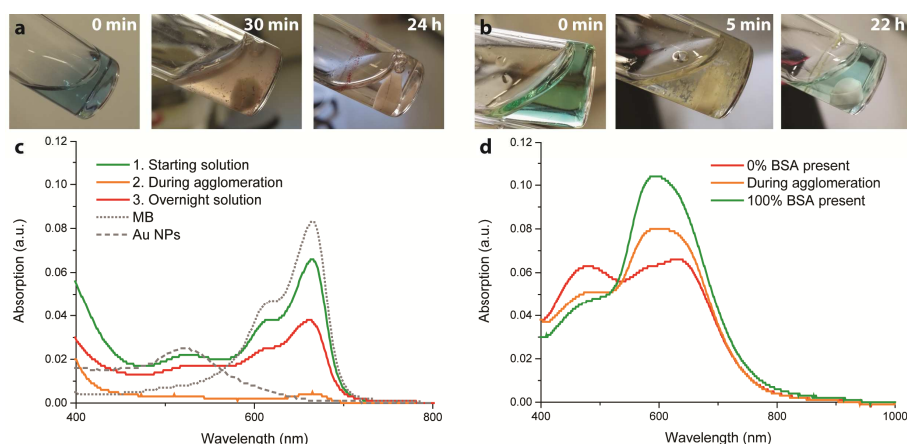
Figure 4.4. Incorporation and release of gold nanoparticles (Au NPs) and Bovine Serum Albumin (BSA) protein in the polymer during the mNAD$^+$/mNADH redox cycle. **(a)** Photos of the reaction mixture with Au NPs before, during (30 min) and after (24 h) the redox cycle. **(b)** Photos of the reaction mixture with BSA proteins before, during (5 min) and after (22 h) the redox cycle. **(c)** The absorption spectrum of the filtrate of the starting solution without sodium formate present (green), during the agglomeration of the polymer (orange) and after the redox cycle is completely finished (red). The absorption of only methylene blue (MB, dotted line) and 10 nm Au NPs (dashed line) are shown in grey. **(d)** Absorption spectrum of the filtrate using the Bradford Assay during the agglomeration (orange) and when 0% (red) or 100% (green) BSA is present. General conditions: 3 identical samples for each measurement were used. T = 20°C, 1 mL MOPS buffer (100 mM, pH 7.5), stirred (500 rpm). Concentrations: 2.86 mg/mL mNAD$^+$-polymer **1** (1.0 mM mNAD$^+$ groups on the polymer), 0.3 mM Rh-catalyst, 0.01 mM MB, 100 mM sodium formate and 2.1 nM 10 nm Au NPs or 0.06 mM BSA proteins. Samples were filtered (0.45 μm) and analyzed at the start, after 2.5 h and overnight.

could only analyze the BSA content of the filtrate during polymer agglomeration (Figure 4.4d, Supplementary Figure S4.16). Using this method, we found out that around 60% of the BSA proteins are sequestered in the polymer agglomerates and the protein is completely redissolved upon dissolution of the polymer as a clear solution is formed upon oxidation. The Au NPs and BSA experiments demonstrate that polymer **1** can transiently sequester hydrophobic particles and release them over time.

4.3. Conclusions

To conclude, we designed a reactive polymer system in which we can control the transient agglomeration behavior of the polymer over time by regulating the kinetics of the coupled chemical reaction network. A water-soluble nicotinamide functionalized polymer was synthesized and coupled to a formate-driven mNAD$^+$/mNADH chemical reaction network. Upon Rh-catalyzed reduction of the mNAD$^+$-polymer by sodium formate, the solubility of the polymer decreases significantly resulting in the collapse

of the polymer into agglomerates. Subsequent oxidation of mNADH groups using the methylene blue catalyst re-disperses the polymer. By changing the kinetics of the reduction and oxidation reactions simultaneously we were able to control the agglomeration timescales of the polymer. Moreover, we show that transient polymer agglomeration can be used to reversibly sequester hydrophobic particles, opening new opportunities for temporal catch-and-release of specific chemical entities from solution.

4.4. References

1.   T. Manouras and M. Vamvakaki, *Polym. Chem.*, 2017, **8**, 74-96.
2.   X. Hu, Y. Zhang, Z. Xie, X. Jing, A. Bellotti and Z. Gu, *Biomacromolecules*, 2017, **18**, 649-673.
3.   M. A. C. Stuart, W. T. S. Huck, J. Genzer, M. Müller, C. Ober, M. Stamm, G. B. Sukhorukov, I. Szleifer, V. V. Tsukruk, M. Urban, F. Winnik, S. Zauscher, I. Luzinov and S. Minko, *Nat. Mater.*, 2010, **9**, 101-113.
4.   S. A. P. van Rossum, M. Tena-Solsona, J. H. van Esch, R. Eelkema and J. Boekhoven, *Chem. Soc. Rev.*, 2017, **46**, 5519-5535.
5.   J. Boekhoven, W. E. Hendriksen, G. J. M. Koper, R. Eelkema and J. H. van Esch, *Science*, 2015, **349**, 1075-1079.
6.   T. Heuser, A.-K. Steppert, C. M. Lopez, B. Zhu and A. Walther, *Nano Lett.*, 2015, **15**, 2213-2219.
7.   G. Wang, J. Sun, L. An and S. Liu, *Biomacromolecules*, 2018, **19**, 2542-2548.
8.   R. Tamate, T. Ueki, M. Shibayama and R. Yoshida, *Soft Matter*, 2017, **13**, 4559-4568.
9.   E. Blanco, H. Shen and M. Ferrari, *Nat. Biotechnol.*, 2015, **33**, 941-951.
10.   G. Weng, U. S. Bhalla and R. Iyengar, *Science*, 1999, **284**, 92-96.
11.   F. Hollmann, B. Witholt and A. Schmid, *J. Mol. Catal. B Enzym.*, 2003, **19-20**, 167-176.
12.   P. Sevcik and H. B. Dunford, *J. Phys. Chem.*, 1991, **95**, 2411-2415.
13.   E. C. Dreaden, A. M. Alkilany, X. Huang, C. J. Murphy and M. A. El-Sayed, *Chem. Soc. Rev.*, 2012, **41**, 2740-2779.
14.   M. M. Bradford, *Anal. Biochem.*, 1976, **72**, 248-254.

4

4.5. Supplementary information

4.5.1. Methods

NMR spectra were recorded on an Agilent-400 MR DD2 (399.7 MHz for ^{1}H, 100.5 MHz for ^{13}C and 376.7 MHz for ^{19}F) at 298 K using residual protonated solvent signals as internal standard. Mass spectra (MS) were obtained on a Shimadzu LCMS-2010 by electrospray ionization in positive and negative mode (ESI+ and ESI-). UV-vis spectroscopic measurements were performed on a Shimadzu UV-1800 spectrophotometer; quartz cuvettes with a path length of 1.0 cm were used. Dynamic Light Spectroscopy (DLS) and zeta-potential measurements were performed on a Malvern Instruments Zetasizer Nano ZS in a 4 mL quartz cuvette. Infrared spectra were recorded on a Thermo Nicolet 6700 FT-IR spectrometer using the FTIR-ATR mode for product **6** and KBr pallets for product **7**. Gel Permeation Chromatography was performed on a Shimadzu system equipped with a LC-20AD high-precision solvent delivery unit, RID-10A highly stable differential refractive index detector with dual temperature control and CTO-20A column oven containing a serial PL gel 5 μm MIXED-C column with THF as solvent at a flow rate of 1 mL/min at 40 °C. Energy-dispersive X-ray spectroscopy (EDX) measurements were performed using a JEOL JSM-6010LV scanning electron microscope equipped with an EDX detector (B to U $\leq$ 133 eV @ MnKα).

4.5.2. Materials

All compounds and solvents were used without further purification. The technical solvents were purchased from VWR and the reaction solvents were purchased from Sigma-Aldrich. All other chemicals were bought from Sigma-Aldrich with the exception of silver triflate (Fluorochem), 3-fluoroaniline (Fluorochem), ammonium chloride (Alfa Aesar) and MOPS (Alfa Aesar).
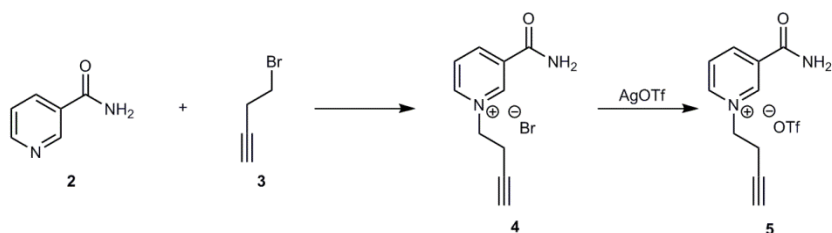
4.5.3. Synthesis

Synthesis procedure of 5

Figure S4.1. Synthesis route to make product **5**.

1-(But-3-yn-1-yl)-3-carbamoylpyridin-1-ium bromide 4. Nicotinamide **2** (2.90 g, 23.9 mmol) was dissolved in acetonitrile (25 mL). 4-bromo-1-butyne **3** (2.47 mL, 26.3 mmol) was added and the reaction mixture was refluxed for 15 h. Next the mixture was cooled down to room temperature and the mixture was precipitated in diethyl ether (40 mL). The precipitate was washed three times with acetonitrile and diethyl ether, to yield the pure product **4** as a brown solid (5.03 g, 82%). M.p. 99-101 °C; ^{1}H-NMR (399.7 MHz, DMSO-d$_6$, ppm): δ 9.56 (s, 1H, ArH), 9.25 (d, J = 6.0 Hz, 1H, ArH), 9.01 (d, J = 8.4 Hz, 1H, ArH), 8.59 (s, 1H, NH2), 8.34 (t, J = 6.4 Hz, 1H, ArH), 8.18 (s, 1H, NH2), 4.83 (t, J = 6.6 Hz, 2H, CH2N), 3.09 (t, J = 2.6 Hz, 1H, CH), 3.01 (m, 2H, CH2). ^{13}C-NMR (100.5 MHz, CD$_3$OD, ppm): δ 162.8 (C=O), 146.6 (C_{Ar}), 145.1 (C_{Ar}), 143.8 (C_{Ar}), 133.7 (C_{Ar}), 127.6 (C_{Ar}), 79.1 (C), 75.3 (CH), 59.0 (CH$_2$), 20.3 (CH$_2$). MS (ESI Pos.) m/z: 174.90 [(M$^+$)] (expected m/z = 175.09).
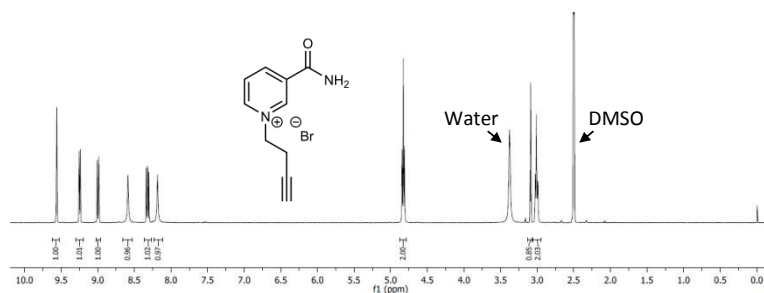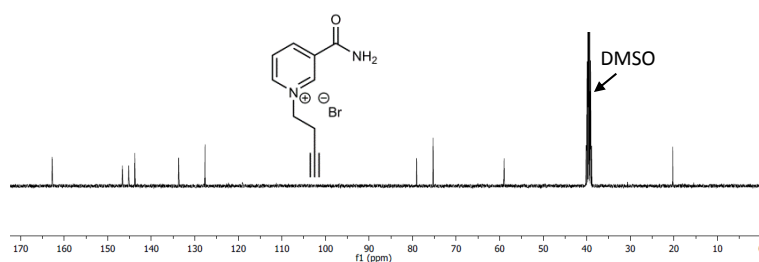

Figure S4.2. ^{1}H-NMR (DMSO-d$_6$) of product **4**.

Figure S4.3. ^{13}C-NMR (DMSO-d$_6$) of product **4**.

1-(But-3-yn-1-yl)-3-carbamoylpyridin-1-ium triflate 5. Product **4** (5.03 g, 19.7 mmol) was dissolved in methanol (~125 mL). Silver triflate (AgOTf, 5.07 g, 19.7 mmol) was dissolved in methanol and added dropwise to a vigorous stirred solution of reactant **4**. The mixture turned immediately into a suspension which reacted at room temperature overnight. Next, the suspension was filtered and the solvent was evaporated to obtain pure product **5** as a brown solid (6.09 g, 95%). 3-fluoroaniline was added to the NMR sample to determine the ion exchange conversion (98%). M.p. 99-100 °C; ^{1}H-NMR (399.7 MHz, CD$_3$OD, ppm): δ 9.47 (s, 1H, Ar*H*), 9.14 (d, J = 6.0 Hz, 1H, Ar*H*), 9.01 (d, J = 8.0 Hz, 1H, Ar*H*), 8.22 (t, J = 6.2 Hz, 1H, Ar*H*), 4.84 (t, J = 6.4 Hz, 2H, C*H*2N), 3.01 (m, 2H, C*H*2), 2.60 (t, J = 2.6 Hz, 1H, C*H*). ^{13}C-NMR (100.5 MHz, CD$_3$OD, ppm): δ 165.0 (*C*=O), 147.9 (*C*$_{Ar}$), 146.4 (*C*$_{Ar}$), 145.5 (*C*$_{Ar}$), 135.8 (*C*$_{Ar}$), 129.2 (*C*$_{Ar}$), 78.9 (*C*), 75.1 (*C*H), 61.4 (*C*H$_2$), 21.7 (*C*H$_2$). ^{19}F-NMR (376.7 MHz, CD$_3$OD, ppm): δ -80.1 (triflate), -116.1 (3-fluoroaniline), MS (ESI Pos.) m/z: 174.90 [(M$^+$)] (expected m/z = 175.09).
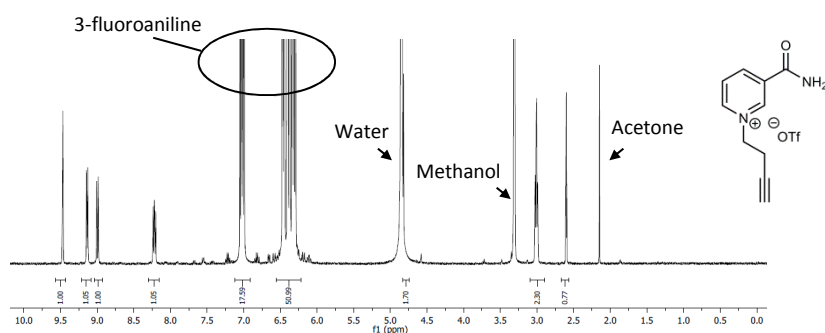
Figure S4.4. ^{1}H-NMR (CD$_3$OD) of product **5** and 3-fluoroaniline.
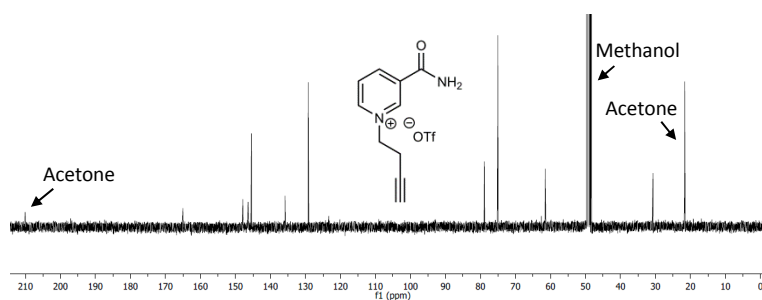
Figure S4.5. ^{13}C-NMR (CD$_3$OD) of product **5**.
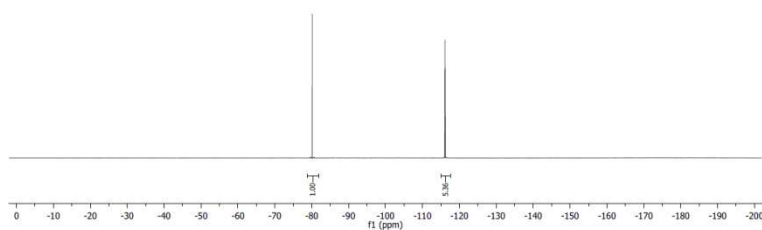
Figure S4.6. ^{19}F-NMR (CD$_3$OD) of product **5** and 3-fluoroaniline.
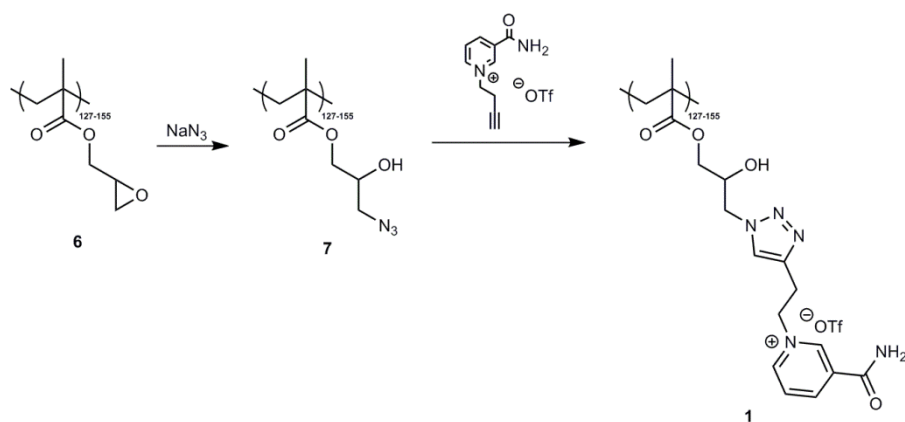
## Synthesis procedure of polymer 1

Figure S4.7. Synthetic route for the formation of mNAD$^+$ functionalized polymer **1**.

Azide functionalized poly(glycidyl methacrylate) 7. Poly(glycidyl methacrylate) **6** (pGMA, M_n = 18-22 kDa, 100 mg) was dissolved in DMF (5 mL) and heated to 50 °C. Sodium azide (0.470 g, 7.23 mmol) and ammonium chloride (0.146 g, 2.73 mmol) were added to the solution which was allowed to react overnight. The product was precipitated from the resulting solution by three times addition of water (40 mL). The solid residue was dried in a vacuum oven at 50 °C to obtain the pure product **7** as a white solid (84.8 mg, 56%). ^{1}H-NMR (399.7 MHz, DMF-d_7, ppm): δ 5.87 (1H, O*H*), 4.09 (1H, C*H*), 3.99 (2H, C*H*2), 3.47 (2H, C*H*2N3), 1.95 (2H, C*H*2), 0.92 (3H, C*H*3). ^{13}C-NMR (100.5 MHz, DMF-d_7, ppm): δ 177.6-176.6 (*C*=O), 68.3 (*C*HOH), 66.5 (*C*H2O), 53.9 (*C*H2N3), 45.2-44.8 (*C*H2), 18.6-16.9 (*C*H3). The quaternary carbon atom is not visible in the 13C-NMR spectrum, either due to overlap with the DMF signal or low intensity; ATR-FTIR (cm^{-1}): 3400 (OH, stretch), 2094 (N3, stretch), 1718 (C=O, stretch); GPC (in THF) shows a decrease in retention time (t_r) between the commercial pGMA (t_r = 8.2 min) and product **7** (t_r = 7.8 min) indicating that the molecular weight has increased.
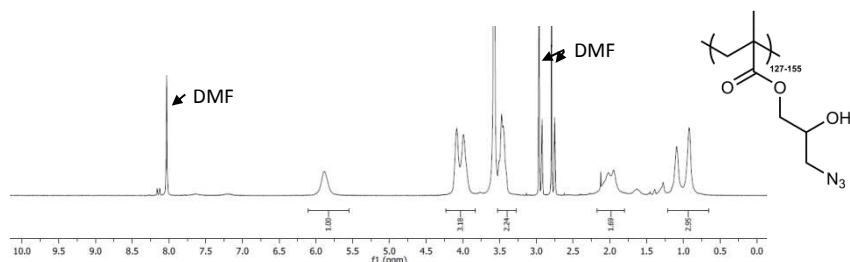
Figure S4.8. ^{1}H-NMR (DMF-d_7) of product **7**.
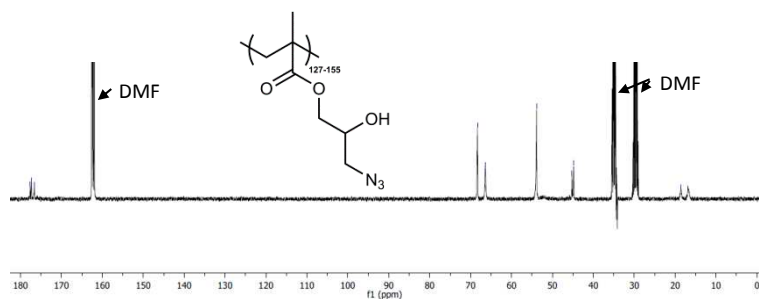
Figure S4.9. ^{13}C-NMR (DMF-d_7) of product **7**.
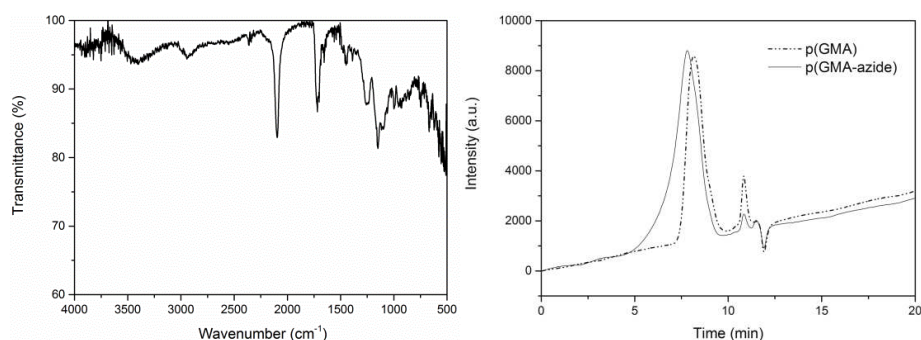
Figure S4.10. Left) Infrared spectrum of product **7** with the azide peak at 2100 cm^{-1}. **Right)** Gel Permeation Chromatography spectrum of the commercial p(GMA) **6** (dashed-dotted line) and the azide functionalized p(GMA) **7** (solid line). The reference time of product **6** and **7** are 8.2 and 7.8 min, respectively.

Nicotinamide functionalized poly(glycidyl methacrylate) 1. Under inert atmosphere, product **7** (0.881 g, 4.76 mmol) was dissolved in DMF (25 mL) and product **5** (1.49 g, 4.76 mmol) and CuBr (0.137 g, 0.952 mmol) were added. The mixture reacted overnight at room temperature and afterwards the DMF was evaporated. The residue was dissolved in water (75 mL) and purified by dialysis (MWCO = 3.5-5 kDa, whereby the water was exchanged four times). The mixture contained solid copper complex, which was separated from the polymer solution by centrifugation and decantation. The water was evaporated, and the product was dried in vacuum at 50 °C. The pure product **1** was obtained as a brown solid (1.66 g, 69%). ^{1}H-NMR (399.7 MHz, D$_2$O, ppm): δ 9.07 (1H, Ar*H*), 8.76 (2H, Ar*H*), 8.01 (2H, Ar*H*), 7.71 (2H, C*H*N3), 4.87 (2H, C*H*2N), 4.41 (2H, C*H*2), 4.17 (1H, C*H*OH), 3.89 (2H, C*H*2N3), 2.0-1.5 (2H, C*H*2), 1.5-0.5 (3H, C*H*3). ^{13}C-NMR (100.5 MHz, D$_2$O, ppm): δ 165.1 (*C*=O), 146.5 (*C*=O), 144.4 (*C*$_{Ar}$), 141.8 (*C*$_{Ar}$), 133.8 (*C*$_{Ar}$), 128.4 (*C*$_{Ar}$), 125.2 (*C*$_{Ar}$), 121.2 (*C*$_{Ar}$), 118.1 (*C*$_{Ar}$), 67.3 (*C*H2O), 61.4 (*C*HOH), 52.5 (*C*H2), 44.7 (*C*H2N), 30.2 (*C*), 26.5 (*C*H2); FTIR (KBr, cm^{-1}): 3000-3700 (CH, NH$_2$, OH, stretch), 1693 (C=O, stretch); EDX shows that 0.42 mol% of the anion is bromide and the 99.58 mol% is triflate.

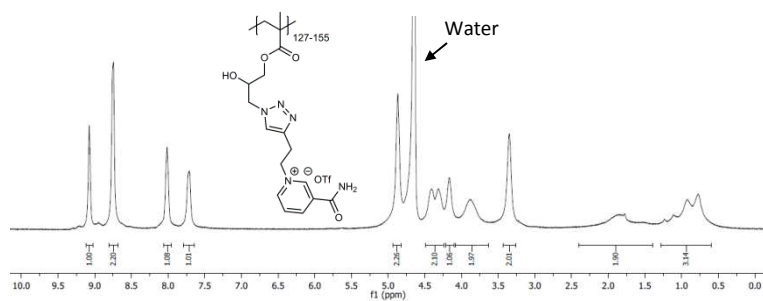**Figure S4.11.** ^{1}H-NMR (D$_2$O) of product **1**.

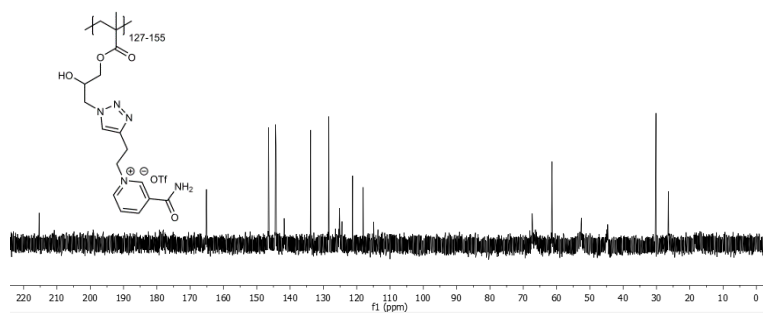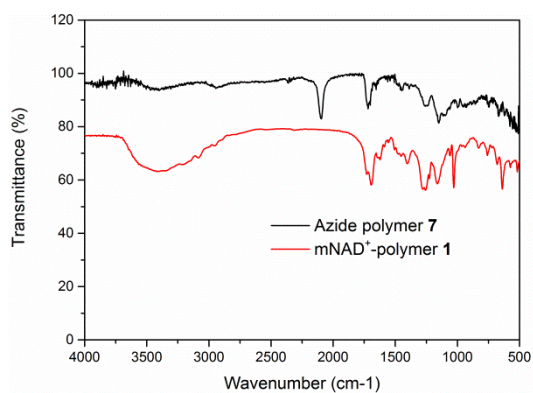**Figure S4.12.** ^{13}C-NMR (D$_2$O) of product **1**.

Figure S4.13. Infrared spectrum of product **7** and **1** showing the complete conversion from the azide (disappearance of the 2094 cm^{-1} peak).

Table S4.1. Energy-dispersive X-ray spectroscopy (EDX) data of polymer **1**.

Element	Mass%	Atom%	Sigma	Net	K ratio	Line
C	51.84	60.40	0.03	100659	0.0825324	K
N	16.42	16.41	0.17	5748	0.0632039	K
O	17.26	15.10	0.08	26026	0.0724697	K
F	8.00	5.89	0.06	18996	0.1074588	K
S	4.06	1.77	0.02	79695	0.0962087	K
Br	2.42	0.42	0.04	26411	0.0468999	L
Total	100.00	100.00				

Synthesis procedure of [Cp*Rh(bpy-OMe)Cl]Cl

The Rh-catalyst was synthesized according to literature procedures. 4-nitro-2,2'-bipyridine-1-oxide was formed from 2,2'-bipyridine.[1] Next, 4-nitro-2,2'-bipyridine-1-oxide is converted to 4-methoxy-2,2'-bipyridine-1-oxide and finally to 4-methoxy-2,2'-bipyridine.[2] Lastly, the [Cp*Rh(bpy-OMe)Cl]Cl (Rh-catalyst) is formed.[3]

4.5.4. Experimental conditions for the kinetics of the redox cycles

The redox cycles of polymer **1** were performed at room temperature (19-20°C) with molecular oxygen bubbling slowly through the solution in an open quartz cuvette (volume = 4 mL, l = 1.0 cm) to ensure a sufficiently high oxygen concentration. The reactions were carried out in MOPS buffer (100 mM, pH 7.5). All reagents were added at the start of the redox cycle and sodium formate was added lastly. Samples were taken after specific time intervals to measure the UV-vis absorbance spectrum in the 1.0 cm cuvette. After the measurement the needle with molecular oxygen was returned into the solution. The used extinction coefficients for the reagents are:

mNAD$^+$-butyne as model for polymer **1** (265 nm):	$4.67 \cdot 10^3$ M^{-1} cm^{-1}
NADH-G-OH as model for the mNADH-polymer (350 nm):	$5.69 \cdot 10^3$ M^{-1} cm^{-1}
Rh-catalyst (300 nm):	$1.22 \cdot 10^4$ M^{-1} cm^{-1}
Rh-catalyst (350 nm):	$2.30 \cdot 10^3$ M^{-1} cm^{-1}
RhOOH complex (350 nm):	$1.22 \cdot 10^3$ M^{-1} cm^{-1}
Methylene blue (350 nm):	$1.41 \cdot 10^3$ M^{-1} cm^{-1}
Methylene blue (665 nm):	$5.76 \cdot 10^4$ M^{-1} cm^{-1}

The extinction coefficient of polymer **1** is difficult to determine, therefore the extinction coefficient of the monomer (mNAD$^+$-butyne) is used as model for the extinction coefficient of polymer **1**. Similar, the extinction coefficient of the mNADH-polymer could also not be determined thus the extinction coefficient of nicotinamide functionalized glycine (NAD$^+$-G-OH) was used as a model for the extinction coefficient of the mNADH-polymer (Chapter 3).

To measure the concentration of the mNADH groups on the polymer over time, the absorbance at 350 nm was subtracted with the absorbance from the Rh-catalyst, the RhOOH complex and methylene blue and is then converted to the concentration of mNADH groups using its extinction coefficient. The in situ concentration of the Rh-catalyst and the degraded RhOOH complex are determined using the previously developed kinetic model (Chapter 3).

4.5.5. Experimental conditions for the kinetics of the agglomeration cycles

The redox cycles of polymer **1** at higher concentrations were performed at room temperature (19 - 20°C) with molecular oxygen slowly bubbling through the solution in an open quartz cuvette (cuvette volume = 4 mL, l = 1.0 cm) to ensure a sufficiently high oxygen concentration. The reactions were carried out in MOPS buffer (100 mM, pH 7.5). All reagents were added to start the redox cycle and sodium formate was added lastly. Dynamic Light Scattering (DLS) measurements were performed at specific times, after which the molecular oxygen bubbling was restarted.

4.5.6. Detailed conditions for the cargo experiments

The cargo experiments were performed at room temperature (19-20°C) in an open vial (volume = 4 mL, Ø = 15 mm). All reagents including the cargo (Au NPs or BSA) were added to start the redox cycle and sodium formate was added lastly. The 1 mL solution was stirred at 500 rpm to maximize molecular oxygen dissolution and to minimize the loss of particles by sticking to the glass. Three redox cycles were performed in different vials to analyze the solution before, during and after the agglomeration, respectively. For obtaining the Au NPs content, the samples were filtered (mesh size = 0.45 µm) before, during and after the agglomeration, and the filtrate was measured by UV-vis spectroscopy in a 1.0 mm quartz cuvette. The Au NPs show a distinctive absorption

peak at 518 nm. The BSA content during the agglomeration was determined by the Bradford assay. Analysis of the homogeneous solution was impossible to analyze using this assay due to the response of polymer **1** to the Bradford assay. Therefore, only the agglomeration state, in which polymer **1** could be removed by filtration, was analyzed. The filtrate was diluted three times by addition of the Bradford reagent. This solution was then measured by UV-vis spectroscopy in a 1.0 mm quartz cuvette. As comparison the absorption spectrum of the Bradford reagent with 0% BSA and 100% BSA was measured and the agglomeration sample was compared to these values at 595 nm. All Bradford assays were measured in duplo (Supplementary Figure S4.16).

4.5.7. DLS measurements during the redox cycle using a low mNAD$^+$-polymer concentration
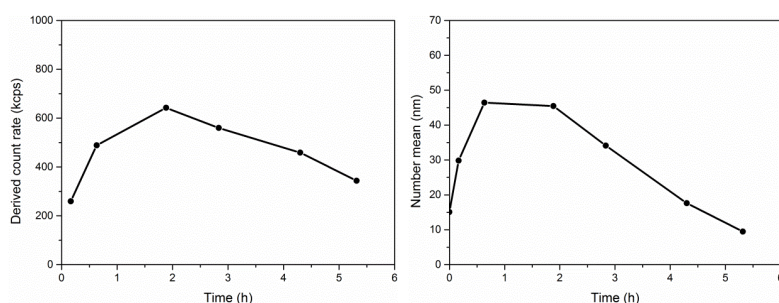
Figure S4.14. Left) Scattering intensity of the transparent solution during the redox cycle. **Right)** Particle size during the redox cycle. Conditions: T = 20°C, slow pure molecular oxygen bubbling, sample volume 3 mL MOPS buffer (100 mM, pH 7.5) in a cuvette, 0.286 mg/mL polymer **1** (1.0 mM mNAD$^+$ groups on the polymer), 0.09 mM Rh-catalyst, 30 mM sodium formate and 0.002 mM methylene blue.

4.5.8. The volume mean of the DLS measurement during the agglomeration cycle
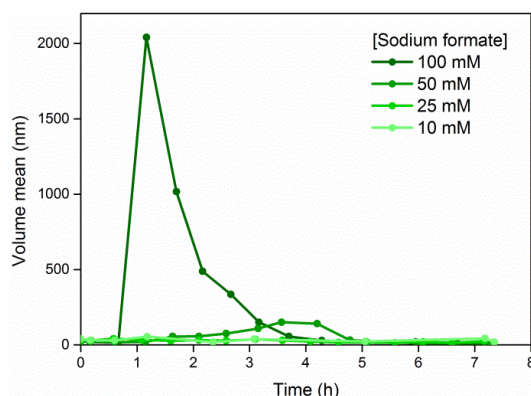
Figure S4.15. The size (number mean) of the polymer agglomerates over time with varying sodium formate concentration. General conditions: T = 20°C, slow pure molecular oxygen bubbling, sample volume 3 mL MOPS buffer (100 mM, pH 7.5) in a cuvette, 2.86 mg/mL polymer **1** (1.0 mM mNAD$^+$ groups on the polymer), 0.3 mM Rh-catalyst and 0.01 mM methylene blue.

4.5.9. BSA content in the polymer agglomerates
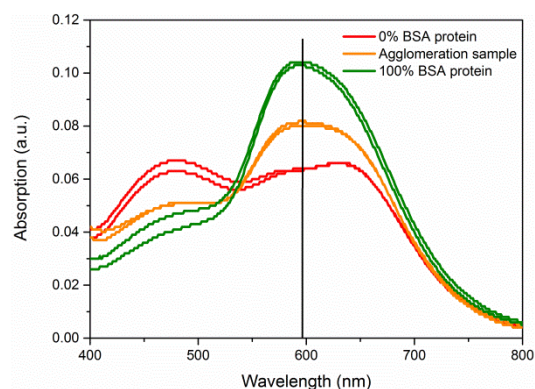
Figure S4.16. Incorporation of BSA protein in the polymer agglomerates. Absorption spectrum of the filtrate using the Bradford Assay during the agglomeration (orange) and when 0% (red) or 100% (green) BSA is present. General conditions: 2 identical samples for each measurement were used. T = 20°C, 1 mL MOPS buffer (100 mM, pH 7.5), stirred (500 rpm). Concentrations: 2.86 mg/mL polymer **1** (1.0 mM mNAD$^+$ groups on the polymer), 0.3 mM Rh-catalyst, 0.01 mM MB, 100 mM sodium formate 0.06 mM BSA proteins. Samples were filtered (0.45 μm) and analyzed by diluting the filtrate three times with the Bradford reagents.

4.5.10. Supplementary references

1.   M. Zalas, B. Gierczyk, M. Cegłowski and G. Schroeder, *Chem. Pap.*, 2012, **66**, 733-740.
2.   D. Wenkert and R. B. Woodward, *J. Org. Chem.*, 1983, **48**, 283-289.
3.   F. Hollmann, B. Witholt and A. Schmid, *J. Mol. Catal. B Enzym.*, 2003, **19-20**, 167-176.

4
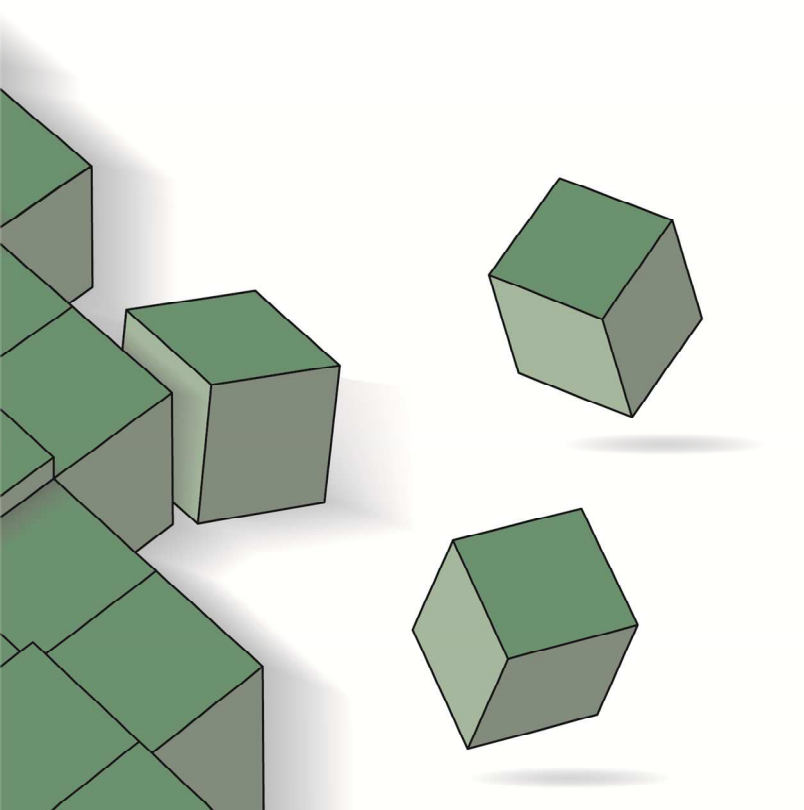
Chapter 5

Responsive colloidal agglomeration in- and towards out-of-equilibrium

Colloidal systems are diverse in morphology and composition making them appealing for a wide range of potential applications from biotechnology to electronics. Combining colloids with out-of-equilibrium chemistry results in an extra benefit as it can control the assembled structure and therefore its function over time. These out-of-equilibrium colloidal systems are investigated intensively, but most often with magnetic and electrical fields as energy source. Using a chemical fuel as energy source is only sparsely investigated, while it facilitates routes to more complex colloidal structures and behaviors. Therefore, we designed a system in which nicotinamide functionalized colloids are transiently agglomerated and redispersed. However, due to undesirable ester hydrolysis within the colloidal brushes we are only able to demonstrate the consecutive agglomeration and redispersion steps of the colloids under thermodynamic reaction control. This system still shows great potential for out-of-equilibrium colloidal assembly after minimizing the degradation. Hence, we also present several suggestions to improve the stability of the colloids enabling to study fuel-driven transient agglomeration.

5.1. Introduction

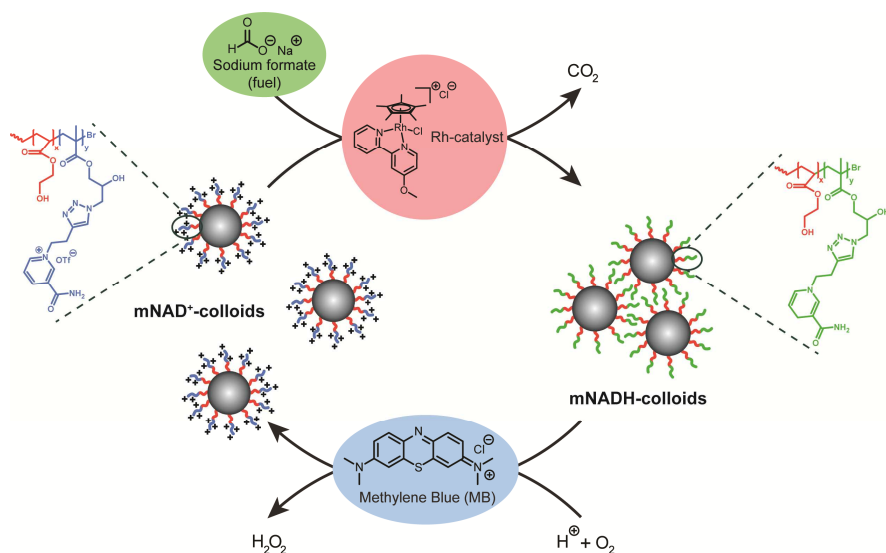In the previous chapters the chemical reaction network (CRN) of nicotinamide (mNAD[+]) is applied to the transient formation of crystals, polymers and surfactants. In this chapter the same CRN of nicotinamide (mNAD[+]) is applied to an out-of-equilibrium colloidal agglomeration system showing the robustness and versatility of the mNAD[+] based CRN. The main features of out-of-equilibrium assembly systems, such as dynamicity, adaptability and the formation of new structures, can also be applied to colloidal systems.[1] Colloidal particles are diverse in size, morphology and composition and they are therefore applied in many fields, from biotechnology to electronics.[2] Moreover, colloidal particles have great potential as models for molecular systems as their interparticle potentials can be tailored to mimic molecular or atomic interactions..[3] Moreover, in contrast to molecules, colloids are large enough to be studied by microscopy.

A significant number of out-of-equilibrium colloidal assembly systems have already been designed, but most of them are based on physical energy inputs, such as light and electrical or magnetic fields.[4] A disadvantage of these systems is that for all these stimuli the energy is supplied by an external source meaning that its effect is immediately stopped when the energy source is removed. Overcoming the need of a continuous external energy supply can be achieved by adding a chemical fuel instead of an external energy source to the system. In this case, the yet unreacted chemical fuel is stored in the system followed by gradual consumption of the fuel. Another benefit of using chemical fuels is the opportunity to make more complex out-of-equilibrium assembly systems, such as feedback loops.[5] Applying chemical fuels to an out-of-equilibrium colloidal assembly has not been investigated intensively. However, a few interesting out-of-equilibrium colloidal assembly systems with chemical fuels are designed by changing the polarity of colloids using a CRN.[6-9]

Here, we would like to extend this area to more complex CRNs by incorporation of catalysis. Van Ravensteijn and coworkers showed severe limitations in fuel concentrations as high fuel concentrations decreased the pH of the system significantly.[6] Catalysis can overcome this problem as variation in the catalyst concentration can now also regulate the assembly rate aside from the fuel concentration. Moreover, catalytic reactions usually require a low catalyst concentration meaning that the system is not influenced significantly by changing its concentrations. Additionally, catalysis facilitates the route towards compartmentalization and feedback loops. Therefore we designed a transient colloidal agglomeration system using a chemical fuel and two catalysts. Dispersed positively charged nicotinamide functionalized colloids (mNAD[+]-colloids, Figures 5.1 and 5.2)

Figure 5.1. Schematic design of the transient agglomeration cycle of mNAD⁺-colloids. Positively charged mNAD⁺-colloids are dispersed in the solution. Reduction in the mNAD⁺/mNADH redox cycle induces agglomeration of the colloids. The repulsive electrostatic forces between the colloids are removed upon reduction with sodium formate and the Rh-catalyst leading to attraction and agglomeration of the particles. Over time the methylene blue catalyst and molecular oxygen re-oxidize all mNADH groups leading to formation of dispersed positively charged colloids.

agglomerate upon reduction of the nicotinamide groups (mNADH), as the charge and therefore the repulsive electrostatic force is removed. Over time the colloids redisperse upon oxidation of the mNADH groups to the mNAD⁺ groups. First, we show successful stepwise agglomeration and redispersion of the colloids under thermodynamic reaction control by sequential addition of fuel and methylene blue catalyst as catalyst for the backward reaction. This shows that the system is most likely suitable for transient colloidal agglomeration under out-of-equilibrium conditions. However, we found out that the colloids degraded over time, resulting in the termination of the project before the out-of-equilibrium kinetics could be properly investigated. Several suggestions are listed to minimize degradation of the colloids resulting in stable mNAD⁺-colloids. After minimizing the degradation rate, the system design is promising for making an out-of-equilibrium colloidal agglomeration system in which agglomeration and redispersion kinetics are controlled by catalysis.

5.2. Results and discussion

The design of the transient agglomerating colloids is based on nicotinamide functionalized colloids. We can control the colloidal charge with the CRN (redox cycle) of the mNAD$^+$ groups (Figure 5.1). The mNAD$^+$ groups on the surface of the colloidal water dispersion are positively charged when at thermodynamic equilibrium leading to electrostatic repulsion of the colloids and a stable dispersion. Upon reduction of the mNAD$^+$ groups, in this case with sodium formate as fuel and [Cp*Rh(bpy-OMe)Cl]Cl (Rh-catalyst) as catalyst, the repulsive electrostatic force is decreased, leading to a situation in which Van der Waals and hydrophobic-driven attractive forces dominate the inter-colloidal potentials and hence drive agglomeration.[10] However, when the mNADH groups are oxidized with molecular oxygen as infinite fuel and methylene blue as catalyst, the repulsive electrostatic force is increased leading to redispersion of the colloids.[11] The DLVO theory named after Derjaguin, Landau, Verwey and Overbeek, dictates that if colloids come too close to each other, the Van der Waals forces become dominant and agglomeration becomes irreversible.[12] To avoid this problem, a steric barrier on the colloids is included by grafting a hydrophilic polymer brush from the colloidal surface. This brush restricts the minimal distance by which the colloids can approach one and other, thereby promoting reversible agglomeration. With this system we should be able to make multiple consecutive colloidal agglomeration cycles in which the agglomeration and redispersion rate can be controlled by both catalyst and fuel concentration.

5.2.1. Synthesis

First, mNAD$^+$-colloids were synthesized according to the synthesis procedures of Van Ravensteijn.[6, 13] Van Ravensteijn and coworkers synthesized spherical bromo-functionalized crosslinked polystyrene colloids (358 nm) using emulsion polymerization.[6] The bromo-groups on the colloidal surface were used as initiating species for grafting a hydrophilic polymer brush, (poly(hydroxyethyl acrylate, p(HEA)) from the colloidal surface via Atom Transfer Radical Polymerization (ATRP) (Figure 5.2).[13] Next, 1 eq. p(HEA) brush was in situ chain extended with 1 eq. glycidyl methacrylate (GMA) to yield polymer brushes with alcohol functionalities on the inside and epoxide functionalities on the outside. Subsequently, the pendent epoxide groups were ring opened with sodium azide to install azide moieties at the outer section of the brush. In the final step positively charged butyne-functionalized nicotinamide was coupled to the particles using copper-catalyzed alkyne-azide cycloaddition chemistry resulting in the targeted nicotinamide functionalized colloids (Figure 5.2 and Supplementary Information). Each reaction step was analyzed by Infrared
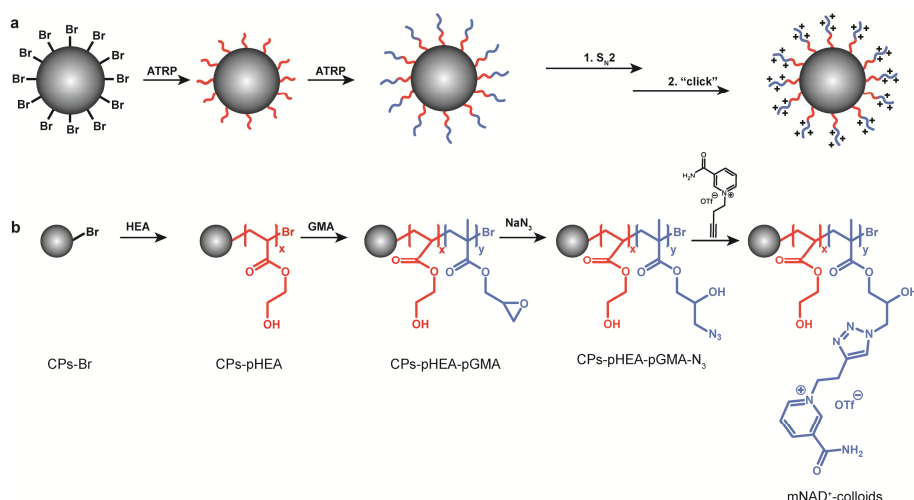
Figure 5.2. Synthetic route to synthesize the mNAD$^+$ functionalized colloids. **(a)** Schematic representation of the structure of the colloids during the synthesis. **(b)** Detailed chemical description of the synthesis route. Starting with polymerization of a hydrophilic monomer (HEA), followed by polymerization of an epoxide functionalized monomer (GMA). Next, the epoxide rings are opened with sodium azide and lastly click chemistry with a butyne-functionalized nicotinamide molecule is performed to obtain the desired mNAD$^+$-colloids.

Spectroscopy (IR) and Dynamic Light Scattering (DLS) showing that the reactions were successful and the mNAD$^+$-colloids were successfully synthesized (Supplementary Information). The final colloids had a diameter of 713 ± 64 nm (determined by Transmission Electron Microscopy, TEM). Moreover, the zeta- potential changed from -80 ± 1.5 mV for the bromo-functionalized polystyrene colloids to +42 ± 0.7 mV for the nicotinamide-functionalized colloids, indicating that many mNAD$^+$ groups are attached and that the colloids repel each other.

5.2.2. Agglomeration cycle

After successfully synthesizing the mNAD$^+$-colloids, we investigated whether these particles could be employed to realize a fuel-driven transient agglomeration cycle based on the mNAD$^+$ based CRN. A stirred solution (750 rpm) of mNAD$^+$-colloids (0.02 wt%) with Rh-catalyst (1.0 mM) or sodium formate (300 mM) in MOPS buffer (100 mM, pH 7.5) showed only small agglomerates (Figure 5.3a and Supplementary Figure S5.3). Upon reduction of the mNAD$^+$ groups with sodium formate (284 mM) the colloids are significantly agglomerated within 2 h (Figure 5.3b). The fractal shape of the colloidal agglomerates indicates that the interaction between the particles is strong and the agglomeration process is diffusion limited. If the agglomeration was reaction

limited, the particles would reorganize themselves, commonly leading to more densely ordered structures.[14] Addition of methylene blue (0.1 mM) led to the redispersion of the agglomerates to individual colloids and small agglomerates (Figure 5.3c). The size of the agglomerates is quantified by isolating the particles from the background and measuring the area of the agglomerates. This quantification showed that the area per agglomerate is doubled upon reduction of the mNAD$^+$ groups (from 8.1 ± 2.9 μm^2 to 17.9 ± 29.9 μm^2) (Figure 5.3d). Furthermore, the increase in standard deviation indicates that the agglomerates are heterogeneous in size. Addition of methylene blue and subsequent redispersion of the colloids results in a decrease to 8.1 ± 6.7 μm^2 showing that the agglomeration process is completely reversible.
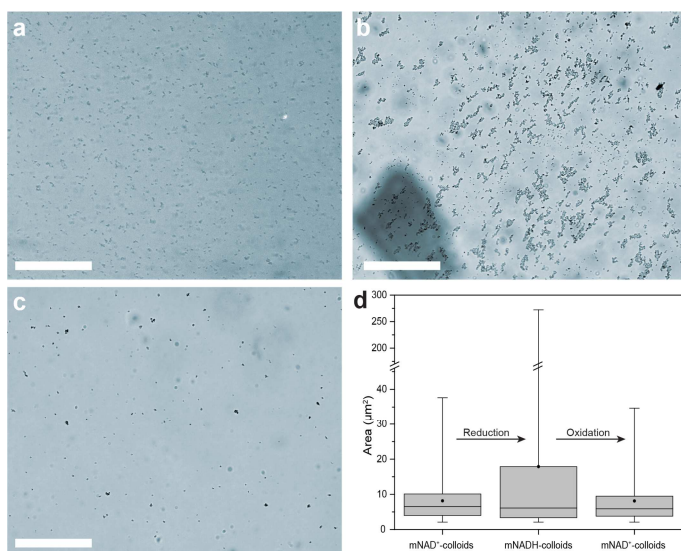
Figure 5.3. Consecutive agglomeration and redispersion of mNAD$^+$/mNADH-colloids observed by optical microscopy. Scale bar is 50 μm. **(a)** A suspension of mNAD$^+$-colloids and Rh-catalyst resulting in only small agglomerates. **(b)** Addition of sodium formate leads to reduction of mNAD$^+$ groups and subsequent agglomeration of the colloids. **(c)** Addition of methylene blue starts oxidation and thereby redispersion of the colloids. **(d)** Box plots of the distribution of the agglomeration size during the mNAD$^+$/mNADH redox cycle. Dot represents the average size.

5.2.3. Degradation of the colloids

To gain more insight in the timescales of the CRN we set out to measure the zeta-potential of the colloids over time. However, the mNAD$^+$-colloids (0.015 wt%) in water had a zeta-potential of -9.1 mV, while the freshly synthesized particles had a zeta-potential of +42 mV. We attribute this dramatic change in surface charge to chemical

| April: 713 ± 64 nm | August: 855 ± 61 nm |
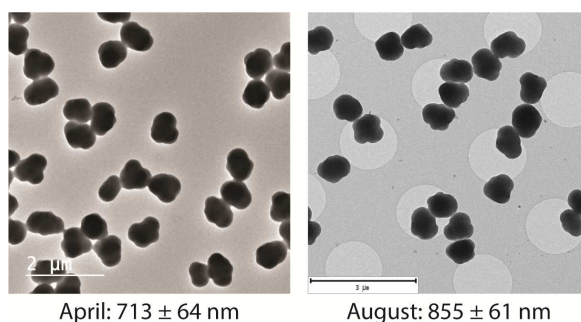
Figure 5.4. TEM images of the mNAD[+]-colloids measured in April (fresh) and in August, showing that the particles have grown.

degradation of the polymer brush upon storage. The most likely contributor to this degradation is the hydrolysis of the ester bonds in the pendent side groups of the polymers immobilized onto the colloid surface. Ester hydrolysis results in the formation of negatively charged carboxylate groups when in aqueous dispersion (pH > 4). The use of DMF as suspension solvent supports this hypothesis as DMF is a hygroscopic solvent in which water will facilitate the hydrolysis of the ester bonds. The negative charges generated by ester hydrolysis results in a low zeta-potential and associated agglomeration of the colloids (PDI$_{DLS}$ = 0.532). DMF not only accelerates the ester hydrolysis, but it is also known to dissolve polystyrene. Increase of the particle size from 713 nm to 855 nm during the degradation could be caused by dissolution of polystyrene cores in DMF resulting in bigger and less dense particles (Figure 5.4).[15] The irregular shape of the colloids is caused by drying required for TEM analysis.[13] Thus to conclude, we believe that DMF as suspension solvent and the ester hydrolysis within the colloids lead to the destabilization of the colloidal dispersion, rendering this system not suitable to study the transient agglomeration behavior as depicted in Figure 5.1 yet.

5.2.4. Recommendations

As a recommendation to increase the stability of the colloids and to enable the use of these polymer grafted colloids in transient agglomeration studies, the mNAD[+]-colloids first have to be synthesized again. Ester hydrolysis rate of the polymers should be decreased to such extent that the chemical structural integrity of the brush can be maintained over the time scales at which the transient clustering experiments take place. The most straightforward strategy to achieve this is by decreasing the water content in the suspension. For this, dry solvents, an inert atmosphere, and maybe even molecular sieves are required during the synthesis and storage of the suspension. This

will increase the lifetime of these particles significantly A second option to increase the stability of the particles is to remove the ester bonds from the synthetic design. This would mean that the HEA and GMA monomers should be replaced by other hydrophilic monomers. Another ester functionalized molecule used in the synthesis is 2-(2-bromoisobutyryloxy) ethyl acrylate (BIEA) which is used to functionalize the core polystyrene particles with bromo-groups. As BIEA is very close to the core particle, it is most likely protected from the hydrophilic environment and does not have to be replaced. My recommendation is to use acrylamides instead of acrylates for the brush growth (Figure 5.5).[16] Similar ATRP reactions can be performed as before, using acrylamide monomers instead of acrylate monomers as the amide groups are stable towards hydrolysis. N-hydroxyethyl acrylamide (HEAA) replaces HEA and 2-aminoethylmethacrylamide (AMEA) is used instead of GMA. The amine group of AMEA is then converted to an azide functionality by a diazotransfer.[17] Lastly, the click reaction with the butyne functionalized nicotinamide can be performed in the same fashion as before.
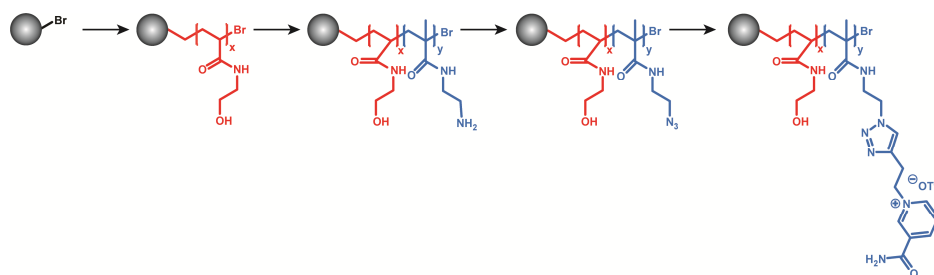
Figure 5.5. Schematic chemical overview of the proposed new synthesis route. Replacing the ester groups by amide functionalized monomers which are much more stable towards hydrolysis. Furthermore, the azide functionality is introduced by the diazotransfer from the amine.

5.3. Conclusions

We present an approach that is highly promising for controlling the kinetics in out-of-equilibrium colloidal assembled structures. $mNAD^+$ functionalized colloids were synthesized and the surface charge of the colloids could be controlled by the chemical reaction network of $mNAD^+$. The $mNAD^+$-colloids are positively charged and dispersed, while reducing the $mNAD^+$ groups leads to a decrease in surface charge resulting in colloidal agglomeration. Subsequent addition of methylene blue leads to oxidation of the mNADH groups and thus the increase in surface repulsion and the redispersion of the colloids. Unfortunately, the synthesized $mNAD^+$-colloids are unstable because the ester bonds in the colloids are slowly hydrolyzed. Using an inert atmosphere or

synthesizing amide-based mNAD$^+$-colloids will reduce hydrolysis resulting in stable mNAD$^+$-colloids. This increase in stability opens the road to investigate out-of-equilibrium colloidal agglomeration and its kinetic behavior using catalysis. In the future this chemical reaction network could be applied to more anisotropic particles to obtain more complex agglomeration behavior or to obtain transient motion.

5.4. References

1. S. A. P. van Rossum, M. Tena-Solsona, J. H. van Esch, R. Eelkema and J. Boekhoven, *Chem. Soc. Rev.*, 2017, **46**, 5519-5535.
2. K. J. Lee, J. Yoon and J. Lahann, *Curr. Opin. Colloid Interface Sci.*, 2011, **16**, 195-202.
3. C. N. Likos, F. Sciortino, E. Zaccarelli and P. Ziherl, *Soft matter self-assembly*, 1st edn., 2016.
4. X. Liu, Y. Yang and M. W. Urban, *Macromol. Rapid. Commun.*, 2017, **38**, 1700030.
5. B. Rieß, C. Wanzke, M. Tena-Solsona, R. K. Grötsch, C. Maity and J. Boekhoven, *Soft Matter*, 2018, **14**, 4852-4859.
6. B. G. P. van Ravensteijn, W. E. Hendriksen, R. Eelkema, J. H. van Esch and W. K. Kegel, *J. Am. Chem. Soc.*, 2017, **139**, 9763-9766.
7. R. K. Grötsch, A. Angı, Y. G. Mideksa, C. Wanzke, M. Tena-Solsona, M. J. Feige, B. Rieger and J. Boekhoven, *Angew. Chem. Int. Ed.*, 2018, **57**, 14608-14612.
8. H. Nabika, T. Oikawa, K. Iwasaki, K. Murakoshi and K. Unoura, *J. Phys. Chem. C*, 2012, **116**, 6153-6158.
9. I. Lagzi, B. Kowalczyk, D. Wang and B. A. Grzybowski, *Angew. Chem., Int. Ed.*, 2010, **49**, 8616-6819.
10. F. Hollmann, B. Witholt and A. Schmid, *J. Mol. Catal. B Enzym.*, 2003, **19-20**, 167-176.
11. P. Sevcik and H. B. Dunford, *J. Phys. Chem.*, 1991, **95**, 2411-2415.
12. H. N. W. Lekkerkerker and R. Tuinier, *Colloids and the depletion interaction*, 2011.
13. B. G. P. van Ravensteijn and W. K. Kegel, *Polym. Chem.*, 2016, **7**, 2858-2869.
14. M. Y. Lin, H. M. Lindsay, D. A. Weitz, R. C. Ball, R. Klein and P. Meakin, *Nature*, 1989, **339**, 360-362.
15. M. T. García, I. Gracia, G. Duque, A. de Lucas and J. F. Rodríguez, *Waste Manag.*, 2009, **29**, 1814-1818.
16. F. Limé and K. Irgum, *J. Polym. Sci. A*, 2009, **47**, 1259-1265.
17. J. Bachl, J. Mayr, F. J. Sayago, C. Cativiela and D. D. Díaz, *Chem. Commun.*, 2015, **51**, 5294-5297.

5

5.5. Supplementary information

5.5.1. Methods

NMR measurements were performed on an Agilent-400 MR DD2 (399.7 MHz for ^{1}H, 100.5 MHz for ^{13}C and 376.7 MHz for ^{19}F) at 298 K using residual protonated solvent signals as internal standard. Mass spectra (MS) were recorded on a Shimadzu LCMS-2010 by electrospray ionization in positive and negative mode (ESI+ and ESI-). Dynamic Light Spectroscopy (DLS) and zeta-potential data were obtained on a Malvern Instruments Zetasizer Nano ZS in a 4 mL quartz cuvette. Infrared spectra were recorded on two different spectrometers. The fresh colloids were measured on a Perkin Elmer FT-IR spectrometer frontier using the FTIR-ATR mode and the colloids measured in August were recorded on a Thermo Nicolet 6700 FT-IR spectrometer using the FTIR-ATR mode. For the Transmission Electron Microscopy pictures about 2 wt% colloidal particle suspension was drop casted on a Formvar/Carbon 200 mesh Cu grids and allowed to dry overnight. The grids were then loaded into a JEOL JEM1400 Electron Microscope on single tilt holder. Images were captured at an acceleration voltage of 120kV. The optical microscope pictures were taken Nikon Eclipse E600 POL microscope. The optical microscope and TEM pictures were processed and analyzed using ImageJ to obtain the particle size distribution.

5.5.2. Synthesis

Synthesis of brominated colloidal initiators (CPs-Br). The brominated colloidal initiators were used from Van Ravensteijn and coworkers.[1] DLS measurements were performed to determine long time stability. The original diameter of the particles was 368 nm (PDI_{DLS} = 0.028) and the diameter after several years (~3-5) is 358 nm (PDI_{DLS} = 0.028) indicating that the suspension is stable.

Atom Transfer Radical Polymerization (ATRP) on CPs-Br: Synthesis of p(St)-g-p(HEA-co-GMA) colloids. 2-hydroxyethyl acrylate (HEA, 0.106 mL, 0.923 mmol) and copper(I) bromide (13.3 mg, 0.0927 mmol) were added to a dry Schlenk flask. A methanol:water mixture was added (0.5 mL, 7:3 v/v). The green suspension stirred for 1 h in air and afterwards the system was set under a nitrogen atmosphere. *N,N,N',N'',N''-*pentamethyldiethylenetriamine (PMDETA, 63.0 µL, 0.364 mmol) was injected into the suspension. Next, the CPs-Br suspension was suspended in a methanol:water mixture

(0.5 mL, 7:3 v/v) to reach a final solid content of 2 wt%. This mixture was set under a nitrogen atmosphere as well. Next, the colloidal suspension was injected into the monomer suspension under inert atmosphere and the resulting white/green suspension reacted at room temperature for 2 h. Meanwhile, glycidyl methacrylate (GMA, 0.132 mL, 0.994 mmol) was dissolved in methanol:water mixture (1.0 mL, 7:3 v/v) and added to the colloidal suspension after these 2 h. The resulting mixture reacted at room temperature overnight and the next morning the reaction was quenched by exposing the mixture to air. The resulting blue suspension was washed (centrifuged, decanted, resuspended) once with demi water, three times with methanol, three times with 50 mM aqueous $NaHCO_3$ solution and once with demi water. Finally, the solid particles were suspended in three drops of water to measure the IR and DLS spectra. Next, the water was removed by centrifugation and the particles were redispersed in DMF (0.5 mL). DLS showed a Z-average diameter of 678 nm and a PDI_{DLS} of 0.476 indicating that the colloids are agglomerating. The FTIR spectrum showed an epoxy peak at 907 cm^{-1} and an increase in intensity of the carbonyl peak (1732 cm^{-1}) (Supplementary Figure S5.1).

Ring opening of GMA with sodium azide: Synthesis of p(St)-g-p(HEA-co-GMA-N₃) colloids. Sodium azide (195 mg, 3.00 mmol) and ammonium chloride (162 mg, 3.03 mmol) were added to a Schlenk flask. The p(St)-*g*-p(HEA-*co*-GMA) particles were suspended in DMF (1 mL) and added to the Schlenk flask as well. The mixture reacted overnight at 70 °C, after which the suspension was cooled down to room temperature and the particles were washed three times with water. The DLS yielded a Z-average diameter of 1966 nm and a PDI_{DLS} of 0.847 indicating that the particles are significantly agglomerating. The FTIR spectrum showed an azide peak at 2100 cm^{-1}.

Synthesis of 1-(but-3-yn-1-yl)-3-carbamoylpyridin-1-ium bromide. This molecule was already synthesized during this research (Supplementary Information Chapter 4) and this batch was also used in this project.

Synthesis of 1-(but-3-yn-1-yl)-3-carbamoylpyridin-1-ium triflate. This molecule was already synthesized during this research (Supplementary Information Chapter 4) and this batch was also used in this project.

Click chemistry of the azide with the nicotinamide derivative: Synthesis of p(St)-g-p(HEA-co-GMA-N₃-mNAD⁺) colloids. Cu(PPh₃)₃Br (204 mg, 0.219 mmol), DIPEA (424 µL, 2.43 mmol) and product 1-(but-3-yn-1-yl)-3-carbamoylpyridin-1-ium triflate (507 mg, 1.56 mmol) were added to a Schlenk flask. Next, DMF (0.5 mL) and the azide functionalized colloid suspension (in 1.0 mL DMF, solid content is 1.0 wt%) were

added. The suspension was heated to 70°C, resulting in a change in color from brown/orange to brown/black. The next morning the mixture was cooled down to room temperature and the suspension was washed four times with DMF. The resulting particles had a brown color and were resuspended in DMF (0.5 mL, solid content = 3.7 wt%, measured gravimetrically). The final particles had a diameter of 713 ± 64 nm determined with transmission electron microscopy (TEM). The zeta-potential was +42 ± 0.7 mV when dispersed in water.
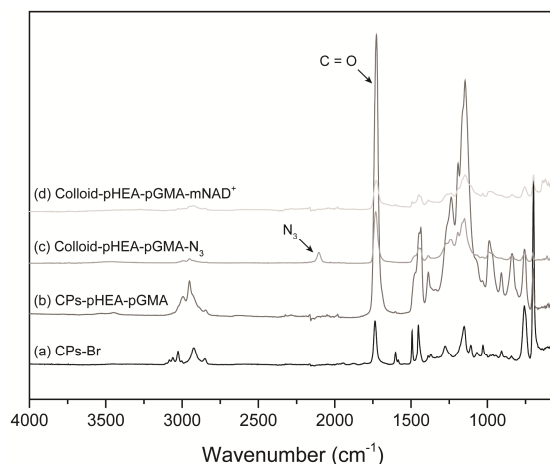
Figure S5.1. Infrared spectra of the products. From bottom to top: **(a)** Original CPs-Br colloids. **(b)** HEA and GMA polymerized colloids. **(c)** Azide functionalized colloids. **(d)** Final mNAD$^+$ functionalized colloids.
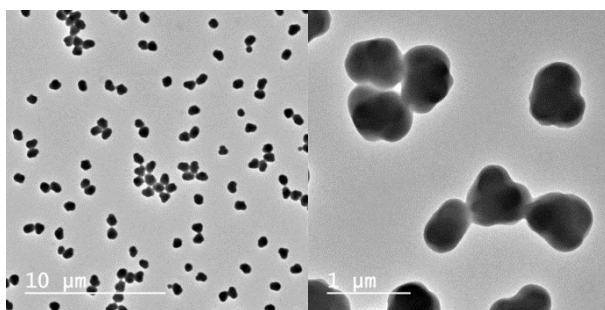
Figure S5.2. TEM pictures of the freshly synthesized mNAD$^+$-colloids.

Synthesis procedure of [Cp*Rh(bpy-OMe)Cl]Cl

The Rh-catalyst was synthesized according to literature procedures. 4-nitro-2,2'-bipyridine-1-oxide was formed from 2,2'-bipyridine.[2] Next, 4-nitro-2,2'-bipyridine-1-oxide is converted to 4-methoxy-2,2'-bipyridine-1-oxide and finally to 4-methoxy-2,2'-bipyridine.[3] Lastly, the [Cp*Rh(bpy-OMe)Cl]Cl (Rh-catalyst) is formed.[4]

5.5.3. Experimental agglomeration cycle

mNAD$^+$-colloids (0.02 wt%) and Rh-catalyst (1.0 mM) were dissolved in MOPS buffer (100 mM, pH 7.5) to reach a final volume of 1 mL. Agglomeration behavior was analyzed by optical microscopy. Next, the mixture was stirred at 750 rpm and 19.31 mg sodium formate (284 mM) was added. After 2 h optical microscopy pictures were again taken. The reaction was continued for 4 h and then an aqueous methylene blue solution (100 µL, 1.0 mM) was added to start the oxidation. The next morning, a sample was again analyzed by optical microscopy. The obtained images were analyzed with ImageJ. To calculate the area per agglomerate the images were threatened with the 'Threshold' function to distinguish between the colloids and the background.

### 5.5.4. Colloidal stability with increasing ionic strength
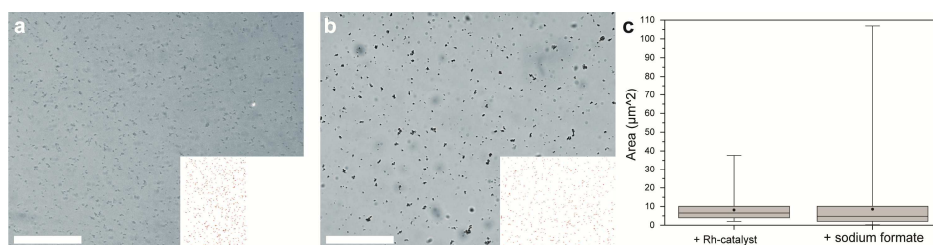
Figure S5.3. mNAD$^+$-colloidal stability in the presence of **(a)** Rh-catalyst and **(b)** sodium formate. **(c)** Box plots of the distribution of the agglomeration size upon addition of Rh-catalyst and sodium formate. Dot represents the average size. Scale bar is 50 µm.

5.5.5. Supplementary references

1. B. G. P. van Ravensteijn, M. Kamp, A. van Blaaderen and W. K. Kegel, *Chem. Mater.*, 2013, **25**, 4348-4353.
2. M. Zalas, B. Gierczyk, M. Cegłowski and G. Schroeder, *Chem. Pap.*, 2012, **66**, 733-740.
3. D. Wenkert and R. B. Woodward, *J. Org. Chem.*, 1983, **48**, 283-289.
4. F. Hollmann, B. Witholt and A. Schmid, *J. Mol. Catal. B Enzym.*, 2003, **19-20**, 167-176.

5
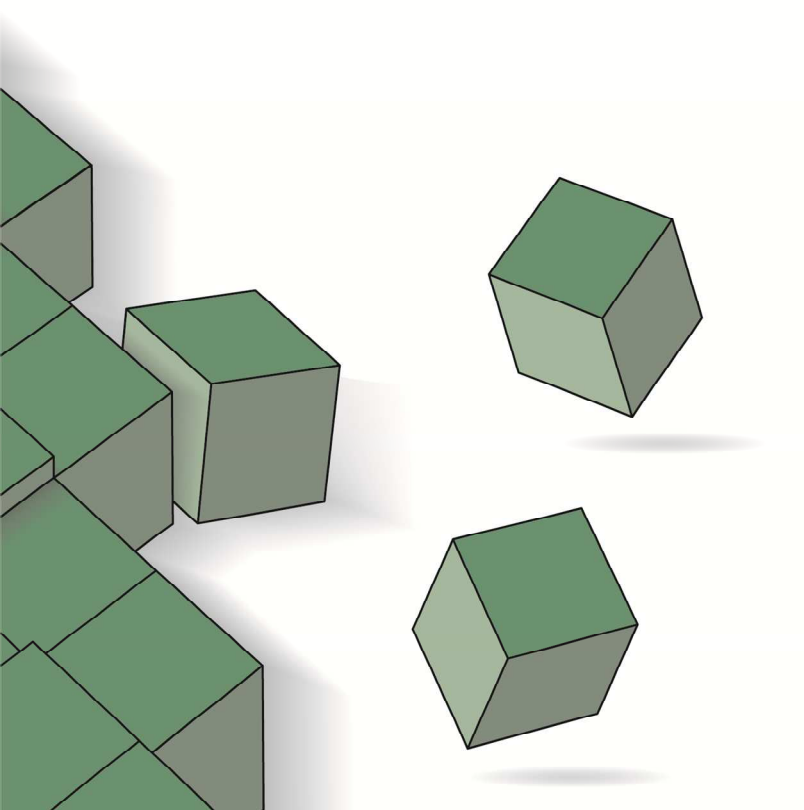
Chapter 6

Nicotinamide functionalized peptides for fuel-driven fiber formation

Control over the formation and degradation rate of out-of-equilibrium hydrogels is particularly appealing for tissue engineering and drug delivery. Therefore, these systems gained a lot of attention the last decade, however the kinetics of most transient hydrogels is only controlled by fuel and enzyme concentrations. To develop more complex systems in which we can more easily control the kinetics, we designed a hydrogel in which the kinetics can be controlled by two synthetic catalysts. Our results show that we can promote gelation by reduction of nicotinamide functionalized dipeptides under thermodynamic reaction control. However, due to difficulties in the kinetic analysis of hydrogel formation we are not yet able to quantify the fiber formation under out-of-equilibrium conditions. Nevertheless, we believe that we are able to make a transient supramolecular fiber system, if a suitable analysis technique is established to quantify the kinetics of fiber growth and shrinkage. The most promising technique is a home-built dynamic light scattering setup which is already used before in literature. When this system is successful it brings us one step closer to catalytic control over transient fiber formation.

6.1. Introduction

Switchable hydrogels are recently extensively researched by many research groups, because of their applications in tissue engineering, drug delivery and as sensors.[1] Moreover, the versatility of triggers, such as pH, temperature and chemical stimuli, make these switchable hydrogels even more attractive. However, these hydrogels also have some disadvantages. For example, each time a change in hydrogel structure is desired, manual addition of a trigger is required. Out-of-equilibrium hydrogels which are activated by the addition of a fuel and spontaneously collapse over time overcomes this disadvantage. This makes out-of-equilibrium hydrogels more applicable for transient tissue engineering or drug delivery as the hydrogel collapses spontaneously in the body without any help from outside. Some out-of-equilibrium hydrogels have been successfully designed in recent years. However, only three research groups made transient supramolecular fibers in which the growth and shrinkage kinetics are controlled by catalysts working on both the activation and deactivation pathways in the chemical reaction network.[2-5] Including catalysis in these out-of-equilibrium systems increases their operation range. Regulating the kinetics by variation in fuel concentration can change the environment significantly, which can be a major drawback.[6] Using catalysis to control the kinetics is an interesting option, because the small catalyst concentration will not influence the system substantially. Moreover, catalysis facilitates the route towards more complex behavior such as spatio-temporal control and feedback loops. The catalysts currently used in literature are enzymes, which apart from their advantages have also the disadvantage of a fairly limited range of possible operating conditions.[3-5, 7] Using synthetic organic or organometallic catalysis instead of using enzymes would expand the range of suitable system conditions significantly for designing out-of-equilibrium systems.

In this research, we developed two peptide-based hydrogels which show great potential to form out-of-equilibrium fibers with two synthetic catalysts in the chemical reaction network (CRN). The CRN of this system is based on the redox chemistry of nicotinamide resulting in a switch in polarity during reduction of the nicotinamide groups. In the previous chapters we connected the nicotinamide-based CRN to many assembled structures. Here, we extend this research by creating nicotinamide-based hydrogels and supramolecular fibers. We are able to induce gelation by reducing nicotinamide functionalized diphenylalanine or isoleucine-leucine methyl ester molecules. These hydrogels were used to investigate out-of-equilibrium formation of supramolecular fibers. However due to a lack in techniques for quantitative analysis of these fibers we are not yet able to investigate the kinetics or fiber growth and shrinkage. We believe that after finding an appropriate analysis technique, we are able

to make and analyze an out-of-equilibrium fiber system in which the kinetics can be controlled by the concentration of two catalysts and a fuel.

6.2. Results and discussion

The goal of this research is to design a molecule which is soluble in its chemical equilibrium, but upon activation with a fuel to a transient out-of-equilibrium state, it gelates. Nicotinamide functionalized molecules are promising for this purpose as nicotinamide functionalized molecules have a positive charge and are therefore most likely soluble in aqueous media, while upon removing the charge by reduction a more hydrophobic molecule is formed. When attractive and repulsive interactions between gelator molecules and solvent are nicely balanced, and the direction of these interactions is controlled, the molecule functions as a gelator resulting in gelation at high concentrations.[8]

Promising nicotinamide functionalized hydrogelators are small peptides functionalized with reduced nicotinamide, as already a lot of research is done on small peptide hydrogelators.[8] Most researched dipeptide hydrogelators are based on amino acid phenylalanine,[9] therefore we synthesized nicotinamide functionalized L-diphenylalanine **1a** (Figure 6.1 and Supplementary Figures S6.1-S6.9). The positive charge of the molecule prevents gelation of **1a** while a decrease in polarity and repulsion of the molecule during the reduction to 1,4-dihydronicotinamide-diphenylalanine **1b** (Figure 6.1) results in gelation. Moreover, Tomasz Piskorz did some unpublished coarse-grained modeling based on the work of Frederix and coworkers to determine which dipeptides are suitable for gelation.[10] He screened all reduced nicotinamide functionalized dipeptide molecules for their gelation properties. The results showed that **1b** is indeed promising for gelation. However, the coarse-grained model has its limitations and cannot give definitive prediction of gelation candidates, because the model decreases the resolution of the molecule. Nonetheless, this model eliminates already many dipeptides that are unsuitable for gelation and thus decreases the synthetic effort significantly. Another interesting structure found with the coarse-grained model is nicotinamide functionalized L-isoleucine-L-leucine as the reduced state shows promising properties for gelation. However, due to synthetic constraints we were only able to synthesize the methyl ester of nicotinamide functionalized L-isoleucine-L-leucine **2a** (Figure 6.1 and Supplementary Figures S6.10-S6.15). Alternative potential gelator molecules that could be investigated in the future are reduced nicotinamide functionalized L-phenylalanine-L-tryptophan, L-proline-L-tryptophan, and L-tyrosine-L-tyrosine. To conclude, coarse-grained modeling provides a facile method for identification of potential nicotinamide derived gelators. The model selects the

6
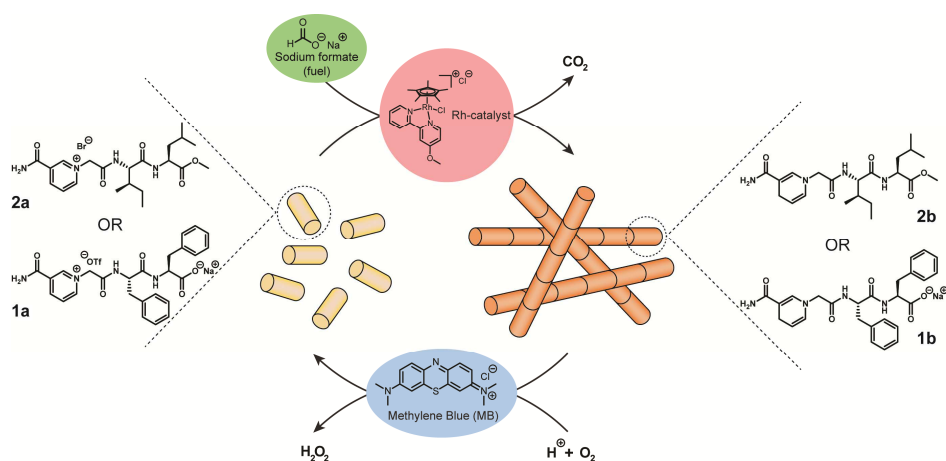
Figure 6.1. Schematic overview of the out-of-equilibrium fibrous system. Nicotinamide functionalized with L-diphenylalanine (**1a**) or functionalized with L-isoleucine-L-leucine methyl ester (**2a**) are used as inactive gelators. Reduction of nicotinamide with sodium formate and a Rh-catalyst is forming active gelators (**1a**, **2b**) resulting in the growth of fibers. These fibers are only transiently present as methylene blue is gradually oxidizing the reduced nicotinamides leading to a soluble oxidized nicotinamide state.

best hydrogelators resulting in a significant decline in synthetic effort.

Gelators **1b** and **2b** are used in the nicotinamide-based CRN (Figure 6.1). Soluble nicotinamide functionalized dipeptides (**1a**, **2a**) are reduced with sodium formate as fuel, catalyzed by [Cp*Rh(bpy-OMe)Cl]Cl (Rh-catalyst).[11] The reduced nicotinamide gelators form supramolecular fibers and/or a hydrogel. Since methylene blue is also present in solution the reduced nicotinamide molecules are in an unstable state and they oxidize slowly to nicotinamide with molecular oxygen.[12] This oxidation will lead to the shrinkage of the supramolecular fibers and the hydrogel collapse, resulting in a homogeneous solution over time. By varying the reduction and oxidation rate in the nicotinamide-based CRN with the catalyst and fuel concentrations we should be able to control the kinetics of growth and shrinkage of the fibers.

6.2.1. Hydrogel and fiber structure

First, both oxidized state and reduced state of **1** and **2** are investigated to determine whether these molecules are suitable for induced gelation. Both **1a** and **2a** are soluble at a concentration of 30 mM (1.9 wt%) and 40 mM (2.0 wt%), respectively (Figures 6.2a and 6.2f). Increasing the concentration of **1a** to 80 mM (4.0 wt%) will result in the formation of a turbid white gel (4.0 wt%) (Figure 6.2b). Thus for this research, a concentration lower than 80 mM is required to investigate a gelation switch. When
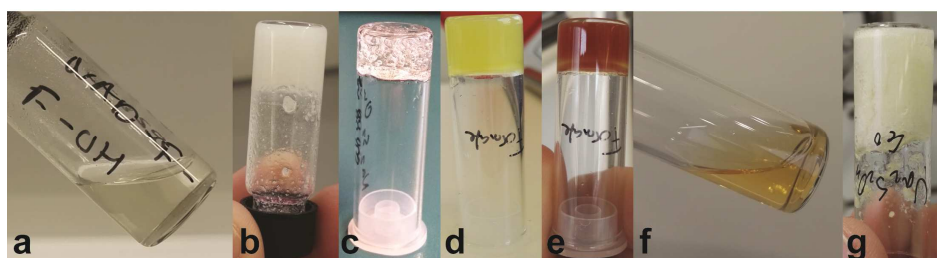
Figure 6.2. Physical states of the investigated nicotinamide functionalized peptides. **(a)** 40 mM **1a** is soluble in MOPS buffer (100 mM, pH 7.5). **(b)** 80 mM **1a** forms a turbid white hydrogel in MOPS buffer. **(c)** Reduction of 40 mM **1a** to **1b** with sodium dithionite (160 mM) leads to a colorless, transparent hydrogel with many bubbles. **(d)** Reduction of 30 mM **1a** with sodium formate (500 mM) and Rh-catalyst (3.0 mM) leads to formation of a homogenous, yellow and turbid hydrogel. **(e)** About 2 h after gelation the gel becomes dark orange in color. **(f)** 40 mM **2a** is soluble in MOPS buffer. **(g)** Reduction of 40 mM **2a** to **2b** with sodium dithionite (100 mM) leads to formation of an off-white turbid hydrogel.

sodium dithionite reduces **1a** or **2a** hydrogelation occurs. A hydrogel made from 20 mM (0.8 wt%) **2b** forms an off-white gel which is heterogeneous in turbidity (Figure 6.2g). Reduction of **1a** to **1b** at a concentration of 40 mM (1.9 wt%) forms a colorless transparent hydrogel containing many bubbles. The bubbles most likely contain carbon dioxide and sulfur dioxide from the reduction with sodium dithionite (Figure 6.2c) which are released during reduction of **1a**. Since gelator **1b** forms a much more homogeneous and transparent hydrogel than gelator **2b**, we decided to investigate this gelator in the CRN of nicotinamide.

The critical gelation concentration of **1b** is between 10 and 20 mM (0.5 wt% and 1.0 wt%, respectively) (Supplementary Figure S6.23) thus the gelation experiments were performed at a concentration of 30 mM (1.4 wt%). In a typical experiment 30 mM **1a** is dissolved in MOPS buffer (100 mM, pH 7.5). The reduction was performed with 3.0 mM Rh-catalyst and 500 mM sodium formate. After about 1.5 h the vial was inverted and a yellow homogenous turbid hydrogel was formed (Figure 6.2d). The yellow color is caused by the Rh-catalyst. In 2 h the color of the hydrogel changed from yellow to dark orange, most likely caused by the anaerobic environment and subsequent transition of the Rh-catalyst (Figure 6.2e). Degradation of **1b** by an acid catalyzed reaction with water results in destruction over the gel overnight (Chapter 3). Strikingly, a large different between the two hydrogels made of **1b** is observed (Figures 6.2cd) even though the same concentration of **1a** is used. Reduction of **1a** with sodium dithionite results in the formation of a transparent gel, while reduction with sodium formate leads to a turbid gel. It is known that hydrogel structures depend on the

kinetic pathway during hydrogel formation and that may also be at the origin of what we observe here.[13]

The fibrous structure is further analyzed with confocal laser scanning microscopy (CLSM) and high resolution transmission electron cryomicroscopy (HR CryoTEM). Bleaching experiments after incorporation of the dye coumarin 1 confirms gelation (Figures 6.3ab). Moreover, the individual fibers or bundles are not visible indicating that the individual fibers and bundles are smaller than the resolution of the microscope. Therefore, HR CryoTEM measurements were performed which showed very thin and long fibers (Figures 6.3d,e). The length of the fibers could not be measured as they exceed the image borders showing that the fibers are in the order of micrometers long. Furthermore, the fibers have a highly uniform diameter of 3.0 ± 0.34 nm and they form bundles from 1 to 14 fibers in thickness. As the molecular size
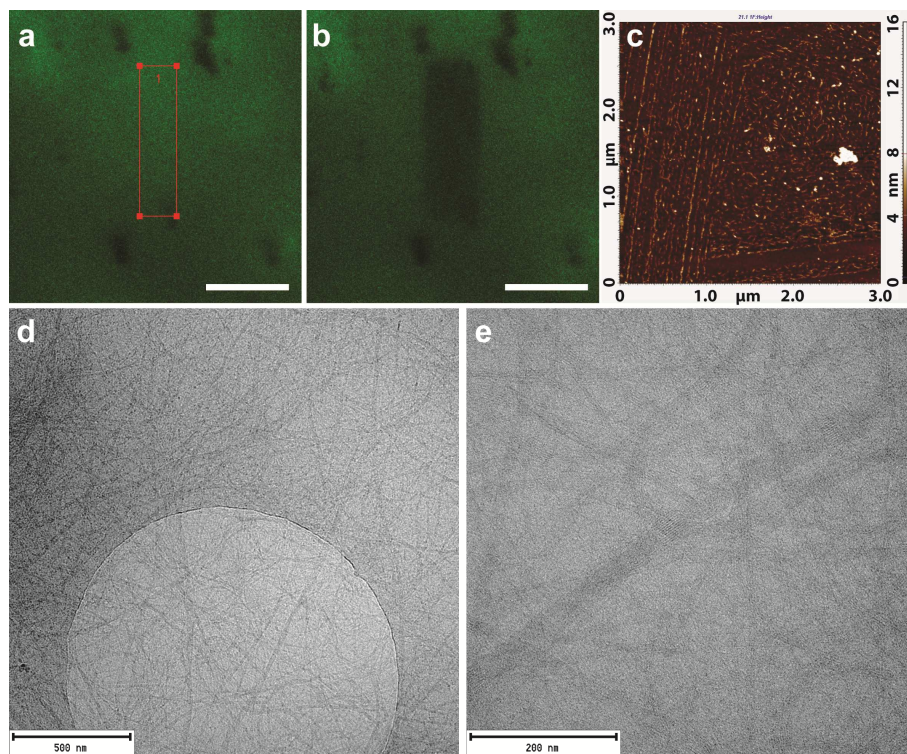

Figure 6.3. Detailed fiber analysis of the hydrogel and stirred fiber solution with **1b** as gelator. **(a)** Fluorescence image of the hydrogel stained with coumarin 1, the red box indicating the area that will be bleached. Scale bar is 20 μm. **(b)** Fluorescence image of the hydrogel just after bleaching within the square box. Scale bar is 20 μm. **(c)** AFM images of the stirred supramolecular fibrous mixture after diluting the sample 100 times. **(d,e)** HR CryoTEM images of the hydrogel showing bundles of extremely long thin fibers.

of **1a** is 1.66 nm in length, the most reasonable molecular orientation would be four fibers in a plane with the hydrophobic parts directed inside and the carboxylate groups directed towards to water. Deviation in molecular size in the fiber compared to the individual molecule could be caused by the interactions with water and other gelator molecules resulting in a rotation of functional groups.

The objective was to obtain a transient hydrogel by re-oxidizing the reduced nicotinamide molecule using molecular oxygen, catalyzed by methylene blue. However, diffusion of molecular oxygen into the hydrogel was too slow to obtain a hydrogel in which its lifetime was dependent on the methylene blue concentration. Therefore, it was decided to not form a transient hydrogel, but to form transient fibers in a stirred solution. Reduction of **1a** showed formation of fibers in a stirred solution (750 rpm) and they were analyzed by Atomic Force Microscopy (AFM) (Figure 6.3c). They showed long, thin fibers with a diameter of 5-6 nm which are most likely bundles formed from the fibers.

6.2.2. Surfactant behavior

Except for forming hydrogels some of these nicotinamide-based peptides also lower the surface tension between water and air, especially in the reduced state. These could be used to transiently changing surface tension by controlling the kinetics of the redox cycle. Moreover, the different nicotinamide-based peptides have different decreases in surface tension. Thus by choosing a specific peptide a distinct surface tension decrease can be obtained. For example, attaching a glycine amino acid to nicotinamide does not create a surfactant (Supplementary Figure S6.25). While linking phenyl alanine to the nicotinamide shows a slight decrease in surface tension to 67 mN at 30 mM when in the oxidized state (**3a**) (Figure 6.4b). Reducing **3a** to **3b** decreases the surface tension even more to 59 mN/m at 23 mM. The surface tension could be even further decreased by using surfactants **1a** or **1b**. Although the surface tension of both states is identical it is decreased significantly within the first 5 mM and then levels off

6
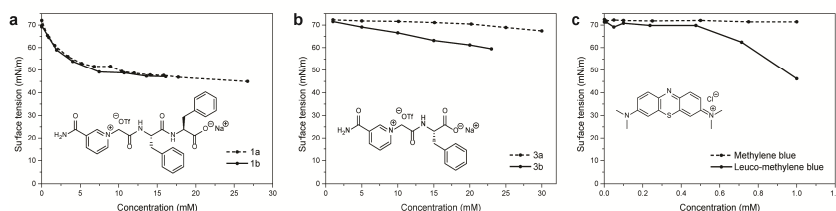
Figure 6.4. Surfactant behavior of several redox components. **(a)** Surface tension of **1a** and **1b**. **(b)** Surface tension of **3a** and **3b**. **(c)** Surface tension of methylene blue and its reduced state leuco-methylene blue.

to a surface tension of 45 mN/m (Figure 6.4a). As a comparison the well-known surfactant sodium dodecyl sulfate (SDS) has a surface tension of ∼35 mN/m at 8 mM.[14]

The next step is to use these surfactants to create a transient decrease in surface tension using the CRN of nicotinamide. Surfactants **1a** and **1b** have exactly the same surface tension, thus these cannot be used, but **3a** and **3b** have a difference and are thus suitable. Investigating a transient decrease in surface tension upon reduction of the nicotinamide-based surfactants turned out to be more complex than expected. Because not only these nicotinamide-based peptides behave as surfactant, but the leuco-methylene blue (MBH) as well. Reduction of methylene blue results in a decrease in surface tension to 46 mN/m at 1.0 mM (Figure 6.4c). The other components, such as the Rh-catalyst and sodium formate, do not show surfactant behavior (Supplementary Figure S6.26). In the future it might be possible to use a different oxidation catalyst that does not behave as a surfactant, resulting in the pure transient surfactant behavior of the nicotinamide functionalized peptides. Moreover, the surfactant properties of **2a** and **2b** and other peptides should also be investigated in the future. All-atomistic models of these molecules may give predictive insight in their surfactant properties to decrease the synthetic effort.[15]

6.2.3. Kinetics of fiber formation

The next step is to investigate the kinetics of the fiber growth and its subsequent shrinkage. Unfortunately, after considering and measuring the fiber kinetics with many analysis techniques we were not able to find a suitable technique which we could use.

Gelation followed by Dynamic Light Scattering (DLS) showed a gradual increase in scattering intensity from 1342 kcps to 3384 kcps in 1 h corresponding to the formation of turbid hydrogels (Figure 6.5a). Moreover, the size of the particles (*Z*-average) increases as the fibers grow (481 nm to 2236 nm) (Figure 6.5b). Still, the absolute particle size values are not particularly reliable as the software assumes that the particles are spherical and monodisperse. However, the relative increase gives a good indication for fiber growth over time.

Analysis of the stirred fiber mixture by DLS did not show a clear trend over time (Figures 6.5ab). The heterogeneousness in size and shape during fiber growth is most likely the cause of this deviation. Similar unreliable results are found for measuring scattering intensity by UV-vis spectroscopy (Supplementary Figure S6.24). Thus DLS and UV-vis measurements are not suitable for investigating the kinetics of fiber growth and shrinkage. A more extended DLS that can measure non-spherical and heterogeneous particles can be used to follow the kinetics of fiber growth and shrinkage. This home-built light scattering setup is already used in literature to follow
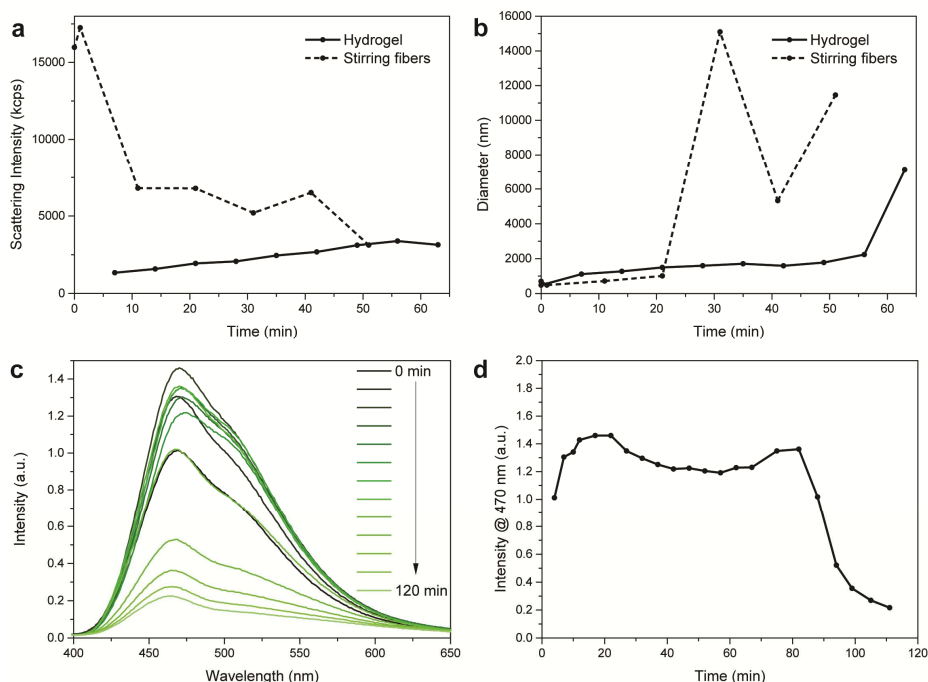
Figure 6.5. Quantitative analysis of the hydrogel and fiber formation. **(a)** Scattering intensity during the gelation (solid line) and during the growth of fibers upon stirring (dashed line). **(b)** Size (*Z*-average) during the gelation (solid line) and during the growth of fibers upon stirring (dashed line). **(c)** Fluorescence intensity during reduction of **1a** to **1b** with the Rh-catalyst and sodium formate resulting in gelation. **(d)** Fluorescence intensity of the sample at 470 nm measured over time.

kinetics of fiber growth and shrinkage under stirring conditions.[2, 16] Thus this technique is our next recommendation to follow the fiber growth kinetics.

Another analysis technique often used to follow kinetics of fiber growth is fluorescence spectroscopy.[17-20] The fluorescence of specific dyes change upon incorporation into fibers due to a change in local polarity or rotational hindrance.[21] However, **1a** is already highly fluorescent and this fluorescence dominates over fluorescence of the dye. Moreover, finding a suitable dye is already difficult as most dyes interfere with the **1a/1b** CRN. Therefore, using a dye to analyze fiber growth is not suitable in this system. The fluorescence of **1a** itself could also not be used as its fluorescence changes upon reduction and upon fiber formation resulting in the observation of multiple phenomena in fluorescence spectroscopy (Figures 6.5cd).

Fiber growth and shrinkage can also be analyzed by circular dichroism (CD) when a chiral gelator is present.[2, 5, 19] However, as a high concentration of **1a** is required the

CD and absorption signal becomes saturated and this technique becomes unsuitable. Using a thin (0.1 mm) cuvette to increase the maximum possible concentration 10 times (20 mM) might solve the problem, but it may lead to linear alignment of the fibers due to confinement within the cuvette. This confinement can result in preferential growth of fibers in one direction and an increase in linear dichroism. Due to these restrictions, CD has not been attempted for analysis of the current system.

Other analysis techniques which we considered are CLSM, AFM, CryoTEM, Scanning Electron Microscopy (SEM), Transmission Electron Microscopy (TEM), Infrared Spectroscopy (FT-IR) and DOSY-NMR, but all have their own limitations. For example, the resolution of CLSM and SEM are not high enough to observe the fibers or bundles. AFM, CryoTEM and DOSY-NMR are not suitable to measure fiber formation/decay over time, because of spatial or time limitations. TEM destroys the sample during drying or imaging, while IR spectroscopy is unsuitable as water vibrations are dominant over hydrogen bond vibrations. Therefore, most of these techniques are only suitable as complementary analysis technique, while a main analysis technique is first required.

Overall, kinetic analysis of the fiber growth is challenging because of the high gelator concentration, the fluorescence limitations and the heterogeneous fiber growth.

6.3. Conclusions

We show here the successful design of a fuel activated hydrogel by combining the redox chemistry of nicotinamide with the gelation properties of specific dipeptides. The hydrogel consists of long fibers with a diameter of 3.0 nm, and some of these fibers form bundles. Quantitative analysis of supramolecular fiber growth in the fuel-driven nicotinamide-based chemical reaction network is not successful yet due to the heterogeneous growth of fibers and problems with fluorescence. Nevertheless, we believe using more specialized analysis equipment (like a home-built scattering setup) may solve this problem. When this problem is overcome the system shows high potential for formation of out-of-equilibrium fibers as both the structure and kinetics of the fiber growth and shrinkage can be easily varied by the dipeptide molecule and catalyst concentrations, respectively. Successful design of this system will lead us one step closer to more complex bioinspired fibers as biological fibrous structures are constantly formed and broken down depending on the presence of fuel and the activity of involved catalysts.

6.4. References

1.   X. Du, J. Zhou, J. Shi and B. Xu, *Chem. Rev.*, 2015, **115**, 13165-13307.
2.   A. Sorrenti, J. Leira-Iglesias, A. J. Markvoort, T. F. A. de Greef and T. M. Hermans, *Chem. Soc. Rev.*, 2017, **46**, 5476-5490.
3.   S. Dhiman, A. Jain, M. Kumar and S. J. George, *J. Am. Chem. Soc.*, 2017, **139**, 16568-16575.
4.   L. Heinen, T. Heuser, A. Steinschulte and A. Walther, *Nano Lett.*, 2017, **17**, 4989-4995.
5.   S. Dhiman, A. Jain and S. J. George, *Angew. Chem. Int. Ed.*, 2016, **55**, 1-6.
6.   B. G. P. van Ravensteijn, W. E. Hendriksen, R. Eelkema, J. H. van Esch and W. K. Kegel, *J. Am. Chem. Soc.*, 2017, **139**, 9763-9766.
7.   A. Sorrenti, J. Leira-Iglesias, A. Sato and T. M. Hermans, *Nat. Commun.*, 2017, **8**, 15899.
8.   S. Fleming and R. V. Ulijn, *Chem. Soc. Rev.*, 2014, **43**, 8150-8177.
9.   T. Das, M. Häring, D. Haldar and D. D. Díaz, *Biomater. Sci.*, 2018, **6**, 38-59.
10.   P. W. J. M. Frederix, G. G. Scott, Y. M. Abul-Haija, D. Kalafatovic, C. G. Pappas, N. Javid, N. T. Hunt, R. V. Ulijn and T. Tuttle, *Nat. Chem.*, 2015, **7**, 30-37.
11.   F. Hollmann, B. Witholt and A. Schmid, *J. Mol. Catal. B Enzym.*, 2003, **19-20**, 167-176.
12.   P. Sevcik and H. B. Dunford, *J. Phys. Chem.*, 1991, **95**, 2411-2415.
13.   J. Boekhoven, J. M. Poolman, C. Maity, F. Li, L. van der Mee, C. B. Minkenberg, E. Mendes, J. H. van Esch and R. Eelkema, *Nat. Chem.*, 2013, **5**, 433-437.
14.   J. Zhang and Y. Meng, *Tribol. Lett.*, 2014, **56**, 543-552.
15.   A. Jusufi, *Mol. Phys.*, 2013, **111**, 3182-3192.
16.   J. Leira-Iglesias, A. Sorrenti, A. Sato, P. A. Dunne and T. M. Hermans, *Chem. Commun.*, 2016, **52**, 9009-9012.
17.   J. Boekhoven, W. E. Hendriksen, G. J. M. Koper, R. Eelkema and J. H. van Esch, *Science*, 2015, **349**, 1075-1079.
18.   M. Tena-Solsona, B. Rieß, R. K. Grötsch, F. C. Löhrer, C. Wanzke, B. Käsdorf, A. R. Bausch, P. Müller-Buschbaum, O. Lieleg and J. Boekhoven, *Nat. Commun.*, 2017, **8**, 15895.
19.   S. Debnath, S. Roy and R. V. Ulijn, *J. Am. Chem. Soc.*, 2013, **135**, 16789-16792.
20.   C. A. Angulo-Pachón and J. F. Miravet, *Chem. Commun.*, 2016, **52**, 5398-5401.
21.   A. S. Klymchenko, *Acc. Chem. Res.*, 2017, **50**, 366-375.

6.5. Supplementary information

6.5.1. Methods

NMR measurements were performed on an Agilent-400 MR DD2 (399.7 MHz for ^{1}H, 100.5 MHz for ^{13}C) at 298 K using residual protonated solvent signals as internal standard. Mass spectra (MS) were recorded on a Shimadzu LCMS-2010 by electrospray ionization in positive and negative mode (ESI+ and ESI-). Dynamic Light Spectroscopy (DLS) data were obtained on a Malvern Instruments Zetasizer Nano ZS in a 4 mL quartz cuvette. UV-vis spectroscopic measurements were performed on a Shimadzu UV-1800 spectrophotometer; quartz cuvettes with a path length of 0.1 cm were used. Confocal laser scanning microscopy (CLSM) measurements were performed on the Zeiss LSM 710 with a x40 oil immersion objective. For the AFM measurement the sample is diluted 100x and the measurement was performed on a NTMDT Ntegra AFM system in tapping mode. Fluorescence microscopy measurements were performed on a Jasco J-815 CD spectrometer using an excitation wavelength of 375 nm. For the CryoTEM measurements plasma treated Quantifoil™ R 1.2/1.3 Cu 200 grids were dipped inside the hydrogel sample for five seconds and loaded into a Leica Vitribot. The grids were then blotted in a humidity controlled chamber (RH-95%, T = 20°C) for three seconds and plunged into liquid ethane (maintained at -185°C) to achieve sample vitrification. The grid was then transferred to a holder docking station from where it was further loaded into the JEOL JEM3200-FSC Cryo-Electron Microscope. Images were recorded at an acceleration voltage of 300 kV at low dosage conditions to prevent destruction of the sample. The recorded images were analyzed using commercial image analysis software (ImageJ) to estimate fiber diameters.

6.5.2. Materials

All compounds and solvents were used without further purification. The technical solvents were purchased from VWR and the reaction solvents were purchased from Sigma-Aldrich. All other chemicals were bought from Sigma-Aldrich with the exception of coumarin 1 (TCI Chemicals), di-L-phenylalanine (Activate Scientific), barium carbonate (Alfa Aesar), sodium iodide (ABCR), silver triflate (Fluorochem), Boc-Ile-OH (Bide Pharmatech), hydroxybenzotriazole (Acros Organics) and MOPS (Alfa Aesar).
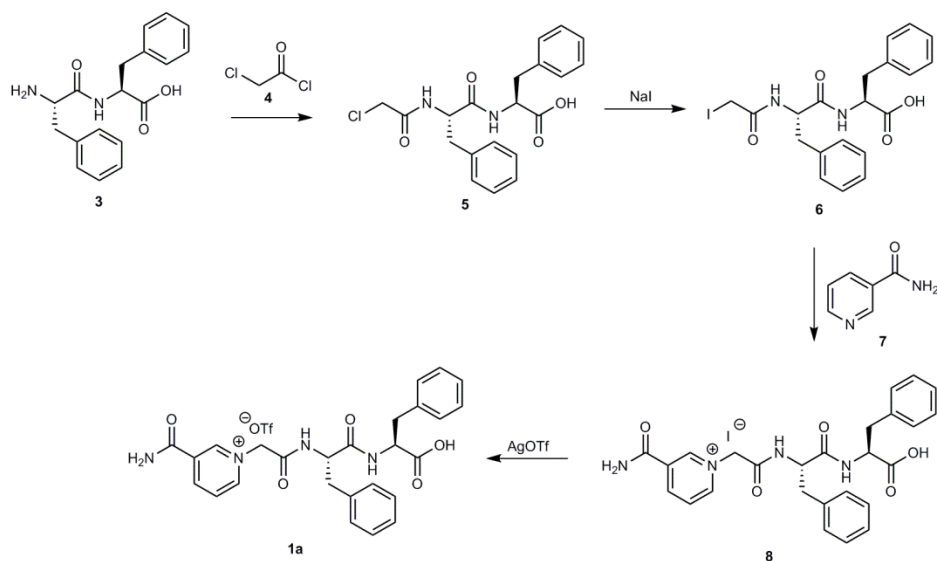
6.5.3. Synthesis

Synthesis procedure of 1a

Figure S6.1. Synthesis route to **1a**.

(2-Chloroacetyl)diphenylalanine 5. Di-L-phenylalanine **3** (5.00 g, 16.0 mmol) was suspended in acetonitrile (100 mL). Chloroacetyl chloride **4** (4.00 mL, 50.3 mmol) was added dropwise to the suspension. The suspension reacted at room temperature overnight. The solvent was evaporated and the solid residue was resuspended in 1 M HCl (125 mL) and the mixture was stirred at room temperature for 1 h. The suspension was filtrated and the solid residue is product **5**, obtained as a white solid (3.00 g, 48%). To increase the yield, the solvent from the filtrate was evaporated and the residue was redissolved in ethanol (150 mL). $BaCO_3$ (2.00 g, 10.1 mmol) was added to deprotonate the residual H_3N^+-PhePhe-OH. The suspension was stirred at room temperature for 1 h and the solid was filtrated. The same procedure as described above was applied to react the residue (H$_2$N-PhePhe-OH) with chloroacetyl chloride resulting in product **5** with a second yield of 1.40 g, 23%. Thus in total product **5** was obtained as a white solid with a final yield of 4.40 g, 71%. M.p. 212 °C (decomposition). ^{1}H-NMR (399.7 MHz, CD$_3$OD, ppm): δ 7.20 (m, 10H, Ar*H*), 4.64 (m, 2H, C*H*), 3.94 (d, 2H, ClC*H*2), 3.18 (m, 1H, C*H*2), 3.09 (m, 1H, C*H*2), 3.00 (m, 1H, C*H*2) 2.88 (m, 1H, C*H*2). ^{13}C-NMR (100.5 MHz, CD$_3$OD, ppm): δ 171.3 (*C*=O), 167.3 (*C*=O), 136.8 (*C*=O), 136.6 (*C*$_{Ar}$), 128.9 (*C*$_{Ar}$),

128.0 (C_{Ar}), 126.4 (C_{Ar}), 54.5 (*CH*), 53.7 (*CH*), 41.5 (Cl*CH₂*), 37.0 (*CH₂*), 29.2 (*CH₂*). MS (ESI Neg.) m/z: 387.15 [(M⁻)] (expected m/z = 387.12).
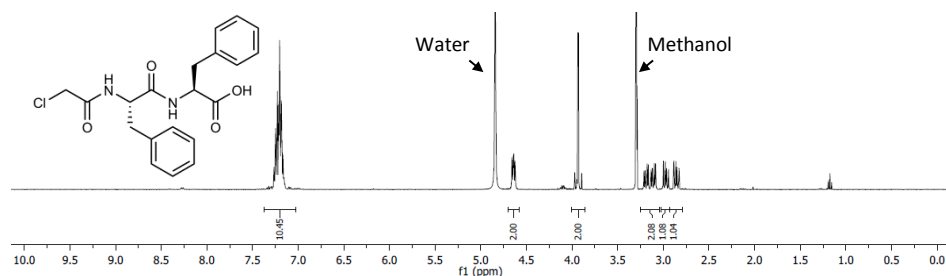

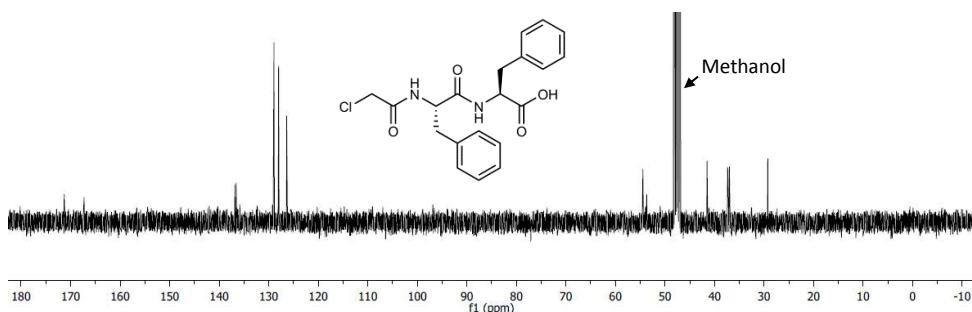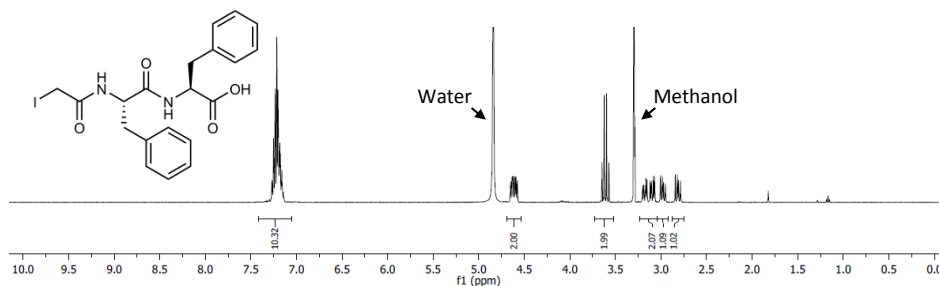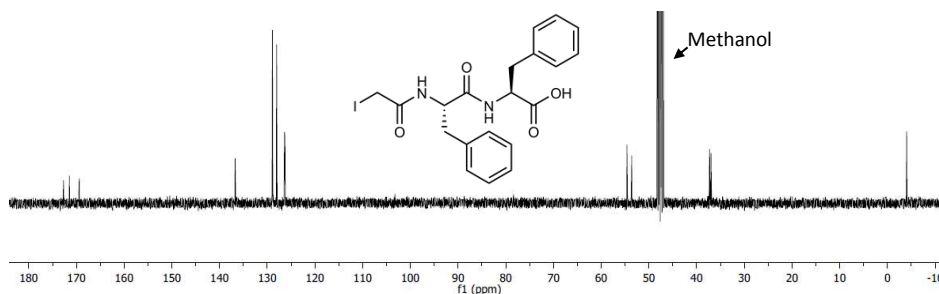**Figure S6.2.** ^{1}H-NMR (CD₃OD) of **5**.

Figure S6.3. ^{13}C-NMR (CD₃OD) of **5**.

(2Iodoacetyl)diphenylalanine 6. Product **5** (4.40 g, 11.3 mmol) was suspended in acetone (120 mL) and methanol (80 mL). Sodium iodide (17.0 g, 0.113 mol) was added and the mixture reaction overnight at 50 °C. The solvent was evaporated and the solid residue was suspended in 1 M HCl (400 mL). The ultrasonic bath was used to grind the big chunks. The suspension was filtered and the residue was dried under vacuum at 55 °C overnight. The residual HCl was removed by dissolving the solid residue in ethanol (250 mL). BaCO₃ (4.20 g, 21.3 mmol) was added and the suspension was stirred at room temperature for 1 h and was filtrated. The solvent from the filtrated was evaporated and the residue was dried under vacuum at 40 °C. Product **6** was obtained as an orange powder (5.00 g, 89%). M.p. 179 °C (decomposition). ^{1}H-NMR (399.7 MHz, CD₃OD, ppm): δ 7.22 (m, 10H, Ar*H*), 4.61 (m, 2H, C*H*), 3.63 (q, 2H, IC*H2*), 3.17 (m, 1H, C*H2*), 3.07 (m, 1H, C*H2*), 2.99 (m, 1H, C*H2*) 2.84 (m, 1H, C*H2*). ^{13}C-NMR (100.5 MHz,

CD$_3$OD, ppm): δ 172.7 (*C*=O), 171.5 (*C*=O), 169.4 (*C*=O), 136.7 (*C*$_{Ar}$), 129.0 (*C*$_{Ar}$), 128.0 (*C*$_{Ar}$), 126.3 (*C*$_{Ar}$), 54.6 (*C*H), 53.6 (*C*H), 37.3 (*C*H$_2$), 37.0 (*C*H$_2$), -4.0 (I*C*H$_2$). MS (ESI Neg.) m/z: 479.05 [(M$^-$)] (expected m/z = 479.05).

Figure S6.4. ^{1}H-NMR (CD$_3$OD) of **6**.

Figure S6.5. ^{13}C-NMR (CD$_3$OD) of **6**.

mNAD$^+$-Phe-Phe-OH I$^-$, product 8. Product **6** (5.00 g, 10.4 mmol) was dissolved in DMF (200 mL). Nicotinamide **7** (1.10 g, 9.20 mmol) was added and the mixture reacted for 3 days at 70 °C. The solvent was evaporated and the residue was suspended in 2-butanone and filtrated afterwards. The solid residue was then dissolved in methanol and precipitated with diethyl ether. The mixture was filtrated and product **8** was obtained as a yellow/orange solid (4.10 g, 66%). M.p. 130 °C. ^{1}H-NMR (399.7 MHz, CD$_3$OD, ppm): δ 9.22 (s, 1H, Ar*H*), 9.00 (d, 1H, Ar*H*), 8.85 (d, 1H, Ar*H*), 8.19 (t, 1H, Ar*H*), 7.19 (m, 10H, Ar*H*), 5.39 (q, 2H, NC*H*2), 4.63 (m, 2H, C*H*), 3.18 (m, 2H, C*H*2), 2.99 (m, 1H, C*H*2) 2.88 (m, 1H, C*H*2). ^{13}C-NMR (100.5 MHz, CD$_3$OD, ppm): δ 173.0 (*C*=O), 171.6 (*C*=O), 164.0 (*C*=O), 163.5 (*C*=O), 147.6 (*C*$_{Ar}$), 146.1 (*C*$_{Ar}$), 144.1 (*C*$_{Ar}$), 136.9 (*C*$_{Ar}$), 136.7 (*C*$_{Ar}$), 134.0 (*C*$_{Ar}$), 128.9 (*C*$_{Ar}$), 128.1 (*C*$_{Ar}$), 128.0 (*C*$_{Ar}$), 127.3 (*C*$_{Ar}$), 126.5 (*C*$_{Ar}$), 126.3 (*C*$_{Ar}$),

61.7 (NCH$_2$), 55.1 (CH), 53.9 (CH), 37.7 (CH$_2$), 37.0 (ClCH$_2$). MS (ESI Pos.) m/z: 475.10 [(M$^+$)] (expected m/z = 475.20).
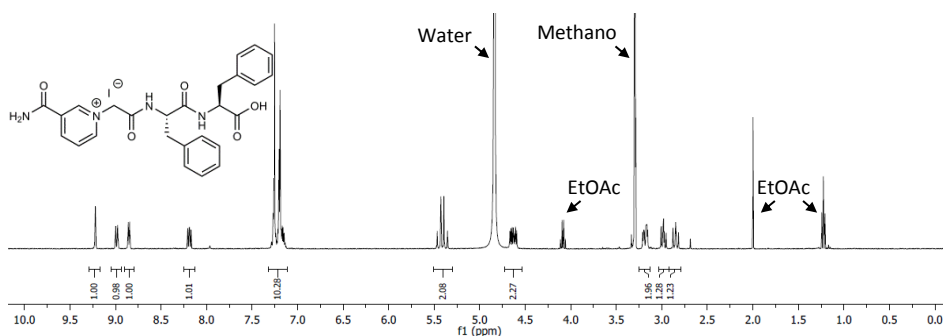

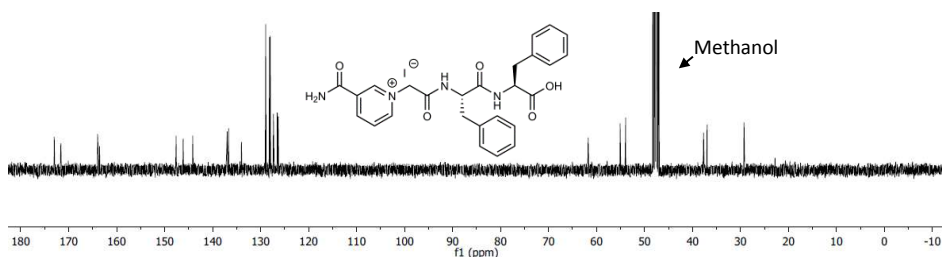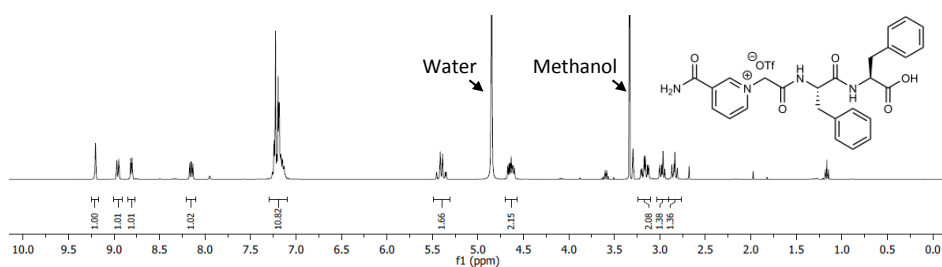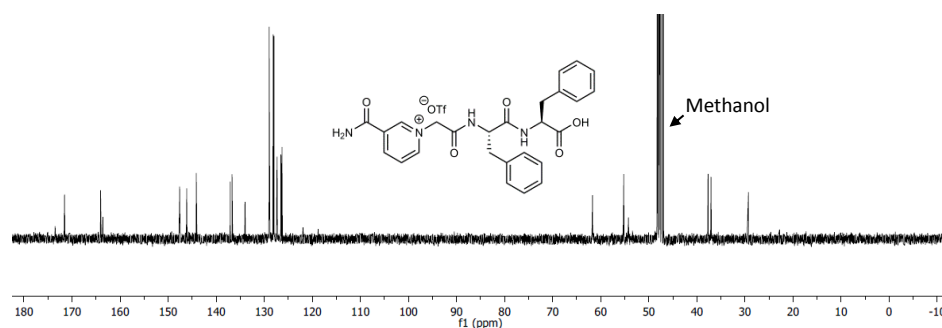**Figure S6.6.** ^{1}H-NMR (CD$_3$OD) of **7**.

Figure S6.7. ^{13}C-NMR (CD$_3$OD) of **7**.

mNAD$^+$-Phe-Phe-OH OTf$^-$ 1a. Product **8** (3.80 g, 6.31 mmol) and silver triflate (1.40 g, 5.45 mmol) were both dissolved in methanol. The silver triflate solution was added dropwise to the stirred solution of product **8**. After 1 h the suspension was filtered and the solvent from the filtrate was evaporated. Product **1a** was obtained as an off-white solid (3.20 g, 82%). M.p. 91 °C. ^{1}H-NMR (399.7 MHz, CD$_3$OD, ppm): δ 9.20 (s, 1H, Ar*H*), 8.97 (d, 1H, Ar*H*), 8.82 (d, 1H, Ar*H*), 8.15 (t, 1H, Ar*H*), 7.22 (m, 10H, Ar*H*), 5.41 (q, 2H, NC*H*2), 4.64 (m, 2H, C*H*), 3.16 (m, 2H, C*H*2), 2.97 (m, 1H, C*H*2), 2.84 (m, 1H, C*H*2). ^{13}C-NMR (100.5 MHz, CD$_3$OD, ppm): δ 173.5 (*C*=O), 171.5 (*C*=O), 164.1 (*C*=O), 163.6 (*C*=O), 147.6 (*C*$_{Ar}$), 146.1 (*C*$_{Ar}$), 144.1 (*C*$_{Ar}$), 137.1 (*C*$_{Ar}$), 136.7 (*C*$_{Ar}$), 134.0 (*C*$_{Ar}$), 129.0 (*C*$_{Ar}$), 128.9 (*C*$_{Ar}$), 128.1 (*C*$_{Ar}$), 128.0 (*C*$_{Ar}$), 127.3 (*C*$_{Ar}$), 126.5 (*C*$_{Ar}$), 126.3 (*C*$_{Ar}$), 61.7 (NC*H*$_2$), 55.2 (*C*H), 54.2 (*C*H), 37.7 (*C*H$_2$), 37.1 (Cl*C*H$_2$). MS (ESI Pos.) m/z: 475.10 [(M$^+$)] (expected m/z = 475.20). MS (ESI Neg.) m/z: 148.90 [(M$^+$)] (expected m/z = 148.95).

Figure S6.8. ^{1}H-NMR (CD$_3$OD) of **1a**.

Figure S6.9. ^{13}C-NMR (CD$_3$OD) of **1a.**

Table S6.1. Energy-dispersive X-ray spectroscopy (EDX) data of **1a**.

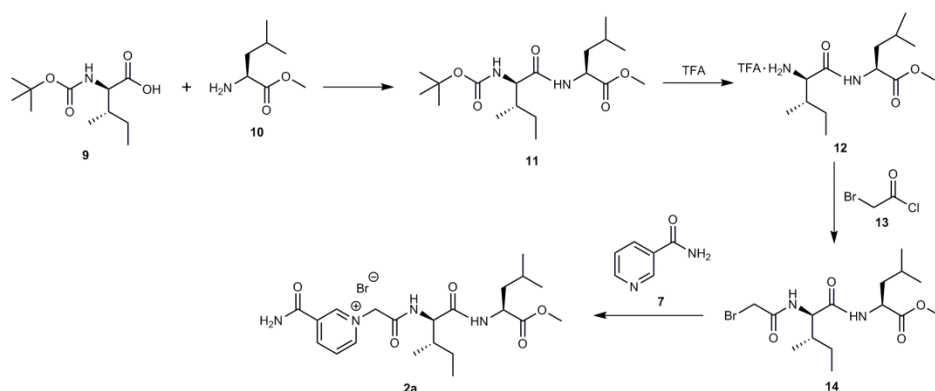| Element	Mass%	Atom%	Sigma	Net	K ratio	Line
N	15.59	19.39	0.42	628	0.0005267	K
O	43.04	46.85	0.47	4061	0.0008629	K
F	31.16	28.57	0.72	1793	0.0007739	K
S	9.34	5.07	0.19	4152	0.0003824	K
Ag	0.41	0.07	0.24	97	0.0000142	L
I	0.46	0.06	0.3	87	0.0000176	L
Total	100.00	100.00				

Synthesis procedure of 2a

Figure S6.10. Synthesis route to **2a**.

Boc-Ile-Leu-OMe 11. HCl·H$_2$N-Leu-OMe (5.00 g, 27.5 mmol) was dissolved in DCM (240 mL). Boc-Ile-OH (5.00 g, 21.6 mmol), hydroxybenzotriazole (8.40 g, 62.2 mmol) and 1-ethyl-3-(3-dimethylaminopropyl)carbodiimide (10.8 g, 56.3 mmol) were added. Lastly, triethylamine (11.0 mL, 78.9 mmol) was added. The mixture reacted overnight at room temperature. The mixture was washed three times with 1 M NaOH and three times with 1 M HCl. The DCM layer was dried with MgSO$_4$, filtered and the solvent was evaporated. Product **11** was obtained as a solid (5.20 g, 65.9%). ^{1}H-NMR (399.7 MHz, CDCl$_3$, ppm): δ 6.21 (m, 1H, N*H*), 5.01 (m, 1H, N*H*), 4.60 (m, 1H, C*H*), 3.90 (t, 1H, C*H*), 3.71 (s, 3H, OC*H*3), 1.85 (m, 1H, C*H*), 1.64 (m, 2H, C*H*2), 1.53 (m, 2H, C*H*2), 1.42 (s, 9H, t-butyl), 1.15 (m, 1H, C*H*), 0.91 (m, 12H, C*H*3).
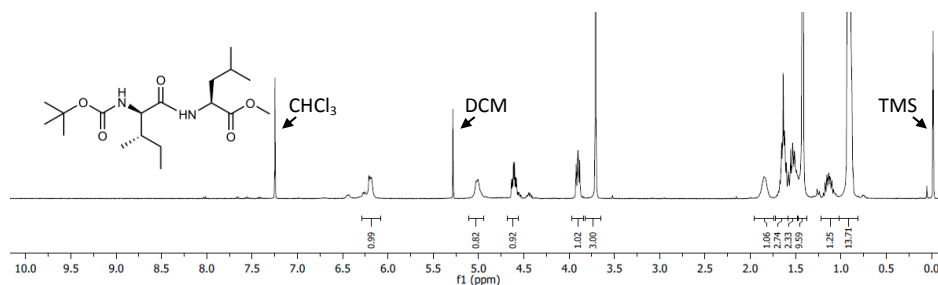

Figure S6.11. ^{1}H-NMR (CDCl$_3$) of **11**.

TFA·H₂N-Ile-Leu-OMe 12. Product **11** (5.20 g, 14.5 mmol) was dissolved in DCM (45 mL) and TFA (38.0 mL, 0.497 mol) was added dropwise. The mixture reacted at room temperature for 1 h. Afterwards, the solvent and remaining TFA was evaporated. The solid residue was washed with toluene and evaporated three times. Product **12** was obtained as a solid (5.10 g, 91.3%). ^{1}H-NMR (399.7 MHz, CD$_3$OD, ppm): δ 4.49 (t, 1H, C*H*), 3.72 (t, 1H, C*H*), 3.69 (s, 3H, OC*H*3), 1.96 (m, 1H, C*H*), 1.65 (m, 4H, C*H*2), 1.24 (m, 1H, C*H*), 0.93 (m, 12H, C*H*3).
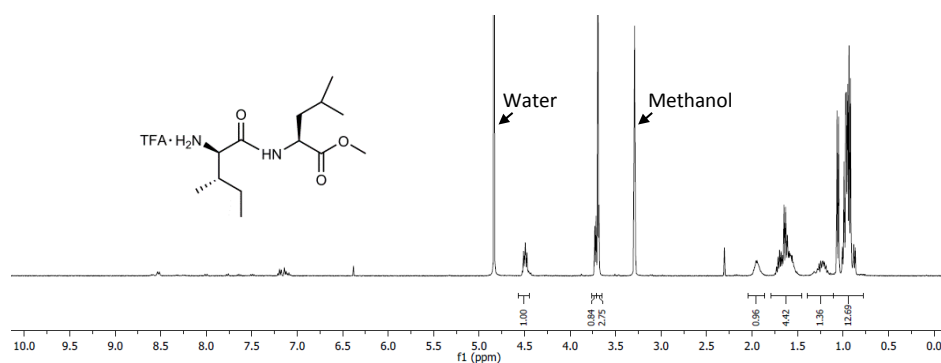
Figure S6.12. ^{1}H-NMR (CD$_3$OD) of **12**.

(Bromoacetyl)-Ile-Leu-OMe 14. Product **12** (5.10 g, 14.9 mmol) was dissolved in water (40 mL) and ethyl acetate (60 mL). K$_2$CO$_3$ (6.70 g, 48.5 mmol) was first added and then bromoacetyl chloride (2.20 mL, 26.4 mmol) was added dropwise. Afterwards, the reaction mixture reacted at room temperature for 2 h. The reaction was purified by washing the mixture three times with 1 M HCl. Next, the organic layer was dried with MgSO$_4$, filtered and the solvent was evaporated. Product **14** was obtained as a solid (4.00 g, 75%). ^{1}H-NMR (399.7 MHz, CDCl$_3$, ppm): δ 7.28 (m, 1H, N*H*), 6.72 (m, 1H, N*H*), 4.55 (m, 1H, C*H*), 4.36 (t, 1H, C*H*), 3.85 (s, 2H, BrC*H*2), 3.70 (s, 3H, OC*H*3), 1.85 (m, 1H, C*H*), 1.60 (m, 2H, C*H*2), 1.53 (m, 2H, C*H*2), 1.14 (m, 1H, C*H*), 0.88 (m, 12H, C*H*3).
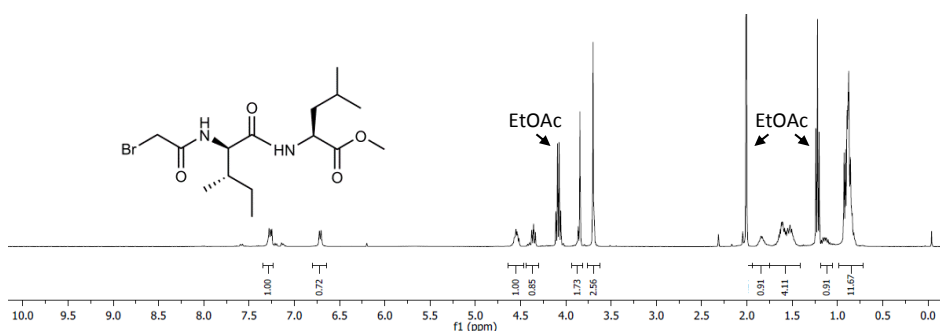
6

Figure S6.13. ^{1}H-NMR (CDCl₃) of **14**.

mNAD⁺-Ile-Leu-OMe 2a. Product **14** (3.95 g, 10.4 mmol) was dissolved in acetonitrile (20 mL) and nicotinamide **7** (1.29 g, 10.6 mmol) was added. The reaction mixture was refluxed overnight. The acetonitrile was evaporated and the residue was dissolved in methanol and the solution was precipitated three times in diethyl ether. Product **2a** was obtained as orange crystals (4.15 g, 76%). M.p. 76 °C. ^{1}H-NMR (399.7 MHz, CD₃OD, ppm): δ 9.38 (s, 1H, ArH), 9.03 (m, 2H, ArH), 8.23 (t,1H, ArH), 5.60 (s, 2H, NCH2), 4.43 (m, 1H, CH), 4.27 (d, 1H, CH), 3.68 (s, 3H, OCH3), 1.90 (m, 1H, CH), 1.60 (m, 4H, CH2), 1.26 (m, 1H, CH), 0.94 (m, 12H, CH3). ^{13}C-NMR (100.5 MHz, CD₃OD, ppm): δ 172.9 (C=O), 172.2 (C=O), 164.5 (C=O), 163.6 (C=O), 147.8 (C_{Ar}$), 146.3 ($C$_{Ar}$), 144.2 (C_{Ar}$), 134.0 ($C$_{Ar}$), 127.4 (C_{Ar}$), 61.8 ($C$H), 58.6 (N$C$H₂), 51.2 ($C$H), 50.8 ($C$H₃), 39.8 ($C$H₂), 36.9 ($C$H₂), 24.4 ($C$H₂), 21.8 ($C$H), 20.4 ($C$H₃), 14.4 ($C$H₃), 10.1 ($C$H₃). MS (ESI Pos.) m/z: 421.15 [(M⁺)] (expected m/z = 421.24).
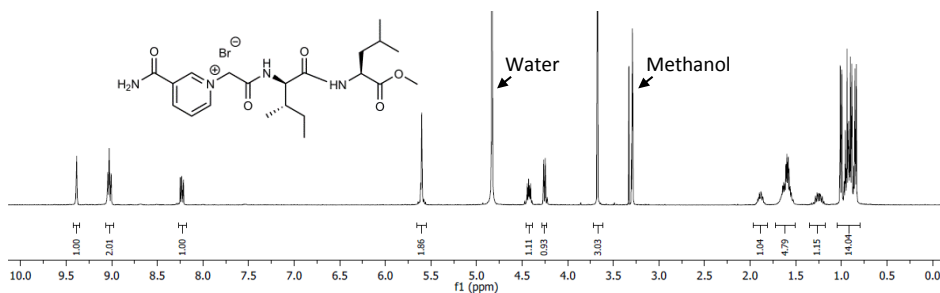
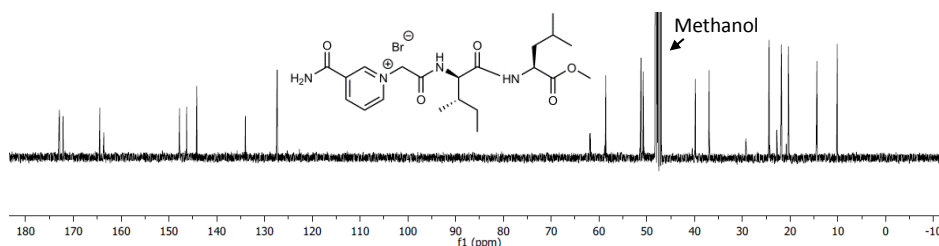**Figure S6.14.** ^{1}H-NMR (CD₃OD) of **2a**.

Figure S6.15. ^{13}C-NMR (CD$_3$OD) of **2a**.

Synthesis procedure of 3a
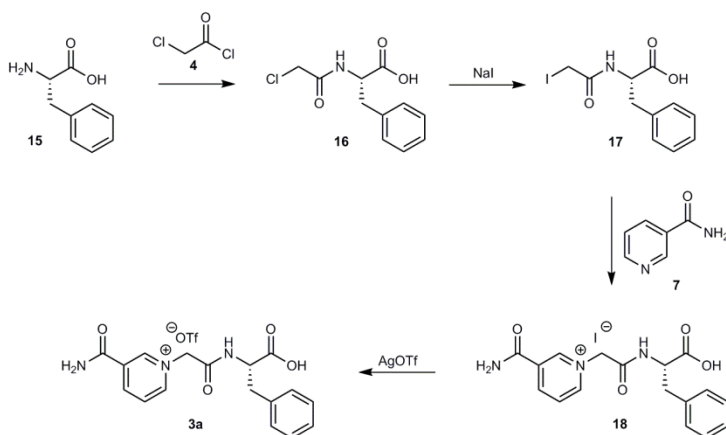
Figure S6.16. Synthesis route to **3a**.

(2-Iodoacetyl)phenylalanine 17. L-Phenylalanine **15** (13.7 g, 82.8 mmol) was suspended in acetonitrile (100 mL). Chloroacetyl chloride (6.50 mL, 81.7 mol) was added dropwise and the mixture reacted overnight at RT. The suspension was filtrated and the solvent and remaining chloroacetyl chloride was evaporated resulting in pure (2-chloroacetyl)phenylalanine **16**. This product (10.2 g, 42.4 mmol) was dissolved in acetonitrile (125 mL) and acetone (75 mL). Next, sodium iodide (56.0 g, 0.374 mol) was added. The mixture reacted overnight at 50 °C. The suspension was filtrated and solvent was evaporated. The solid residue was suspended in 1 M HCl (250 mL). The ultrasonic bath was used to grind the big chunks. The suspension was filtered after 1 h stirring. The residual HCl was removed by dissolving the solid residue in ethanol. BaCO$_3$ (17.0 g, 86.1 mmol) was added and the suspension was stirred at room temperature for 30 minutes and was filtrated. The solvent from the filtrated was evaporated and

the residue was dried under vacuum overnight at 55 °C. Product **17** was obtained as an orange powder (8.23 g, 60%). M.p. 158 °C (decomposition). ^{1}H-NMR (399.7 MHz, CD$_3$OD, ppm): δ 7.24 (m, 5H, Ar*H*), 4.63 (m, 1H, C*H*), 3.69 (q, 2H, IC*H*2), 3.19 (m, 1H, C*H*2), 3.00 (m, 1H, C*H*2). ^{13}C-NMR (100.5 MHz, CD$_3$OD, ppm): δ 172.9 (*C*=O), 169.5 (*C*=O), 136.7 (*C*$_{Ar}$), 128.9 (*C*$_{Ar}$), 128.1 (*C*$_{Ar}$), 126.4 (*C*$_{Ar}$), 54.1 (*C*H), 36.9 (*C*H$_2$), -4.1 (I*C*H$_2$). MS (ESI Neg.) m/z: 331.95 [(M$^-$)] (expected m/z = 331.99).
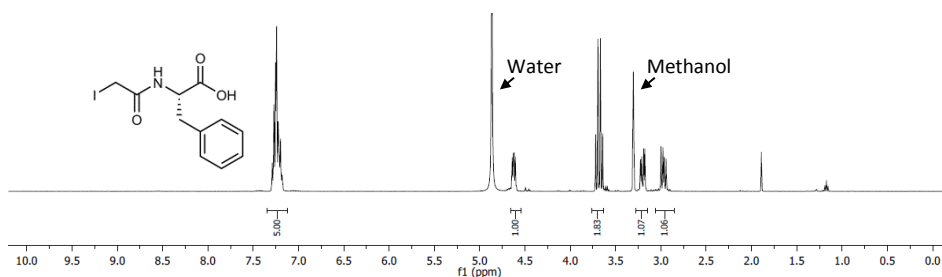
Figure S6.17. ^{1}H-NMR (CD$_3$OD) of **17**.
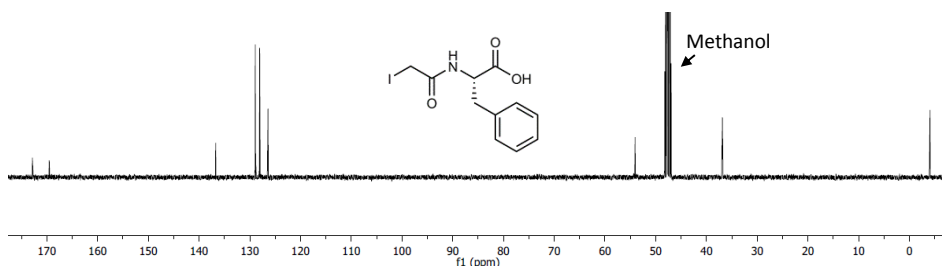
Figure S6.18. ^{13}C-NMR (CD$_3$OD) of **17**.

mNAD$^+$-Phe-Phe-OH I$^-$ 18. Product **17** (8.23 g, 24.7 mmol) was dissolved in acetonitrile (200 mL). Nicotinamide **7** (3.27 g, 26.8 mmol) was added and the mixture refluxed overnight. The solvent was evaporated and the residue was suspended in 2-butanone and filtrated afterwards using the ultrasonic bath. The solid residue was then dissolved in methanol and precipitated with diethyl ether. The mixture was filtrated and product **18** was obtained as a yellow/orange solid (3.32 g, 30%). M.p. 133 °C. ^{1}H-NMR (399.7 MHz, CD$_3$OD, ppm): δ 9.30 (s, 1H, Ar*H*), 8.99 (d, 1H, Ar*H*), 8.93 (d, 1H, Ar*H*), 8.21 (t, 1H, Ar*H*), 7.28 (m, 5H, Ar*H*), 5.52 (q, 2H, NC*H*2), 4.70 (m, 1H, C*H*), 3.27 (m, 1H, C*H*2), 3.03 (m, 1H, C*H*2). ^{13}C-NMR (100.5 MHz, CD$_3$OD, ppm): δ 173.4 (*C*=O), 164.1 (*C*=O), 163.6 (*C*=O), 147.7 (*C*$_{Ar}$), 146.2 (*C*$_{Ar}$), 144.2 (*C*$_{Ar}$), 136.9 (*C*$_{Ar}$), 134.0 (*C*$_{Ar}$), 128.9 (*C*$_{Ar}$), 128.2

(C_{Ar}), 127.4 (C_{Ar}), 126.5 (C_{Ar}), 61.8 (NCH_2), 54.7 (CH), 37.2 (CH_2). MS (ESI Pos.) m/z: 328.10 [(M$^+$)] (expected m/z = 328.13).
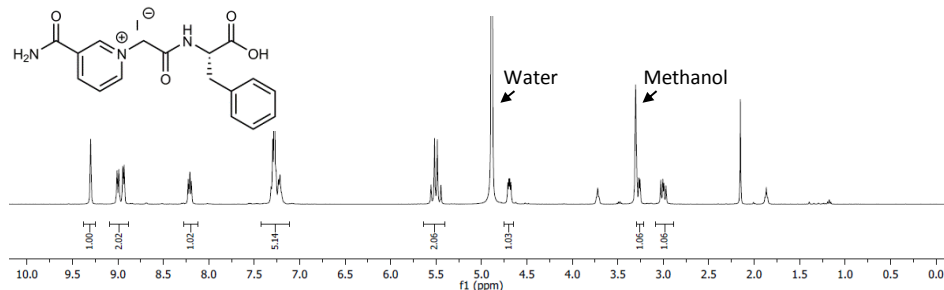
Figure S6.19. ^{1}H-NMR (CD$_3$OD) of **18**.
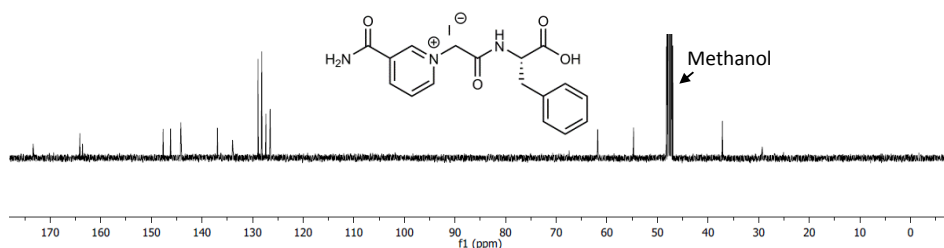
Figure S6.20. ^{13}C-NMR (CD$_3$OD) of **18**.

mNAD$^+$-Phe-Phe-OH OTf$^-$ 3a. Product **18** (3.32 g, 7.28 mmol) was dissolved in water (125 mL) and silver triflate (1.68 g, 6.55 mmol) was dissolved in water (5 mL). The silver triflate solution was added dropwise to the stirred solution of product **18**. After 1 h the suspension was filtered and the solvent from the filtrate was evaporated. EDX showed 1 wt% silver in the product. The product was dissolved in water and a diluted sodium chloride solution was dropwise added until no precipitation was formed anymore. The mixture was filtrated and the water was evaporated to obtain product **3a** as a white solid (3.33 g, 96%). M.p. 62-64 °C. ^{1}H-NMR (399.7 MHz, CD$_3$OD, ppm): δ 9.27 (s, 1H, Ar*H*), 9.00 (d, 1H, Ar*H*), 8.92 (d, 1H, Ar*H*), 8.19 (t, 1H, Ar*H*), 7.27 (m, 5H, Ar*H*), 5.49 (q, 2H, NC*H2*), 4.70 (m, 1H, C*H*), 3.29 (m, 1H, C*H2*), 3.02 (m, 1H, C*H2*). ^{13}C-NMR (100.5 MHz, CD$_3$OD, ppm): δ 165.1 (*C*=O), 164.1 (*C*=O), 163.6 (*C*=O), 147.5 (C_{Ar}), 146.1 (C_{Ar}), 144.1 (C_{Ar}), 137.0 (C_{Ar}), 134.0 (C_{Ar}), 128.9 (C_{Ar}), 128.2 (C_{Ar}), 127.3 (C_{Ar}), 126.5 (C_{Ar}), 54.8 (NCH_2), 48.4 (CH), 37.2 (CH_2). The other peaks in the ^{13}C-NMR spectrum are from 3-

fluoroaniline to determine the ion exchange conversion. MS (ESI Pos.) m/z: 328.05 [(M$^+$)] (expected m/z = 328.13). MS (ESI Neg.) m/z: 148.85 [(M$^+$)] (expected m/z = 148.95).
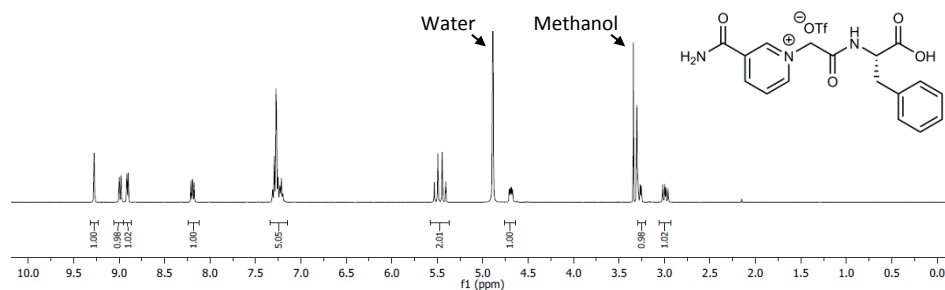
Figure S6.21. ^{1}H-NMR (CD$_3$OD) of **3a**.
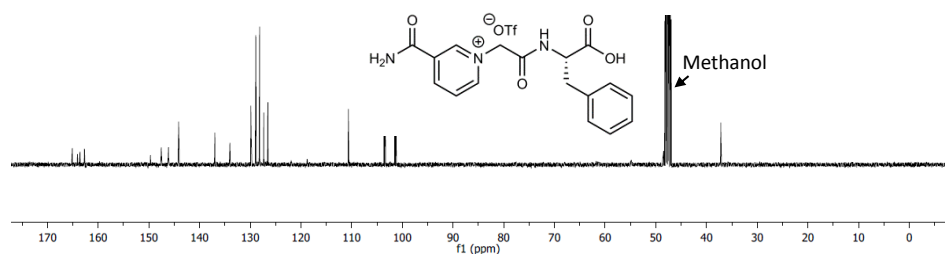
Figure S6.22. ^{13}C-NMR (CD$_3$OD) of **3a**.

Table S6.2. Energy-dispersive X-ray spectroscopy (EDX) data of the final product **3a**.

Element	Mass%	Atom%	Sigma	Net	K ratio	Line
N	11.90	11.80	0.15	5244	0.0288318	K
O	16.73	14.52	0.07	36512	0.0508347	K
F	8.35	6.10	0.05	28784	0.0814174	K
Na	0.17	0.10	0.05	28784	0.0814174	K
S	6.01	2.61	0.02	1701112	0.1026804	K
Ba	0.84	0.08	0.03	8105	0.0122385	L
Total	100.00	100.00				

6

Synthesis procedure of [Cp*Rh(bpy-OMe)Cl]Cl

The Rh-catalyst was synthesized according to literature procedures. 4-nitro-2,2'-bipyridine-1-oxide was formed from 2,2'-bipyridine.[1] Next, 4-nitro-2,2'-bipyridine-1-oxide is converted to 4-methoxy-2,2'-bipyridine-1-oxide and finally to 4-methoxy-2,2'-bipyridine.[2] Lastly, the [Cp*Rh(bpy-OMe)Cl]Cl (Rh-catalyst) is formed.[3]

6.5.4. Details about the hydrogelation and fiber formation experiments

Gelators **1b** and **2b** are made in two different ways. One is using the reduction with sodium dithionite and the second is with sodium formate and a Rh-catalyst. Both experimental procedures are described here.

In a typical gelation experiment with sodium dithionite, 20.44 mg **1a** is dissolved in water (1.0 mL) to reach a concentration of 40 mM. The whole system is set under nitrogen atmosphere and 20 mg (240 mM) sodium bicarbonate and 27.86 mg (160 mM) sodium dithionite are added, respectively. The solution is rested for 1 h forming the hydrogel.

In a typical gelation experiment with sodium formate, 30 mM **1a** is dissolved in 1 mL MOPS buffer (100 mM, pH 7.5) by heating and the ultrasonic bath. Next, solid Rh-catalyst (1.47 mg) and then solid sodium formate (71.55 mg) are added and dissolved. The solution reacts for 1.5 h without any disturbances. After this time, the hydrogel is analyzed.

For the fiber formation experiments the same procedure is carried out as with the reduction with sodium formate and Rh-catalyst. Only in this procedure the mixture is stirred at 750 rpm for 1.5 h.

6

6.5.5. Critical Gelation Concentration (CGC) tests

Figure S6.23. Critical gelation concentration tests with gelator **1b**. Concentrations of **1b** from left to right: 20 mM, 30 mM, 10 mM, 1 mM. The images show that the CGC of **1b** is between 10 and 20 mM. The precipitate in the first vial is caused by mechanical disturbances. 0.18 eq. Rh-catalyst and 90 eq. sodium formate are added compared to [**1a**].

6.5.6. UV-vis scattering measurements upon gelation
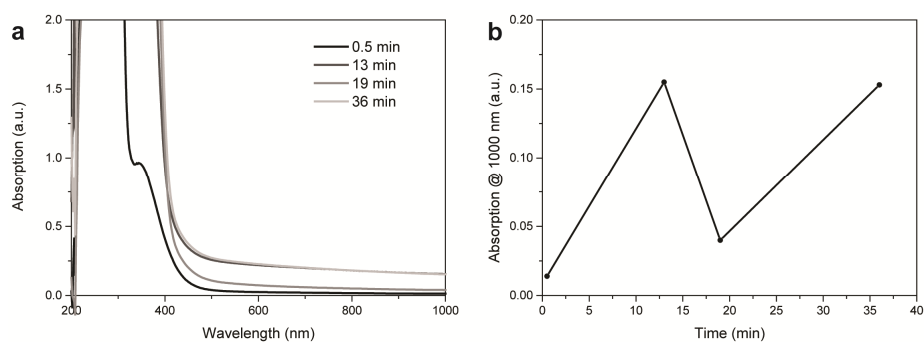
Figure S6.24. UV-vis absorption measurements during the gelation of **1b** (30 mM) with Rh-catalyst (3.0 mM) and sodium formate (500 mM) in MOPS buffer (100 mM, pH 7.5). **(a)** Absorption spectra during the gelation. **(b)** Absorption at 1000 nm during the gelation.

6.5.7. Surface tension of the components in the chemical reaction network
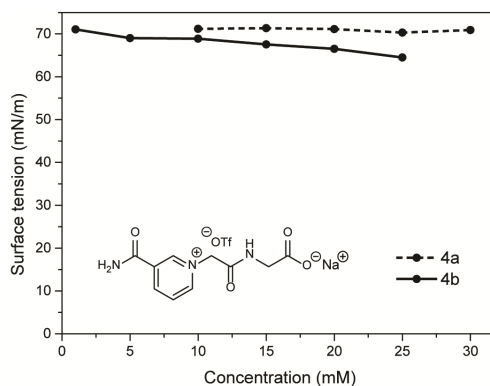
Figure S6.25. Surface tension of nicotinamide-functionalized glycine in the oxidized **4a** and the reduced state **4b**.
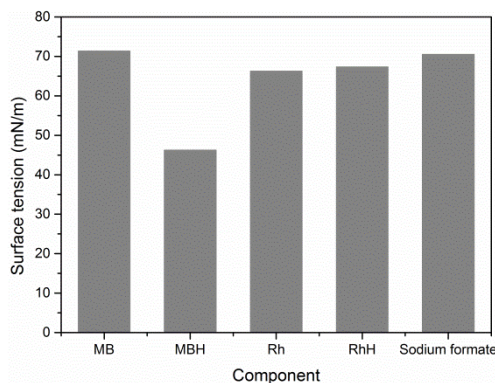
Figure S6.26. Surface tension of the different components during the chemical reaction network. From left to right: methylene blue (MB), leuco-methylene blue (MBH), Rh-catalyst (Rh), hydrido Rh-complex, sodium formate.

6.5.8. Supplementary references

1.   M. Zalas, B. Gierczyk, M. Cegłowski and G. Schroeder, *Chem. Pap.*, 2012, **66**, 733-740.
2.   D. Wenkert and R. B. Woodward, *J. Org. Chem.*, 1983, **48**, 283-289.
3.   F. Hollmann, B. Witholt and A. Schmid, *J. Mol. Catal. B Enzym.*, 2003, **19-20**, 167-176.

6

Summary

Nature is capable of constantly adapting some of its assembled structures in response to external and internal signals. For instance, microtubuli grow and shrink upon cell division and cellular transport. Furthermore, actin fibers play a major role in muscle contraction and cell signaling. To achieve these transient functions, such assembled structures operate in an out-of-equilibrium state. Energy input and dissipation enables structure growth and subsequent collapse. Regulating the energy input with fuel concentration and the activity of associated enzymatically catalyzed processes leads to a high level of kinetic control in biological out-of-equilibrium processes.

The biological processes described above are extremely complex and dependent on many factors. Achieving out-of-equilibrium assembly in which the kinetics of the underlying chemical reaction network can be controlled using separate synthetic catalysts would already constitute a major step forward to more control and flexibility in out-of-equilibrium assembly. Regulating the kinetics by catalysis and investigating the functions of out-of-equilibrium assembly is the main goal of this doctoral research.

In Chapter 2 we present a literature overview of out-of-equilibrium assembly over the past 20 years. We discuss the procedures and functions that are obtained using out-of-equilibrium assembly. Moreover, an outlook is given for the expected challenges and research directions in the future.

Chapter 3 describes the development of a new chemical reaction network (CRN) for use in an out-of-equilibrium assembly system with catalytic control. Using a model reaction in which all molecular components are soluble we show that we can kinetically control the formation and depletion rate of the activated building blocks, and its maximum concentration by varying the concentrations of the fuel and two catalysts. The kinetic behavior is further investigated using a kinetic model describing all reaction rates in the network. By coupling the CRN to an assembling building block we are able to achieve transient crystallization. We performed multiple consecutive crystallization cycles. Similar to the soluble model reaction, we can control the crystallization and dissolution rate using the catalysts and fuel concentrations.

In Chapter 4 we coupled the established CRN to a coil-globule transition of a polymer. A water-soluble, positively charged nicotinamide functionalized polymer was synthesized. Upon reduction of the nicotinamide groups with sodium formate, catalyzed by a Rh-catalyst, the polymer becomes hydrophobic and large polymer agglomerates are formed. Upon spontaneous oxidation of the reduced nicotinamide groups, catalyzed by methylene blue, the water-soluble polymer is again obtained.

Kinetics of the coil-globule transitions and thus polymer agglomeration is regulated by the Rh-catalyst, methylene blue and sodium formate concentration. Moreover, as the agglomerate interior is hydrophobic we can transiently transport cargo, such as proteins and nanoparticles, inside the polymer.

The research described in Chapter 5 is in collaboration with the University of Utrecht and presents the initial results towards an out-of-equilibrium colloidal agglomeration system. We synthesized nicotinamide functionalized polystyrene colloids which are repulsive in their stable state as the positive charges repel each other. Upon reduction of the nicotinamide groups, the colloids start to attract each other leading to colloidal agglomeration. Upon addition of methylene blue, the reduced nicotinamides are oxidized and the colloids redisperse. Unfortunately, the ester groups within the nicotinamide functionalized colloids hydrolyze over time leading to irreversible degradation and agglomeration of the colloids. This prevented further investigation of the behavior of this colloidal system. We do however suggest several solutions to prevent colloidal degradation, opening the road to further investigation of out-of-equilibrium colloidal agglomerations.

Chapter 6 describes the design, synthesis and use of nicotinamide-dipeptide-based hydrogelators for fuel-driven assembly. Coarse-grained modeling can predict the most promising dipeptides for hydrogel formation which substantially minimizes the synthetic effort. The two synthesized hydrogels were based on the dipeptides diphenylalanine and isoleucine-leucine methyl ester resulting in visually distinct hydrogel structures in homogeneity and turbidity. The diphenylalanine hydrogel was further investigated showing the presence of thin (3 nm) and long (>2 μm) fibers. This gelator showed a gradual increase in scattering upon gelation, but irregular scattering upon stirred fiber growth. Stirring is required for sufficient oxygen diffusion in the mixture. These difficulties in quantitatively analyzing these fibers upon stirring resulted in the premature closure of the project.

To conclude, in this doctoral thesis we show the broad range of out-of-equilibrium and in-equilibrium assembled structures that are achieved using a nicotinamide-based CRN. The versatility of these assemblies in their properties, structures and functions all based on the same CRN, makes the CRN of nicotinamide particularly applicable for future work. Moreover, we can control the kinetics of structure formation and decay using the concentrations of both catalysts and fuel.

Samenvatting

In de natuur kunnen sommige geassembleerde structuren constant veranderen als reactie op externe en interne signalen. Microtubuli groeien en breken bijvoorbeeld tijdens celdeling of celsignalering. Om deze tijdelijke functies te bereiken, opereren deze geassembleerde structuren onder uit-evenwicht condities. De toevoer en dissipatie van energie maakt het groeien en krimpen van structuren mogelijk. Het reguleren van de energietoevoer met behulp van brandstofconcentratie en de activiteit van betrokken enzymgekatalyseerde processen leidt tot een hoge kinetische controle in biologische uit-evenwicht processen.

De biologische processen die hierboven beschreven zijn, zijn enorm complex en afhankelijk van veel factoren. Het bereiken van uit-evenwicht assemblages waarbij de kinetiek van het onderliggende chemische reactienetwerk gecontroleerd kan worden door afzonderlijke synthetische katalysatoren, zou al een grote stap voorwaarts zijn voor meer controle en flexibiliteit in uit-evenwicht assemblages. Het reguleren van de kinetiek door katalyse en het onderzoeken van de verkregen functies in uit-evenwicht assemblages is het hoofddoel van dit doctoraal onderzoek.

In Hoofdstuk 2 presenteren we een literatuuroverzicht van uit-evenwicht assemblages in de afgelopen 20 jaar. We bediscussiëren de procedures en functies die verkregen kunnen worden met behulp van uit-evenwicht assemblage. Bovendien geven we een vooruitzicht voor de verwachte uitdagingen en onderzoeksrichtingen in de toekomst.

Hoofdstuk 3 beschrijft de ontwikkeling van een nieuwe chemisch reactienetwerk (CRN) voor een uit-evenwicht assemblagesysteem met katalytische controle. Door middel van een modelreactie waarin alle moleculaire componenten oplosbaar zijn, laten we zien dat we kinetische controle hebben over de vorming- en afbraaksnelheid van de geactiveerde bouwstenen, en zijn maximum concentratie, door te variëren in de concentratie van de brandstof en de twee katalysatoren. Het kinetische gedrag is verder onderzocht met behulp van een kinetisch model dat alle reactiesnelheden in het netwerk beschrijft. Door de koppeling van het CRN aan een bouwsteen dat kan assembleren, hebben we tijdelijke kristallisatie bereikt. We hebben meerdere kristallisatiecycli uitgevoerd. Net zoals de modelreactie waarbij alles oplosbaar is, kunnen we de kristallisatie- en oplossingssnelheid controleren met behulp van de katalysatoren- en brandstofconcentraties.

In Hoofdstuk 4 hebben we het gevestigde CRN gekoppeld aan de polymeertransitie tussen een willekeurige kronkeling en een bolletje. Een

wateroplosbaar, positief geladen nicotinamidegefunctionaliseerd polymeer is gesynthetiseerd. Reductie van de nicotinamidegroepen met natriumformiaat, gekatalyseerd door een Rh-katalysator, resulteert in de vorming van een hydrofoob polymeer dat aggregeert. Spontane oxidatie van de gereduceerde nicotinamidegroepen, gekatalyseerd door methyleenblauw, resulteert in de vorming van het originele wateroplosbare polymeer. De kinetiek van deze aggregatietransitie is gereguleerd door de concentratie van de Rh-katalysator, methyleenblauw en natriumformiaat. Bovendien, kunnen we tijdelijk vracht transporteren, zoals eiwitten en nanodeeltjes, in de hydrofobe polymeeraggregaten.

Het onderzoek beschreven in Hoofdstuk 5 is in samenwerking met Universiteit Utrecht en laat de eerste resultaten zien op weg naar een uit-evenwicht colloïdaal aggregatiesysteem. We hebben polystyreencolloïden gefunctionaliseerd met nicotinamidegroepen die afstotend zijn in hun stabiele toestand doordat de positieve lading elkaar afstoot. Reductie van de nicotinamidegroepen leidt tot aantrekking van de colloïden en dus de vorming van colloïdale aggregaten. Na toevoeging van methyleenblauw worden de gereduceerde nicotinamidegroepen geoxideerd en wordt er weer een stabiele colloïdale dispersie gevormd. Helaas hydrolyseerden de estergroepen in de nicotinamidegefunctionaliseerde colloïden over tijd, dat leidde tot irreversibele degradatie en aggregatie van de colloïden. Dit verhinderde verder onderzoek naar het gedrag van dit colloïdale systeem. We suggereren wel verscheidene oplossingen om colloïdale degradatie te voorkomen. Dit heropent de weg naar het verder onderzoeken van uit-evenwicht colloïdale aggregatie.

Hoofdstuk 6 beschrijft het ontwerp, de synthese en het gebruik van nicotinamidedipeptide gebaseerde hydrogelatoren voor brandstof aangedreven assemblage. 'Coarse-grained' modellen kunnen de meest veelbelovende dipeptiden voor hydrogelvorming voorspellen. Dit vermindert de synthetische inspanning significant. De twee gesynthetiseerde hydrogels zijn gebaseerd op de dipeptiden difenylalanine en isoleucine-leucine methylester resulterend in twee duidelijk verschillende hydrogelstructuren qua homogeniteit en troebelheid. De difenylalanine hydrogel was verder onderzocht en liet de aanwezigheid van dunne (3 nm) en lange (> 2 µm) fibers zien. De lichtverstrooiing van deze gelator nam toe tijdens de gelatie, maar roeren van het mengsel tijdens de fibervorming resulteerde in onregelmatige verstrooiing. Het roeren is nodig voor voldoende diffusie van zuurstof in het mengsel. Deze tegenslagen in het kwantitatief analyseren van de fibers tijdens het roeren, resulteerde in het voortijdig stopzetten van het project.

Ter conclusie, in dit doctoraal proefschrift laten we een breed scala van uit-evenwicht en in-evenwicht geassembleerde structuren zien die bereikt zijn met het

nicotinamidegebaseerde CRN. De verscheidenheid in de eigenschappen, structuren en functies van de assemblages, allemaal gebaseerd op hetzelfde CRN, maakt de nicotinamidegebaseerde CRN bijzonder toepasbaar voor toekomstig onderzoek. Bovendien kunnen we de kinetiek van structuurvorming en -afbraak controleren door de concentraties van beide katalysatoren en de brandstof te variëren.

Samenvatting voor een breder publiek

Zou het niet mooi zijn als we papier kunnen recyclen door inkt te laten verschijnen en laten verdwijnen wanneer wij dat willen. Tijdens mijn PhD onderzoek heb ik onderzocht hoe we geordende structuren kunnen vormen en afbreken, zoals het kleuren van inkt. Deze methode kunnen we niet alleen gebruiken voor het recyclen van papier, maar hebben nog vele andere toepassingen, zoals het vervoeren en loslaten van medicijnen in deze structuren. Of het vormen van tijdelijke kunstmatige huid dat weer afgebroken wordt wanneer je eigen huid is hersteld. Behalve deze biologische toepassingen zijn er ook toepassingen voor materialen, zoals het tijdelijk kleuren van zonnebrilglazen. Of we kunnen materialen laten bewegen en weer laten stoppen op ons bevel wat we kunnen toepassen in bijvoorbeeld robots en pompen.

Om deze geordende structuren beter te begrijpen, introduceer ik hier eerst een aantal processen en begrippen, zoals irreversibel en reversibel, zelf-assemblages en het verschil tussen stabiele en niet-stabiele structuren.

Irreversibel vs. reversibel

Vaak wanneer men denkt aan scheikunde, denkt men aan chemische reacties waarbij er één of meerdere producten worden gevormd uit moleculen (reactanten, Figuur 1). Een voorbeeld hiervan is het zwart worden van vlees tijdens het barbecueën. Scheikundig gezien komt dit door het vormen van acroleine (product B, Figuur 1) van glycerol uit de vetten in het vlees (reactant A, Figuur 1). Het zwarte vlees kan niet meer teruggedraaid worden en daardoor noemt met de reactie irreversibel. Voor de synthese van chemische stoffen zijn deze irreversibele chemische reacties voordelig omdat er dan veel product wordt gevormd. Het zwart worden van vlees is natuurlijk niet gewenst, maar acroleine is soms ook nuttig en wordt op grote schaal geproduceerd in de industrie voor bijvoorbeeld onkruidverdelging.
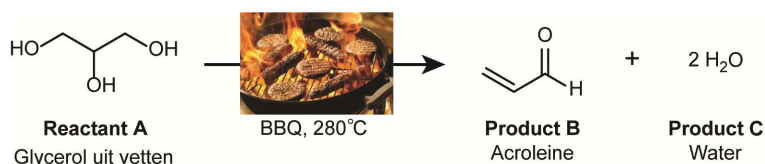
Figuur 1. De chemische reactie tijdens het zwart worden van vlees op de barbecue. Hierbij wordt glycerol uit vetten in het vlees (reactant A) omgezet in acroleine (product B) en water (product C).

In tegenstelling de irreversibele chemische reactie hierboven gebruikt de natuur vaak ook reacties die omkeerbaar zijn (reversibel). Hierdoor kan zij bepalen welke structuur aanwezig en welke functie wordt uitgevoerd. Een geschikte manier om reversibele structuren te maken is bijvoorbeeld het proces zelf-assemblage; waarbij kleine bouwstenen (vaak moleculen) grote geordende structuren vormen die reversibel weer uit elkaar kunnen vallen.

Een goed voorbeeld van zelf-assemblage is zeep. Als zeepmoleculen in het zeepblok oplossen in water bewegen deze moleculen willekeurig en ongestructureerd door het water (Figuur 2). Maar als de concentratie hoger wordt vormen samen bolvormige structuren in het water, micellen genaamd. De functie van deze micellen is het verwijderen van de waterafstotende vetten op je vieze handen en deze op te nemen in de micellen, zodat je handen schoon worden. De zeepmoleculen vormen micellen doordat een gedeelte van het molecuul van water houdt (blauwe bol, Figuur 2) en een gedeelte waterafstotend is (rode kronkelende lijn, Figuur 2). Door de micellen te vormen kunnen de waterafstotende gedeeltes van de zeepmoleculen worden afgeschermd van het water. De binnenkant neemt dan ook de waterafstotende vetten op. De moleculen in micellen wisselen heel snel uit met de individuele zeepmoleculen in het water en daarom worden micellen reversibel genoemd; de structuur is omkeerbaar.
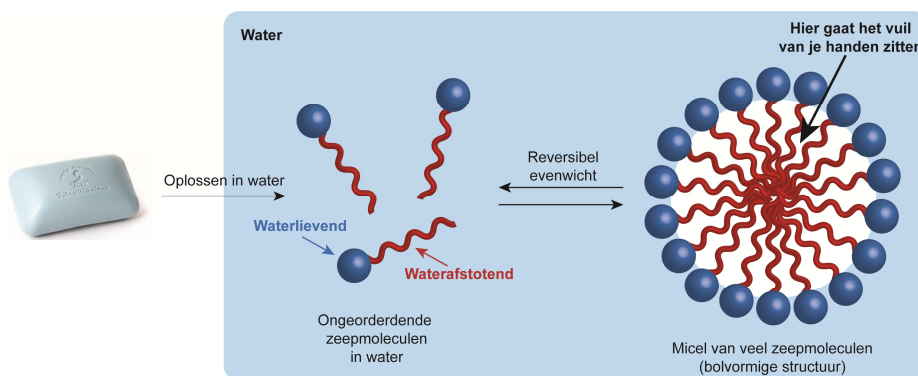
Figuur 2. Als je je handen wast met een zeepblok lossen de zeepmoleculen langzaam op in water in een ongestructureerde manier. Als de concentratie zeepmoleculen hoog genoeg is, vormen ze bolvormige structuren (micellen) om de waterafstotende gedeeltes beschermen van het water. In deze micellen gaat ook het vuil zitten als je je handen wast.

Zelf-assemblage betekent alleen dat er reversibele geordende structuren worden gevormd. Maar wat voor structuren is niet gedefinieerd. Daardoor zijn er veel soorten
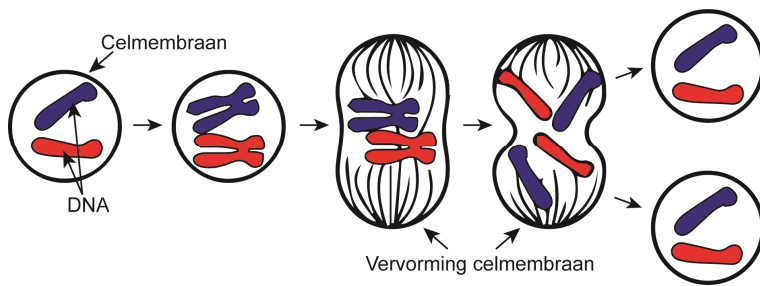
Figuur 3. De celmembranen die het omhulsel van de cel vormen zijn dynamisch en reversibel zodat het van vorm kan veranderen tijdens celdeling.

geordende structuren mogelijk, zoals haargel dat van vorm kan veranderen tijdens het aanbrengen in het haar. Of het biologische voorbeeld van celmembranen. Een celmembraan is het omhulsel van een cel dat van vorm moet veranderen tijdens de celdeling van één naar twee cellen (Figuur 3). Deze celdeling gebeurt constant in het lichaam, omdat cellen ziek of oud worden en dood gaan, of huidcellen die achterblijven op alles wat je aanraakt.

Stabiel vs. niet-stabiel
De bovengenoemde zelf-assemblage structuren vormen spontaan, zonder dat je iets moet doen. Omdat ze spontaan gebeuren zijn deze geordende structuren stabiel. De individuele zeepmoleculen die opgelost zijn in water zijn niet-stabiel omdat hun waterafstotende gedeelte in contact is met water. Om stabiel te worden vormen ze micellen waarbij de waterafstotende gedeeltes afgeschermd is van water. Omdat deze micellen stabiel zijn verandert de verhouding tussen de zeepmoleculen in de micellen en de individuele moleculen in het water niet. Voor elk zeepmolecuul dat uit het water naar de micel gaat, zal er ook een ander zeepmolecuul uit de micel naar het water gaan.

In eerder genoemde voorbeelden zijn de geordende structuren stabiel maar wij willen in dit onderzoek graag onstabiele structuren maken. Hiermee kunnen we controleren wanneer de structuren worden gevormd en wanneer ze uit elkaar vallen. Vele verschillende functies kunnen aan en uitgezet worden op deze manier. Een medisch voorbeeld is het transporteren van medicijnen in het lichaam in niet-stabiele geordende structuren die uit elkaar vallen wanneer de medicijnen moeten worden afgeleverd. Een ander voorbeeld is tijdelijke kleurverandering van een materiaal. In het onderzoek in Figuur 4 hebben ze rode deeltjes die als je er uv-licht op schijnt assembleren en geordende structuren vormen die een andere kleur hebben dan de individuele deeltjes, namelijk blauw. Als je het uv-licht weghaalt vallen de structuren

162

weer uit elkaar en heb je weer rode deeltjes. Door het uv-licht op bepaalde plekken van het materiaal te laten schijnen, kun je blauwe letters vormen. Ze laten hier zien dat je deze deeltjes kunt gebruiken voor geheime boodschappen of het hergebruiken van papier.
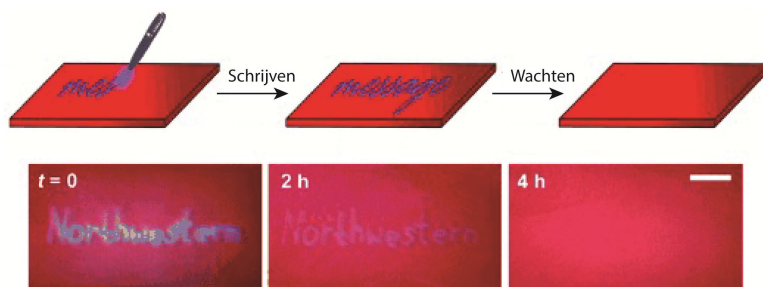
Figuur 4. Uv-licht laat rode individuele deeltjes assembleren tot geordende blauwe structuren. Als je het uv-licht weghaalt vallen de structuren spontaan uit elkaar in weer de rode deeltjes. Door uv-licht te schijnen op bepaalde plekken van het materiaal kun je letters vormen. Dit is te gebruiken voor geheime boodschappen of het recyclen van papier.

Om de vorming en afbraak van geordende structuren te controleren hebben we niet-stabiele structuren nodig. Alleen wanneer er energie wordt toegevoegd zal deze niet-stabiele structuur ontstaan en als de energie weer wegvloeit, zal de structuur weer uit elkaar vallen in stabiele moleculen. De natuur gebruikt deze niet-stabiele structuren veel om te reageren op de omgeving.

Een voorbeeld is een school kabeljauwen. Deze vissen leven een individueel bestaan en vormen alleen een school als er een vijand aanwezig is (Figuur 5). In de aanwezigheid van een vijand (meeuw) produceert de kabeljauw hormonen (energie) die de kabeljauw activeert. De geactiveerde kabeljauwen weren zich nu tegen de meeuw door samen een school te vormen. Deze vergroot de overlevingskansen doordat de meeuw gedesillusioneerd is door de school. Bovendien vergroot de school de kans dat een specifieke vis het doelwit is. De school is aanwezig zolang de hormonen aanwezig zijn, maar als de meeuw vertrekt verlaagt de hormoonconcentratie ook en zal de school vissen uit elkaar vallen. Dus de school vissen is een niet-stabiele structuur doordat de school alleen aanwezig is als de vijand aanwezig is en anders zal deze spontaan uit elkaar vallen tot individuele vissen.
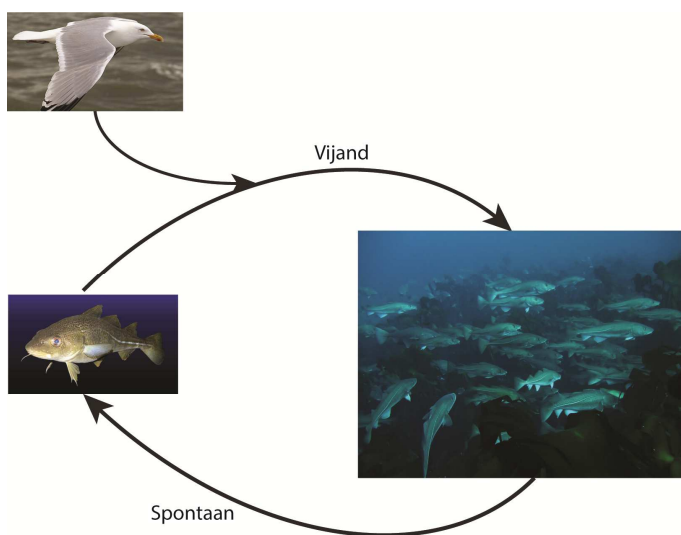
Figuur 5. Kabeljauwen leven individueel tenzij er een vijand aanwezig is, dan vormen ze een samen een school. Als de vijand verdwenen is, valt de school kabeljauwen uit elkaar. De school kabeljauwen is dus in een niet-stabiele toestand.

Mijn PhD onderzoek

Dit voorbeeld van een niet-stabiele structuur komt niet alleen voor in het dierenrijk, maar ook op de moleculaire schaal. Wij kunnen nu controleren wanneer moleculen geordende structuren vormen en wanneer deze weer uit elkaar vallen en hebben dit toegepast op vele soorten structuren, zoals kristallen, polymeren, deeltjes en gels. Bepaalde moleculen (groen, Figuur 6) zijn oplosbaar, maar met een brandstof (energiebron) reageren deze tot een waterafstotend product (donkerblauw, Figuur 6). Net zoals de zeepmoleculen willen deze niet in contact zijn met water en vormen daarom geordende structuren. Deze structuren zijn alleen niet stabiel en als de brandstof op raakt reageren de moleculen (donkerblauw) in de structuren weer terug tot stabiele wateroplosbare moleculen (groen). Omdat de originele moleculen (groen) weer aanwezig zijn, kunnen we nu nog een keer de niet-stabiele structuur maken door weer brandstof toe te voegen.

Nu is het in de chemie zo dat een reactie sneller verloopt wanneer er meer reactant aanwezig is, dus wanneer er meer brandstof wordt toegevoegd zal de niet-stabiele structuur sneller worden gevormd. Daarnaast duurt het langer tot de niet-stabiele structuur weer wordt afgebroken, omdat de originele moleculen meteen weer kunnen reageren met de overgebleven brandstof tot de niet-stabiele structuur, totdat alle brandstof is verbruikt. Dus door de hoeveelheid brandstof te variëren, kunnen we
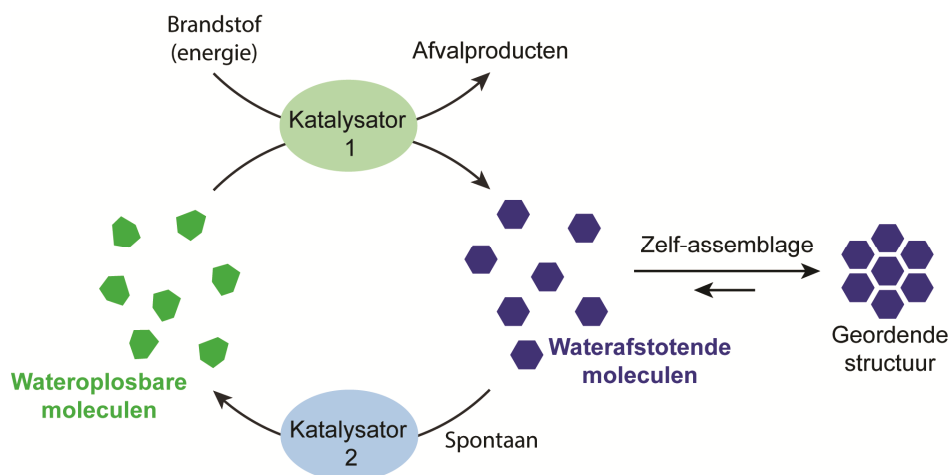
Figuur 6. Wateroplosbare moleculen (groen) reageren met een brandstof/energiebron met behulp van katalysator 1 tot waterafstotende moleculen (donkerblauw). Deze moleculen vormen een geordende structuur afhankelijk van de gebruikte moleculen. Deze structuur is alleen niet stabiel en valt spontaan uit elkaar en reageert terug naar de wateroplosbare moleculen met behulp van katalysator 2.

bepalen hoe lang de geordende structuur aanwezig is.

Ongeveer 10 jaar geleden is de wetenschap begonnen met onderzoeken hoe deze systemen werken en in de meeste onderzoeken kun je alleen met de hoeveelheid brandstof controleren hoe lang de niet-stabiele structuur aanwezig is. In hoofdstuk 2 laten wij een overzicht zien van welke ontwikkelingen er zijn geweest in de afgelopen jaren en bediscussiëren wij wat de volgende ontwikkelingen in de toekomst zijn.

In de rest van de hoofdstukken beschrijven wij ons ontwikkelde systeem en hoe wij deze hebben toegepast op verschillende niet-stabiele geordende structuren. In ons systeem hebben we een katalysator toegevoegd naast die de brandstof ook bepaalt hoe snel de niet-stabiele structuur wordt gevormd. Een katalysator is een molecuul dat de reactie versnelt zonder dat de katalysator verbruikt wordt. Dus één molecuul katalysator (katalysator 1, Figuur 6) kan velen wateroplosbare moleculen omzetten in waterafstotende moleculen met behulp van de brandstof zonder dat deze kapot gaat. En hoe meer katalysator aanwezig is, hoe sneller de reactie zal gaan. Nu hebben wij niet alleen een katalysator toegevoegd voor het vormen van de structuur, maar we hebben een tweede katalysator toegevoegd die de afbraak van de structuur versnelt (katalysator 2, Figuur 6).

In hoofdstuk 3 van dit proefschrift laten we zien wat de invloed is van de concentraties van katalysator 1 en katalysator 2. Zo laten ze zien dat als we meer katalysator 1 hebben de waterafstotende moleculen sneller worden gevormd. En als

we meer katalysator 2 hebben worden de waterafstotende moleculen juist sneller afgebroken. De waterafstotende moleculen in dit onderzoek vormen kristallen als niet-stabiele geordende structuur. Dus wij kunnen bepalen wanneer en hoe snel kristallen worden gevormd en hoe snel ze weer afbreken.

In hoofdstuk 4 hebben we polymeren gebruikt als niet-stabiele structures. Een polymeer is een hele lange keten van vele moleculen zoals een verjaardagsslinger bestaat uit vele vlaggetjes. De polymeren zijn stabiel en oplosbaar in water (groen, Figuur 7), maar als we brandstof toevoegen wordt het polymeer waterafstotend en vormt het samengeklonterd deeltjes die je met het oog kunt zien (donkerblauw, Figuur 7). Omdat deze waterafstotende polymeren niet stabiel zijn zullen deze ook terug reageren tot de originele wateroplosbare polymeren. Zoals we bij zeep het vuil op onze handen kunnen opnemen in de micellen, laten we hier ook zien dat we waterafstotende deeltjes (roze, Figuur 7) kunnen opnemen in de samengeklonterde polymeren en deze daarna weer kunnen loslaten. Hierdoor kunnen we in de toekomst op deze manier misschien wel medicijnen vervoeren en loslaten in het lichaam.
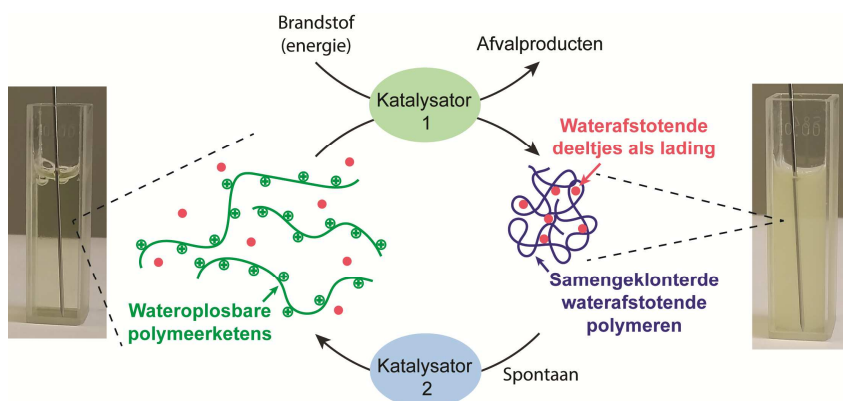
Figuur 7. Wateroplosbare polymeren (groene kronkelende lijnen) kunnen vrij rond bewegen in het water, maar als brandstof wordt toegevoegd worden de polymeren waterafstotend (donkerblauwe kronkelende lijnen) en klonteren ze samen. Deze samengeklonterde polymeren kunnen dan ook waterafstotende deeltjes (roze) meenemen als lading.

Hoofdstuk 5 is in samenwerking met de Universiteit van Utrecht uitgevoerd en daarin hebben we deeltjes gemaakt van 800 nanometer (0.0008 millimeter) groot. Omdat deze deeltjes zo klein zijn kunnen we ze met het blote oog niet zien dus we hebben een microscoop nodig om ze goed kunnen bekijken (Figuur 8). Doordat we ze met de microscoop en moleculen veel te klein zijn voor de microscoop, kunnen we het gedrag van de deeltjes gebruiken om het gedrag van moleculen beter te begrijpen. De

deeltjes die we hebben gemaakt zijn positief geladen, waardoor de deeltjes elkaar afstoten, net zoals twee magnetische pluspolen elkaar afstoten (linker foto, Figuur 8). Door brandstof aan deze deeltjes toe te voegen verwijderen we de positieve lading en zullen de deeltjes elkaar gaan aantrekken. Hierdoor vormen ze geordende structuren van allemaal deeltjes aan elkaar vast (rechter foto, Figuur 8). Na het toevoegen van katalysator 2 vallen de klonten uit elkaar. Graag wilden we ook katalysator 2 al vanaf het begin in het systeem toevoegen zodat we niet-stabiele structuren vormen die spontaan uit elkaar vallen. Maar omdat onze deeltjes kapot gingen over tijd konden we deze experimenten niet meer uitvoeren. In het hoofdstuk beschrijven we wel ideeën om te zorgen dat deze deeltjes niet kapot gaan in de toekomst.
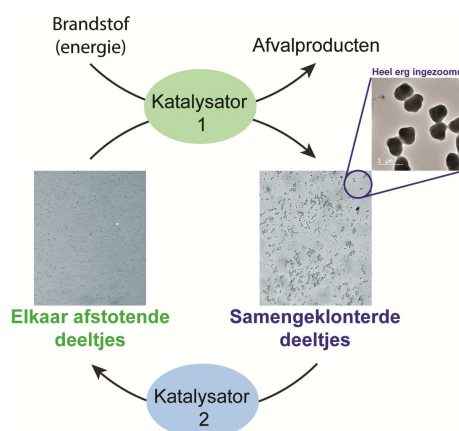
Figuur 8. Deeltjes van 800 nanometer (0.0008 millimeter) gezien door een microscoop als ze elkaar afstoten (links). Als er brandstof wordt toegevoegd klonteren ze samen (rechts) die daarna uit elkaar vallen als katalysator 2 wordt toegevoegd.

Het laatste hoofdstuk is ook een gedeeltelijk afgerond onderzoek waarbij wij niet-stabiele gels wilden maken. Met deze gels kunnen we dan misschien medicijnen vervoeren of kunstmatige huid maken, zoals aan het begin geschreven. Helaas lukte het niet om de niet-stabiele gels goed analyseren, daarom hebben wij tot nu toe alleen stabiele gels gemaakt. Een gel is een vaste stof die toch uit 99% vloeibaar water bestaat. De andere 1% bestaat uit zogenoemde gelator moleculen die alle water moleculen vasthoudt en samen vormen ze daardoor een gel. Wij hebben een wateroplosbaar molecuul gemaakt die het gelatormolecuul vormt als het reageert met de brandstof en katalysator 1 (Figuur 9). Deze gel ziet er met het blote oog uniform uit, maar als je met een microscoop inzoomt op de gel, zie je dat deze uit heel veel lange draden bestaat die allemaal kriskras door elkaar heen lopen. Deze draden zijn heel dun

(3 nanometer, deze draden allemaal kriskras door elkaar lopen kunnen ze het water vasthouden en een gel vormen. Ook aan dit onderzoek moet nog verder gewerkt worden, zodat we kunnen controleren wanneer deze draden worden gemaakt en afgebroken, Hierdoor kunnen we dan bepalen wanneer er een gel aanwezig is en wanneer een vloeistof.
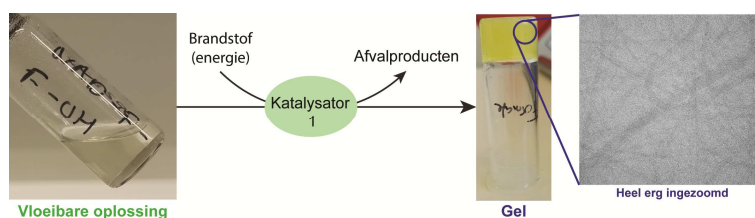
Figuur 9. Een oplossing van 1% molecuul in water dat met de brandstof en katalysator 1 een gelator molecuul vormt die het water vasthoudt, resulterend in een gel. Als je inzoomt op deze gel zie je dat de gel uit vele draden bestaat die kriskras door elkaar lopen.

Acknowledgements

Slowly all the colleagues whom I started my PhD with are leaving and today it is my turn. Upon preparing all the funny PhD defense movies for my friends during the last months I realized how much I will miss the group and our activities (marl caves, golf, Sinterklaas, dinners, pizza and board games, among others). Therefore I would like to thank all of you.

First of all, I would like to thank Rienk, my daily supervisor and promotor, for giving me the opportunity to do my PhD research in your group. During our meetings you always encouraged me with your new ideas and positive mindset to continue and excel. Thank you for making me a more confident and proactive researcher. My promotor, Jan, when we spoke you consistently stimulated me to be critical on my results. Furthermore, you always had new suggestions how to improve my system and how to extend it into new systems. Thank you not only for the research related ideas, but also for the great atmosphere in the group. Ger, your focus on safety in the lab and your patience in teaching is impressive and I will try to master these qualities during my new job as a teacher. Eduardo, your free mind always thought of an amazing story or philosophy when I talked to you. Stephen Picken, I did not talk to you a lot, but thanks for all your effort within the group. Furthermore, I would like to thank the committee members, Subi, Pol, Anja, Willem and Ulf for critically reading, assessing and discussing my thesis. Additionally, my research could not be performed without funding, therefore I would like to thank the Netherlands Organisation for Scientific Research (NWO) for subsidizing my research.

Of course, without the help of all of my colleagues and friends I never would have made it. Fanny, your openness for everything and everyone is highly inspiring to me. Thank you for all the hours of chatting while we actually had to work and for being my paranymph. Michelle, my new office friend after Fanny left. Your enthusiasm about sports (especially when you told me that you like leg lunges) amazes me. I loved our dinners together and hope we will stay in contact. Peggy, my passionate, chattering friend. Thank you for all the help with organic synthesis and all the fun we had inside and outside the lab. You will figure out where your heart lies and which path you should follow. Tomasz, thank you for all the wonderful (and childish) activities we had in Glasgow, Walibi and the Biesbosch. Enjoy your stay in Oxford! Bowen, I am proud to see your change in openness and self-esteem (including dancing the Macarena at CHAINS!). Thanks for all the help in the lab and our discussions about DSA. Vasu, I

really liked all your philosophical conversations we had about being a PhD researcher and about what we are looking for in life. Tobias, thanks for all the 'gezellige' drink and pizza gatherings you organized and I really appreciate your ride to the Rijksmuseum when I was not able to. Hendrik, I loved and will miss our discussions about the Dutch and German language as I never thought of these things before. Jos, you are still not rid of me. Please continue with all you funny word jokes. Matija, you always join the party and drinks and could never stop talking (even if you do not remember). Thanks for all the nice talks including the scholekster bird. Serhii, I really enjoyed the canoeing in the Biebosch. Thank you for helping me in the job application stage and for always being there when I or somebody else needed help in the lab. Benjamin, your drive to make the top is astonishing and inspiring. You even asked me on parties research related questions. Glad I could help! Guotai, my new office neighbor whom is always working. Thank you for all the insights in organic chemistry. Kai, you always came into my office with a Dutch letter. You are a great and proud father. Vincent, thank you for all your help with MatLab, without you I would never have succeeded. Wouter, you already did a lot of work about the nicotinamides before me resulting in a strong support. Thank you for all your help and work. Qian, every time I talked to you I was amazed by your motivation and work ethics. I am convinced you will become a great professor in China. Emma, your photo of Alice and Maya coloring in their Sinterklaas book will always stay in my mind. Thank you for all the nice talks. Fan, when I heard someone running over the corridor it was always you. Good luck with your defense soon and please do not work too hard. Irene, I am happy to see you always joining the drinks and parties! Good luck with your PhD. Cansel, thank you for the Sinterklaas gift you made together with Lars. I will never forget this. Furthermore, I would like the rest of the group: Angie, Chandan, Elena, Elmira, Frank Versluis, Karolis, Mariano, Reece, Sahil, Sander, Suellen, Yiming, Yongjun, thank you all for the nice time working and chatting together.

Additionally, I would like to thank all the staff members for helping me with my measurements. Although, our relations on a more personal level were way more important. Lars, I am happy that I will never hear you talk about ducks anymore (hopefully not on the defense party as well) and thank you for the nice time we had during the PBV courses. Marcel, thank you for sharing the most vivid stories about volleyball, holidays and your children. Ben, I still remember our conversion about saying 'no' at the end of my PhD. Thanks for the advice, I have completed my PhD because of this lesson. Stephen Eustace, I am still amazed about all the languages you speak. Thank you for all the ^{19}F-NMR measurements you obtained for me. Duco, you

are also slowly integrated in ASM. Thank you for helping us with the lab management. Veby, our loving 'mother' of the group. You always gave me a warm and happy feeling when talking to you. Tonny Schuit, thank you for all the advice about chemicals, the lab and of course for setting my chair and desk when my back hurt. Louw, your directness and decisiveness helped us arise from the chaos, thanks! Arco, thank you for always immediately helping me when I had problems with my laptop, even at the very end.

Job and Marta, thank you for the pleasant and critical collaboration which resulted in a very good review. Frank Hollmann and Caroline, your knowledge about nicotinamides is amazing. Thank you for sharing your knowledge with me over the recent years. Bas van Ravensteijn, Kanvaly and Willem, unfortunately a publication was not yet reachable within our collaboration, but I am convinced that an article can be published in the future! Thank you for the warm welcome at the UU and I really liked to work with colloids again.

Supervising all the students during my PhD research really opened my eyes and gave me a lot of satisfaction. Therefore I would like to thank you all for directing me towards my new career as a chemistry teacher. Pepijn, we always had a lot of fun working together in front of the fumehood! Hope you will graduate soon and we keep in touch. Martijn, working with you already gave me insights in working at the Hogeschool. You are a very attentive and social person. Allan Starkholm, you were my first student to supervise during a period I was still learning a lot. I am proud that you are now doing a PhD as well. LO2 students, Charley, Matthijs, Menno en Olivier. We had a lot of fun together and I am happy to see that you made your projects work! Thank you for the addition of your research into my thesis.

Janneke, jij moest het met mij uithouden tijdens mijn PhD en alle verhalen aanhoren. Ik ben blij dat we dit overleefd hebben en nog steeds vriendinnen zijn. Mijn volleybalteam en trainers, Anouk, Hedy, Ilse, Kelly, Laura, Linde, Lizette, Manon, Marjolein, Sabine, Nico, Rik en Teus. Dank jullie allemaal voor al het gelach, de filmpjes en audioberichten in het weekend (waar Thijs altijd zo blij mee was…). En natuurlijk voor de heerlijke trainingen om alle stress en werk gerelateerde problemen te vergeten. De ex-huisgenoten van Thijs: Cynthia, Wesley, Patrick, Sophie en Rik, ik ben blij dat ik jullie heb ontmoet en jullie mij omarmden als een echte huisgenoot. Ik heb weer zin in de vakantie volgend jaar! Nieuwe collega's van de Hogeschool Rotterdam, te veel om allemaal op te noemen. Bedankt voor het warme onthaal, ik hoop dat we een gezellige tijd tegemoet gaan.

En dan natuurlijk als laatste mijn directe familie. Mijn schoonouders, Leonie en Robert, bedankt voor jullie warme ontvangst en alle steun die jullie hebben gegeven. Jullie zijn altijd heel attent en geïnteresseerd, dit geeft mij iedere keer een goed gevoel. Jorinde, met jou is altijd wat te beleven, bedankt voor alle verhalen. Ik geniet steeds van onze gesprekken waarbij we elkaar uitdagen, zoals laatst bij Catan. Thomas, ik ken je nog niet zo lang, maar het eerste contact is gezellig.

Bas, bedankt dat je in een pinguïnpak rond wil lopen als paranimf. En voor onze goede band waarbij we verassend genoeg nooit meer ruzie hebben en gezellig Netflix kijken of wat gaan doen samen. Lieve mam en pap, dank jullie wel voor jullie steun en dat ik altijd bij jullie terecht kan. Het voelt als een grote steun dat jullie trots op me zijn.

Lieve Thijs, mijn grote liefde. Samen hebben we al heel wat meegemaakt en we zijn dankzij elkaar sterker geworden. Dankjewel dat je voor mij zorgde als ik weer eens eenzaam of eigenwijs was. Jij geloofde altijd in mij. Bedankt voor al je liefde en steun tijdens onze reis.

About the author

Susanne Alida Petronella (Susan) van Rossum was born on 4th of November in Vlist, The Netherlands. She started the Bachelor *Chemistry* in 2009 at Utrecht University finishing with a bachelor thesis about synthesizing anisotropic organic. After obtaining her Bachelor in 2012 she started the Master *Nanomaterials: Chemistry and Physics* at Utrecht University. The master thesis was focused on the synthesis and analysis PbS quantum dots and its usage for self-assembled structures using the oriented attachment method. The Master was finished with an internship at Croda BV, Gouda about self-healing polymers. In 2014 her PhD about catalytic control in out-of-equilibrium systems started at Delft University of Technology under the supervision of Prof. dr. Jan H. van Esch and dr. R. Eelkema. The project focuses mainly on out-of-equilibrium systems using different assembly materials, such as crystals, polymers, colloids and hydrogels.

List of publications

- F. Trausel, B. Fan, <u>S. A. P. van Rossum</u>, J. H. van Esch, R. Eelkema, Aniline catalyzed hydrazone formation reactions show a large variation in reaction rates and catalytic effects, *Adv. Synth. Catal.*, 2018, **360**, 2571-2576.

- C. van Overbeek, J. Peters, <u>S. A. P. van Rossum</u>, M. Smits, M. van Huis, D. Vanmaëkelbergh, Interfacial self-assembly and oriented attachment in the family of PbX (X=Se, S, Te) nanocrystals, *J. Phys. Chem. C*, 2018, **122**, 12464-12473.

- <u>S. A. P. van Rossum</u>, M. Tena-Solsona, J. H. van Esch, R. Eelkema, J. Boekhoven, Dissipative out-of-equilibrium assembly of man-made supramolecular materials, *Chem. Soc. Rev.*, 2017, **46**, 5519-5535.

- M. P. Boneschanscher, W. H. Evers, J. J. Geuchies, T. Altantzis, B. Goris, F. T. Rabouw, <u>S. A. P. van Rossum</u>, H. S. J. van der Zant, L. D. A. Siebbeles, G. van Tendeloo, I. Swart, J. Hilhorst, A. V. Petukhov, S. Bals, and D. Vanmaekelbergh, Long-range orientation and atomic attachment of nanocrystals in 2D honeycomb superlattices*, Science,* 2014, **344**, 1377-1380.

Manuscripts submitted or in preparation

- B. Fan, Y. Men, <u>S. A. P. van Rossum</u>, G. Li, R. Eelkema, A fuel-driven chemical reaction network based on conjugate addition and elimination chemistry, *accepted by ChemSystemsChem*.

- <u>S. A. P. van Rossum</u>, W. E. Hendriksen, V. A. A. le Sage, F. Hollmann, R. Eelkema, J. H. van Esch, Catalytic control over individual kinetic pathways in a chemical reaction network leading to transient crystallization, *in preparation*.

- <u>S. A. P. van Rossum</u>, P. R. Bouwmans, J. H. van Esch, R. Eelkema, Catalytic control over transient polymer agglomeration and its use for transient compartmentalization, *in preparation*.

- F. Trausel, <u>S. A. P. van Rossum</u>, H. H. P. J. Gerlings, M. Lovrak, M. P. van der Helm, T. Brevé, J. H. van Esch, R. Eelkema, Reversible control over catalytic activity through host-guest chemistry, *submitted*.